Semiconductors, Vol. 38, No. 2, 2004, pp. 125–147. Translated from Fizika i Tekhnika Poluprovodnikov, Vol. 38, No. 2, 2004, pp. 129–150.

REVIEW

Radiation Resistance of SiC and Nuclear-Radiation Detectors Based on SiC Films

A. A. Lebedev, A. M. Ivanov, and N. B. Strokan

Ioffe Physicotechnical Institute, Russian Academy of Sciences, Politekhnicheskaya ul. 26, St. Petersburg, 194021 Russia

e-mail: alexandr.ivanov@pop.ioffe.rssi.ru

Submitted March 5, 2003; accepted for publication April 30, 2003

Abstract—Available results of studying the radiation resistance of SiC and developing the nuclear-radiation detectors based on SiC are analyzed. The data on the ionization energies, capture cross sections, and plausible structure of the centers formed in SiC as a result of irradiation with various particles are reported. The effect of irradiation on the charge-carrier concentration and recombination processes is considered. Two aspects are covered in describing the results of designing SiC-based detectors and studying the detector parameters. First, the specific potential of SiC detectors for solving problems in nuclear physics is considered; typical examples of detector applications are given. Second, the relationship between detector characteristics and the properties of the starting material is considered; a number of methods for determining the specific parameters of SiC based on the characteristics of detectors are described. It is concluded that recent progress in the growth of high-quality SiC films (the difference impurity concentration ranges from 3×10^{14}–3×10^{15} cm^{-3} and the density of micropipe defects is no higher than 1 cm^{-2}) makes it possible to include SiC in the class of materials that can be used to fabricate advanced nuclear detectors. The technological potential of SiC has been far from exhausted; undoubtedly, various configurations of SiC-based detectors (including multielement configurations) will be developed in the near future. © *2004 MAIK "Nauka/Interperiodica".*

1. INTRODUCTION

Modern civilization needs increasingly more consumable-energy sources in order to sustain progress in society. Atomic energy and the solar-radiation conversion using ground-based and orbital converters will probably be the main energy sources in future. Efforts to improve the reliability of both atomic power plants and space-technology systems should be based on the use of radiation-resistant electronics. Radiation resistance typically means that the semiconductor or semiconductor-device parameters are not affected by exposure to nuclear radiation: the higher the radiation dose corresponding to the onset of variation in parameters, the higher the radiation resistance. Semiconductors with a high bonding energy, such as diamond, BN, and SiC, are traditionally thought of as radiation-resistant materials. The advances in technology achieved in the last 10–15 years have made it possible to develop SiC-based devices that have fulfilled the expected high potential of SiC in respect to switching power and high operation temperatures. It is now of current practical interest to check to what extent the radiation resistance of SiC corresponds to theoretical predictions. In this context, the aim of this review is to summarize the available experimental data and assess the correspondence between the parameters of SiC-based devices and theoretical predictions.

In Sections 2 and 3 of this review, we consider both general concepts of radiation resistance of semiconductors as applied to SiC and the properties of radiation defects that appear in SiC as a result of irradiation with gamma-ray photons and various particles. In Section 4, we consider the parameters of nuclear-radiation detectors based on SiC, since these detectors make it possible to compare in the most straightforward way the radiation resistance of materials from which these detectors are manufactured. Nuclear detectors are most sensitive to a large number of properties, including the degradation of parameters of the charge-carrier transport and the emergence of inhomogeneity in these parameters, the temporal stability of the magnitude (and sign) of volume charge of impurities, and the presence of deep-level centers in the case of both capture and generation of charge carriers.

Sections 2 and 3 were written by A.A. Lebedev, and Section 4 was written by N.B. Strokan and A.M. Ivanov.

2. RADIATION DEFECTS FORMED IN SIC EXPOSED TO VARIOUS TYPES OF RADIATION

2.1. Threshold Energy for Defect Production

As mentioned above, the radiation resistance is typically higher for semiconductors with a higher bonding energy. In order to characterize the correlation between

Table 1. Calculated and experimental values of threshold energy for defect production in several semiconductors

Parameter	GaAs	Si	3*C*-SiC	Diamond	6*H*- and 4*H*-SiC
Lattice constant a_0, Å	5.65	5.431	4.36	3.57	3.08
E_d, eV (calculation using (1))	9	12.8	37	80	153
E_d, eV (experiment)	8–20 [2]	13–20 [2]	106 [4]	60–80 [2]	97 [6]
			54–90 [5]		20–35 [7]

the radiation resistance and the bonding energy, the threshold energy for defect production (E_d) is introduced as an important parameter. By this we mean the minimal energy that should be transferred by a particle to the semiconductor atom to form a Frenkel pair (i.e., a vacancy and an interstitial atom) in the lattice [1, 2]. Theoretical calculation of the value of E_d is related to solving the many-body problem and encounters a number of difficulties related to the choice of the type and parameters of the interaction potentials (among other parameters) [2]. When the energy E_d is experimentally determined, the variation in a single chosen parameter under the effect of irradiation is usually monitored, although radiation affects all properties of a semiconductor simultaneously. As a result, the values of E_d exhibit a large spread and depend on experimental conditions. According to Corbett and Bourgoin [3], the quantity E_d and the lattice constant a_0 of a specific semiconductor are related by the following phenomenological formula:

$$1.117E_d = (10/a_0)^{4.363}. \quad (1)$$

Here, E_d is expressed in eV and a_0 is expressed in Å.

The values of E_d calculated using formula (1) for a number of semiconductors and experimental data on E_d are listed in Table 1. As can be seen from Table 1, there is an appreciable spread in the experimental values of E_d for silicon carbide. This spread is possibly related to the low structural quality of SiC crystals, especially those dealt with in studies carried out before the mid-1990s. It is noteworthy that the experimental value of E_d is found to be larger than the values calculated using formula (1) for cubic silicon carbide (3*C*-SiC) and is larger than those for hexagonal silicon carbide (6*H*- and 4*H*-SiC). Since the structural quality of 3*C*-SiC crystals is so far much lower than that of 6*H*- and 4*H*-SiC crystals, we may assume that the value of E_d does not exceed 30–35 eV for all SiC polytypes. This value of E_d is larger than those for Si and GaAs by a factor of 1.5–2 and is smaller than that for diamond by a factor of 2–2.5. However, additional experiments aimed at determining the exact value of E_d and carried out with present-day high-quality epitaxial SiC films are needed. It is also important to determine the temperature dependence of E_d for SiC as a material that is promising for applications in high-temperature electronics.

Table 2. Number of primary radiation defects produced by a single particle or photon in a number of semiconductors; this number was normalized to the corresponding value for silicon carbide

Semiconductor	Protons	Pions	Cosmic rays
Diamond	1.2	0.7	0.5
Silicon	2.4	4.1	3.3
Gallium arsenide	12	43.8	27.5

The values of threshold energies make it possible to calculate the number of primarily produced radiation defects. The data in [8] for materials that are relevant to problems in the physics of high energies (detection of relativistic and cosmic-ray particles) are listed in Table 2. It can be seen that, with respect to the number of primary defects, SiC ranks insignificantly below diamond but is appreciably superior to silicon (and even more so, to gallium arsenide).

2.2. Parameters of Radiation Defects

2.2.1. Irradiation with electrons. Deep levels located at $E_c - 0.35$, $E_c - 0.6$, and $E_c - 1.1$ eV were found in the band gap of *n*-6*H*-SiC irradiated with 3.5- to 4-MeV electrons [9]. The corresponding deep-level centers were annealed out at a temperature of ~1300 K. Taking into account the ionization energies of these centers, the latter can identified with the known structural defects S (E_1/E_2) and Z_1/Z_2 and with the center with a level at $E_c - 1.06$ eV [10]. The research reported in [9] was later continued for *n*-6*H*-SiC irradiated with 2-MeV electrons [11]. In addition to an increase in the background concentration of the E_1/E_2 and Z_1/Z_2 centers, new centers E_3/E_4 ($E_c - 0.57$ eV) were detected. Such an increase in the concentration of the S (E_1/E_2) centers was subsequently observed after irradiation with 2-MeV electrons [12]. In addition, deep-level centers ($E_c - 0.51$ eV) were detected; these centers were annealed out at a temperature of ~1100 K. The *S* centers were found to have the highest thermal stability; they were annealed out at temperatures no lower than ~1300 K.

A number of new deep-level centers were observed in 4*H*-SiC after irradiation of 4*H*-SiC with 2 to 2.5-MeV electrons [12–14], in addition to an increase in the concentration of the background Z_1 centers. These deep-level centers are referred to as EH_1 ($E_c - 0.45$ eV), EH_2 ($E_c - 0.68$ eV), EH_4 ($E_c - 0.72$ eV), EH_5 ($E_c - 1.15$ eV), EH_6/EH_7 ($E_c - 1.65$ eV), and HH_1 ($E_v +$

Table 3. Parameters and properties of radiation defects in 6*H*-SiC

Irradiation with protons [38, 39]			Irradiation with neutrons [24]	Irradiation with electrons [17]	Structural defects	Plausible structure
ionization energy E_t, eV	σ_n, cm^2	annealing temperature, K	ionization energy E_t, eV	the type of defect	the type of defect	
0.16–0.2	6×10^{-17}	800–950	0.13; 0.24	L_1/L_2		A primary defect [39]
0.36/0.4	2×10^{-15}	1100–1800		L_3/L_4	E_1/E_2 [15]; S [40]	A V_{Si} complex [41, 42]
0.5	5×10^{-15}	800–950	0.5	L_6		V_C [17, 42]
0.7	4×10^{-15}	1100–1800		L_7/L_8	Z_1/Z_2 [15]	$V_C + V_{Si}$ [15, 39]
0.8	4×10^{-15}	1100–1800		L_9		
1.1–1.22	2×10^{-15}	1100–1800		L_{10}	R [40]	$V_C + V_{Si}$ [39, 43]

Note: Energy E_t is reckoned from the bottom of the conduction band; σ_n is the cross section for electron capture.

0.35 eV). Many of these centers also appeared after implantation with He and some other ions [15]. Recently [16, 17], it was reported that several new centers had been observed: $E_c - 0.2$ eV, $E_c - 0.32$ eV, and $E_c - 1.34$ eV. The majority of all the aforementioned deep-level centers are also present in unirradiated 4*H*-SiC. The structure of these centers was typically identified with that of defects. Puntilie *et al.* [18] analyzed the effect of the growth conditions of 4*H*-SiC on the concentration of $Z_{1,2}$ centers and suggested that this center was a complex that included a nitrogen atom and an interstitial C atom or, which is less probable, a N atom and a Si vacancy (V_{Si}). The structure of the center with the level at $E_c - 0.5$ eV was also related to that of an impurity–vacancy complex, since this center featured low thermal stability and a low ultimate concentration.

Two types of deep-level centers ($E_v + 0.55$ eV and $E_v + 0.78$ eV) were observed in *p*-6*H*-SiC irradiated with 1.7-MeV electrons [19]. Both types of centers were annealed out at temperatures of 500–800 K. According to the data obtained using the electron spin resonance (ESR) measurements, irradiation of *p*-6*H*-SiC with 300-keV electrons gives rise to Frenkel pairs V_{Si}–Si_I in addition to individual silicon vacancies. Irradiation with 2-MeV electrons gives rise only to monovacancies V_{Si} [20]. Photo-ESR studies of *p*-4*H*-SiC irradiated with 2.5-MeV electrons suggested that the deep-level center ($E_v + 1.47$ eV) could be identified with a positively charged carbon vacancy [21].

2.2.2. Irradiation with neutrons. A number of types of deep-level centers ($E_c - 0.5$ eV, $E_c - 0.24$ eV, and $E_c - 0.13$ eV) were observed in SiC irradiated with neutrons [22–24]. It was assumed [25, 26] that stable vacancy-related complexes were formed as a result of annealing; these complexes were presumably electrically inactive. It was found that weak *n*-type conductivity could be detected in *p*-SiC irradiated with neutrons and not subjected to postirradiation annealing [24, 27]. There were also other publications concerned with the effect of neutron radiation on the properties of SiC [28, 29]. The effect of neutron radiation on the current–voltage characteristics of various devices has been studied in most detail. It has been established that the carrier-removal rate (the number of removed carriers per one neutron and one centimeter) amounts to ~4.5 cm^{-1}, which is lower than that in silicon by a factor of approximately 3 [30]. The centers with a deep level at $E_c - 0.49$ eV were detected in 3*C*-SiC irradiated with neutrons; these centers were annealed out at a temperature of ~650 K [31]. The measured carrier-removal rate is equal to 7.2 cm^{-1}, which is close to the value of 7.8 cm^{-1} measured for silicon irradiated with neutrons with the identical spectrum. Two annealing stages (at 350 and 500 K) were observed in studies of the charge-carrier mobility in *n*-SiC irradiated with reactor neutrons [32].

2.2.3. Irradiation with alpha particles. It was reported [33] that irradiation of *n*- and *p*-6*H*-SiC with alpha particles only brought about an increase in the concentration of already existing background defects. It was concluded that the radiation resistance of SiC is no lower than the radiation resistance of InP, which is another radiation-resistant material. The effect of irradiation with He^+ ions on 4*H*- and 6*H*-SiC was considered in detail by Dalibor *et al.* [15]. The parameters of observed radiation defects coincided to a large extent with those of radiation defects detected previously in SiC irradiated with electrons.

2.2.4. Irradiation with gamma-ray photons. The results of studying the ESR spectra of *p*-4*H*- and *p*-6*H*-SiC crystals irradiated with gamma-ray photons were reported by Il'in *et al.* [34]. Three types of paramagnetic centers were detected; these centers decomposed at 160°C. It was assumed that the corresponding ESR spectrum was related to a single type of centers that involved carbon vacancies or to a complex composed of an Al impurity atom and a C atom that occupies the silicon or interstitial sites.

2.2.5. Irradiation with protons. Deep-level centers formed in 4*H*- and 6*H*-SiC of *n*-type conductivity as a result of irradiation with 8-MeV protons were previ-

Table 4. Parameters and properties of radiation defects in 4*H*-SiC

Irradiation with photons [39]			Irradiation with electrons [12–14, 16, 17]	Implantation of He^+ [15]	Structural defects	Plausible structure
ionization energy E_t, eV	σ_n, cm^2	annealing temperature, K	ionization energy, defect type	the type of defect	ionization energy, defect type	
0.18	6×10^{-15}	800–950	$E_c - 0.2$ eV	P_1/P_2	$E_c - (0.18–0.2)$ eV [44]	A primary defect [39]
			EH_1 ($E_c - 0.45$ eV)			Vacancy + impurity [16]
0.63–0.7	5×10^{-15}	1100–1800	EH_2, EH_4	Z_1	Z_1 [15]	V_C [39], a V_{Si} complex [45] N + V_{Si}, [18]
0.96	5×10^{-15}	1100–1800		$RD_{1/2}$	$E_c - 1.1$ eV [46]	$V_C + V_{Si}$ [39, 47]
1.0	1×10^{-16}	1100–1800	EH_5	RD_3		
1.5	2×10^{-13}	1100–1800	EH_6/EH_7	RD_4		

Note: Energy E_t is reckoned from the bottom of the conduction band; σ_n is the cross section for electron capture.

ously studied in detail [33–37]. The parameters of these centers are close to those of the centers detected previously in SiC irradiated with electrons (Tables 3, 4). The ESR data show that the observed centers are either carbon vacancies ($E_c - 0.5$ eV in 6*H*-SiC and $E_c - (0.63–0.7)$ eV in 4*H*-SiC) or pairs of vacancies in the carbon or silicon sublattices. Apparently, the different thermal-ionization energies of centers that presumably have the same structure ($V_{Si} + V_C$) can be attributed to dissimilar distances between the components of the pairs (vacancies); these distances are characteristic of each of the aforementioned radiation defects. The above results were obtained using the method of positron spectroscopy for *n*-6*H*-SiC irradiated with low-energy protons [43, 48]. It was found that irradiation with protons gave rise to various types of divacancies $V_{Si} + V_C$, as well as individual vacancies that were annealed out at a temperature of ~900°C [48]. It was also assumed that a certain divacancy was responsible for a center with a deep level near the midgap [43]. At the same time, only silicon monovacancies annealed out at a temperature of ~1100°C were observed in the *n*-6*H*- and *n*-4*H*-SiC samples irradiated with 12-MeV protons [49]. Davydov *et al.* [50] analyzed the results of studying *n*-6*H*-SiC irradiated with protons with various energies. It was shown that the *R* centers ($E_c - 1.1$ eV) featured the highest production rate: 0.17, 70, and 700 cm^{-1} for protons with energies of 1 GeV, 8 MeV, and 150 keV, respectively.

2.3. Defect-Related Luminescence

Short-wavelength luminescence with photon-emission energies ranging from 2.3 to 2.6 eV in *n*-6*H*-SiC crystals irradiated with K and Li ions and then annealed was first observed by V.V. Makarov in 1966 [51]. The luminescence spectrum consisted of (i) two triplets of narrow lines (*H* and *L* lines) near an energy of 2.6 eV and (ii) a broad featureless band with an emission peak at 2.35 eV. It was ascertained [52, 53] that the broad band did not result from the development of a fine structure. It was assumed that this band was related to radiative recombination involving a donor nitrogen level and an acceptor center that was produced in the course of implantation. Patrick and Choyke [54] studied in detail the structure of the *H* and *L* lines and the temperature dependences of the luminescence spectrum; the latter was called the D_1 spectrum. This spectrum was observed in SiC after irradiation with electrons [55], neutrons [56], and ions of various types [53], which made it possible to use 6*H*-SiC ion-implanted with Al as a material for fabricating efficient light-emitting diodes that operated in the green region of the spectrum [57]. Irradiation of other SiC polytypes gave rise to luminescence with similar properties [52]. Since this luminescence emerged as a result of irradiation or implantation of SiC with various ions, it was assumed that a center acting as the activator of luminescence had either a pure defect-related structure or was a complex which consisted of an intrinsic defect and an atom of a background impurity [58–60]. Choyke [61] detected excitons bound to deep-level centers in SiC. However, the levels related to these centers were not observed. It was assumed that the D_1 spectrum could be related to the Z_1 centers in 4*H*-SiC [15] or to the *i* centers in 6*H*-SiC [62].

It may be concluded from the consideration of the summarized results of studying the radiation defects in SiC that the spectrum of radiation defects in each of the silicon carbide polytypes is almost independent of the methods for growing the samples and the type of particles used for irradiation (protons, electrons, alpha particles). In addition, irradiation mainly brings about an increase in the concentration of deep-level centers that already exist in the material. According to ESR data, the vast majority of radiation defects consist of elementary lattice defects, i.e., vacancies and interstitial atoms

Table 5. Values of V_d for SiC and Si according to various publications

Semiconductor	$N_d^+ - N_a^-$, cm^{-3}	Particles/energy/dose	V_d, cm^{-1}	References
4*H*-SiC	1×10^{15}	α/1.7 MeV/2×10^9 cm^{-2}	4×10^5	[65, 66]
	2×10^{18}	H^+/350 keV/1×10^{14} cm^{-2}	2×10^4	[67]
		Protons/8 MeV/6×10^{14} cm^{-2}	130	[39]
		The same	67*	[39]
6*H*-SiC		α/55 MeV/2×10^{11} cm^{-2}	7.8×10^4	[33]
		Neutrons	4.5	[69]
	4×10^{16}	Protons/8 MeV/6×10^{14} cm^{-2}	17	[39]
	The same	The same	–45*	[39]
3*C*-SiC	10^{16}	Neutrons/1 MeV/10^{14} cm^{-2}	7.2	[68]
		Electrons/1 MeV	0.014	[70]
Si		α/1.7 MeV/2×10^9 cm^{-2}	5×10^4	[65, 66]
		Neutrons/1 MeV/10^{14} cm^{-2}	7.8	[68]
		Electrons/1 MeV	0.01–0.1	[2]
		Protons/8 MeV/6×10^{14} cm^{-2}	200–350	[71, 72]

* T = 650 K. Other quantities were measured at T = 300 K.

(or their combinations). Irradiation of SiC was carried out at temperatures of 295 K or lower in all the studies cited above. Apparently, primary radiation defects in SiC at the aforementioned temperatures have a low mobility and cannot form complex secondary defects that include, for example, impurity atoms.

3. EFFECT OF RADIATION ON MATERIAL PROPERTIES

3.1. The Lifetime of Minority Charge Carriers

It is known that radiation is used to reduce the lifetime of charge carriers in fast-response devices based on Si. Such a method for reducing the lifetime has practically not been employed in the case of SiC, since the problem of increasing the lifetime of minority charge carriers is more urgent for this material. Nevertheless, this problem may arise in future. At present, there is no generally accepted opinion as to which deep-level centers control the lifetime in SiC. For 6*H*-SiC, it was shown that the *R* centers with the level at $E_c - 1.1$ eV (near the midgap of this polytype) can act as the aforementioned lifetime-controlling centers [63]. Lebedev *et al.* [37] measured the hole diffusion length (L_p) in *n*-6*H*-SiC irradiated with various doses of 8-MeV protons. Figure 1 shows the dependence of L_p^2 on the concentration of *R* centers (N_R). As can be seen from Fig. 1, the dependence $L_p^2 \propto 1/N_R$ is the same for irradiated samples as for unirradiated samples. Thus, the radiation-based method for controlling the lifetime may turn out to be promising in *n*-6*H*-SiC where the production rate of *R* centers exceeds that of other radiation defects.

3.2. The Rate of Removal of Charge Carriers in Silicon Carbide

The formation of radiation defects with deep levels in the band gap of a semiconductor brings about a redistribution of charge carriers and a change in the conductivity of the material. If a material with *n*-type conductivity is irradiated, electrons are transferred from the

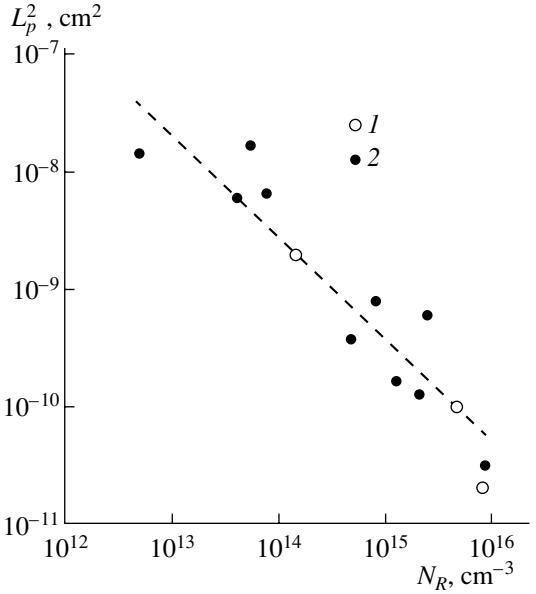

Fig. 1. Dependence of the hole diffusion length on the concentration of the *R* centers [37]. Unfilled circles *1* correspond to the sample after irradiation with several doses and annealing; filled circles *2* correspond to an unirradiated samples.

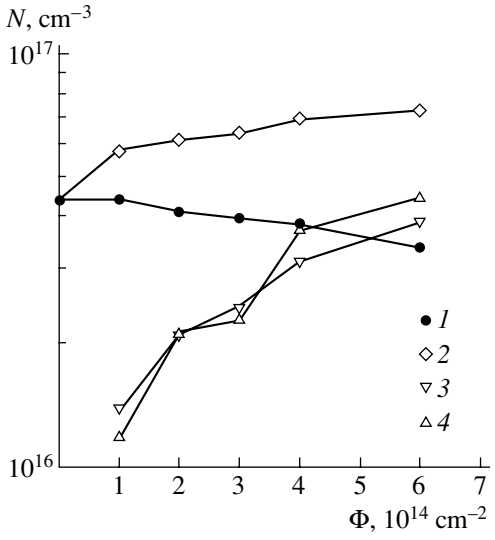

Fig. 2. Dependences of characteristic concentrations N in 6*H*-SiC on the dose of irradiation with protons [39]. Curves *1* and *2* correspond to $N_d^+ - N_a^-$ at $T = (1)$ 300 and (*2*) 650 K; curve *3* represents the difference between curves *2* and *1*; and curve *4* represents the concentration of the centers with the level at $E_c - (1.1–1.22)$ eV.

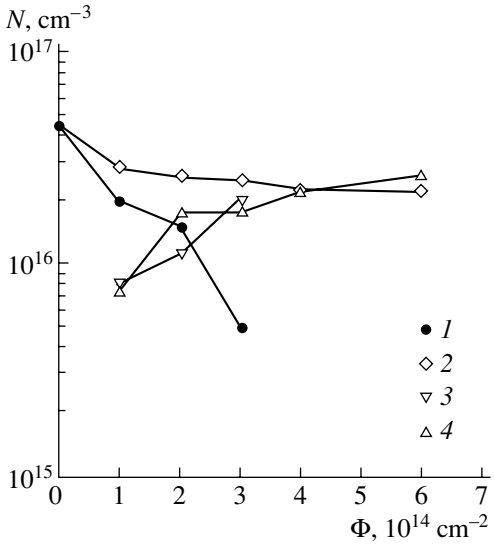

Fig. 3. Dependences of characteristic concentrations N in 4*H*-SiC on the dose of irradiation with protons [39]. Curves *1* and *2* correspond to $N_d^+ - N_a^-$ at $T = (1)$ 300 and (*2*) 650 K; curve *3* represents the difference between curves *2* and *1*; and curve *4* represents the total concentration of radiation defects $RD_{1,2} + RD_3 + RD_4$.

conduction band to deep levels of acceptor-type radiation defects.

As a result, the conductivity of the material decreases, so that the semiconductor can become an insulator if the radiation doses are high. In order to describe this process in various materials, the removal rate for charge carriers V_d is used; this parameter is defined as

$$V_d = \Delta n/\Phi = (n_0 - n)/\Phi, \qquad (2)$$

where n_0 and n are the concentrations of charge carriers in the conduction band before and after irradiation and Φ is the radiation dose. Lebedev *et al.* [64] considered the special features of determining the parameter V_d for silicon carbide and wide-gap semiconductors (WGSs) in general. Deep-level centers with an ionization energy of $\gtrsim 1$ eV can be formed in irradiated semiconductors with a wide band gap E_g. Such centers will virtually not be ionized at room temperature, and the quantity V_d will exhibit a temperature dependence that will become less pronounced with increasing temperature of measurements even at temperatures higher than 295 K.

We now consider experimental studies in which the quantity V_d was determined when SiC was irradiated with particles of various types. The results of these studies and the available values of V_d for silicon obtained under the same irradiation conditions are listed in Table 5.

According to the data obtained in the majority of studies, $V_d(\mathrm{Si}) \geq V_d(\mathrm{SiC})$ at 300 K. Data obtained recently [65, 66] contradict the general pattern: $V_d(\mathrm{SiC})/V_d(\mathrm{Si}) \sim 10$. Crystals were irradiated with 1.7-MeV alpha particles with a dose of 2×10^9 cm^{-2} [65, 66]. The ion ranges were equal to 3.8 μm for SiC and 5.9 μm for Si. It is worth noting that only the effects at the end of the particle ranges were monitored in [65, 66]; therefore, the effect could be attributed mainly to helium clusters formed at this depth rather than to radiation defects.

In addition, the results reported so far [65–70] were obtained at room temperature, in which case the value of V_d is still large. The deep-level centers formed in *n*-4*H*- and *n*-6*H*-SiC as a result of irradiation with 8-MeV protons were studied in [35–39]. It was established that the difference concentration of ionized donors and acceptors $N_d^+ - N_a^-$ measured at room temperature decreased after irradiation. At the same time, it was observed that this concentration increased after heating the structure to 650 K. The value of $N_d^+ - N_a^-$ measured at 650 K in irradiated 6*H*-SiC was even larger than in unirradiated samples. As the radiation dose increased, this difference between the irradiated and unirradiated samples increased (Figs. 2, 3). Thus, the measurements performed at high temperatures support the conclusion that for SiC either $V_d(300\ \mathrm{K}) > V_d(650\ \mathrm{K})$ (for 4*H*-SiC) or the value of V_d (650 K) becomes negative (for 6*H*-SiC) [39]. Evidently, both donor and acceptor radiation defects (with donors being dominant) are formed as a result of irradiation of *n*-6*H*-SiC. Apparently, the same mechanism is also active for *p*-6*H*-SiC, in which case the change in the conductivity type ($p \longrightarrow n$) is observed as a result of irradiation [39].

An approach to the formation of radiation defects in WGSs was previously developed [73] in which a mechanism similar to the self-compensation of conductivity was considered. According to Vinetskiĭ and Smirnov [73], the change in the conductivity type as a result of irradiation is characteristic only of narrow-gap semiconductors, whereas the conductivity of WGSs tends to intrinsic conductivity as the radiation dose increases. Indeed, this inference is consistent with experiment only if the irradiation of WGSs is carried out at room temperature. However, if the temperature dependence of V_d is taken into account, the aforementioned approach is valid only for 4*H*-SiC. An increase in the difference concentration of donors and acceptors $N_d^+ - N_a^-$ as a result of irradiation is observed in 6*H*-SiC and, apparently, in 3*C*-SiC [74].

Thus, measurements of V_d at room temperature cannot clarify whether the devices based on WGSs are suitable for operation at high temperatures.

3.3. Radiation-Induced Doping (Compensation) of SiC

Another important aspect of the interaction of ionizing radiation with semiconductors is the phenomenon of radiation-induced doping. As a result of this doping, local regions with the high resistivity required for fabricating a specific device can be formed in a semiconductor. It is generally believed that the radiation resistance and the feasibility of radiation-induced doping are contradictory characteristics of a material; i.e., if a semiconductor is radiation-resistant, this material is considered as not suitable for compensation by the method of radiation-induced doping.

In what follows, we will show that the above assessment is not quite correct in the case of SiC. It is known that SiC is a promising material not only in relation to high-temperature electronics but also with respect to applications in a number of devices that are not designed for operation at high temperatures. These devices primarily include high-frequency devices (Schottky diodes and certain types of field-effect transistors) whose structure involves a metal–semiconductor contact. As a rule, such a contact degrades rapidly with increasing temperature, irrespective of the limiting operation temperatures of the semiconductor itself. If the operation temperatures of the device are not much higher than 300 K, we can use the values of V_d obtained at 300 K in order to estimate the efficiency of radiation-induced doping of SiC. The largest value of resistivity (ρ_M) that can be attained in the semiconductor is another important characteristic of the efficiency of radiation-induced doping.

As a result of irradiation, the Fermi level in an *n*-type material should shift to the deepest level of the radiation defects produced. The value of ρ_M should be controlled by the concentration of charge carriers in the conduction band of a semiconductor, i.e., by the level depth and degree of ionization of a given deep-level center. If the semiconductor's band gap becomes wider, radiation defects with deeper levels and with a lesser degree of ionization can be formed in this semiconductor. Thus, WGSs offer clear advantages over narrow-gap semiconductors in the production of high-resistivity layers. It is important that the semi-insulating properties of these layers are also retained at temperatures higher than 295 K. As shown by Anikin *et al.* [63], the resistivity of 4*H*-SiC at T = 450°C is equal to the largest value attained for GaAs (~10^9 Ω cm) at room temperature.

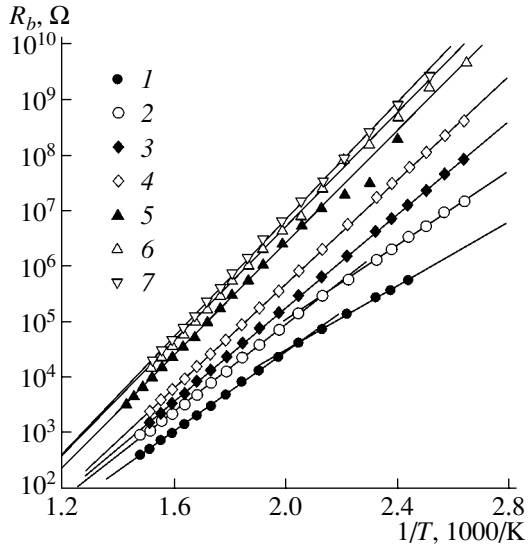

Fig. 4. Temperature dependences of the forward resistance of a Schottky diode based on 6*H*-SiC after proton irradiation with doses Φ = (*1*) 3×10^{14}, (*2*) 4×10^{14}, (*3*) 6×10^{14}, (*4*) 1×10^{15}, (*5*) 2×10^{15}, (*6*) 5×10^{15}, and (*7*) 1×10^{16} cm^{-2}.

A number of researchers have studied the feasibility of proton (hydrogen) passivation of silicon carbide [67, 75–78]. It was shown that the resistivity of *n*-4*H*-SiC at room temperature exceeded 8×10^6 Ω cm after irradiation with 350-keV protons with a dose of 1×10^{14} cm^{-2} [67]; the resistivity decreased rapidly with increasing temperature. Irradiation with 8-MeV protons [39] also brought about an increase in the ohmic resistance of 4*H*- and 6*H*-SiC structures subjected to forward biases (R_b) at room temperature. In contrast to 6*H*-SiC, a decrease (rather than an increase) in total concentration of uncompensated donor centers is observed in 4*H*-SiC samples irradiated with protons. This observation shows that irradiation stimulates the formation of acceptor centers with levels in the lower half of the band gap or the destruction of donor centers with levels in the upper half of the band gap. In addition, irradiation gives rise to acceptor centers with deep levels to which electrons transfer from shallower donor levels.

According to data published [39], the value of R_b decreased exponentially with increasing temperature and featured activation energy ε_A (Figs. 4, 5). As the radiation dose increased, the energy ε_A became higher and tended asymptotically to ~1.1 eV for 6*H*-SiC and

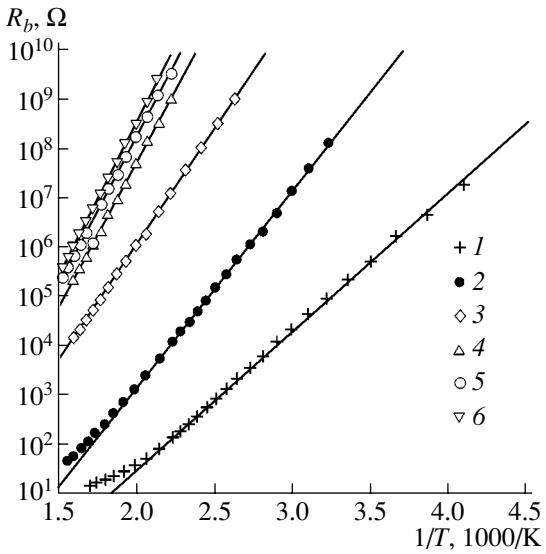

Fig. 5. Temperature dependences of the forward resistance of a Schottky diode based on 4*H*-SiC after proton irradiation with doses Φ = (*1*) 6×10^{14}, (*2*) 1×10^{15}, (*3*) 2×10^{15}, (*4*) 5×10^{15}, (*5*) 1×10^{16}, and (*6*) 2×10^{16} cm^{-2}.

1.25 eV for 4*H*-SiC [39]. This behavior resulted in the formation of *n*-6*H*-SiC layers that were semi-insulating at room temperature. Such layers can be used in the fabrication of devices that are not designed for operation at high temperatures, for example, photodetectors or various radiation detectors.

3.4. Amorphization of SiC as a Result of Irradiation

Amorphization of SiC samples was observed after irradiation with electrons [79], neutrons [80], protons, and various ions (He, Ar, Cr) [81]. It was also noted [81] that the process of amorphization in SiC differed from that characteristic of Si. Only ions that are heavier than B can amorphize silicon at room temperature; lighter ions only give rise to heavily damaged layers of crystalline material even at high implantation doses. At the same time, amorphization of SiC sets in if the critical specific implantation energy (23 eV/atom) is attained, irrespective of the ion mass. It was noted [81] that this difference between Si and SiC may be related to a higher mobility of defects in silicon at room temperature and to the partial annealing (recombination) of these defects directly within the ion track during implantation.

It was also observed [79, 80] that annealing of amorphized layers of hexagonal SiC polytypes led not only to the recovery of the starting-polytype structure but also to the formation of inclusions of the cubic polytype 3*C*-SiC. In our opinion, these results are very important since the physical theory of mutual transformations of SiC polytypes is far from adequate. We believe that it is especially important to gain insight into the causes of changes in the polytype in an already grown epitaxial layer or a device structure. Recently, there have been a number of publications concerned with studies of stacking faults that consisted of inclusions of cubic SiC within diodes based on 4*H*- or 6*H*-SiC. These inclusions were formed when forward current flowed through the diodes under consideration [82–84].

The effect of the above inclusions is usually considered as detrimental since stacking faults represent the regions of efficient recombination of charge carriers and the formation of these regions results in the degradation of parameters of high-power devices based on silicon carbide. At the same time, it was shown that stacking faults with a thickness on the order of several lattice constants act as 3*C*-SiC quantum wells within the wider-gap 4*H*-SiC. As a result of dimensional quantization, the above circumstance resulted in the appearance of intense photoluminescence in the blue region of the spectrum (photon energy $h\nu = 2.5$ eV) [85]. It was also observed that quantum-dimensional stacking-fault structures were formed in a heavily doped 4*H*-SiC layer after additional heat treatment [86]. Unfortunately, the process of formation of stacking faults and related quantum wells in SiC is hitherto uncontrollable.

Even before the first studies of stacking faults, it was inferred from an analysis of the properties and structure of deep-level centers in silicon carbide that intrinsic-defect concentration characteristics existed for each polytype [10, 87]. A variation in the intrinsic-defect concentration can then lead to transformation of a polytype. It was assumed that irradiation (possibly, up to the onset of amorphization) with subsequent annealing can be used to change the defect concentration in a grown structure.

The development of the technology described above would make it possible to radically expand the range of SiC applications and affect the studies of other polytype compounds. However, this method of forming heterostructures requires extensive studies of the irradiation and annealing conditions and preliminary doping of the starting epitaxial layers in order to prove its feasibility.

The formation of hydrogen or helium bubbles in the case of high implantation doses with subsequent exfoliation of the top semiconductor layer in the course of annealing is one of the difficulties in carrying out the aforementioned studies [88, 89]. At the same time, significant progress has been achieved in recent years in the fabrication of heteropolytype SiC structures using epitaxial methods [90–92].

4. THE USE OF SiC FOR DETECTION OF NUCLEAR RADIATION

4.1. History

Nuclear detectors based on SiC occupied a prominent place among detectors even in the first attempts in the 1960s to replace a gas in ionization chambers with a more condensed (semiconductor) medium.

It should be recalled that the typical design of a detector (by analogy with a gas-filled chamber) includes a p^+–n- (n^+–p-) or p^+–i–n^+ diode structure. This structure operates under conditions of reverse bias, which forms an operation (active) zone, i.e., a space-charge region (SCR) with a strong electric field. The p^+- and n^+-type regions act as electrodes. Nuclear particles (or photons) produce ionization in a semiconductor when they are slowed down. Thus, the tracks of nonequilibrium electron–hole pairs are formed in the detector's operation volume. The separation of charge carriers in an electric field of SCR and their subsequent drift to electrodes generate a current pulse in the detection circuit.

Ionization occurs with relatively small fluctuations in the number of generated electron–hole pairs; as a result, this number is found to be strictly related to the absorbed energy. Therefore, in the case of complete transfer of charge carriers to electrodes, the charge that flows through the circuit represents a measure of the absorbed particle (photon) energy.

In order to successfully implement the "ionization" principle of measuring the energy of nuclear radiation, the starting material should feature a certain set of properties. These properties include a low concentration of impurities (an extended region of the electric field); bipolar conductivity (the absence of a space-charge accumulation that distorts the electric field); large drift length for charge carriers (charge-carrier transport with an efficiency close to unity); a band gap ensuring the low-rate thermal generation of charge carriers (a low noise and a low dissipated power); and, if possible, a large atomic number of relevant elements (efficient absorption of the X- and gamma-ray radiation). Since the ion tracks occupy a small fraction of the detector volume, a high local uniformity of conditions of the charge-carrier transport is required for the pulses to be identical.

Unfortunately, the improvement rate for the SiC properties in the 1960s–1970s was appreciably lower than that for competing materials. For example, perfect monatomic Ge and Si crystals were rapidly obtained and methods for high-degree compensation of residual p-type conductivity using the donor lithium impurity were developed. At the same time, materials with a wider band gap and larger atomic number than those for Ge and Si (CdTe and CdZnTe solid solutions, the compounds GaAs and HgI_2) were developed. The aforementioned materials were found to be very efficient in the spectroscopy and detection of various types of nuclear radiation. The advantages of planar technology were exploited, and various designs of silicon detectors (including multielement detectors) became widely implemented. As a result, interest in SiC as a material for detectors was temporarily reduced, although the first results of using SiC to fabricate nuclear detectors were encouraging [93–95].

The successful attempt of Tikhomirova *et al.* [96–98] to introduce a beryllium acceptor impurity into n-type crystals should be mentioned among studies concerned with SiC that were carried out in the 1970s. Detectors with n-type conductivity compensated with beryllium operated with good results as counters of neutrons (conversion reactions with emission of short-range particles were used) and fission fragments directly in the reactor channel; these counters could operate at temperatures as high as 600°C.

Considerable advances have been made recently in controlling the properties of SiC: the requirements imposed on most important characteristics of SiC are now satisfied quite adequately. Consequently, a renewed interest in designing SiC-based detectors is clearly observed. In what follows, we will do our best to describe the current situation in this field.

The difference concentration of donors and acceptors $N_d^+ - N_a^- = 5 \times 10^{14}$–$3 \times 10^{15}$ cm^{-3} is standard for "pure" SiC films. This concentration makes it possible to obtain an SCR with extent $W \approx 15$–30 μm at a bias voltage $U = 500$ V. Lifetimes on the order of several hundreds of nanoseconds for holes with lower mobility combined with large values of saturation drift velocity ensure an almost 100% efficiency of the charge transport. As mentioned above, the high radiation resistance and chemical resistance of SiC and its high thermal stability (SiC-based devices can operate at temperatures of several hundreds of degrees centigrade) are the most attractive characteristics of SiC. Much attention in recent publications has been given to studying the above properties of SiC and to tests of SiC-based detectors for detection and spectrometry of various types of nuclear radiation.

In turn, the diode structures of detectors are convenient for studying the electrical characteristics of the material. In this context, deep-level transient spectroscopy (DLTS) and electron-beam-induced current (EBIC) are widely used. The main method for determining the transport characteristics is the amplitude analysis of transport of calibrated bunches of nonequilibrium charge carriers.

4.2. Detection of Short-Range Particles

The majority of studies concerned with analyzing the operation of SiC detectors have been carried out using epitaxial n-4H- or n-6H-SiC films with $N_d^+ - N_a^- = 10^{15}$ cm^{-3}. The film thickness was equal to ~10 μm, i.e., was comparable with the slowing-down length of short-range ions. Single-crystal SiC wafers that were doped to the level of $(3.0$–$6.0) \times 10^{18}$ cm^{-3} and had a thickness of ~300 μm were used as the substrates. As a rule, the rectifying contact was prepared in the form of a Schottky barrier. The latter was formed using magnetron sputtering of Ni [99, 100] or by depositing a thin (100 nm) Au film [101].

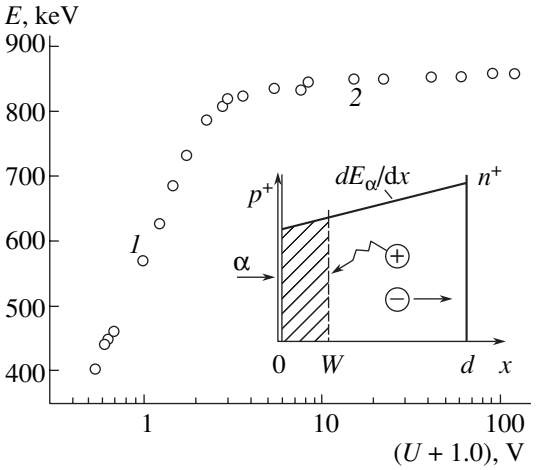

Fig. 6. Amplitude of the signal corresponding to alpha particles (energy E measured by instrumentation) as a function of the voltage applied to the detector's diode structure (see [99]). Circles *1* corresponds to the structure before depletion, and circles *2* corresponds to complete depletion. The inset illustrates the configuration used in the analysis of diffusion; the quantity W corresponds to the SCR boundary; and E_α stands for the energy of incident alpha particles.

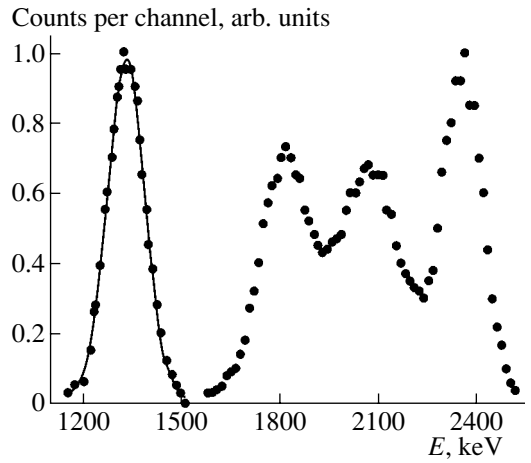

Fig. 7. Alpha-particle energy spectrum obtained using an n–p–n^+ structure based on a 4*H*-SiC film. The solid line represents the approximation of the low-energy line using a Gaussian function at the relative full width at the half-maximum of the line FWHM = 8.6%.

It is convenient to use natural-radioactivity alpha particles with energies of 5–6 MeV as a highly ionizing radiation. The detection of nonequilibrium charge induced by individual alpha particles is performed using standard nuclear spectrometry instrumentation. This instrumentation includes a charge-sensitive preamplifier, an amplifier with the passband controlled by integrating/differentiating *RC* circuits, and a pulse-height analyzer. In order to calibrate the energy width of an analyzer channel, a precision silicon detector is used. The spectrum shape and the average amplitude and full width of the spectrum at half-maximum were determined in the studies under consideration.

The typical dependence of the signal amplitude (energy E dissipated in the film) on the bias voltage applied to the detector is shown in Fig. 6 for a film with thickness $d \approx 10$ μm [99]. ^{244}Cm alpha particles with range $R \sim 20$ μm were used; i.e., the particle range exceeded the film thickness, so that the induced ionization virtually corresponded to the linear portion of the Bragg curve for specific energy losses $dE_\alpha/dx = f(x)$. The observed two stages in the signal growth correspond to voltages U before and after complete depletion of the structure. As long as the SCR occupies only a fraction of the n-type base volume, the diffusion of holes in the base is involved in the charge transport in addition to the drift of charge carriers in the field region; the diffusion proceeds much more slowly than the drift. Appreciable losses of charge due charge-carrier recombination become significant. In the first approximation, the signal increases in proportion to the SCR width $W \propto U^{1/2}$ (a similar result was reported by Nava *et al.* [101].

When the SCR occupies the entire film thickness, electrons and holes are efficiently separated by the field and the losses of charge are controlled by localization at the capture centers that retain the charge carriers for a time that exceeds the pulse-shaping time in the detecting instrumentation (on the order of several microseconds). The signal increases insignificantly owing to an increase in the drift velocity. Finally, the charge transport is assumed to be complete at the stage of signal saturation.

The shape of the spectral line was found to be Gaussian [99, 101]; an appreciable transformation of the line as the average value of the amplitude increased was not observed (see 4.3.3 below).

Figure 7 illustrates the feasibility of detecting a spectrum that consists of four lines of the ^{226}Ra alpha decay. The decay energies were reduced owing to a slowing-down of alpha particles in air and were equal to 2432, 3469, 4125, and 6189 keV. The ranges of all the particles were smaller than the film thickness; however, the charge transport included a diffusion component, which reduced the amplitude and brought about the observed overlap of the lines [102].

4.3. An Analysis of the Material Parameters that Control the Charge Transport in Detectors

The aforementioned data on detection of alpha particles are used with good results in analyzing the most important parameters of SiC as a medium for detection of hard radiation. These parameters include the mean energy for formation of an electron–hole pair ε, the diffusion length for holes $L_D = (D\tau_0)^{1/2}$, the degree of inhomogeneity of the hole lifetime $\Delta\tau/\tau_0$ in the diode-structure base, and the lifetime of charge carriers until they become localized at the capture centers during the drift

in the SCR. Here, D is the diffusion coefficient and τ_0 is the mean lifetime of holes in the base.

4.3.1. Determination of the mean energy for formation of an electron–hole pair. The energy dissipated in the film E is determined first in order to calculate ε using mathematical simulation of the slowing-down of an alpha particle (the TRIM software package [103]). As mentioned above, the detected signal is proportional to the charge generated by a particle $Q_0 = eN$ (N is the number of produced electron–hole pairs and e is the elementary charge). This circumstance makes it possible to write the relation $N = E/\varepsilon = E_{sat}/\varepsilon_{Si}$. Here, $\varepsilon_{Si} = 3.62$ eV is the energy required for generation of an electron–hole pair in Si and E_{sat} is the experimental saturation energy (see Fig. 6); the value of E_{sat} is determined from the signal calibration using a silicon detector. Thus, we use the data shown in Fig. 6 to find that $\varepsilon = 8.6$ eV, which is close to the value $\varepsilon = 8.4$ eV reported by Rogalla *et al.* [104].

4.3.2. Determination of the hole diffusion length. Diffusion–drift transport was previously considered [105, 106] for the case of the steady-state and spatially uniform generation of charge carriers. As a result, the following expression, which is equivalent to that for the case of pulsed ionization in detectors, was derived:

$$Q/Q_0 = 1 - \lambda = (W + L_D)/d. \quad (3)$$

Here, $\lambda = 1 - Q/Q_0$ accounts for the deficit in the detected charge Q.

In the case of generation of charge carriers by alpha particles in thin films ($R > d$), dE_α/dx is assumed to be a linear function of x. This assumption complicates formula (3) but makes it possible to carry out the fitting procedure for the function $\lambda(W)$ using two parameters, L_D and d (Fig. 8) [99]. The quantity λ was calculated using the data in Fig. 6 as $\lambda = (E_{sat} - E)/E_{sat}$, and the value of W was determined from the capacitance measurements. As a result, we determined the quantity L_D ($L_D = 2.42$ μm) and refined the value of d ($d = 9.76$ μm).

4.3.3. The shape of the pulse-height spectrum and its relation to the lifetime of holes τ. The statistics of the signal amplitude manifests itself in the shape of the spectral line and is a specific characteristic of detectors. It is common practice to describe the straggling in the signals using the full width at the half-maximum (FWHM) of the line. The origin of the straggling is related to a number of factors; however, nonequilibrium-carrier transport is the dominant mechanism of straggling if the charge transport is incomplete. The shape of the line was analyzed previously [99, 107] taking into account special features of the charge-carrier diffusion characteristic of SiC.

The question of the shape of the line is also important methodologically since the use of alpha particles makes it possible to assess the microscale nonuniformity of τ over the film area [107]. Indeed, the tracks of alpha particles contain dense clusters of electron–hole pairs and have a diameter of ~10 μm (taking into account the spread caused by the diffusion and drift). Therefore, the magnitude of charge generated by each particle depends on the conditions of the carrier transport in a microscopic volume. The statistics of distribution of lifetime τ over the sample surface manifests itself as a result of random incidence of particles upon the detector. It is important that the charge-carrier lifetime is the parameter that is most sensitive to structural defects.

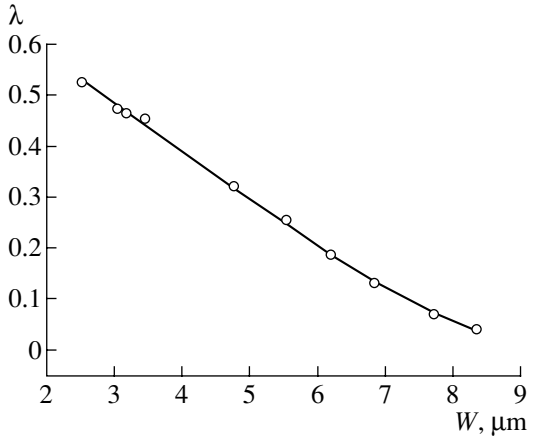

Fig. 8. Dependence of the signal deficit on the position of the SCR boundary. Circles correspond to the experimental data, and the solid line represents the result of the approximation according to Lebedev *et al.* [99].

We now consider the calculation of the spectrum shape. The pulse-height spectrum is plotted as $dN/dq = f(q)$, where dN is the number of pulses within the pulse-height range dq and $q = Q/Q_0$. In order to plot the spectrum, Strokan [107] used the identity $dN/dq = (dN/d\tau) \cdot (d\tau/dq)$; thus, the problem amounted to determining the shape of distribution for τ and the form of the function $q = f(\tau)$. The distribution of $dN/d\tau$ was assumed to be Gaussian with variance σ since a Gaussian function is most probable under conditions of small deviation of the parameter τ from the mean value τ_0, i.e., $|\tau - \tau_0| < \tau_0$. The FWHM of the spectrum as $\Delta\tau = 2.35\sigma$ was introduced similarly to the pulse-height spectrum. For simplicity, the charge-carrier generation rate was assumed to uniform over the film depth; the form of $d\tau/dq$ was then determined from expression (3). As a result, the following system of equations was derived (with numerical factors discarded):

$$dN/dq = (\tau/\tau_0)^{1/2}\exp[-(\tau/\tau_0 - 1)^2/0.362(\Delta\tau/\tau_0)^2],$$
$$q = (W + L_D\sqrt{\tau/\tau_0})/d. \quad (4)$$

Three dimensionless parameters in Eqs. (4), i.e., W/d, L_D/d, and $\Delta\tau/\tau_0$, affect the shape of the pulse-height spectrum in different ways. For example, the quantity W/d only shifts the position of the peak without affecting the value of FWHM. In contrast, the nonuniformity of τ only affects the FWHM of the spectral

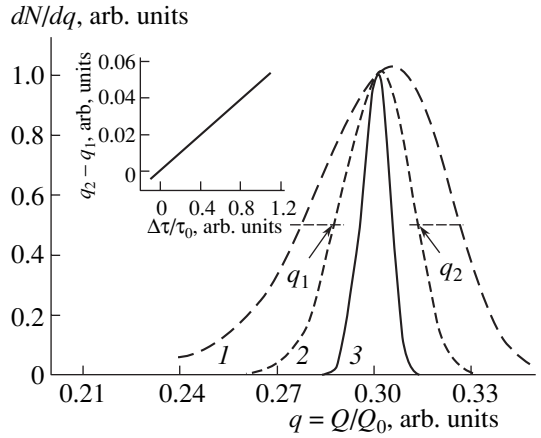

Fig. 9. Calculated shape of the pulse-height spectrum for various degrees of nonuniformity of lifetime of holes that diffuse in the base (see [99]). $\Delta\tau/\tau_0$ = (*1*) 100, (*2*) 50, and (*3*) 20%. $W/d = 0.2$ and $L_D/d = 0.1$. The width of the spectral line as a function of $\Delta\tau/\tau_0$ is shown in the inset.

line. Finally, the values of L_D/d affect the spectrum as a whole.

The plotting of the spectrum for several values of $\Delta\tau/\tau_0$ showed that the spectra were symmetric up to a nonuniformity of 50% ($\Delta\tau/\tau_0 = 0.5$) [99]. As the value of $\Delta\tau/\tau_0$ increases to unity, an asymmetry arises owing to the appearance of an extended region of small amplitudes at the left-hand wing of the spectrum. However, the value of FWHM is a linear function of $\Delta\tau/\tau_0$ in the entire range of $\Delta\tau/\tau_0$ under consideration (see inset in Fig. 9).

Moreover, the dependence FWHM = $f(L_D/d)$ was also found to be linear with a slope that was proportional to $\Delta\tau/\tau_0$. As a result, the quantity FWHM is defined as

$$\text{FWHM} = 0.48(\Delta\tau/\tau_0)(L_D/d). \tag{5}$$

It can be seen that the line width is independent of the value of W/d, i.e., the bias voltage. The latter circumstance corresponds to the formulation of the problem where fluctuations in the detected charge are related to the stage of the charge-carrier diffusion and to the results of the measurements mentioned in 4.2.

The shape of the pulse-height spectrum was recorded for films with $L_D = 2.4$ μm and $d = 9.76$ μm; as a result, the value FWHM = 0.075 was obtained. According to formula (5), this value corresponds to $\Delta\tau/\tau_0 = (0.075/0.48)(d/L_D) \approx 0.6$, which almost coincides with the degree of nonuniformity determined in studying the charge-carrier transport in detector-grade silicon.

4.3.4. The drift transport and the capture time of charge carriers. We first consider the calculated parameters. The problem concerning the drift of charge carriers in a linearly varying field was considered by Eremin *et al.* [108]. In the case of "thin" SiC detectors, one should additionally take into account the fact that the charge-carrier generation rate increases linearly with the coordinate, and one should determine the mean charge magnitude detected experimentally under specified conditions.

The concentration of charge carriers as a function of the coordinate x in the course of their generation at a point y was determined first as a result of calculations. The charge $q(y)$ induced at the electrodes was then determined, and finally the mean value of this charge was calculated taking into account the generation-rate profile $G(y)$. For example, the above procedure yields the following formulas for holes:

$$\begin{aligned} p(x) &= G(y)\exp\left(-\int_y^x \frac{dx}{\mu_h\tau_h F}\right), \\ q(y) &= \frac{1}{d}\int_y^d p(x)dx, \\ \bar{q} &= \frac{1}{d}\int_0^d G(y)q(y)dy. \end{aligned} \tag{6}$$

Here, F is the electric-field strength, μ_h is the hole mobility, and τ_h is the lifetime of holes until they are localized at the capture centers. The charge q is normalized to the value determined by the absorbed energy.

For simplicity, the capture rate is assumed to be low and is given by the linear term in the expansion of the exponential function. For a uniform field ($F(x)$ = const) and equiprobable generation rate ($G(y) = 1$), the solutions are descriptive in form and are the same for both electrons and holes. In the notation for holes, we have

$$\begin{aligned} q(y) &= (1 - y/d)\left[1 - \frac{d-y}{2\mu_h\tau_h F}\right], \\ \bar{q} &= 0.5\left(1 - \frac{d}{3\mu_h\tau_h F}\right). \end{aligned} \tag{7}$$

The linear behavior of $F(x)$ complicates relations (7) by introducing a logarithmic dependence on voltage [108]. It is worth noting that the identity of expressions for the charges transported by electrons and holes is retained in the case of a uniform generation rate of charge carriers. The charge-carrier generation rate that is nonuniform over the depth gives rise to different formulas for electrons and holes. The expressions become less clearly conceived. However, although these expression are cumbersome, they make it possible to determine τ_h using this parameter as an adjustable parameter [99].

We now consider the experimental data. The charge losses under the drift conditions can be analyzed using the data shown in Fig. 6. The voltage dependence of losses should be compared with calculated dependences on the value of τ_h. The small value of rms deviation serves as the criterion for agreement between

Table 6. Energy levels, concentrations, and impurities involved in a defect for trapping centers detected in SiC with the use of DLTS and ICTS [109]

Defect type	*S*0	*S*1	*S*2	*S*3	*S*4	*S*5
Energy, eV	0.10	0.19	0.32	0.91	0.40*	0.75*
Concentration, cm^{-3}	2×10^{11}	8.9×10^{12}	6×10^{11}	2.2×10^{13}	4.5×10^{12}	1.4×10^{13}
Impurity	Nitrogen	Chromium		Vanadium		

* At the interface between Au and epitaxial SiC film.

experimental and calculated values. The rms deviation was found to be much smaller in the case of the predominance of losses in the hole charges. The value obtained for the hole lifetime is equal to 35 ns. This value is smaller than that determined from the diffusion transport (62 ns; see Fig. 8, where L_D = 2.42 μm was found). This difference may be related to dissimilar occupation of the capture centers: diffusion occurs under conditions of equilibrium occupation of centers, whereas drift proceeds in nonequilibrium conditions where the occupancy of the centers under consideration is much lower.

The aforementioned results illustrate the methodological potential that follows from analyzing diffusion–drift transport of a nonequilibrium charge in diode structures of detectors. In this context, the question of how analytical expressions for describing the charge deficit and the shape of the amplitude spectrum are derived on the basis of known assumptions was assessed. These expressions are used to determine the key parameters of the charge-carrier transport: the lifetimes of charge carriers in the course of their drift, the diffusion length of nonequilibrium charge carriers in the base, and the degree of lifetime nonuniformity over the film area.

Nava *et al.* [109] used the DESSIS software package [110] to describe the diffusion–drift transport of charge carriers. Films of a higher structural quality were used, and unprecedentedly high values of charge-carrier lifetimes (500 ns and 95 μs for holes and electrons, respectively) were obtained.

The origin of the centers that capture the charge carriers was studied by Nava *et al.* [109] using DLTS and isothermal capacitance transient spectroscopy (ICTS). Comparison of the results obtained by the above methods made it possible to determine the characteristics of traps with a high accuracy, including the shallow-level traps that are not resolved by DLTS at the specified temperatures. The data on the energy position of the capture states, their concentration, and their possible relation to impurities are summarized in Table 6.

Thus, we may state that the level of drift-transport parameters that ensures almost 100% efficiency of charge transport is undoubtedly attained in modern SiC films. How to further decrease the impurity concentration, which would make it possible to attain larger widths of SCR, is a problem that remains to be solved.

Recent results of studies in this field seem to be very encouraging. For example, Kimoto *et al.* [111] attained a reproducible difference concentration of impurities of $(1–3) \times 10^{13}$ cm^{-3}. It is planned that the total concentration of traps will be reduced to 5×10^{11} cm^{-3}. The resulting SiC material approaches silicon in purity and makes it possible to fabricate detectors that are designed to operate with short-range ions and have a completely depleted base with a thickness of ~100 μm.

Good results were also obtained with respect to the formation of blocking contacts (shallow p^+–n junctions) in the detectors. The contact problem is solved by using an Al implantation [112, 113]. As a result, SiC structures reliably detect alpha particles at temperatures as high as 500°C.

4.4. The Use of SiC-based Detectors for Detection of Penetrating Radiation

4.4.1. Spectrometry of X-ray radiation. In order to ensure the mode of spectrometry, it is necessary that a complete deposition of the particle (photon) energy occurs in the detector's operation volume. In this context, the data reported by Bertuccio *et al.* [114, 115] and concerned with X-ray radiation spectroscopy with an energy $E_\gamma < 60$ keV are of interest. In this energy region, the mechanism of photoabsorption with transfer of the photon energy to the generated photoelectron is dominant. The photoelectron ranges increase superlinearly with the energy ($\propto E_\beta^{1.4}$); nevertheless, these ranges do not exceed 10 μm. Therefore, the photoelectron energy (especially, for E_γ < 20 keV) will be completely absorbed in the SCR of the detector, which is exactly characteristic of the spectrometry mode.

Bertuccio and Casigaghi [115] used *n*-4*H*-SiC films produced by CREE Research Inc. [116]. The films were 70-μm thick and had a difference impurity concentration of 9×10^{14} cm^{-3}. Special technology was used to form a Schottky barrier with an area of 0.03 mm^2 on an epitaxial layer. Spectrometric measurements were carried out at the reverse voltage of 300 V. The choice of this voltage was the result of compromise between the desire to attain an extended SCR (W = 18 μm) and the requirement for a moderate noise power. The average electric-field strength in these conditions exceeded 10^5 V/cm. However, the reverse-current density was no higher than 5×10^{-12} A/cm^2. For comparison, the

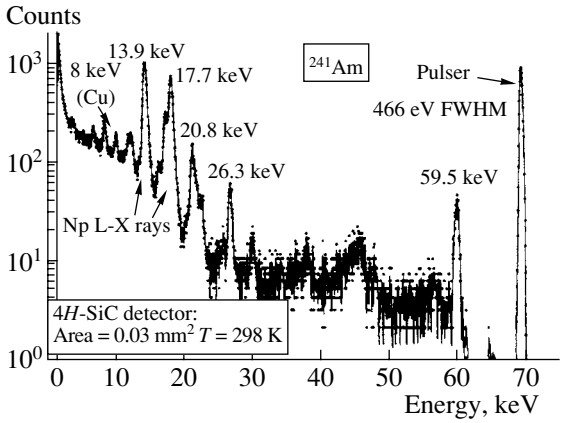

Fig. 10. Spectrum of ^{241}Am X-ray radiation measured at room temperature using a SiC detector (see [115]). The noise-induced straggling of the line was generated by a stable-amplitude oscillator (FWHM = 466 eV).

reverse-current densities in advanced silicon detectors are in the range $(0.5–1.0) \times 10^{-9}$ A/cm^2.

In Fig. 10, we show the ^{241}Am X-ray spectrum detected at 25°C; it can be seen that the characteristic X-ray energies are well resolved. The linearity of detected signal is retained in the entire range of measured peak energies (8.0–59.5 keV). However, it should be taken into consideration that the measured intensities of the lines are appreciably decreased as the energy of X-ray photons increases. This fact is related to a drastic decrease in the absorption of high-energy photons in the SCR due to the small width of this region.

An increase in the SCR width would reduce both the decrease in the line intensity and the detector capacitance (at the unchanged detector area). A decrease in the capacitance would make it possible to reduce the noise power.

4.4.2. Dosimetry of electrons and gamma-ray photons. The response of SiC detectors to the above types of ionizing radiation is of interest from the standpoint of radiotherapy. The detectors were typically irradiated with 22-MeV electrons and 6-MeV photons; the latter were produced by electrons accelerated to an energy of 6 MeV in a linear accelerator. The range of absorbed doses was 1–10 Gy at intensities of 2–7 Gy/min [117].

In the above conditions of irradiation, the performance of dosimeters based on SiC, Si, and CVD diamond films was compared. It was found that the sensitivity of silicon dosimeters degraded and dropped to 35% after exposure to an electron dose of 3 kGy. The diamond films have a polycrystalline structure and exhibit an appreciable nonuniformity of properties. This nonuniformity significantly lowers the spatial resolution of the detector. In addition, so-called "pumping" is required to stabilize the detector's sensitivity. This pumping consists in preliminary exposure of the sample to the radiation of an X-ray tube (with an anode voltage of 50 kV) with a typical dose of 10 Gy [118].

The best results for electron dosimetry were obtained using Schottky diodes fabricated on epitaxial 4*H*-SiC films that had $N_d^+ - N_a^- = 2.2 \times 10^{15}$ cm^{-3}, were 30-μm thick, and were produced by CREE. The diodes operated at a bias voltage of 150 V. The dependence of the induced charge on the absorbed electron dose was linear in the range 1–10 Gy and had a slope of 16.37 nC/Gy.

In turn, in the case of irradiation with 6-MeV gamma-ray photons (with a dose rate of 2.1–6.5 Gy/min), the induced-current dependence on the dose was also linear and had a slope of 3.5×10^{-10} A min/Gy. The width of the active zone was $W + L_D = (8.5 + 12.2)$ μm.

However, an attempt to use a semi-insulating "bulk" (230-μm thick) 6*H*-SiC sample failed: the sensitivity to electrons was too low. This fact should be related to the large number of structural defects. Recombination centers reduce the efficiency of charge transport, and microvoids bring about an increase in the dark currents.

The data listed in Table 7 make it possible to compare the performance of dosimeters of various types; it can be seen that diode structures based on epitaxial SiC films are quite suitable for dosimetry of electrons and gamma-ray photons.

4.4.3. Detection of relativistic particles. Naturally, silicon carbide was among the materials considered as suitable when experiments with high radiation rates were planned at next-generation accelerators (such as the Large Hadron Collider at CERN).

The potential of SiC as a material for a track detector was studied by Rogalla *et al.* [119]. They used

Table 7. Comparison of sensitivity and the ratio of sensitivity to volume for a dosimeter based on epitaxial SiC, those for commercial (Scanditronix) Si-based dosimeters, and those for two dosimeters based on CVD diamond films [117]

Dosimeter	Voltage, V	Active volume, mm^3	Sensitivity, nC/Gy	Sensitivity/volume, nC/(Gy mm^3)
Silicon	0	0.295	150	509
CVD diamond	50	3.7	690	190
CVD diamond	400	4.7	420	90
Silicon carbide	150	0.06	16.4	273

Note: The silicon dosimeter had been preliminarily irradiated with 20-MeV electrons at a dose of 10 kGy so that the subsequent irradiation did not affect the sensitivity.

310-μm-thick semi-insulating 4*H*-SiC substrates produced by CREE. The contacts formed on both surfaces of the sample were ohmic. In addition, a guard ring was used, which made it possible to observe a linear current–voltage characteristic with a resistivity of 5.1×10^{10} Ω cm in the voltage range ±500 V.

In order to imitate high-energy particles, the ^{90}Sr electrons with the highest energy (2.2 MeV) were used. The signals produced by only the high-energy electrons that traveled through the sample and induced the lowest ionization in SiC were analyzed. In order to select these ionization events, a conventional silicon detector was installed behind the SiC sample. Signals from this detector that corresponded to an energy of ≤1 MeV were distinguished, whereas the signals corresponding to the absorption of an energy of >1 MeV were fed to the coincidence circuit. The tracks of the latter electrons In SiC contained 17000 electron–hole pairs.

Experiments showed that the signal and noise spectra were well resolved; however, two adverse factors were observed [119]. First, the carrier-transport efficiency was as low as $\eta \approx 12\%$. Second, the signal amplitude decayed exponentially with time constant $\theta = 14.2$ min. The above observations indicate that the value of the charge-carrier lifetime is small and deep levels are involved in the formation of the electric field. It is significant that the introduction of radiation defects (as a result of irradiation with 8-GeV protons at a dose of 4.16×10^{14} cm^{-2}) brought about an additional decrease in η by 23% and in θ to 3.6 min. Simultaneously, the resistivity of the samples increased threefold.

We emphasize that Rogalla *et al.* [119] were the first to design a detector based on semi-insulating 4*H*-SiC. The observed signal instability and the relatively low efficiency of the charge transport should be attributable to the inadequate quality of the material (corresponding approximately to the state of the art in 1998). It will be recalled that the low sensitivity of semi-insulating SiC to electrons was also observed by Bruzzi *et al.* [117].

4.4.4. Detection of neutrons in the reactor channel. The problem of detection is related to the determination of neutron fluxes and the control of the reactor operation. It is characteristic that the solution to this problem is based simultaneously on the high radiation, thermal, and chemical stability of SiC.

Since neutrons do not directly produce ionization, the reactions in which the neutron energy is transferred to other (short-range) ionizing particles, such as alpha particles or fission fragments that can be detected by SiC diodes, should be used. As far back as the 1960s, good agreement between the data for SiC diodes coated with a ^{235}U layer and the results of measurements using the conventional method of activation of gold foils was observed [120].

It was also ascertained that SiC-based diodes can detect alpha particles after having been irradiated with high doses of thermal neutrons (6×10^{15} cm^{-2}). Regarding fast neutrons (with energies higher than 1 MeV), the dose can be as high as ~10^{17} cm^{-2} [121]. SiC-based detectors exhibited a radiation resistance which exceeded that of silicon detectors by almost a factor of 5 when the ^{233}U fission fragments were detected directly in the reactor channel [98]. The neutron-flux density was 10^8 cm^{-2} s^{-1}, and the exposure time was 340 h. In this context, the feasibility of evaluating a neutron spectrum if SiC detectors are complemented with a set of ^{233}U, ^{234}U, ^{235}U, ^{238}U, ^{232}Th, and ^{239}Pu converters was discussed.

Recent progress in the field of the growth of high-purity SiC films makes it possible to solve a problem that is typical of reactors and consists in measuring the field of combined neutron and gamma-ray radiation. The experiments were carried out in the TRIGA reactor [122, 123] under conditions of low-power radiation (50–290 W). An array of 22 Schottky diodes with diameters of 200 or 400 μm was used. The diodes could be connected in parallel, thus increasing the total area. A LiF layer installed near the detector surface served as a converter; the neutron flux was measured on the basis of triton counts, according to the reaction ^{6}Li(n, α)^{3}H.

The portions related to direct detection of the background of tritons and gamma-ray photons are resolved in the observed pulse-height spectrum. As a result, these radiation types are detected separately; consequently, it was possible to determine the distributions of neutrons and gamma-ray photons in the form of a function of the distance from the channel's center line. The measurements take about 30 min when 12 diodes are connected in parallel.

In determining gamma-ray and neutron fluxes, the SiC detectors showed a high accuracy (the errors were 0.6 and 1.9%, respectively). We may state that small-size SiC detectors can be used with good results to monitor the operation not only of the reactor assemblies but also of its active zones.

4.5. Radiation Resistance of Detectors

The radiation resistance of SiC with respect to nuclear radiation was discussed to some extent in each of the previous subsections. We now turn our attention to the aforementioned (4.4.3) case of relativistic particles in connection with planned large-scale experiments at the Large Hadron Collider at CERN. In these experiments, detectors are expected to operate continuously for ten years. Furthermore, the doses of irradiation with relativistic particles range from 2×10^{14} to 5×10^{15} cm^{-2}, depending on the distance from the site where the beams interact. Under these conditions, the use of advanced silicon detectors encounters serious difficulties even at doses as low as ~10^{14} cm^{-2} [124].

First, the dissipated power increases appreciably (the reverse currents and the voltages corresponding to depletion of the structure increase). Second, the efficiency of nonequilibrium-charge transport and, correspondingly, the signal amplitude are reduced. In this

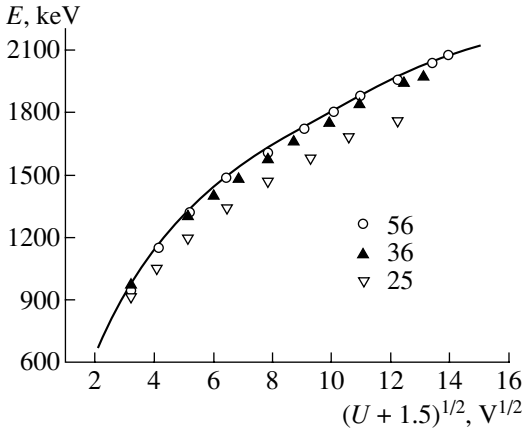

Fig. 11. Reverse-voltage dependence of the energy deposited by an alpha particle in the sensitive region of the detector's diode structure before irradiation with protons (see [126]). The numbers 56, 36, and 25 correspond to designations of the samples. The nonlinearity of the dependence (solid line) is caused by the nonuniform distribution of impurities in the SiC film.

context, Verbitskaya *et al.* [125] studied the results of cooling Si detectors and the feasibility of varying the field profile by controlled injection of charge carriers from the contact. Complication of the conditions of operation for silicon detectors has led to a search for materials with a higher radiation resistance.

Ivanov *et al.* [126, 127] analyzed the performance of a SiC detector irradiated with 1-GeV protons with a dose increasing from 3×10^{14} to 1.3×10^{15} cm^{-2}.

Schottky diodes that had a diameter of 600 μm and were formed by magnetron sputtering of Ni onto the surface of high-quality 6*H*-SiC films were used. The films were grown by sublimation epitaxy in vacuum [128]. The difference concentration of ionized impurities varied from 5×10^{14} cm^{-3} at the surface to 8×10^{15} cm^{-3} at depth $d = 7$ μm. Such a distribution of $N_d^+ - N_a^-$ concentration made it possible to form a pulling field in the diode structure, which increased the effective diffusion length of charge carriers [129].

The detectability of SiC structures was analyzed using ^{244}Cm alpha particles (see 4.2). The characteristics of the deep-level centers formed were determined using DLTS. A typical voltage dependence of the signal amplitude $E(U)$ is shown in Fig. 11. It is significant that the values of E for different samples almost coincide, which is indicative of the fairly high uniformity of SiC properties over the film area.

Irradiation with a dose of 3×10^{14} cm^{-2} reduced the value of L_D for holes by less than 30%; variations in $N_d^+ - N_a^-$ compared to initial values were insignificant.

Measurements of the spectrum of deep-level centers showed that only the concentration of *R* centers changed appreciably (see Table 8). Lebedev *et al.* [130] studied the introduction of these centers as a result of irradiation with 8-MeV protons; it was ascertained that these centers were related to vacancies. Therefore, the TRIM software package was used to compare the number of primary vacancies for proton energies of 8 MeV and 1 GeV. The ratio of these numbers was found to equal 110 : 1, which is a consequence of a decrease in the cross section for proton scattering by Si and C atoms as the proton energy increases.

Experimentally, concentrations of the *R* centers in the two above cases (irradiation with 8-MeV and 2-GeV protons) are related as 400 to 1. Thus, the result expected from the concept of primary defects is found to be inconsistent with the number of secondary (actual) centers that are formed in SiC as a result of physicochemical reactions. Evidently, there is a difference between the energy transferred to primarily displaced Si and C atoms in the course of defect production by the 8-MeV and 1-GeV protons.

In the case of irradiation with high-energy protons, more compact Frenkel pairs are formed; recombination of vacancies and interstitial atoms occurs more efficiently for these pairs. Accordingly, a lesser number of vacancies is transferred from the tracks of recoil atoms to the film bulk with subsequent formation of the *R* centers. Emtsev *et al.* [131] considered in detail the above mechanism of recombination for components of Frenkel pairs (using silicon as an example) taking into account the possible recharging of these components. We note that the opposite situation of a low recombination rate for vacancies and interstitial atoms, which is characteristic of diamond, raises the crucial question as to the radiation resistance of diamond [132].

Irradiation with a total proton dose of 1.3×10^{15} cm^{-2} [127] brought about certain changes in the characteristics of the structure. The conductivity of SiC became heavily compensated. In addition, a high-resistivity base was formed in the diode structure of the detector; the Maxwell relaxation time in this base exceeded the characteristic time of signal shaping by the instrumentation electronics. Under these conditions, a characteristic falloff of the signal by *W*/*d* times should be observed (the signal amplitude is proportional to $\propto W^2 \propto U$) if the structure is incompletely depleted [133]. However, it was ascertained for alpha particles that penetrated through the base that relaxation of the base in structures with semi-insulating SiC films is promoted as a result of the presence of a high concentra-

Table 8. Deep-level centers in SiC before and after irradiation with 1-GeV protons at a dose of 3×10^{14} cm^{-2} according to DLTS measurements [126]

Center type	Energy, eV	Concentration of the centers, cm^{-3}	
		before irradiation	after irradiation
E_1/E_2	0.35–0.4	$(1–2) \times 10^{13}$	$(1–2) \times 10^{13}$
R	1.1–1.2	$<5 \times 10^{12}$	5×10^{13}

tion of nonequilibrium charge carriers in the track [134, 135]. Indeed, the dependence $W_{\text{eff}} = f(U + 1.5)^{1/2}$ remained linear after irradiation with an alpha-particle dose of 1.3×10^{15} cm^{-2} [127]. However, the accuracy of experiment gave no way of separating the terms of the quantity $W_{\text{eff}} = W + L_D$.

Figure 12 illustrates the value of the charge transported in the structure for two proton doses. The voltage required for attaining the same value of the charge after the second dose was found to be higher by a factor of 3. Most likely, this fact may be related to the existence of local inhomogeneities in the course of compensation of the material. The same conclusion can be reached if we take into account that the WFHM of the spectrum is reduced to 10%; i.e., the conditions of charge-carrier transport through the detector bulk become leveled off.

The drift length of holes in an electric field F was determined [126] from the expression

$$L_F^h = (\mu_h \tau_h)F = (L_D)^2(Fe/kT), \quad (8)$$

where k is the Boltzmann constant. Introducing $L_D = 1$ μm and $F = 10^5$ V/cm (after the irradiation with a dose of 3×10^{14} cm^{-2}), we obtain $L_F^h = 400$ μm for the hole transport.

The drift length of electrons was only estimated. The estimation was based on the initial value of the product of the mobility by lifetime for electrons $\mu_e\tau_e = 7 \times 10^{-9}$ cm^2/V. This value was obtained [134] for SiC irradiated with 8-MeV protons at a dose of 8×10^{15} cm^{-2}. Assuming that the decrease in τ_e was caused by the R centers, a coefficient accounting for the number of produced R centers for 1-GeV protons with a dose of 3×10^{14} cm^{-2} was introduced. As a result, we obtain $L_F^e \leq 1$ cm. Thus, we may assume that the drift lengths of charge carriers are satisfactorily large for detectors with an SCR (operating zone) with a width of several hundreds of micrometers. Data on the drift length of charge carriers in the structures irradiated with a total proton dose of 1.3×10^{15} cm^{-2} were not reported [127].

It is significant [126, 130] that the proton energy only slightly affects the nature of the radiation defects produced. In both cases (the 8-MeV and 1-GeV protons), the main role is played by the R center with a level that is 1.1–1.2 eV below the bottom of the conduction band.

To summarize the results for SiC detectors, we may state that a proton dose of 3×10^{14} cm^{-2} represents [126, 127] a threshold for radiation-induced changes in the properties of SiC with a given level of purity. If the dose does not exceed the threshold value, the lifetime of charge carriers does not decrease appreciably and the conductivity is not compensated significantly as a result of irradiation.

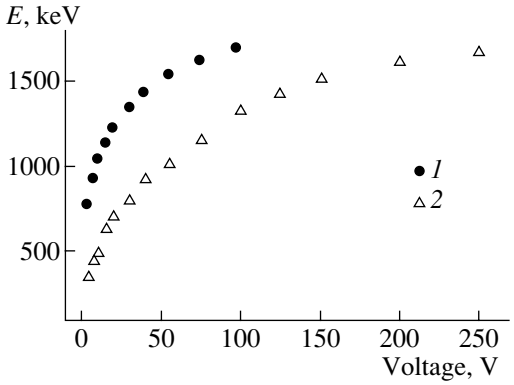

Fig. 12. Signal amplitude as a function of applied voltage for relativistic-proton doses equal to (*1*) 3×10^{14} and (*2*) 1.3×10^{15} cm^{-2}.

4.6. Feasibility of Signal Amplification

We specified above the quantities that are characteristic of charge-carrier transport in SiC. We also gave examples of the successful performance of SiC-based detectors in a number of important fields. It is evident that the main disadvantage of SiC detectors is the small width of the active (operating) zone. This circumstance is especially perceptible when penetrating (weakly ionizing) radiation is detected. In this context, it seems to be of interest to consider the feasibility of increasing the effective width of the operating zone, for example, by attaining a signal amplitude larger than the energy dissipated in the detector.

4.6.1. The principle of a through conducting channel. This principle was formulated in the late 1950s and was applied to semi-insulating films with monopolar conductivity [136, 137]. While the contacts block the transfer of charge carriers from the external circuit in detectors of the ionization-chamber type, the opposite situation (the contacts did not limit the current) was considered in [136, 137]. It was also a necessary condition that a highly ionizing particle penetrate through the film. Consequently, conducting tracks of particles shunted the film resistance.

If the monopolar character of conductivity is caused by the short lifetime of charge carriers (to be precise, holes), the nonequilibrium holes produced by a particle are localized at the capture centers and are immobilized. In contrast, the transport of electrons is possible through the track and external circuit. Thus, a through conducting channel comes into existence in the semi-insulating film. The charge Q transported through the circuit is related to the charge Q_0 generated by ionizing particles by the following expression:

$$Q = Q_0[(\mu_e\tau_e)_e F/d] = Q_0(\tau_e/t_{\text{dr}}). \quad (9)$$

Here, $t_{\text{dr}} = d/\mu_e(F)$ is the time of electron drift through the film. If the inequality $\tau_e/t_{\text{dr}} > 1$ is valid, amplification of the signal is observed.

A similar situation was simulated [134] for the p^+–n–n^+ structures that are based on 6*H*-SiC films with introduced radiation defects and biased in the conducting direction. The films had the initial concentration of uncompensated donors $N_d^+ - N_a^- = 4.5 \times 10^{16}$ cm^{-2} and a thickness of several micrometers. Irradiation with 8-MeV protons with a dose of 8×10^{15} cm^{-2} brought about an increase in the film resistivity to 5×10^9 Ω cm.

When alpha particles penetrated through the film, the bias dependence of the signal was linear in accordance with expression (9) and corresponded to $\mu_e\tau_e = 7 \times 10^{-9}$ cm^2/V. A gain of 1.7 was attained at a bias voltage of 25 V.

Strokan *et al.* [134] attribute the fact that the gain is low to the high total concentration of structural defects in the film (~10^{17} cm^{-3}). Therefore, the experiment described above clarifies to a great extent the principle of amplification but leaves the attainable gain unclear.

4.6.2. Amplification in a transistor structure. The charge amplification with the same coefficient τ_e/t_{dr} can also be attained in a transistor structure (see, for example, [138, 139]). The corresponding experiment with SiC films was described elsewhere [140, 141].

p-6*H*-SiC films served as starting base regions for the structures under consideration: films with a thickness of ~10 μm were grown by sublimation on n^+-type substrates. The difference concentration of impurities $N_a^- - N_d^+$ in the films was equal to 2.8×10^{15} cm^{-3}. A Schottky barrier obtained by sputtering Ni was used as the second electrode.

The structures were studied in the mode of connection with a floating base and were irradiated with 5.8-MeV ^{244}Cm alpha particles (the range in SiC was equal to 20 μm) directed onto the side of the Schottky barrier. The nonequilibrium charge produced in the base corresponded to the absorption of the energy that was no higher than 2 MeV. The shape of the signal spectrum and the dependence of the mean signal amplitude on the bias voltage *U* applied to the structure were measured using the conventional pulse-height analysis (see 4.2).

The barrier regions in the structures differed widely. The Schottky barrier corresponded to an abrupt junction; however, the change in the *p*-type conductivity was gradual on the side of the n^+-type substrate. Therefore, we compared two polarities of connection: the role of the collector was played either by the p–n^+ junction of the substrate (case I) or by the Schottky barrier (case II).

In case I, the signal amplitude *E* exceeded only twofold the value of energy deposited by a particle in the base. The dependence *E*(*U*) was sublinear and exhibited a tendency towards leveling off. Strokan *et al.* [141] attribute this behavior of the signal to the low injection efficiency of the emitter (the Schottky barrier) and short lifetime of charge carriers at the barrier. The shape of the spectral line was Gaussian (FWHM ≈ 10%), which indicates that the conditions of charge transport in the film were fairly uniform.

In case II, where the Schottky barrier acted as a collector, the dependence *E*(*U*) was superlinear. The signal amplitude now corresponded to 60–80 MeV. The shape of the spectrum was found to be Gaussian, as in case I; the straggling was FWHM ≈ 9%, nearly the same as in case I.

Strokan *et al.* described qualitatively the results reported in [141] in the context of the model suggested by S.M. Ryvkin in his monograph [138]. The primary minority charge carriers (in the case under consideration, electrons) generated in the base when an alpha particle is slowed down diffuse to the emitter and collector junctions where these carriers become involved in the drift caused by existing fields. Nonequilibrium holes are found residing in a potential well and charge it positively in reference to the emitter. Variation in the emitter–base potential difference increases the secondary-electron current injected by the emitter.

In order to describe the effect quantitatively, it was assumed that the primary-current gain in the phototransistor amounted to $(1 - \alpha_T)^{-1}$, where α_T is the transport coefficient for electrons in the base. Thus, it was implicitly assumed that the emitter efficiency was equal to unity. The expression for α_T in the case when transport of the charge enters into the base with a δ-shaped voltage pulse applied to the emitter–base junction is written as

$$\alpha_T = [(d - W)/L_D]/\sinh[(d - W)/L_D], \qquad (10)$$

where *W* and L_D are the SCR width at the collector junction and the diffusion length of electrons, respectively. Expression (10) forms the basis for a final formula used in [141] to describe the detector signal in relation to *d*, *W*, and L_D.

The dependence *E*(*U*) was measured in the course of the experiment. Therefore, the values of *U* were converted to the values of *W*. In Fig. 13, we show the results of fitting the calculated values of α and L_D to experimental data for two samples.

Alpha particles belong to the class of highly ionizing radiation. At the same time, the response of transistor structures to weakly ionizing radiation (X- and gamma-ray radiation, high-energy particles), in which case the initial dissipation of energy in the film is insignificant, is more important in practice.

Strokan *et al.* [102] detected the X-ray and optical photons. In the case of X-ray detection, the radiation of an X-ray tube was used (anode voltage, 20 kV). For optical-photon detection, the detectors were exposed to light from a mercury lamp. The transistor structures of detectors included a thin (~5 μm) base doped to the level of $N_a^- - N_d^+ = (1–3) \times 10^{-15}$ cm^{-3}. The area of the Schottky barriers was 1.2 mm^2.

The response to the X-ray radiation as a function of U was superlinear. In Fig. 14, we show a portion of the dependence of photocurrent on $(U + 1.5)^{1/2}$; the current was normalized to its value of 13.5 nA at $(U + 1.5)^{1/2} = 4.1\ V^{1/2}$. It is significant that a drastic increase in the current (by a factor of 25 relative to the initial value) is observed within a comparatively narrow range of variations in the argument.

When processing the data of Fig. 14, Strokan *et al.* [102] used the following formula for the steady-state collector current (see [143]):

$$I_c = I_{ph}/(1 - \alpha_T), \quad \alpha_T = \{\cosh[(d - W)/L_D]\}^{-1}. \quad (11)$$

Here, I_{ph} is the primary photoelectron current in the collector and α_T is the transport coefficient for electrons injected into the base owing to a steady-state photovoltage at the emitter–base junction. An expression for I_{ph} in [102] accounted for both the drift transport of electrons from the SCR with the width W and the contribution of electron diffusion from the neutral base.

The comparison shown in Fig. 14 between the experimental data and the results of calculations yielded film thickness $d = 4.66$ μm and diffusion length $L_D \approx 0.35$ μm, which was consistent with the film growth conditions.

A semitransparent Ni electrode was used when charge carriers were generated by optical phonons. Similar processing of dependences $I_c(U)$ yielded $d = 4.67$ μm, which coincided with the corresponding value obtained in the case of X-ray radiation. However, the quantity $L_D = 0.83$ μm exceeded by almost a factor of 2 the value of L_D obtained from the data in Fig. 14. This increase in L_D can be attributed to the fact that the currents in the case of optical excitation of charge carriers were larger by two orders of magnitude than those under excitation with X-ray photons.

It is significant that the signal amplification observed by Strokan *et al.* [102, 141] is not noticeably affected by the features of the charge-carrier generation. The polar cases here are the effects of alpha particles and X-ray photons. Individual alpha particles produce dense charge-carrier tracks in the shape of cylinders with a diameter of ~10 μm, whereas the X-ray photons generate charge carriers with a low density and equiprobably throughout the entire volume of the base in a transistor structure. However, the superlinear increase in the signal amplitude with almost identical amplification coefficients is observed in both cases. As a result, the features of radiation-induced introduction of nonequilibrium charge carriers into the base have almost no effect on the resulting signal. This inference is consistent with a phototransistor model according to which the current flowing through the base is controlled by photovoltage at the emitter–base junction; this photovoltage is generated by the primary charge itself.

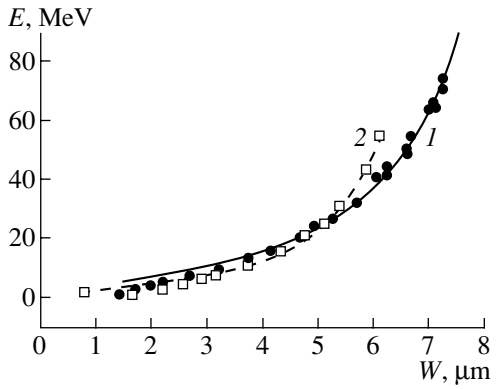

Fig. 13. Dependence of the alpha-particle signal expressed in energy units on the width of the space-charge region at the collector junction (Schottky barrier). The squares and filled circles correspond to experimental data, and the lines represent the results of approximation (see [140]) for the following values of adjustable parameters: diffusion length $L_D = 8.85$ and 5.85 μm and film thickness $d = 10.75$ and 8.53 μm for samples *1* and *2*, respectively.

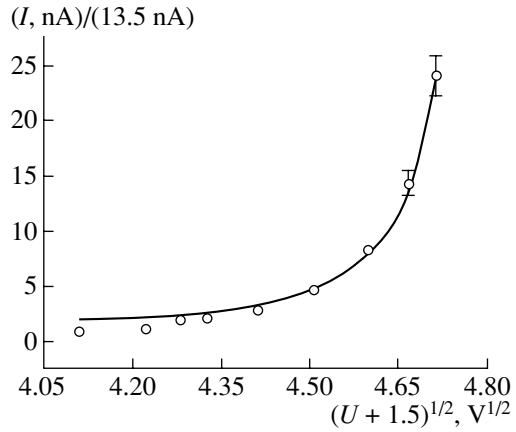

Fig. 14. Dependence of the current induced by the radiation of an X-ray tube on the voltage applied to the detector's diode structure. The solid curve represents the results of approximation (see [102]) at a current normalized to the value of 13.5 nA. The values of the parameters are the following: film thickness $d = 4.66$ μm and electron diffusion length $L_D = 0.35$ μm. The voltage applied to the anode of the X-ray tube was equal to 20 kV.

Thus, internal amplification of the signal by at least tenfold can be accomplished in detectors based on SiC films with a reduced concentration of impurities. This amplification is attained in structures that are comparatively easy to fabricate and include the Schottky barrier; the latter is used as the collector. It is important from the practical standpoint that comparatively thin (on the order of tens of micrometers in thickness) SiC films can be used to detect penetrating radiation. Significantly, the effective thickness of these films is found to be larger than the initial thickness by a factor that is equal to the signal amplification coefficient.

5. CONCLUSION

Naturally, recent advances in the development of growth technology for SiC films have also affected the application field of SiC. In particular, interest in the use of SiC in nuclear physics and in technical applications of SiC as a detecting medium has been renewed. We attempted to present the results of studying the problem of SiC applications in the context of two approaches. First, we tried to give existing examples of using the potential of SiC in typical problems in physics and technology. Second, we did our best to clarify the relation between the detector characteristics and the key parameters of the material. We also mentioned methods for solving the inverse problem, i.e., the problem of determining the electrical characteristics of SiC samples from parameters of detector structures based on these samples.

Concerning the properties of radiation defects in silicon carbide, it is shown that, at room temperature, the concentrations of intrinsic defects that already exist in the material increases irrespective of both the growth technology of the material and the type of incident particles.

The radiation defects produced can be either donors or acceptors. In relation to 6*H*-SiC, this fact brings about, on the one hand, compensation of the material at room temperature and, on the other hand, an increase in $N_d^+ - N_a^-$ at temperatures higher than 600 K. In the case of 4*H*-SiC, the concentration of the acceptors introduced is prevalent. As a result, the concentration $N_d^+ - N_a^-$ is found to be lower than the initial concentration even at elevated temperatures. As a consequence, the estimation of the SiC radiation resistance cannot be restricted to measurements at room temperature because of the significant temperature dependence of the carrier-removal rate.

Numerical values of the radiation-defect production rate at least do not exceed the characteristic values for silicon, which is the main material in contemporary electronics.

Concluding our consideration of problems in SiC detectors, we note that recent progress attained in the growth technology of impurity-free and structurally perfect SiC films (with a density of micropipe defects of ~1 cm^{-2}) has transferred SiC to the class of materials suitable for producing detectors. At present, it is premature to state that an experimental batch of such devices has been fabricated. Publications dealing with research into the structures or testing of detectors in various operational conditions far outnumber those concerned with a direct solution to scientific and technical problems of nuclear physics.

However, the potential of SiC for fabricating a number of SiC-based customized detectors that retain their operation characteristics at high radiation loads, in conditions of an aggressive medium, and at elevated temperatures (as high as 500°C), has been clearly recognized. These specialized detectors can be used in systems for monitoring in acid-containing media with alpha-particle radioactivity and in systems that are designed for determining the fields of X- and gamma-ray radiation and retain normal operation after doses at least as high as tens of megarads. Other applications include SiC detectors for measuring thermal-neutron fields (with ^{10}B as the conversion medium), for detection of high-energy neutrons using the reaction $^{12}C(n_0, \alpha)^9Be$, and for analysis of narrow high-power pulses of X-ray radiation.

A separate class of problems comprises applications in medicine, which are related to the similarity of the stopping powers of silicon carbide and tissues of biological species (tissue equivalence).

ACKNOWLEDGMENTS

We thank Professor V.V. Kozlovskiĭ for his helpful discussion of the manuscript.

REFERENCES

1. *Problems in Radiation Technology of Semiconductors*, Ed. by L. S. Smirnov (Nauka, Novosibirsk, 1980).
2. *Physical Processes in Exposed Semiconductors*, Ed. by L. S. Smirnov (Nauka, Novosibirsk, 1977).
3. J. W. Corbett and J. C. Bourgoin, in *Point Defect in Solids* (Plenum, New York, 1975), Vol. 2, p. 1.
4. B. Hudson and B. E. Sheldon, J. Microsc. **97**, 113 (1973).
5. I. A. Honstvet, R. E. Smallman, and P. M. Marquis, Philos. Mag. A **41**, 201 (1980).
6. H. Inui, H. Mori, and H. Fujita, Philos. Mag. B **61**, 107 (1990).
7. W. Jiang, S. Theunthasan, W. J. Weber, and R. Grotzschel, Nucl. Instrum. Methods Phys. Res. B **161–163**, 501 (2000).
8. I. Lazanu and S. Lazanu, Preprint (Elsevier, 2002).
9. V. S. Balandovich and G. N. Violina, Cryst. Lattice Defects Amorphous Mater. **13**, 189 (1987).
10. A. A. Lebedev, Fiz. Tekh. Poluprovodn. (St. Petersburg) **33**, 129 (1999) [Semiconductors **33**, 107 (1999)].
11. H. Zhang, G. Pensl, P. Glasow, and S. Leibenzeder, in *Extended Abstracts of Electrochemical Society Meeting* (1989), p. 714.
12. J. P. Doyle, M. O. Adoelfotoh, B. G. Svensson, *et al.*, Diamond Relat. Mater. **6**, 1388 (1997).
13. C. Hemmingson, N. T. Son, O. Kordina, *et al.*, Mater. Sci. Eng. B **46**, 336 (1997).
14. C. Hemmingson, N. T. Son, O. Kordina, *et al.*, J. Appl. Phys. **81**, 6155 (1997).
15. T. Dalibor, G. Pensl, H. Matsunami, *et al.*, Phys. Status Solidi A **162**, 199 (1997).
16. M. Gong, S. Fung, C. D. Beiling, and Zhipu You, J. Appl. Phys. **85**, 7604 (1999).
17. V. S. Ballandovich, Fiz. Tekh. Poluprovodn. (St. Petersburg) **33**, 1314 (1999) [Semiconductors **33**, 1188 (1999)].

18. I. Pintilie, L. Pintilie, K. Irmscher, and B. Thomas, Appl. Phys. Lett. **81**, 4841 (2002).
19. M. Gong, S. Fung, C. D. Beiling, and Zhipu You, J. Appl. Phys. **85**, 7120 (1999).
20. H. J. von Bardeleben, J. L. Cantin, L. Henry, and M. F. Barthe, Phys. Rev. B **62**, 10841 (2000).
21. N. T. Son, B. Magnusson, and E. Janzen, Appl. Phys. Lett. **81**, 3945 (2002).
22. V. V. Evstropov and A. M. Strel'chuk, Fiz. Tekh. Poluprovodn. (St. Petersburg) **30**, 92 (1996) [Semiconductors **30**, 52 (1996)].
23. I. M. Pavlov, M. I. Iglitsyn, M. G. Kosagonov, and V. N. Solomatin, Fiz. Tekh. Poluprovodn. (Leningrad) **9**, 1279 (1975) [Sov. Phys. Semicond. **9**, 845 (1975)].
24. A. I. Veĭnger, A. A. Lepneva, G. A. Lomakina, *et al.*, Fiz. Tekh. Poluprovodn. (Leningrad) **18**, 2014 (1984) [Sov. Phys. Semicond. **18**, 1256 (1984)].
25. R. N. Kyutt, A. A. Lepneva, G. A. Lomakina, *et al.*, Fiz. Tverd. Tela (Leningrad) **30**, 1500 (1988) [Sov. Phys. Solid State **30**, 1500 (1988)].
26. A. I. Girka, V. A. Kuleshin, A. D. Mokroshin, *et al.*, Fiz. Tekh. Poluprovodn. (Leningrad) **23**, 1270 (1989) [Sov. Phys. Semicond. **23**, 790 (1989)].
27. R. N. Kyutt, A. A. Lepneva, G. A. Lomakina, *et al.*, Fiz. Tverd. Tela (Leningrad) **30**, 2606 (1988) [Sov. Phys. Solid State **30**, 1500 (1988)].
28. V. V. Evstropov, A. M. Strel'chuk, A. L. Syrkin, and V. E. Chelnokov, Inst. Phys. Conf. Ser. **137**, 589 (1994).
29. O. Okada, T. Kimura, T. Nakata, *et al.*, Inst. Phys. Conf. Ser. **142**, 469 (1996).
30. H. Matsunami and T. Kimoto, Mater. Sci. Eng. R **20**, 125 (1997).
31. V. Nagesh, J. W. Farmer, R. F. Davis, and H. S. Kong, Appl. Phys. Lett. **50**, 1138 (1987).
32. S. Kanazawa, M. Okada, J. Ishil, *et al.*, Mater. Sci. Forum **389–393**, 517 (2002).
33. G. C. Rubicki, J. Appl. Phys. **78**, 2996 (1995).
34. I. V. Il'in, E. N. Mokhov, and P. G. Baranov, Fiz. Tverd. Tela (St. Petersburg) **35**, 1409 (2001) [Phys. Solid State **35**, 1347 (2001)].
35. A. A. Lebedev, D. V. Davydov, A. M. Strel'chuk, *et al.*, Mater. Sci. Forum **338–342**, 973 (2000).
36. A. M. Strel'chuk, V. V. Kozlovskii, N. S. Savkina, *et al.*, Mater. Sci. Eng. **61–62**, 441 (1999).
37. A. A. Lebedev, A. M. Strel'chuk, V. V. Kozlovskii, *et al.*, Mater. Sci. Eng. **61–62**, 450 (1999).
38. A. A. Lebedev, A. I. Veĭnger, D. V. Davydov, *et al.*, Fiz. Tekh. Poluprovodn. (St. Petersburg) **34**, 1058 (2000) [Semiconductors **34**, 1016 (2000)].
39. A. A. Lebedev, A. I. Veinger, D. V. Davydov, *et al.*, J. Appl. Phys. **88**, 6265 (2000).
40. M. M. Anikin, A. N. Andreev, A. A. Lebedev, *et al.*, Fiz. Tekh. Poluprovodn. (Leningrad) **25**, 328 (1991) [Sov. Phys. Semicond. **25**, 198 (1991)].
41. A. Kawasuso, F. Redmann, R. Krause-Rehberg, *et al.*, J. Appl. Phys. **90**, 3377 (2001).
42. A. Kawasuso, F. Redmann, R. Krause-Rehberg, *et al.*, Mater. Sci. Forum **353–356**, 537 (2001).
43. M. F. Barthe, P. Desgardin, L. Henry, *et al.*, Mater. Sci. Forum **389–393**, 493 (2002).
44. A. A. Lebedev, D. V. Davydov, N. S. Savkina, *et al.*, Fiz. Tekh. Poluprovodn. (St. Petersburg) **34**, 1183 (2000) [Semiconductors **34**, 1133 (2000)].
45. A. Kawasuso, F. Redmann, R. Krause-Rehberg, *et al.*, Appl. Phys. Lett. **79**, 3950 (2001).
46. W. C. Mitchel, R. Perrin, J. Goldstein, *et al.*, J. Appl. Phys. **86**, 5040 (1999).
47. A. I. Veĭnger, V. A. Il'in, Yu. M. Tairov, and V. F. Tsvetkov, Fiz. Tekh. Poluprovodn. (Leningrad) **15**, 1557 (1981) [Sov. Phys. Semicond. **15**, 902 (1981)].
48. D. T. Britton, M. F. Barthe, C. Corbel, *et al.*, Appl. Phys. Lett. **78**, 1234 (2001).
49. H. J. von Bardeleben, J. L. Cantin, I. Vickridge, and G. Battisting, Phys. Rev. B **62**, 10126 (2000).
50. D. V. Davydov, A. A. Lebedev, V. V. Kozlovskii, *et al.*, Physica B (Amsterdam) **308–310**, 641 (2001).
51. V. V. Makarov and N. N. Petrov, Fiz. Tverd. Tela (Leningrad) **8**, 1602 (1966) [Sov. Phys. Solid State **8**, 1272 (1966)].
52. V. Makarov, Fiz. Tverd. Tela (Leningrad) **9**, 596 (1967) [Sov. Phys. Solid State **9**, 457 (1967)].
53. N. V. Kodrau and V. V. Makarov, Fiz. Tekh. Poluprovodn. (Leningrad) **15**, 1408 (1981) [Sov. Phys. Semicond. **15**, 813 (1981)].
54. L. Patrick and W. J. Choyke, Phys. Rev. B **5**, 3253 (1972).
55. V. V. Makarov and N. N. Petrov, Fiz. Tverd. Tela (Leningrad) **8**, 3393 (1966) [Sov. Phys. Solid State **8**, 2714 (1966)].
56. V. V. Makarov, Fiz. Tverd. Tela (Leningrad) **13**, 2357 (1971) [Sov. Phys. Solid State **13**, 1974 (1971)].
57. V. M. Gusev, K. D. Demakov, V. M. Efimov, *et al.*, Fiz. Tekh. Poluprovodn. (Leningrad) **15**, 2430 (1981) [Sov. Phys. Semicond. **15**, 1413 (1981)].
58. Yu. A. Vodakov, G. A. Lomakina, E. N. Mokhov, *et al.*, Fiz. Tekh. Poluprovodn. (Leningrad) **20**, 2153 (1986) [Sov. Phys. Semicond. **20**, 1347 (1986)].
59. Yu. M. Suleĭmanov, A. M. Grekhov, and V. M. Grekhov, Fiz. Tverd. Tela (Leningrad) **25**, 1840 (1983) [Sov. Phys. Solid State **25**, 1060 (1983)].
60. Yu. A. Vodakov, A. I. Girka, A. O. Konstantinov, *et al.*, Fiz. Tekh. Poluprovodn. (St. Petersburg) **26**, 1857 (1992) [Sov. Phys. Semicond. **26**, 1041 (1992)].
61. W. J. Choyke, in *Physics and Chemistry of Carbides, Nitrides and Borides*, Ed. by R. Freer (Kluwer, Dordrecht, 1990).
62. A. N. Andreev, M. M. Anikin, A. A. Lebedev, *et al.*, Fiz. Tekh. Poluprovodn. (St. Petersburg) **28**, 729 (1994) [Semiconductors **28**, 430 (1994)].
63. M. M. Anikin, A. S. Zubrilov, A. A. Lebedev, *et al.*, Fiz. Tekh. Poluprovodn. (Leningrad) **25**, 479 (1991) [Sov. Phys. Semicond. **25**, 289 (1991)].
64. A. A. Lebedev, V. V. Kozlovskiĭ, N. B. Strokan, *et al.*, Fiz. Tekh. Poluprovodn. (St. Petersburg) **36**, 1352 (2002) [Semiconductors **36**, 1270 (2002)].
65. B. G. Svensson, A. Hallen, M. K. Linarson, *et al.*, Mater. Sci. Forum **353–356**, 549 (2001).
66. A. Hallen, A. Henry, P. Pellegrino, *et al.*, Mater. Sci. Eng. **61–62**, 378 (1999).

67. R. K. Nadella and M. A. Capano, Appl. Phys. Lett. **70**, 886 (1997).
68. V. Nagesh, J. W. Farmer, R. F. Davis, and H. S. Kong, Appl. Phys. Lett. **50**, 1138 (1987).
69. J. McGarrity, F. McLean, M. Dealancey, *et al.*, IEEE Trans. Nucl. Sci. **39**, 1974 (1992).
70. H. Itoh, M. Yoshikawa, I. Nashiyama, *et al.*, Springer Proc. Phys. **56**, 143 (1992).
71. V. S. Vavilov, N. Yu. Isaev, B. N. Mukashev, and A. B. Spitsyn, Fiz. Tekh. Poluprovodn. (Leningrad) **6**, 1041 (1972) [Sov. Phys. Semicond. **6**, 907 (1972)].
72. Yu. V. Bulgakov and T. I. Kolomenskaya, Fiz. Tekh. Poluprovodn. (Leningrad) **1**, 422 (1967) [Sov. Phys. Semicond. **1**, 346 (1967)].
73. V. L. Vinetskiĭ and L. S. Smirnov, Fiz. Tekh. Poluprovodn. (Leningrad) **5**, 176 (1971) [Sov. Phys. Semicond. **5**, 153 (1971)].
74. D. V. Davydov, A. A. Lebedev, A. S. Tregubova, *et al.*, Mater. Sci. Forum **338–342**, 221 (2000).
75. A. O. Konstantinov, V. N. Kuz'min, L. S. Lebedev, *et al.*, Zh. Tekh. Fiz. **54**, 1622 (1984) [Sov. Phys. Tech. Phys. **29**, 949 (1984)].
76. A. O. Konstantinov, N. S. Konstantinova, O. I. Kon'kov, *et al.*, Fiz. Tekh. Poluprovodn. (St. Petersburg) **28**, 342 (1994) [Semiconductors **28**, 209 (1994)].
77. P. A. Ivanov, O. I. Kon'kov, V. N. Panteleev, and T. P. Samsonova, Fiz. Tekh. Poluprovodn. (St. Petersburg) **31**, 1404 (1997) [Semiconductors **31**, 1212 (1997)].
78. N. Atchtziger, J. Grillenberger, W. Witthuhn, *et al.*, Appl. Phys. Lett. **73**, 945 (1998).
79. H. Inui, H. Mori, and H. Fujita, Philos. Mag. B **1**, 107 (1990).
80. A. A. Lepneva, E. N. Mokhov, V. G. Oding, and A. S. Tregubova, Fiz. Tverd. Tela (Leningrad) **33**, 2217 (1991) [Sov. Phys. Solid State **33**, 1250 (1991)].
81. P. Musumeci, L. Calcagno, M. G. Grimaldi, and G. Foti, Nucl. Instrum. Methods Phys. Res. B **116**, 327 (1996).
82. A. Galeskas, J. Linnros, and P. Pirous, Appl. Phys. Lett. **81**, 883 (2002).
83. K. Kojima, T. Ohno, T. Fujimoto, *et al.*, Appl. Phys. Lett. **81**, 2974 (2002).
84. T. A. Kuhr, J. Q. Liu, H. J. Chung, *et al.*, J. Appl. Phys. **92**, 5863 (2002).
85. R. Okojie, M. Xhang, P. Pirouz, *et al.*, Appl. Phys. Lett. **79**, 3056 (2001).
86. L. J. Brillson, S. Tumakha, G. H. Jessen, *et al.*, Appl. Phys. Lett. **81**, 2785 (2002).
87. Yu. A. Vodakov, G. A. Lomakina, and E. N. Mokhov, Fiz. Tverd. Tela (Leningrad) **24**, 1377 (1982) [Sov. Phys. Solid State **24**, 780 (1982)].
88. E. Oliviero, M. L. David, M. F. Beaufort, *et al.*, J. Appl. Phys. **91**, 1179 (2002).
89. V. A. Kozlov, V. V. Kozlovskiĭ, A. N. Titkov, *et al.*, Fiz. Tekh. Poluprovodn. (St. Petersburg) **36**, 1310 (2002) [Semiconductors **36**, 1227 (2002)].
90. A. Fissel, B. Schroter, U. Kaiser, and W. Richter, Appl. Phys. Lett. **77**, 2418 (2000).
91. A. A. Lebedev, A. M. Strel'chuk, D. V. Davydov, *et al.*, Appl. Surf. Sci. **184**, 419 (2001).
92. A. A. Lebedev, A. M. Strel'chuk, N. S. Savkina, *et al.*, Pis'ma Zh. Tekh. Fiz. **28** (23), 78 (2002) [Tech. Phys. Lett. **28**, 1011 (2002)].
93. R. V. Babcock, S. L. Ruby, F. D. Schupp, and K. H. Sun, *Miniature Neutron Detectors*, Westinghouse Elec. Co. Materials Engineering Report No. 5711-6600-A (1957).
94. R. V. Babcock and H. C. Chang, in *International Atomic Energy Agency Symposium Proceedings* (1963), Vol. 1, p. 613.
95. R. V. Babcock, *Radation Damage in SiC*, Westinghouse Research and Development Center Document No. 64-8C2-432-P1 (1964).
96. V. A. Tikhomirova, O. P. Fedoseeva, and G. F. Kholuyanov, Fiz. Tekh. Poluprovodn. (Leningrad) **6**, 957 (1972) [Sov. Phys. Semicond. **6**, 831 (1972)].
97. V. A. Tikhomirova, O. P. Fedoseeva, and G. F. Kholuyanov, At. Énerg. **34** (2), 122 (1973).
98. V. A. Tikhomirova, O. P. Fedoseeva, and V. V. Bol'shakov, Izmer. Tekh., No. 6, 67 (1973).
99. A. A. Lebedev, N. S. Savkina, A. M. Ivanov, *et al.*, Fiz. Tekh. Poluprovodn. (St. Petersburg) **34**, 249 (2000) [Semiconductors **34**, 243 (2000)].
100. A. A. Lebedev, N. S. Savkina, A. M. Ivanov, *et al.*, Mater. Sci. Forum **338–342**, 1447 (2000).
101. F. Nava, P. Vanni, C. Lanzieri, and C. Canali, Nucl. Instrum. Methods Phys. Res. A **437**, 354 (1999).
102. N. B. Strokan, A. M. Ivanov, M. E. Boĭko, *et al.*, Fiz. Tekh. Poluprovodn. (St. Petersburg) **37**, 65 (2003) [Semiconductors **37**, 65 (2003)].
103. *Ion Implantation: Science and Technology*, Ed. by J. F. Ziegler (Academic, Orlando, 1984).
104. M. Rogalla, K. Runge, and A. Soldner-Rembold, Nucl. Phys. B **78**, 516 (1999).
105. R. A. Logan and A. G. Chynoweth, J. Appl. Phys. **33**, 1649 (1962).
106. V. V. Makarov, Fiz. Tekh. Poluprovodn. (Leningrad) **9**, 1098 (1975) [Sov. Phys. Semicond. **9**, 722 (1975)].
107. N. B. Strokan, Pis'ma Zh. Tekh. Fiz. **24** (5), 44 (1998) [Tech. Phys. Lett. **24**, 186 (1998)].
108. V. K. Eremin, S. G. Danengirsh, N. B. Strokan, and N. I. Tisnek, Fiz. Tekh. Poluprovodn. (Leningrad) **8**, 556 (1974) [Sov. Phys. Semicond. **8**, 355 (1974)].
109. F. Nava, P. Vanni, G. Verzellesi, *et al.*, Mater. Sci. Forum **353–356**, 757 (2001).
110. *DESSIS-6.0 Reference Manual, ISE Integrated Systems Engineering AG* (Zurich, Switzerland).
111. T. Kimoto, S. Nakazawa, K. Fujihira, *et al.*, Mater. Sci. Forum **389–393**, 165 (2002).
112. E. Kalinina, G. Kholujanov, V. Solov'ev, *et al.*, Appl. Surf. Sci. **184**, 323 (2001).
113. G. N. Violina, E. V. Kalinina, G. F. Kholuyanov, *et al.*, Fiz. Tekh. Poluprovodn. (St. Petersburg) **36**, 750 (2002) [Semiconductors **36**, 710 (2002)].
114. G. Bertuccio, R. Casigaghi, and F. Nava, IEEE Trans. Nucl. Sci. **48**, 232 (2001).
115. G. Bertuccio and R. Casigaghi, IEEE Trans. Nucl. Sci. **50**, 175 (2003).
116. CREE Research, Durham, NC 27 713, USA.

117. M. Bruzzi, F. Nava, S. Russo, *et al.*, Diamond Relat. Mater. **10**, 657 (2001).

118. P. Bergonzo, D. Tromson, C. Mer, *et al.*, Phys. Status Solidi A **185**, 167 (2001).

119. M. Rogalla, K. Runge, and A. Soldner-Rembold, Nucl. Phys. B **78**, 516 (1999).

120. R. R. Ferber and G. N. Hamilton, *Silicon Carbide High Temperature Neutron Detectors for Reactor Instrumentation*, Westinghouse Research and Development Center Document No. 65-1C2-RDFCT-P3 (1965).

121. A. R. Dulloo, F. H. Ruddy, and J. G. Seidel, *Radiation Response Testing of SiC Semiconductor Neutron Detectors for Monitoring Thermal Neutron Flux*, Westinghouse Science and Technology Report No. 97-9TK1-NUSIC-R1 (1997).

122. F. H. Ruddy, A. R. Dulloo, J. G. Seidel, *et al.*, IEEE Trans. Nucl. Sci. **45**, 536 (1998).

123. A. R. Dulloo, F. H. Ruddy, J. G. Seidel, *et al.*, IEEE Trans. Nucl. Sci. **46** (3), 275 (1999).

124. G. Lindstrom, M. Moll, and E. Fretwurst, Nucl. Instrum. Methods Phys. Res. A **426**, 1 (1999).

125. E. Verbitskaya, M. Abreu, V. Bartsch, *et al.*, IEEE Trans. Nucl. Sci. **49**, 258 (2002).

126. A. M. Ivanov, N. B. Strokan, D. V. Davydov, *et al.*, Fiz. Tekh. Poluprovodn. (St. Petersburg) **35**, 495 (2001) [Semiconductors **35**, 481 (2001)].

127. A. M. Ivanov, N. B. Strokan, D. V. Davydov, *et al.*, Appl. Surf. Sci. **184**, 431 (2001).

128. N. S. Savkina, A. A. Lebedev, D. V. Davydov, *et al.*, Mater. Sci. Eng. B **77**, 50 (2000).

129. M. M. Anikin, N. I. Kuznetsov, A. A. Lebedev, *et al.*, Fiz. Tekh. Poluprovodn. (St. Petersburg) **28**, 457 (1994) [Semiconductors **28**, 278 (1994)].

130. A. A. Lebedev, A. I. Veinger, D. V. Davydov, *et al.*, J. Appl. Phys. **88**, 6265 (2000).

131. V. V. Emtsev, T. B. Mashovets, and V. V. Mikhnovich, Fiz. Tekh. Poluprovodn. (St. Petersburg) **26**, 22 (1992) [Sov. Phys. Semicond. **26**, 12 (1992)].

132. G. Davies, Physica B (Amsterdam) **273–274**, 15 (1999).

133. V. Eremin, N. Strokan, E. Verbitskaya, and Z. Li, Nucl. Instrum. Methods Phys. Res. A **372**, 388 (1996).

134. N. B. Strokan, A. A. Lebedev, A. M. Ivanov, *et al.*, Fiz. Tekh. Poluprovodn. (St. Petersburg) **34**, 1443 (2000) [Semiconductors **34**, 1386 (2000)].

135. A. A. Lebedev, N. B. Strokan, A. M. Ivanov, *et al.*, Mater. Sci. Forum **353–356**, 763 (2001).

136. S. M. Ryvkin, Zh. Tekh. Fiz. **26**, 2667 (1956).

137. N. A. Vitovskiĭ, P. I. Maleev, and S. M. Ryvkin, Zh. Tekh. Fiz. **28**, 460 (1958) [Sov. Phys. Tech. Phys. **3**, 434 (1958)].

138. S. M. Ryvkin, *Photoelectric Effects in Semiconductors* (Fizmatgiz, Moscow, 1963; Consultants Bureau, New York, 1964).

139. A. Rose, *Concepts in Photoconductivity and Allied Problems* (Interscience, New York, 1963; Mir, Moscow, 1966).

140. A. A. Lebedev, N. B. Strokan, A. M. Ivanov, *et al.*, Appl. Phys. Lett. **79**, 4447 (2001).

141. N. B. Strokan, A. M. Ivanov, D. V. Davydov, *et al.*, Appl. Surf. Sci. **184**, 455 (2001).

142. A. A. Grinberg, Fiz. Tverd. Tela (Leningrad) **1**, 31 (1959) [Sov. Phys. Solid State **1**, 11 (1959)].

143. S. M. Sze, *Physics of Semiconductor Devices*, 2nd ed. (Wiley, New York, 1981; Mir, Moscow, 1984).

Translated by A. Spitsyn

Semiconductors, Vol. 38, No. 2, 2004, pp. 148–149. Translated from Fizika i Tekhnika Poluprovodnikov, Vol. 38, No. 2, 2004, pp. 151–152.

ATOMIC STRUCTURE AND NONELECTRONIC PROPERTIES OF SEMICONDUCTORS

Molecular-Beam Epitaxy Doping of Gallium Nitride with Magnesium from Ammonia

A. A. Vorob'ev*, V. V. Korablev*, and S. Yu. Karpov**

**St. Petersburg State Technical University, ul. Politekhnicheskaya 29, St. Petersburg, 195251 Russia*
e-mail: type@bk.ru
***Soft-Impact, P.O. Box 83, St. Petersburg, 194156 Russia*
Submitted March 25, 2003; accepted for publication July 7, 2003

Abstract—A model of doping with magnesium is verified for molecular-beam epitaxy of gallium nitride using ammonia as a source of Group V reactive component. The good quantitative agreement with experiment makes it possible to compare the *p*-doping efficiency for molecular-beam epitaxy from plasma-activated nitrogen and ammonia within this model. In this case, it is possible to attain a high Mg content in the crystal due to the increased V/III ratio in the incident flows. *© 2004 MAIK "Nauka/Interperiodica".*

Currently, Group III nitrides are basic materials for optoelectronics of the blue–green, violet, and ultraviolet spectral regions, as well as for high-temperature and high-frequency electronics. To produce nitride-based device heterostructures, metal-organic vapor (hydride) phase epitaxy (MOVPE) and molecular-beam epitaxy (MBE) are widely used. One of the topical problems of these growth technologies is *p*-type doping control, in which atomic magnesium (MBE) or its organometallic compounds (MOVPE) are conventionally used. Despite numerous studies of the doping mechanisms, a commonly accepted model describing the features of this process that are observed experimentally has not yet been developed. We recently suggested [1] a model of GaN doping with magnesium in MBE using plasma-activated nitrogen as a reactive component of Group V. The model is based on the assumption that Mg and Ga compete to be incorporated into the GaN cationic sublattice; as a result, the magnesium content n_{Mg} in GaN becomes related to the incident flux F_{Mg} and the crystal growth rate V_g (monolayers per second (ML/s) as

$$n_{Mg} = \frac{N_A \rho_{GaN}}{M_{GaN}} \frac{F_{Mg}}{V_g + k_{Mg}\omega\theta_{Ga}}, \quad (1)$$

where N_A is Avogadro's number; ρ_{GaN} and M_{GaN} are the GaN density and molar mass, respectively; $k_{Mg} = 7.71 \times 10^{12}\exp(-14994/T)$ s^{-1} and θ_{Ga} are the coefficient of Mg desorption from the GaN surface [1] and the surface coverage with gallium; and $\omega(T) = 3.523 \times 10^5\exp(-21070/T)$ is the equilibrium constant corresponding to the Mg transition from the adsorbed layer into the crystal bulk. This constant was determined in [1] by fitting the temperature dependence of the introduced impurity content to the data of [2].

In this paper, it will be shown that the model suggested in [1] quantitatively describes GaN doping with magnesium in MBE with ammonia as a reactive nitrogen source. This allows one to compare the doping efficiency in two MBE types, from plasma-activated nitrogen and ammonia.

The GaN growth rate in ammonia MBE was calculated within the kinetic model [3], allowing one to predict the surface coverage with gallium and nitrogen atoms. This model takes into account the hydrogen adsorbed at the surface by introducing an effective coefficient of nitrogen molecule desorption, which is noticeably smaller than that in the absence of hydrogen. The Mg content in the crystal was determined from expression (1). To validate the model, we used the experimental data of [4] on GaN doping with magnesium in ammonia MBE. Figure 1 shows that the model's predictions are in good quantitative agreement with the experiment. We can see that the inclined tem-

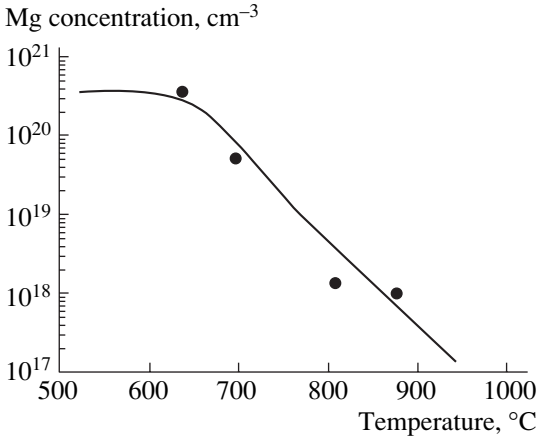

Fig. 1. Temperature dependence of the magnesium content in GaN: experimental data of [4] (circles) and theoretical predictions (curve). The fluxes F of Ga, NH_3, and Mg are 1.1, 32, and 0.008 ML/s, respectively.

perature dependence of the Mg content in the crystal flattens at temperatures lower than ~650°C. This transition corresponds to the change in the impurity trapping mechanism discussed in [1]. At $T \geq 650$°C and $T \leq 650$°C, the Mg content in the adsorbed layer is mainly controlled by the balance between the incident and desorbed Mg flows and the balance between the arrival of Mg on the growing surface and its escape into the crystal, respectively. In the latter case, the Mg content in the solid phase becomes dependent on the ratio F_{Mg}/V_g (as follows from expression (1)) at $V_g \gg k_{Mg}\omega\theta_{Ga}$, rather than on temperature.

The good agreement between theory and experiment allows one to carry out a comparative analysis of the efficiency of Mg introduction into MBE GaN, using various sources of the Group V reactive component, i.e., plasma-activated nitrogen and ammonia. To this end, we chose typical growth conditions for these two technologies, assuming that the incident Ga flow is ~1 ML/s in both cases. In MBE from plasma-activated nitrogen (PEMBE), it is possible to attain for a short time only a small excess of the nitrogen flux over the gallium flux because of GaN surface faceting during growth. Therefore, we took the V/III ratio in the calculations as $F_N/F_{Ga} = 1.1$. Appreciably larger V/III ratios in the incident fluxes are characteristic of ammonia MBE (NH_3-MBE). Taking into account the small sticking coefficient of ammonia at the GaN surface ($\alpha_{NH_3} = 0.04$ [5]), this ratio is $\alpha_{NH_3}F_{NH_3}/F_{Ga} = 4.0$.

The values of Mg content in the crystal, calculated for MBE from plasma-activated nitrogen and ammonia with magnesium flux $F_{Mg} = 0.003$ ML/s, are compared in Fig. 2. We can see that, in the case of direct trapping of the impurity by the crystal ($T \leq 650$°C for MBE from plasma-activated nitrogen and $T \leq 700$°C for MBE from ammonia), both technologies feature identical efficiency of impurity introduction, whose content can be as high as 10^{20} cm^{-2}. However, at higher temperatures favorable for producing high-quality GaN crystals, a higher Mg content can be attained in MBE from ammonia (Fig. 2a). This is directly associated with the influence of the efficiency of introduction of Mg coverage over the gallium growth surface, which decreases as the V/III ratio increases in the incident fluxes (Fig. 2b). This factor, combined with higher achievable growth temperatures [3], additionally emphasizes the advantages of ammonia MBE for growing device heterostructures for optoelectronics.

Thus, the model of GaN doping with magnesium [1] was verified for MBE from ammonia. The doping efficiency was compared for two types of reactive component source from Group V: ammonia and plasma-activated nitrogen. It was shown that, with respect to the doping efficiency, ammonia MBE is more advantageous compared to MBE from plasma-activated nitrogen due to the possibility of using a higher V/III ratio in incident fluxes.

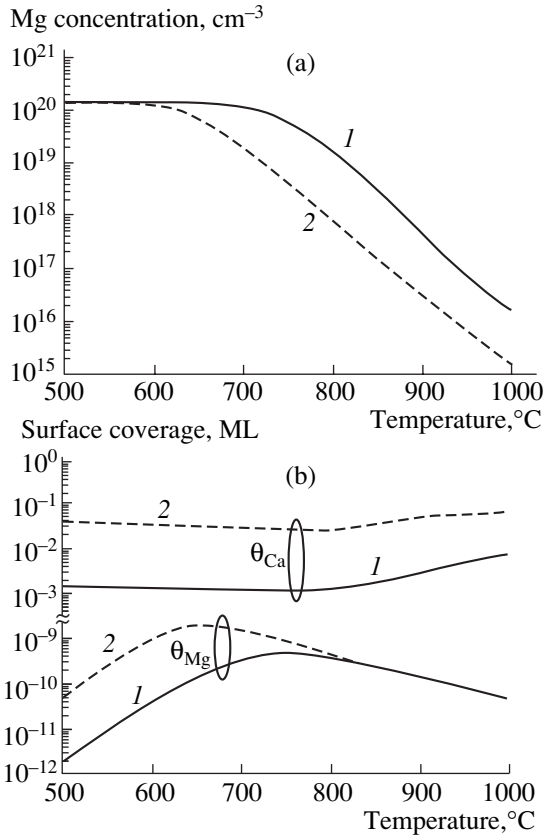

Fig. 2. (a) Magnesium content and (b) degrees of surface coverage with magnesium and gallium in relation to the growth temperature, calculated for typical GaN growth conditions using (*1*) MBE from ammonia (NH_3–MBE) and (*2*) plasma-activated nitrogen (PEMBE).

REFERENCES

1. A. A. Vorob'ev, V. V. Korablev, and S. Yu. Karpov, Fiz. Tekh. Poluprovodn. (St. Petersburg) **37**, 866 (2003) [Semiconductors **37**, 838 (2003)].
2. S. Guha, N. A. Bojarzuk, and F. Cardone, Appl. Phys. Lett. **71**, 1685 (1997).
3. S. Yu. Karpov, R. A. Talalev, Yu. N. Makarov, *et al.*, Surf. Sci. **450**, 191 (2000).
4. M. Kamp, M. Mayer, A. Pelzmann, and K. J. Ebeling, MRS Internet J. Nitride Semicond. Res. **2**, 26 (1997).
5. M. Mesrine, N. Grandjean, and J. Massies, Appl. Phys. Lett. **72**, 350 (1998).

Translated by A. Kazantsev

Semiconductors, Vol. 38, No. 2, 2004, pp. 150–152. Translated from Fizika i Tekhnika Poluprovodnikov, Vol. 38, No. 2, 2004, pp. 153–155.

ATOMIC STRUCTURE AND NONELECTRONIC PROPERTIES OF SEMICONDUCTORS

A Simple Model for Calculating the Growth Rate of Epitaxial Layers of Silicon Carbide in Vacuum

S. Yu. Davydov*, A. A. Lebedev*, N. S. Savkina*, M. Syvajarvi, and R. Yakimova****

**Ioffe Physicotechnical Institute, Russian Academy of Sciences, Politekhnicheskaya ul. 26, St. Petersburg, 194021 Russia*

e-mail: sergei_davydov@mail.ioffe.ru

***Linkoping University, S-581 83 Linkoping, Sweden*

Submitted December 29, 2002; accepted for publication June 3, 2003

Abstract—The temperature dependence of the growth rate of epitaxial layers of silicon carbide in vacuum was calculated within the simple model based on the Hertz–Knudsen equation, taking into account the temperature-dependent sticking coefficient. The calculation results fit the experimental data well. © *2004 MAIK "Nauka/Interperiodica".*

Sublimation epitaxy of silicon carbide is generally used to produce 3D crystals [1]. The process is carried out in inert gas, which allows growth rates of up to several centimeters per hour. Epitaxial growth of thin films imposes increased requirements upon the layer–substrate interface and gas; however, the requirements for growth rates are lower (a rate of 10 μm/h is acceptable). All these factors allow one to use SiC sublimation epitaxy and, in particular, vacuum epitaxy, to produce device structures, e.g., diodes.

The simulation of epitaxial growth is a very difficult problem, since one needs to consider the various physicotechnical processes and complex configurations of practical setups, as one does in simulating vapor-phase growth [2, 3]. No matter how paradoxical this may seem, the mathematical model of vacuum growth, where everything seems to be much simpler compared to the transport of molecules that form a crystal in an inert gas, is the least well developed of all such models. The point is that an inert gas aligns the "working material" flux in a certain way; in vacuum, a stochastic process takes place [4], which is simulated, as a rule, using the Monte Carlo method. Fortunately, along with intricate numerical calculations based on hydrodynamic equations, there are simplified schemes based on the Hertz–Knudsen equation according to which the molar flux J of a material is given by (see, e.g., [5–7])

$$\begin{aligned} J &= X(T)p(T), \\ X &= (2\pi MRT)^{-1/2}, \end{aligned} \tag{1}$$

where M is the molar mass of transported material, R is the universal gas constant, T is the temperature, and p is the equilibrium vapor pressure of the transported material. Conceptually, the Hertz–Knudsen equation describes the evaporation rate of solid molecules into vacuum, i.e., the number of particles leaving a unit area of solid per unit time [8]. The growth rate G defined by formula (1) is given by

$$G = \frac{M}{\rho}J, \tag{2}$$

where ρ is the density of the growing material.

As follows from [5], in order to describe the growth of the SiC epitaxial layer, we introduce the sticking coefficient α. We will assume that this coefficient depends on temperature; i.e., we assume that a certain potential barrier should be overcome for atoms to be adsorbed at the substrate surface. This means that we use the model suggested in [9] to describe the growth of silicon and germanium crystals. As in [4–6, 8], we disregard (for simplicity) the temperature gradient in a cell, assuming that its influence on the process rate is weak, although the presence of this gradient is a necessary condition for growth. We can then write

$$\begin{aligned} G &= \frac{M_{\mathrm{SiC}}}{\rho_{\mathrm{SiC}}}X_{\mathrm{SiC}}(T)p_{\mathrm{SiC}}(T)\alpha(T), \\ X_{\mathrm{SiC}} &= (2\pi M_{\mathrm{SiC}}RT)^{-1/2}, \\ p_{\mathrm{SiC}}(T) &= B\exp(-Q/RT), \quad \alpha(T) = A\exp(-E_a/RT), \end{aligned} \tag{3}$$

where Q is the heat of SiC sublimation and A and B are coefficients. In this paper, devoted to the calculation of the growth rate of SiC epitaxial layers on SiC substrates, we will proceed from these expressions. Certainly, we recognize that SiC, SiC_2, Si, Si_2C, and C are actually involved in the transport, rather than SiC molecules (see, e.g., [6, 7]). However, according to the model in [5], we disregard this factor for simplicity.

The experimental setup and the growth cell are described in [10] in detail. We only note that growth in an "open" system is simulated. This means that some

molecules of the material leave the growth region without participating in mass transfer. The experimental temperature dependence of the growth rate for the epitaxial film in such a system is shown in Fig. 1 (curve *1*). For comparison, Fig. 1 also shows a similar dependence for a "quasi-closed" system (curve *2*) described in [11].

To describe the experimental data, it is convenient to introduce the dimensionless growth rate $g \equiv G/G_0$, where G is the growth rate at the temperature T, and G_0 is the highest growth rate (1000 μm/h) corresponding to temperature $T_0 = 2326$ K. Introducing the dimensionless parameters

$$\omega = \omega_q + \omega_a = \frac{Q + E_a}{RT_0} = \frac{Q}{RT_0} + \frac{E_a}{RT_0}$$
$$\text{and } \xi = \frac{T_0}{T} \geq 1\ldots, \quad (4)$$

we obtain

$$g \equiv G/G_0 = \sqrt{\xi}\exp[-\omega(\xi - 1)]. \quad (5)$$

We can see from Fig. 2 that the results of the calculations fit the experimental data well when $\omega = 48$ (curve *1*, this study) and $\omega = 30$ (curve *2*, [12]).

Let us analyze this result. According to [13], the equilibrium pressure of silicon carbide is defined by the parameters $B = 4.3323 \times 10^{13}$ Pa and $Q = 567.35$ J/mol = 5.88 eV per molecule. Hence, $\omega_q \equiv Q/RT_0 = 29.4$, then $\omega_a \equiv E_a/RT_0 = 18.6$. The latter equality suggests that $E_a = 3.73$ eV per molecule, which is in satisfactory agreement with the bonding energy (per bond) of silicon carbide, which equals 3.17 eV [12]. Proceeding from the fact that $G_0 = 1000$ μm/h, we have $A = 0.286 \times 10^8$, which yields the sticking coefficient $\alpha = 0.24$ at $T_0 = 2326$ K. Hence, every fourth molecule sticks to the substrate, which seems to be quite reasonable.

The second series of growth experiments was carried out in a quasi-closed system on a 6*H*-SiC silicon surface. The angle of the substrate-surface misorientation was 3.5° along the $\langle 11\bar{2}0\rangle$ direction. The growth reactor consisted of a quartz tube and water-cooled steel flanges. The growth cell, growth source, and substrate were inside a graphite container heated by an induction coil using an HF oscillator. The growth temperature ranged from 1700 to 1800°. In the case of polycrystalline SiC as a growth source at low pressures, the layer-growth rate was controlled by the source evaporation rate [11]. An analysis of the parameters for the quasi-closed system with $T_0 = 2273$ K, $G_0 = 1394$ μm/h, and the same values of B and Q yields $\omega_q = 30$, $\omega_a = 0$, and $\alpha = 0.6$. Here it is particularly interesting that there is no adsorption barrier ($E_a = 0$), which results in an increase in the sticking coefficient by a factor of 2.5 and a corresponding increase in the growth rate compared to the open system. These differences seem to be associated with the substrate-surface state and the design features of the setup.

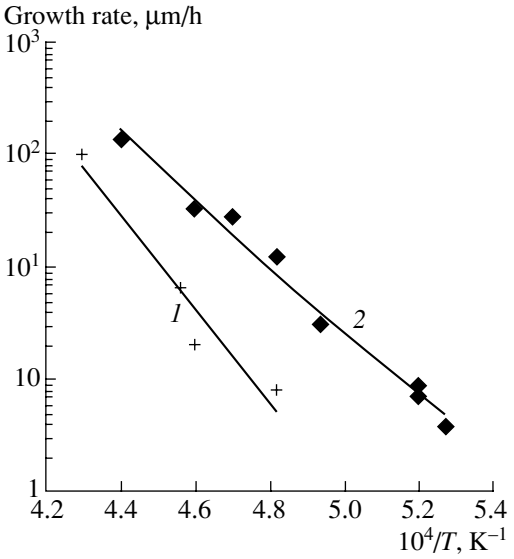

Fig. 1. Experimental growth rates of silicon carbide layers in relation to inverse temperature according to the data of (*1*) [10] and (*2*) [11].

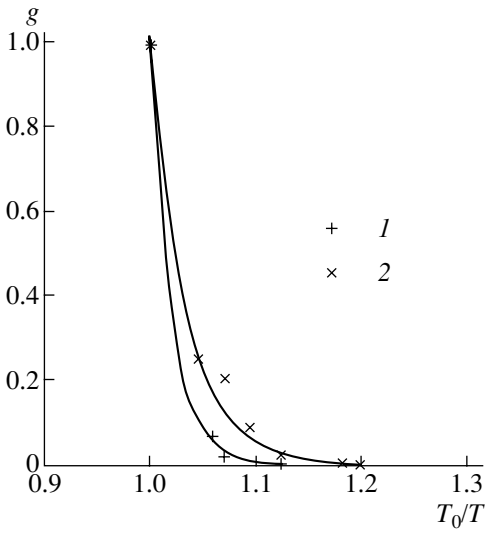

Fig. 2. Comparison of the growth rates $g \equiv G/G_0$ calculated as a function of reduced inverse temperature T_0/T with the experimental data: (*1*) this study, $\omega = 48$, and (*2*) [12], $\omega = 30$.

As the authors of [9], we specified the sticking coefficient α purely empirically, assuming that, in order to be stuck at the surface, a molecule should overcome a certain potential barrier E_a. At high temperatures, such an approximation seems to be acceptable, since it takes into account the increase in the probability that a molecule is captured by the surface as T increases, which conforms to the results obtained, for example, in theoretical studies [14, 15].

We are grateful to V.V. Zelenin for helpful discussions.

This study was supported by the grants INTAS-01-0603 and NATO SfP N978011.

REFERENCES

1. Yu. M. Tairov, in *Electric Refractory Materials*, Ed. by Y. K. Kumashiru (Marcel Dekker, New York, 2000), p. 409.
2. A. I. Zhmakin, Yu. N. Makarov, D. Kh. Ofengeĭm, and M. S. Ramm, in *Problems in Mathematical Physics and Applied Mathematics* (Fiz.–Tekh. Inst. Ross. Akad. Nauk, St. Petersburg, 2001), p. 208.
3. M. Selder, L. Kadinsky, and F. Durst, in *Problems in Mathematical Physics and Applied Mathematics* (Fiz.–Tekh. Inst. Ross. Akad. Nauk, St. Petersburg, 2001), p. 235.
4. K. F. Jensen, *Handbook of Crystal Growth* (North-Holland, Amsterdam, 1994), Vol. 3.
5. T. Kaneko, J. Cryst. Growth **69**, 1 (1984).
6. D. D. Avrov, A. S. Baskin, S. I. Dorozhkin, *et al.*, J. Cryst. Growth **198–199**, 1011 (1999).
7. Q.-S. Chen, H. Zhang, V. Prasad, *et al.*, J. Cryst. Growth **224**, 101 (2001).
8. L. D. Landau and E. M. Lifshitz, *Course of Theoretical Physics*, Vol. 5: *Statistical Physics*, 3rd ed. (Nauka, Moscow, 1976; Pergamon Press, Oxford, 1980), Part 1.
9. J. A. Bootsma and H. J. Gassen, J. Cryst. Growth **10**, 223 (1971).
10. N. S. Savkina, A. A. Lebedev, D. V. Davydov, *et al.*, Mater. Sci. Eng. B **61–62**, 50 (2000).
11. M. Syväjärvi, R. Yakimova, M. Tuominen, *et al.*, J. Cryst. Growth **197**, 155 (1999).
12. W. A. Harrison, *Electronic Structure and the Properties of Solids: The Physics of the Chemical Bond* (Freeman, San Francisco, 1980; Mir, Moscow, 1983).
13. S. K. Lilov and I. Y. Yanchev, Cryst. Res. Technol. **28**, 495 (1993).
14. A. Hurkmans, E. G. Overbosh, D. R. Olander, and J. Los, Surf. Sci. **54**, 154 (1976).
15. F. O. Goodman, Surf. Sci. **92**, 185 (1980).

Translated by A. Kazantsev

Semiconductors, Vol. 38, No. 2, 2004, pp. 153–160. Translated from Fizika i Tekhnika Poluprovodnikov, Vol. 38, No. 2, 2004, pp. 156–163.

ATOMIC STRUCTURE AND NONELECTRONIC PROPERTIES OF SEMICONDUCTORS

Adsorption of Solvated Hydrosulfide Ions at a GaAs(100) Surface: The Role of a Solvent in Surface Structure Modification

M. V. Lebedev*, Th. Mayer, and W. Jaegermann****

**Ioffe Physicotechnical Institute, Russian Academy of Sciences, Politekhnicheskaya ul. 26, St. Petersburg, 194021 Russia*
e-mail: mleb@triat.ioffe.ru
***TU-Darmstadt, FB Material- und Geowissenschaften, FG Oberflächenforschung,*
Petersenstr. 23, Darmstadt, 64287 Germany
Submitted June 2, 2003; accepted for publication June 3, 2003

Abstract—Adsorption of HS^- hydrosulfide ions solvated by different amphiprotic solvents (water, alcohols) at the oxide-free GaAs(100) surface was studied by photoemission spectroscopy. The adsorption was carried out from ammonium sulfide solutions in an inert oxygen-free ambient. In the core-level spectra, the chemical shift of the component stemming from the As–S bonds in reference to the component related to As–Ga bulk emission is shown to increase as the permittivity of the solvent used decreases. This fact points to the increase in the ionicity of forming As–S bonds. The ionization energy of the semiconductor after adsorption also depends on the solvent from which the adsorption occurs. Such a dependence is retained after annealing of the surface and disappearance of the As–S bonds, which indicates that the solvent affects the surface atomic structure. It is shown that the solvent modifies the ion chemical properties and reactivity via solvation, which results in a change in the mechanism of interaction of ions with semiconductor surface atoms. *© 2004 MAIK "Nauka/Interperiodica".*

1. INTRODUCTION

Modern semiconductor devices are comparable in size with the lattice constant of semiconductor crystals. Therefore, the properties of surfaces and interfaces are of critical importance. In this context, the methods for chemical engineering of surface electronic properties (surface states spectrum, surface potentials, etc.) have been actively developed in the last few years in order to extend the potential of semiconductor materials in electronics [1]. Chemical modification of surface electronic properties occurs due to interaction of the adsorbing atoms, ions, or molecules with atoms or states at semiconductor surface, as well as due to charge transfer between the adsorbates and the semiconductor.

Many semiconductor technological processes occur at the semiconductor/electrolyte interface. It is known that the solvation of ions or molecules by the polar solvents results in modification of the electronic shell of solutes, which can cause radical changes in their chemical properties [2]. This effect may be most pronounced when coordination hydrogen bonds can be formed between the solute and solvent molecules. These hydrogen bonds can change considerably the electronic density distribution in the solvated ion or molecule.

It has been found experimentally that the solvent where adsorption occurs can considerably affect the electronic structure of the forming surface, even without being involved in direct reaction. For instance, when sulfur is adsorbed in the form of HS^- hydrosulfide ions from the electrolyte solutions, the electronic properties of the adsorbate-covered surface correlate with the value of the static permittivity of the solvent. A more efficient reduction in surface recombination velocity of GaAs [3] and GaN [4], as well as of the surface states density in GaAs [3], InP [5], and InGaAs solid solutions [6], is obtained when the surface treatment is carried out in a solution with a lower permittivity. The treatment of laser mirrors with low-permittivity alcoholic sulfide solutions results in an appreciable improvement in semiconductor laser performance; this increase in laser efficiency also depends on the solvent used [7, 8]. The effect of the solvent on the photoluminescence intensity was observed after treatment of GaAs with HCl solutions as well [9].

It would seem reasonable to suppose that the influence of the solvent from which the adsorption proceeds on the electronic properties of the semiconductor surface stems from the modification of the adsorbates' chemical properties by solvation, which alters chemical reactions in the surface processes. It was theoretically shown [10] that solvation could affect the length and character of the chemical bonds formed in the course of the reactions in solutions. Accordingly, the character of the chemical bonds between the adsorbate and the surface atoms at the semiconductor/solution interface can vary if the adsorbate is solvated by different solvents.

In this study, the chemical processes at the interface between GaAs(100) and sulfide solution are analyzed by photoemission spectroscopy, and the role of the solvent in forming chemical bonds between the solvated hydrosulfide ions and semiconductor surface atoms is investigated.

1063-7826/04/3802-0153$26.00 © 2004 MAIK "Nauka/Interperiodica"

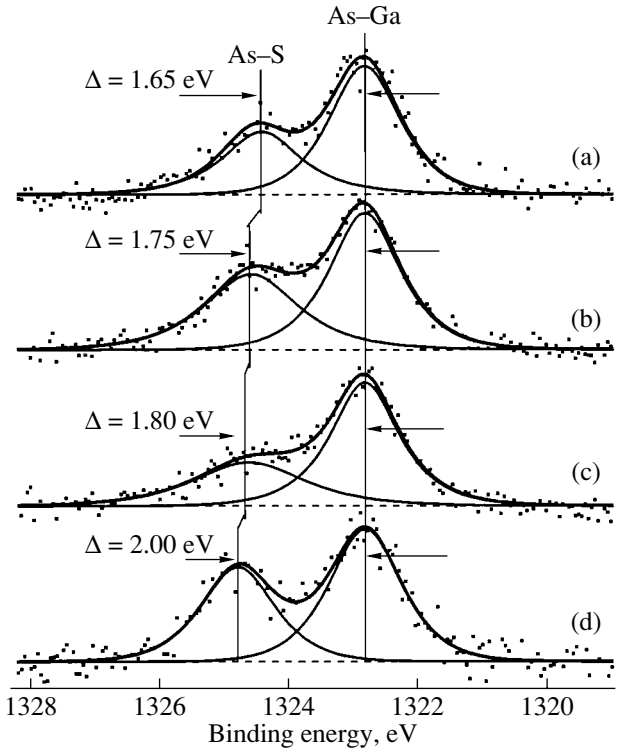

Fig. 1. As 2*p* core-level spectra of an oxide-free GaAs(100) surface sulfidized using the following solutions: (a) $(NH_4)_2S + H_2O$, (b) $(NH_4)_2S + CH_3OH$, (c) $(NH_4)_2S + i\text{-}C_3H_7OH$, and (d) $(NH_4)_2S + t\text{-}C_4H_9OH$.

2. EXPERIMENTAL

This study was carried out on specially prepared *n*-GaAs(100) ($n = 2 \times 10^{17}$ cm^{-3}) wafers. First of all, the wafers were placed into the ultrahigh vacuum (UHV) chamber, where they were cleaned by Ar ion bombardment for 30 min and then annealed at 550°C for 1 hour. After such treatment, the sample surface contained no oxygen and carbon. For sulfur treatment, the samples were transferred (without any contact with ambient air) to a special electrochemical chamber [11] constructed of standard glass elements. This glass chamber was purged with dry, carbon-free N_2-atmosphere and was directly connected to an UHV chamber of the measuring system.

The sulfur treatment was carried out by depositing a droplet of the solution onto the sample surface. We used ammonium sulfide [$(NH_4)_2S$] solutions in water (H_2O), methanol (CH_3OH), isopropanol ($i\text{-}C_3H_7OH$), and *tert*-butanol ($t\text{-}C_4H_9OH$). The concentration of ammonium sulfide in aqueous solution amounted to 25 vol % and in alcoholic solutions, 2–3 vol %. The sample surfaces were exposed to the solution for 10 min and then the residual solution was blown off by a dry nitrogen jet. Only freshly prepared solutions were used in the experiments. Afterwards, the samples were transferred back to the UHV chamber without contacting the ambient air.

For photoelectron spectroscopy analysis, a PHI 5700 MultiTechnique system was used. Core-level spectra were measured using a monochromatic AlK_α source ($h\nu$ = 1486.6 eV). The binding energies of core levels were reckoned from the Fermi energy. The energy scale of the spectrometer was calibrated by using the Au binding energy $E_b(\text{Au}4f_{7/2}) = 84.00$ eV. Valence-band spectra were measured under normal emission using radiation from a helium lamp (He I, $h\nu$ = 21.2 eV). During the measurements of the valence-band spectra, the sample was biased by –1.5 V relative to both the analyzer and the vacuum chamber. The ionization energy of all surfaces was determined using the measurement of the full width of the valence-band energy distribution curves, i.e., the energy separation between the onset of emission from the edge of the valence band and the onset of the secondary electron emission. To obtain the value of ionization energy, the full width of the valence band spectrum was subtracted from the excitation energy (21.2 eV) [12]. The measurements of the spectra were carried out before and after sulfur treatment, as well as after several successive annealing steps, each of approximately 10 min. The annealing temperature at each next step was higher than at the preceding step. The annealing temperature was measured using a thermocouple positioned in the vicinity of the sample.

3. RESULTS

3.1. X-Ray Photoemission Spectroscopy

The survey X-ray photoemission spectra of initial surfaces (after Ar-ion sputtering and annealing) contain only Ga- and As-related peaks. After the sulfur treatment, sulfur, oxygen, and carbon peaks appear in the survey spectra. The intensity of the oxygen and carbon peaks was in all cases much lower than the intensity of these peaks at the surface covered by the native oxide, as well as at the Ar-ion bombarded and annealed contaminant-free surface, which was deliberately oxidized for 3 min in ambient air before clear evidence of gallium and arsenic oxides appear in the spectra.

Resolution of the As 2*p* core-level spectra of the surfaces treated with different solutions (Fig. 1) shows that, along with the bulk component stemming from the As–Ga chemical bonds, an additional component with a higher-binding energy appears in the spectra. As a reference for the shape of the bulk contribution, the spectrum of an initial Ar-ion bombarded and annealed surface was used. This higher-binding energy component can be attributed to the formation of the arsenic sulfides at the surface, since the formation of arsenic oxides can be excluded because the concentration of oxygen at these surfaces is quite low and, moreover, the chemical shift of the arsenic oxides should be considerably higher (3 eV or more [13–15]). The chemical shift of the arsenic-sulfide-related component in reference to the As–Ga bulk signal was different for the surfaces

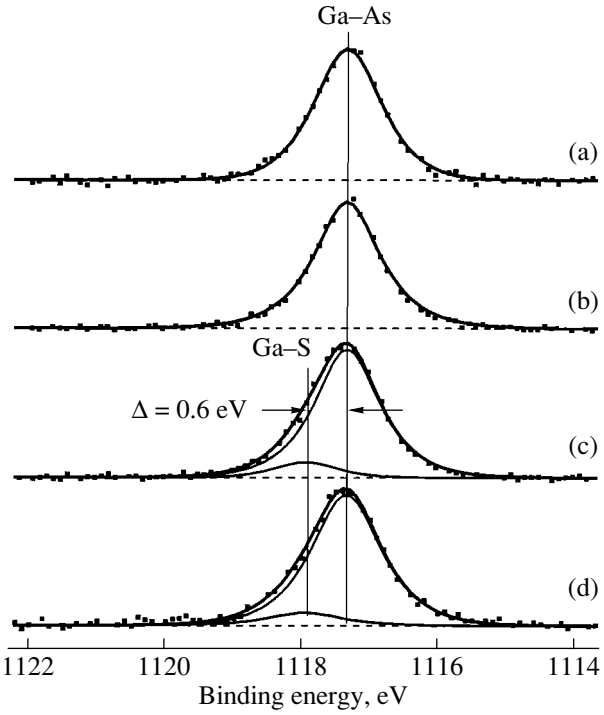

Fig. 2. Ga 2*p* core-level spectra of the oxide-free GaAs(100) surface sulfidized using the following solutions: (a) $(NH_4)_2S + H_2O$, (b) $(NH_4)_2S + CH_3OH$, (c) $(NH_4)_2S + i\text{-}C_3H_7OH$, and (d) $(NH_4)_2S + t\text{-}C_4H_9OH$.

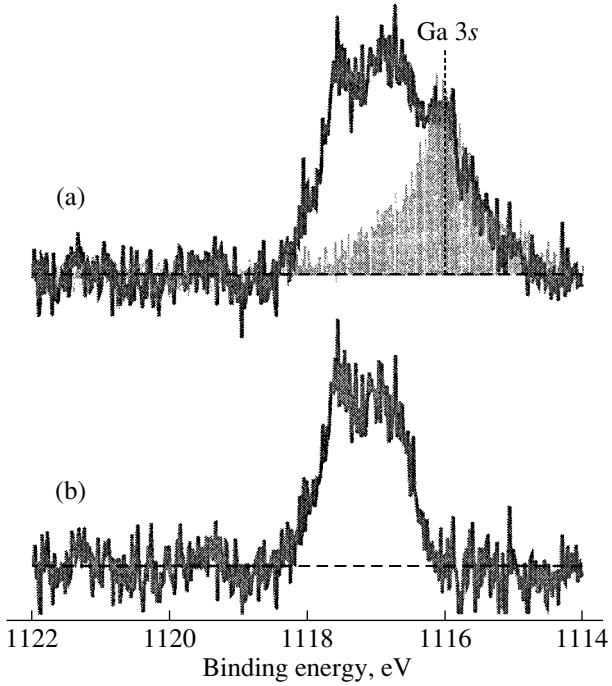

Fig. 3. (a) S 2*p* core-level spectrum of the GaAs(100) surface sulfidized using the $(NH_4)_2S + t\text{-}C_4H_9OH$ solution; the overlapping Ga 3*s* core level of an oxide-free unsulfidized GaAs(100) surface is shadowed. (b) Difference between spectrum (a) and the Ga 3*s* core-level spectrum of an oxide-free unsulfidized GaAs(100) surface.

treated in different solvents. In particular, the As–S bonds formed in the course of treatment with aqueous sulfide solution have the lowest chemical shift (Fig. 1a), whereas the bonds obtained after the treatment with the *tert*-butanol-based sulfide solution have the highest chemical shift (Fig. 1d). This difference in chemical shifts of the As–S component was found both in As 2*p* core-level spectra (Fig. 1) and in As 3*d* core-level spectra as well.

No detectable changes in Ga 3*d* core-level spectra were observed after sulfur treatment. At the same time, in Ga 2*p* core-level spectra of the surfaces treated with isopropanol- and *tert*-butanol-based sulfide solutions, a low-intensity component with a chemical shift of 0.6 eV in reference to the Ga–As bulk component was observed (Fig. 2). This low-intensity component indicates that Ga–S chemical bonds are formed at the surface [16].

It is difficult to analyze sulfur core levels at the GaAs surface when an AlK_α source is used because the S 2*p* level (binding energy of about 160 eV) and the S 2*s* level (binding energy of about 220 eV) are overlapped with the Ga 3*s* and the Auger As $L_2M_{45}M_{45}$ levels, respectively. Figure 3 shows the spectral region of the S 2*p* core level for a surface treated with the $(NH_4)_2S + t\text{-}C_4H_9OH$ solution. The overall spectrum is shown in Fig. 3a, where the Ga 3*s* core level of the untreated sample is indicated. To obtain a pure S 2*p* signal, the shadowed Ga 3*s* core level was subtracted from this overall spectrum. The difference spectrum is shown in Fig. 3b. The spectra of the S 2*p* core level for all other sulfide-treated surfaces appear similar.

Annealing a surface treated with an aqueous sulfide solution results in the apparent disappearance of the As–S bonds just after the first annealing step (at 300 °C) and in the appearance of Ga–S bonds (shifted from the bulk component by 0.6 eV). When surfaces treated with alcoholic sulfide solutions (isopropanol- and *tert*-butanol-based), where the As–S bonds have the larger chemical shift, are annealed, this initially causes the transformation of the As–S bonds into As–S bonds with a smaller chemical shift (Fig. 4). New Ga–S bonds, in addition to the existing ones, are also formed.

3.2. Ultraviolet Photoemission Spectroscopy

The valence-band spectrum of the initial GaAs(100) surface (obtained by Ar ion bombardment and subsequent annealing) contains four distinct features (peaks) with binding energies of 1.0, 2.7, 4.0, and 6.7 eV in reference to the valence-band maximum (Fig 5a). The first feature can be attributed to the emission from the As–As dimer-related surface states [17]. The remaining features originate from the bulk critical points X_5, $\Sigma_I^{\min}$, and X_3, respectively [17, 18].

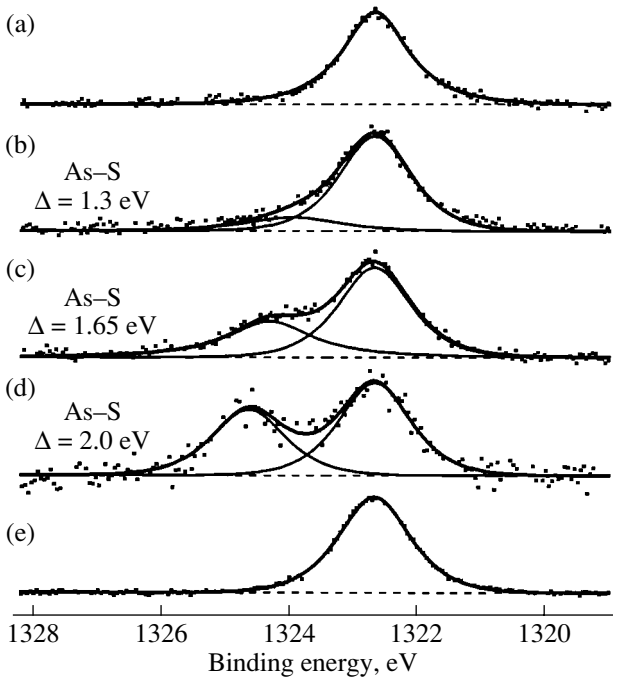

Fig. 4. Evolution of As 2*p* core-level photoemission spectrum of the oxide-free GaAs(100) surface after sulfidization using the $(NH_4)_2S$ + t-C_4H_9OH solution and subsequent annealing at temperatures of (a) 500, (b) 400, and (c) 300°C; (d) without annealing (as-treated); and (e) before sulfidization.

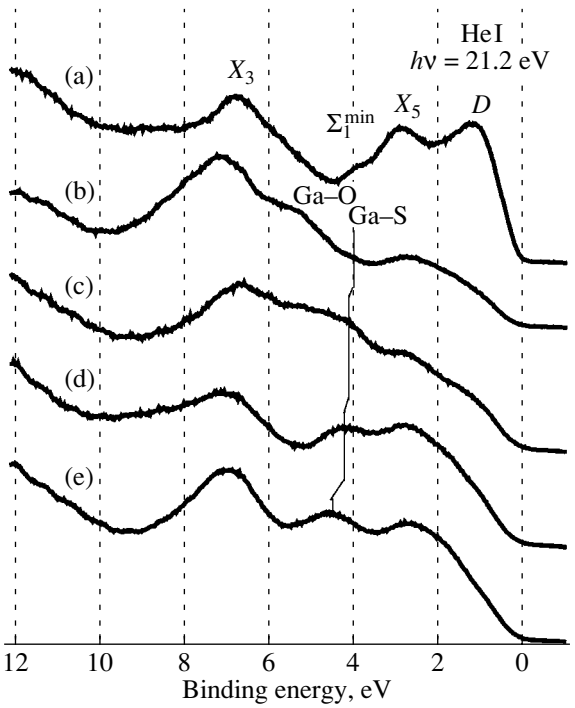

Fig. 5. Valence band photoemission spectra of oxide-free GaAs(100) surface (a) before sulfidization and after sulfidization using the (b) $(NH_4)_2S$ + H_2O, (c) $(NH_4)_2S$ + CH_3OH, (d) $(NH_4)_2S$ + i-C_3H_7OH, or (e) $(NH_4)_2S$ + t-C_4H_9OH solutions and annealing at 400°C. $E_{VBM} = 0$.

As was discovered previously [19], immediately after the treatment, the spectra of all surfaces consist of only two broad bands in the vicinity of the bulk critical points X_5 and X_3. The absence of a fine structure in these spectra may be caused by some amount of carbon contamination on the surface after sulfur treatment. Annealing these surfaces leads to the desorption of carbon, and some new features appear in the spectra as a result. Figure 5 shows the valence-band spectra of all the samples after annealing at 400°C (curves *b*–*e*). Further annealing at 500°C results in only minor changes in the shape of the valence-band spectra. All the spectra contain distinct peaks near the bulk critical points X_5 (2.7 eV) and X_3 (6.7 eV), as well as a shoulder corresponding to the emission from the As–As dimer-related surface state (0.8–1.0 eV).

In addition, the spectra of the surfaces treated with aqueous sulfide solution (Fig. 5b) and methanol-based solution (Fig. 5c) contain a feature with a binding energy of 5.4 eV. A similar feature was observed after exposure of the clean GaAs(100) surface to oxygen with subsequent annealing and was attributed to gallium oxides [20]. At the same time, the O 2*p* core level [21], which has a high photoionization cross section on excitation with a He I source ($h\nu$ = 21.2 eV), has a similar binding energy [22]. Since there is a small amount of residual oxygen on the surfaces treated with aqueous sulfide solution and methanol-based solution, attributing the feature at 5.4 eV to the occurrence of oxygen traces seems reasonable.

An additional emission line located at 4.0–4.5 eV below the maximum of the valence band can be observed in all spectra. This line was observed with the highest intensity in the spectra of the surfaces treated with $(NH_4)_2S$ + i-C_3H_7OH solution (at 4.25 eV) (Fig. 5d) and with $(NH_4)_2S$ + t-C_4H_9OH solution (at 4.5 eV) (Fig. 5e). On the one hand, this emission is in the region of the bulk critical point $\Sigma_I^{\min}$. However, since this line is sensitive to surface treatment, it follows that the surface makes a considerable contribution to this feature. On the other hand, the valence-band spectrum of a GaS layer on a GaAs surface includes a peak with a binding energy of about 4.0 eV [23], and a peak corresponding to the S 3*p* core level, which has a high photoionization cross section for excitation with a He I source, can also be found in this spectral region. Therefore, we may conclude that this feature, with a binding energy that depends on the solvent from which the adsorption of hydrosulfide-ions proceeds, can be related to the presence of sulfur atoms at the GaAs surface (Ga–S chemical bonds).

The ionization energy of the initial GaAs(100) surface after Ar-ion bombardment and subsequent anneal-

ing is equal to 4.7 eV. After the treatment with aqueous sulfide solution, the ionization energy considerably decreased, whereas after the treatment with an alcoholic sulfide solution it increased by a value specific for each solution (Fig. 6). After annealing, the ionization energy of all the studied sulfur-treated surfaces increased. However, at every annealing temperature, the ionization energy is found to be different for surfaces treated with different sulfide solutions.

The evolution of the surface Fermi level position relative to the valence-band edge as a result of the annealing of GaAs(100) surfaces treated with aqueous sulfide solution and with the $(NH_4)_2S$ + i-C_3H_7OH solution is illustrated in Fig. 7. Before the sulfur treatment, but after Ar-ion bombardment and annealing, the surface features rather pronounced band bending (~1 eV). The treatment with sulfur using an aqueous solution results in a noticeable decrease in the surface band bending (Fig. 7a). The treatment with sulfur using alcohol-based solutions has a minor effect on the surface band bending (e.g., Fig. 7b). Note that, during annealing at temperatures above 400°C, the Fermi level at the surface treated with an aqueous sulfide solution shifts back toward the valence band (Fig. 7a), whereas at the surface treated with a $(NH_4)_2S$ + i-C_3H_7OH solution (Fig. 7b), as well as with the other alcoholic solutions considered above, it continues to shift toward the conduction band. This evolution of the surface Fermi level determined from the analysis of the valence-band spectra is in qualitative agreement with the change in the positions of peaks of the bulk components in the As 2p and Ga 2p core levels after sulfide treatment and subsequent annealing, which can also serve as a measure of the valence-band edge position relative to the surface Fermi level.

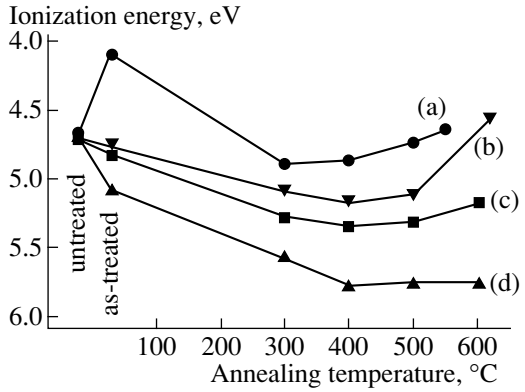

Fig. 6. Evolution of the ionization energy of oxide-free GaAs(100) after sulfidizing treatment with (a) $(NH_4)_2S$ + H_2O, (b) $(NH_4)_2S$ + CH_3OH, (c) $(NH_4)_2S$ + i-C_3H_7OH, or (d) $(NH_4)_2S$ + t-C_4H_9OH solutions and subsequent annealing.

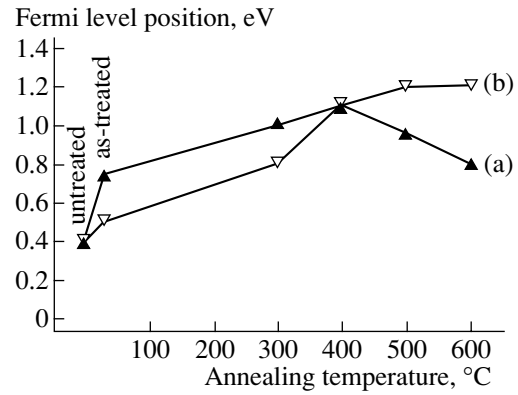

Fig. 7. Position of the surface Fermi level on an oxide-free GaAs(100) surface after sulfidizing treatment with (a) $(NH_4)_2S$ + H_2O and (b) $(NH_4)_2S$ + i-C_3H_7OH solutions and subsequent annealing. E_{VBM} = 0.

4. DISCUSSION

The adsorption of hydrosulfide ions from different solvents results in the formation of As–S bonds with a different chemical shift relative to the As–Ga bulk component (Fig. 1). Similarly to many of the electronic properties of sulfur-treated surfaces [3–5, 7, 24], this chemical shift correlates well with the static permittivity of the solvent (Fig. 8).

The change in chemical shift of the As–S-related component is an indication of the different oxidation state of arsenic atoms bonded with sulfur atoms. In particular, a larger chemical shift is indicative of a higher charge state of atoms and/or a higher ionicity of the bond. The change in ionicity of the As–S bonds at the surfaces treated with different sulfide solutions is also supported by the dependence of the ionization energy on the static permittivity of the solvent used (Fig. 9a). Since the change in ionization energy characterizes the surface dipole induced by the chemical bonds formed [25], it may be concluded that the GaAs(100) surface

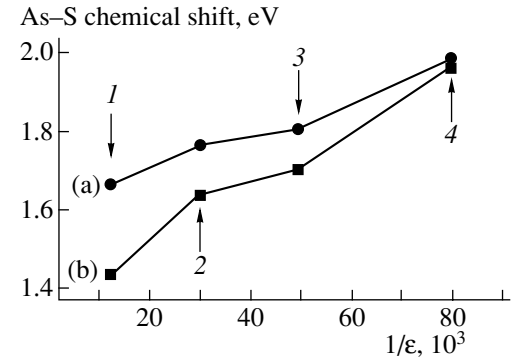

Fig. 8. Chemical shift of the As–S component with respect to As–Ga bulk photoemission in (a) As 2p and (b) As 3d core-level spectra of the oxide-free GaAs(100) surfaces treated with different sulfide solutions as a function of the permittivity of the solvent from which adsorption was carried out. The solutions were (*1*) $(NH_4)_2S$ + H_2O, (*2*) $(NH_4)_2S$ + CH_3OH, (*3*) $(NH_4)_2S$ + i-C_3H_7OH, and (*4*) $(NH_4)_2S$ + t-C_4H_9OH.

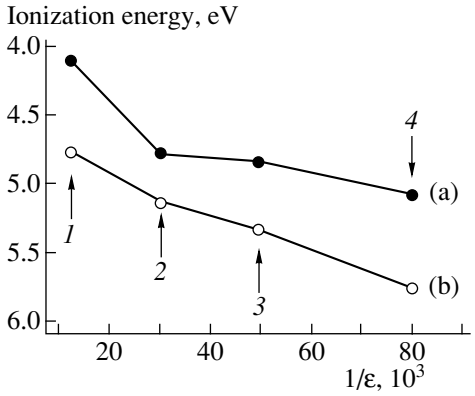

Fig. 9. Ionization energy of the oxide-free GaAs(100) surfaces treated with different sulfide solutions as a function of the permittivity of the solvent from which adsorption was carried out: (a) immediately after sulfidization and (b) after annealing of the sulfidized surface at 500°C. The sulfidizing solutions were (*1*) $(NH_4)_2S + H_2O$, (*2*) $(NH_4)_2S + CH_3OH$, (*3*) $(NH_4)_2S + i\text{-}C_3H_7OH$, and (*4*) $(NH_4)_2S + t\text{-}C_4H_9OH$.

treated with $(NH_4)_2S + t\text{-}C_4H_9OH$ solution exhibits the largest dipole moment, whereas the surface treated with aqueous solution features the smallest dipole moment. Thus, the sulfur adsorption from different solvents results in the formation of a different surface atomic structure.

Different causes may give rise to these solvent effects. First, it is possible that sulfur in different solutions exists in different chemical states. The most plausible sulfur species that can in principle exist in the solutions under consideration are hydrosulfide ions HS^- and sulfide ions S^{2-}. The presence of polysulfide species like HS_n^- or S_n^{2-} seems to be unlikely because reasonable amounts of polysulfides are only expected if some pure sulfur is added to the solution [26]. The existence of sulfide ions S^{2-} in the pH range of aqueous ammonium sulfide solution (around pH 8) can also be disregarded [27]. The existence of such highly charged species in alcohols is completely unlikely since the further dissociation of HS^- is impossible in a low-permittivity medium. Therefore, the hydrosulfide ions HS^- are expected to be the only sulfur species interacting with the GaAs surface in all the solutions considered.

Alternatively, the chemical properties of the ions in solution may be strongly modified by the surrounding solvation shells. However, simultaneous semiconductor surface modification by solvation cannot be excluded as an additional effect [28]. To the first approximation, the change of solvent is accompanied by variations in the permittivity of the medium surrounding the ion, which leads to a change in the reaction field that affects the electronic shell of the ion [2]. Such a variation may affect the charge transfer between reacting atoms and can result in a change in the length and character of the chemical bond that forms in the solution [10]. Furthermore, the change of solvent results in changes in the composition and structure of the solvation shell. In addition, during both hydration and solvation of the hydrosulfide ions by alcohol molecules, hydrogen bonds are formed between sulfur atoms and solvent molecules. These hydrogen bonds will cause the partial collectivization of the ionic charge between the ion and the surrounding solvent molecules, which results in further variation in chemical properties and reactivity of the ion.

The reactivity of the hydrosulfide ion HS^- solvated by different solvents was considered using *ab initio* quantum-chemical calculations of the reactivity indices [29, 30]. According to these calculations, the sulfur atom in the hydrated ion (solvated by water molecules) can both donate and accept electrons in the course of chemical reaction. In contrast, the sulfur atom in the ion solvated by molecules of alcohol is essentially nucleophilic: it is ready to donate electrons but hardly accepts them. The relative nucleophilicity of the sulfur atom (which describes how difficult it is for an atom to accept electrons) increases with the polarizability of the solvent molecule. The increase in the polarizability of the solvent molecule corresponds to the decrease in the static permittivity of the solvent [31].

The difference in reactivity of hydrosulfide ions solvated by different solvents results in a difference in the mechanism of their interaction with the surface of a semiconductor. On a GaAs(100) surface, the empty dangling bonds are localized at the gallium atoms, and the filled dangling bonds are at the arsenic atoms. The sulfur atom in the hydrated HS^- ion can be both a donor and an acceptor of electrons during adsorption, and the bonds formed with the gallium and arsenic are mainly covalent (strong collectivization of the electronic shells).

The sulfur atom in the ion solvated by alcohol molecules can also easily donate electrons. Therefore, when such ions react with gallium, covalent Ga–S bonds will be formed as well. However, when they react with arsenic, the sulfur atom cannot take an electron from the filled orbitals, and the bonds that form are mostly ionic (little or no collectivization of the electronic shells). Specifically, the ionicity of the surface As–S bonds that form should increase as the permittivity of the solvent decreases and the relative nucleophilicity of the sulfur atom in the solvated HS^- ion is correspondingly increased, which is indeed observed in the experiment (Figs. 1, 8). Note that the sulfidizing of a semiconductor in solution is a redox reaction [32], and protons in the solution will capture the excess valence electrons.

It should be emphasized that the effect of the solvent from which the adsorption proceeds on the ionization energy of sulfidized GaAs(100) also remains after surface annealing (Fig. 6). Figure 9b shows the ionization

energy of the surfaces after annealing at 500°C (i.e., after the known disappearance from the surface of all traces of the physically sorbed solvent molecules (carbon- and oxygen-related peaks) and all As–S bonds whose chemical shift and character depend on the solvent) as a function of the permittivity of the solvent from which the adsorption proceeded. Here the difference between the highest and the lowest ionization energy (for surfaces treated with $(NH_4)_2S$ + t-C_4H_9OH and $(NH_4)_2S$ + H_2O solutions, respectively) is about 1.0 eV, as in the case of the as-treated surfaces (Fig. 9a). This indicates that the solvation of the adsorbing ions affects not only the character of the forming As–S bonds, but also promotes more profound modification of the surface atomic structure.

6. CONCLUSION

The adsorption of sulfur in the form of hydrosulfide ions HS^- solvated by different amphiprotic solvents (water, methanol, isopropanol, *tert*-butanol) on the oxide-free GaAs(100) surface was studied by the X-ray and ultraviolet photoemission spectroscopy in order to clarify the role that the solvent plays in the course of adsorbate interaction with surface atoms at the semiconductor/electrolyte interface. The adsorption was carried out from different ammonium sulfide solutions in an inert oxygen-free ambient.

It was found that, during the adsorption, the component stemming from the As–S chemical bonds appears in As 2*p* and As 3*d* core-level spectra. The chemical shift of this component with respect to the bulk As–Ga component depends on the solvent from which the adsorption was carried out. This observed chemical shift increases as the permittivity of the solvent decreases and is accompanied by an increase in ionization energy of the as-treated semiconductor.

Annealing the surface results in the decomposition of As–S bonds and in the appearance of Ga–S bonds instead. The ionization energy of the surface increases but still depends on the solvent from which the adsorption proceeded. The position of the surface Fermi level with respect to the semiconductor's band edges and its evolution during the annealing of the sulfide-treated surfaces also differ for surfaces treated with different solutions.

It is suggested that the effect of the solvent from which the adsorption of hydrosulfide ions is carried out on the atomic structure and properties of the surface is caused by the solvation-induced modification of chemical properties and reactivity of the ions before adsorption. Solvation by different solvents results in a different mechanism of hydrosulfide ion interaction with the surface atoms of the semiconductor and, hence, in a different atomic structure of the surface, which "remembers" the solvent from which the adsorption was carried out even after annealing and the disappearance of the As–S bonds.

ACKNOWLEDGMENTS

One of the authors (M.V. Lebedev) is grateful to colleagues from the Surface Science Division (FG Oberflächenforschung) from the Technical University of Darmstadt (Germany) for their hospitality, friendly collaboration, and creative climate, which was a great help in carrying out this research, as well as to Alexander von Humboldt-Stiftung for a research fellowship.

REFERENCES

1. F. Seker, K. Meeker, T. F. Kuech, and A. B. Ellis, Chem. Rev. **100**, 2505 (2000).
2. J. Tomasi and M. Persico, Chem. Rev. **94**, 2027 (1994).
3. V. N. Bessolov, M. V. Lebedev, and D. R. T. Zahn, J. Appl. Phys. **82**, 2640 (1997).
4. C. Huh, S.-W. Kim, H.-S. Kim, *et al.*, J. Appl. Phys. **87**, 4591 (2000).
5. V. N. Bessolov, M. V. Lebedev, and D. R. T. Zahn, Fiz. Tekh. Poluprovodn. (St. Petersburg) **33**, 429 (1999) [Semiconductors **33**, 416 (1999)].
6. M. Kemerink, J. V. Gerritsen, P. M. Koenrad, *et al.*, Appl. Phys. Lett. **75**, 3656 (1999).
7. V. N. Bessolov, M. V. Lebedev, Yu. M. Shernyakov, and B. V. Tsarenkov, Mater. Sci. Eng. B **44**, 380 (1997).
8. R. Hakimi and M.-C. Amann, Semicond. Sci. Technol. **12**, 778 (1997).
9. K. Akita, M. Taneya, Y. Sugimoto, and H. Hidaka, J. Electrochem. Soc. **137**, 2081 (1990).
10. J. Cioslowski and M. Martinov, J. Chem. Phys. **103**, 4967 (1995).
11. M. Beerbom, O. Henrion, A. Klein, *et al.*, Electrochim. Acta **45**, 4663 (2000).
12. I. M. Vitomirov, A. D. Raisanen, A. E. Finnefrock, *et al.*, J. Vac. Sci. Technol. B **10**, 1898 (1992).
13. T. Ishikawa and H. Ikoma, Jpn. J. Appl. Phys. **31**, 3981 (1992).
14. G. Hollinger, R. Skheyta-Kabbani, and M. Gendry, Phys. Rev. B **49**, 11159 (1994).
15. C. C. Surdu-Bob, S. O. Saied, and J. L. Sullivan, Appl. Surf. Sci. **183**, 126 (2001).
16. M.-G. Kang and H.-H. Park, J. Vac. Sci. Technol. A **17**, 88 (1999).
17. P. K. Larsen, J. F. van der Veen, A. Mazur, *et al.*, Phys. Rev. B **26**, 3222 (1982).
18. T.-C. Chiang, J. A. Knapp, M. Aono, and D. E. Eastman, Phys. Rev. B **21**, 3513 (1980).
19. M. V. Lebedev and M. Aono, J. Appl. Phys. **87**, 289 (2000).
20. C. J. Spindt, M. Yamada, P. L. Meissner, *et al.*, Phys. Rev. B **45**, 11108 (1992).

21. Z. Liu, Y. Sun, F. Machuca, *et al.*, J. Vac. Sci. Technol. A **21**, 212 (2003).
22. J. J. Yeh and I. Lindau, At. Data Nucl. Data Tables **32**, 1 (1985).
23. X.-A. Cao, H.-T. Hu, X.-M. Ding, *et al.*, J. Vac. Sci. Technol. B **16**, 2656 (1998).
24. V. N. Bessolov, M. V. Lebedev, A. F. Ivankov, *et al.*, Appl. Surf. Sci. **133**, 17 (1998).
25. W. Mönch, *Semiconductor Surfaces and Interfaces*, 2nd ed. (Springer, Berlin, 1995).
26. J.-F. Fan, H. Oigawa, and Y. Nannichi, Jpn. J. Appl. Phys. **27**, L1331 (1988).
27. S. Licht, F. Forouzan, and K. Longo, Anal. Chem. **62**, 1356 (1990).
28. N. Gayathri, S. Izvekov, and G. A. Voth, J. Chem. Phys. **117**, 872 (2002).
29. M. V. Lebedev, J. Phys. Chem. B **105**, 5427 (2001).
30. M. V. Lebedev, Fiz. Tekh. Poluprovodn. (St. Petersburg) **35**, 1347 (2001) [Semiconductors **35**, 1291 (2001)].
31. V. I. Minkin, O. A. Osipov, and Yu. A. Zhdanov, *Dipole Moments in Organic Chemistry* (Khimiya, Leningrad, 1968; Plenum, New York, 1970).
32. V. N. Bessolov, M. V. Lebedev, E. B. Novikov, and B. V. Tsarenkov, J. Vac. Sci. Technol. B **11**, 10 (1993).

Translated by M. Lebedev

Semiconductors, Vol. 38, No. 2, 2004, pp. 161–162. Translated from Fizika i Tekhnika Poluprovodnikov, Vol. 38, No. 2, 2004, pp. 164–165.

ELECTRONIC AND OPTICAL PROPERTIES OF SEMICONDUCTORS

Current–Voltage Characteristics of $MnIn_2S_4$ and $MnGa_2S_4$ Single Crystals

N. N. Niftiev and O. B. Tagiev

State Pedagogical University, Baku, 370000 Azerbaijan

Submitted May 23, 2003; accepted for publication June 2, 2003

Abstract—Current–voltage (I–V) characteristics $I(U)$ of $MnIn_2S_4$ and $MnGa_2S_4$ single crystals are studied in the dark and under exposure to light. The I–V characteristic of the $MnIn_2S_4$ single crystal contains $I \propto U$, $I \propto U^2$, and $I \propto U^3$ portions in the dark and $I \propto U$, $I \propto U^{3/2}$, and $I \propto U^{2.5}$ portions under exposure to light. It is shown that the current under exposure to light exceeds the current in the dark by a factor of almost 10^4. In the $MnGa_2S_4$ single crystals exposed to light, the I–V characteristic has $I \propto U$ and $I \propto U^{3/2}$ portions. An interpretation is given for these dependences. © *2004 MAIK "Nauka/Interperiodica".*

The active advancement of optoelectronics poses the problem of researching and developing new efficient semiconductor materials. Recently, considerable attention has been given to semimagnetic II–III_2–VI_4 semiconductors (II = Mn, Fe, Co, Ni; III = Ga, In; VI = S, Se, Te) [1–4]. These compounds are promising as a basis for developing lasers, light modulators, photodetectors, and other functional devices controlled by magnetic field.

In this paper, we consider the current–voltage (I–V) characteristics of $MnIn_2S_4$ and $MnGa_2S_4$ single crystals in the dark and under exposure to light. Single-crystal $MnIn_2S_4$ and $MnGa_2S_4$ samples were prepared by the method of chemical transport reactions. X-ray diffraction studies showed that $MnGa_2S_4$ crystallizes in space symmetry group $I4$ (the lattice parameters are a = 5.46 Å and c = 10.50 Å; thus, c/a = 1.92 [4]). $MnIn_2S_4$ has a cubic structure (space symmetry group is $Fd3m$); the lattice parameter is a = 10.71 Å [5]. Contacts to the samples were formed by indium fusing in a sandwich design. A PZh-220 incandescent lamp was used as a light source. Figure 1 shows the I–V characteristics $I(U)$ of the In–$MnIn_2S_4$–In structure in the dark (curve *1*), in the dark after preliminary exposure to light (curve *2*), and under exposure to white light (curve *3*) at temperature T = 293 K. We can see that the I–V characteristic of unilluminated samples contains the linear ($I \propto U$), quadratic ($I \propto U^2$), and cubic ($I \propto U^3$) portions. The current in the quadratic portion is caused by monopolar injection, and the cubic portion is associated with double injection [6, 7]. The dark I–V characteristics after preliminary exposure to light contain a linear portion ($I \propto U$) and a portion corresponding to $I \propto U^{3/2}$. Since traps are filled with electrons as crystals are exposed to white light, while holes are trapped by recombination centers and electrons are transferred from the valence bands to the conduction band, nonequilibrium carriers arise. After the exposure of the sample to light and a certain time in the dark, we can see that the dark current after

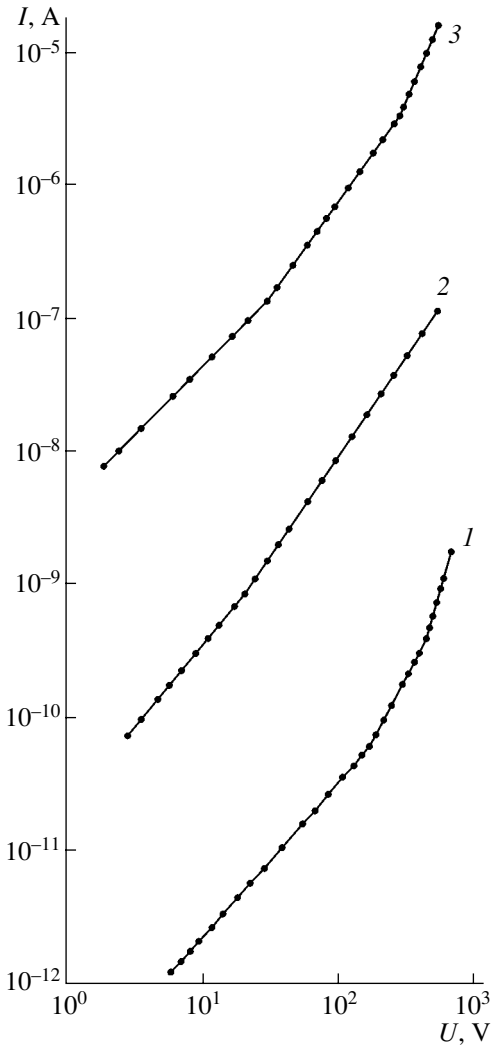

Fig. 1. I–V characteristics of the In–$MnIn_2S_4$–In structures at a temperature of 293 K (*1*) in the dark, (*2*) in the dark after a subsequent exposure to light, and (*3*) under exposure to white light with an illuminance of 200 lx.

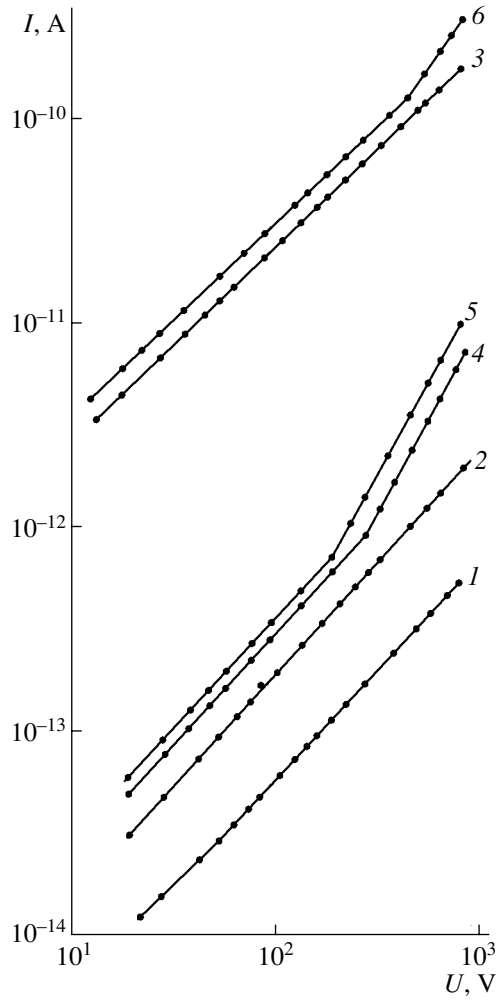

Fig. 2. *I–V* characteristics of the In–$MnGa_2S_4$–In structures (*1–3*) in the dark and (*4–6*) under exposure to white light at (*1*, *4*) 293, (*2*, *5*) 340, and (*3*, *6*) 409 K.

preliminary exposure to light is almost hundred times higher than the dark current without exposure to light. Nonequilibrium carriers cause additional conduction [8].

For the samples exposed to light (curve *3*), the *I–V* characteristic includes the linear portion ($I \propto U$), as well as the portions corresponding to $I \propto U^{3/2}$ and $I \propto U^{2.5}$. In the case of the joint effect of an electric field and exposure to light, the probability that electrons will appear in the conduction band and holes will appear in the valence band increases, which results in an increase in the conductivity of the sample. It is obvious that the current under exposure to light is higher than the current in the dark by a factor of almost 10^4. When the quadratic portion begins in the dark *I–V* characteristic, the *I–V* characteristic under exposure to light contains a portion of $I \propto U^{2.5}$. Illuminating a sample in which the monopolar injection current is maintained can cause an increase in the space-charge-limited current in the case where a fraction of the space charge is trapped and carriers in traps can gain energy from incident light. A trapped carrier can directly absorb a photon and be ejected to one of the allowed bands [7].

Figure 2 shows the *I–V* characteristics of the In–$MnGa_2S_4$–In structures in the dark and under exposure to white light at various temperatures. We can see that the *I–V* characteristics in the dark have only a linear portion. In the samples exposed to light, the *I–V* characteristics contain the linear portion ($I \propto U$) and the portion described by the $I \propto U^{3/2}$ dependence. As temperature increases, the current under exposure to light differs slightly from the current in the dark.

Thus, the study of the *I–V* characteristics of $MnIn_2S_4$ single crystals shows the presence of $I \propto U$, $I \propto U^2$, and $I \propto U^3$ portions in the dark and $I \propto U$, $I \propto U^{3/2}$, and $I \propto U^{2.5}$ portions under exposure to light. It is shown that the current under exposure to light exceeds the current in the dark by a factor of 10^4. Under exposure to light, the *I–V* characteristic of $MnGa_2S_4$ single crystals has portions with $I \propto U$ and $I \propto U^{3/2}$ dependences. As the temperature increases, the current under exposure to light differs only slightly from the current in the dark.

REFERENCES

1. S. Methfessel and D. C. Mattis, in *Handbuch der Physik*, Ed. by H. P. J. Wijn (Springer, Berlin, 1968; Mir, Moscow, 1972), Vol. 18, Part 1.
2. R. N. Bekimbetov, Yu. V. Rud', and M. A. Tairov, Fiz. Tekh. Poluprovodn. (Leningrad) **21**, 1051 (1987) [Sov. Phys. Semicond. **21**, 642 (1987)].
3. R. N. Bekimbetov, N. N. Konstantinova, Yu. V. Rud', and M. A. Tairov, Izv. Akad. Nauk SSSR, Neorg. Mater. **24**, 1969 (1988).
4. N. N. Niftiev, O. B. Tagiev, and A. G. Rustamov, Fiz. Tekh. Poluprovodn. (Leningrad) **24**, 758 (1990) [Sov. Phys. Semicond. **24**, 478 (1990)].
5. T. Kanomata, H. Ido, and T. Kaneko, J. Phys. Soc. Jpn. **34**, 554 (1973).
6. N. N. Niftiev and O. B. Tagiev, Solid State Commun. **81**, 693 (1992).
7. M. A. Lampert and P. Mark, *Current Injection in Solids* (Academic, New York, 1970; Mir, Moscow, 1973).
8. R. H. Bube, *Photoconductivity of Solids* (Wiley, New York, 1960; Inostrannaya Literatura, Moscow, 1962).

Translated by A. Kazantsev

Semiconductors, Vol. 38, No. 2, 2004, pp. 163–164. Translated from Fizika i Tekhnika Poluprovodnikov, Vol. 38, No. 2, 2004, pp. 166–167.

ELECTRONIC AND OPTICAL PROPERTIES OF SEMICONDUCTORS

Electrical Properties of $MnIn_2S_4$ Single Crystals

N. N. Niftiev

Azerbaijani State Pedagogical Institute, Baku, 370000 Azerbaijan

Submitted March 3, 2003; accepted for publication March 25, 2003

Abstract—The temperature dependence of current and current–voltage (*I–U*) characteristics have been studied in $MnIn_2S_4$ single crystals in various conditions. It was shown that the current transport mechanism corresponding to the nonlinear portion of the *I–U* characteristic is associated with space-charge-limited currents (SCLC). It was established that $MnIn_2S_4$ single crystals are strongly compensated semiconductors. © *2004 MAIK "Nauka/Interperiodica".*

This communication presents data obtained in a study of the electrical properties of $MnIn_2S_4$ single crystals.

$MnIn_2S_4$ single crystals were grown using the method of chemical transport reactions. An X-ray diffraction analysis demonstrated that the single crystals have a spinel structure with lattice constant $a = 10.71$ Å [1]. Studies of some physical properties of $MnIn_2S_4$ single crystals have been reported more than once [2, 3]. $MnIn_2S_4$ single crystals exhibit *n*-type conduction. Contacts to the samples were fabricated by fusing-in indium at their opposite surfaces. The interelectrode spacing was varied within 50–300 μm.

Figure 1 shows current–voltage (*I–U*) characteristics of In–$MnIn_2S_4$–In structures at different temperatures. The following portions are revealed in the *I–U* characteristics: linear ($I \propto U$), quadratic ($I \propto U^2$), and cubic ($I \propto U^3$).

Such a behavior indicates that the primary role in current transport is played by space-charge-limited currents (SCLC). In addition, it was established that the dependences of the current density *J* on the interelectrode spacing *L* have the form $J \propto L^{-3}$ and $J \propto L^{-5}$ for the quadratic and cubic regions, respectively [4, 5].

Measurements of the *I–U* characteristics at different temperatures furnish an opportunity to determine the depth of monoenergetic levels, which is related to the voltage V_{1-2} of transition from the ohmic portion of a characteristic to the trap-controlled quadratic ($I \propto U^2$) portion by the formula [6]

$$V_{1-2}^{-1} \propto \exp[(E_t - E_c)/kT].$$

The slope of this dependence, which is plotted in Fig. 2, gives the activation energy $E_t = 0.53$ eV.

Studying the *I–U* characteristics in relation to temperature makes it possible to determine, from their quadratic portions, the trap concentration $N_t = 2 \times 10^{15}$ cm^{-3} [7].

According to [8], a temperature-independent voltage of the transition from the ohmic to quadratic portion of a *I–U* characteristic, V_{1-2}, indicates a weak compensation of the crystal studied, whereas a temperature-dependent V_{1-2} points to its strong compensation. The fact that the voltage V_{1-2} depends on temperature in the case in question demonstrates that $MnIn_2S_4$ single crystals are strongly compensated semiconductors.

Figure 3 shows the temperature dependence of current at different constant voltages. The lower straight line (curve *1*) corresponds to the ohmic portion of the

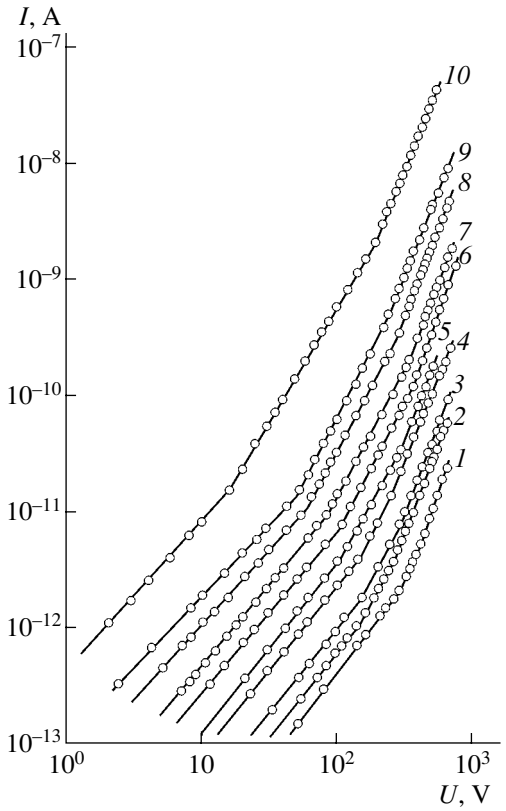

Fig. 1. Dark *I–U* characteristics of $MnIn_2S_4$ single crystals at different temperatures *T*: (*1*) 242, (*2*) 251, (*3*) 256, (*4*) 264, (*5*) 270, (*6*) 276, (*7*) 280, (*8*) 288, (*9*) 296, and (*10*) 308 K.

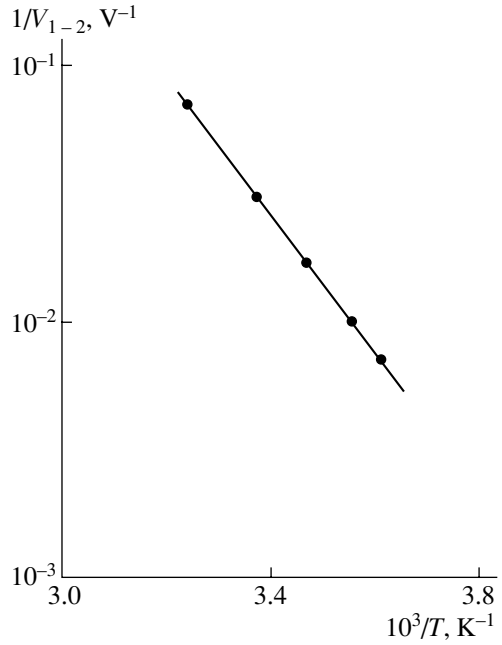

Fig. 2. Temperature dependence of the reciprocal of the transition voltage, $1/V_{1-2}$.

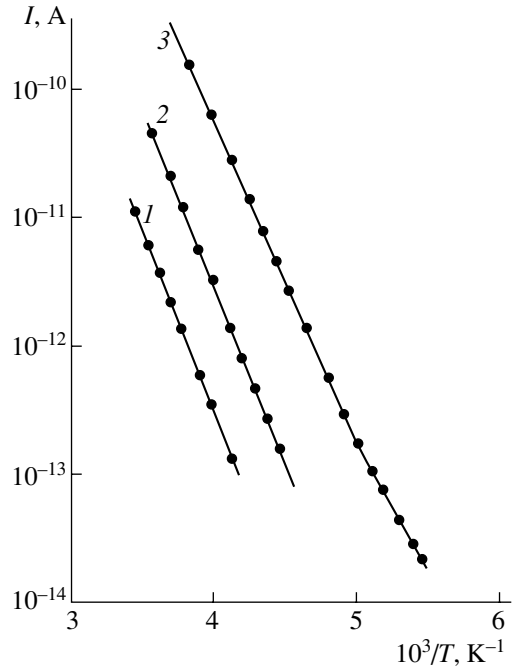

Fig. 3. Temperature dependence of current at different voltages U: (*1*) 50, (*2*) 200, and (*3*) 500 V.

I–U characteristic; curve *2*, to the quadratic portion. The next curve, which consists of two linear portions with different slopes (curve *3*) corresponds to the cubic portion of the *I–U* characteristic. The activation energies of charge carriers in $MnIn_2S_4$ single crystals, determined from the two slopes, are as follows: $E_1 = 0.45$ eV and $E_2 = 0.38$ eV. It can be seen that the slopes of curves *1*, *2*, and *3* (higher-temperature portion) decrease in the range 0.53–0.45 eV with increasing external voltage. It should be noted that the levels at 0.53 and 0.38 eV have also been revealed when studying thermally stimulated currents in $MnIn_2S_4$ single crystals [3].

Thus, a study of *I–U* characteristics and temperature dependences of current in single-crystal $MnIn_2S_4$ revealed that the current transport mechanism in this material is associated with the space-charge-limited currents. The main parameters of local levels were determined. It was established that strong compensation takes place in $MnIn_2S_4$ single crystals.

REFERENCES

1. T. Kanomata, H. Ido, and T. Kaneko, J. Phys. Soc. Jpn. **34**, 554 (1973).
2. N. N. Niftiyev, Solid State Commun. **92**, 781 (1994).
3. N. N. Niftiev, Fiz. Tekh. Poluprovodn. (St. Petersburg) **36**, 836 (2002) [Semiconductors **36**, 782 (2002)].
4. K. Kao and W. Hwang, *Electrical Transport in Solids* (Pergamon Press, Oxford, UK, 1981; Mir, Moscow, 1984), Part 1.
5. A. G. Milnes, *Deep Impurities in Semiconductors* (Wiley, New York, 1973; Mir, Moscow, 1977).
6. N. S. Grushko, L. A. Gerasimenko, and T. I. Goglidze, in *Physics of Semiconductors and Dielectrics* (Shtiintsa, Chisinau, 1982), p. 82.
7. M. A. Lampert and P. Mark, *Current Injection in Solids* (Academic, New York, 1970; Mir, Moscow, 1973).
8. A. V. Malovichko, V. G. Chalaya, and E. T. Shul'ga, Ukr. Fiz. Zh. **20**, 209 (1975).

Translated by M. Tagirdzhanov

Semiconductors, Vol. 38, No. 2, 2004, pp. 165–168. Translated from Fizika i Tekhnika Poluprovodnikov, Vol. 38, No. 2, 2004, pp. 168–171.

ELECTRONIC AND OPTICAL PROPERTIES OF SEMICONDUCTORS

Photosensitive Structures Based on the Compound $AgIn_{11}S_{17}$

I. V. Bodnar'*, V. Yu. Rud', and Yu. V. Rud'*****

**Belarussian State University of Informatics and Radioelectronics, ul. Brovki 17, Minsk, 220072 Belarus*
e-mail: chemzav@gw.bsuir.unibel.by
***St. Petersburg State Polytechnical University, Politekhnicheskaya ul. 29, St. Petersburg, 195251 Russia*
e-mail: rudvas@spbstu.ru
****Ioffe Physicotechnical Institute, Russian Academy of Sciences, Politekhnicheskaya ul. 26, St. Petersburg, 194021 Russia*

Submitted April 9, 2003; accepted for publication April 21, 2003

Abstract—The Bridgman–Stockbarger method (horizontal implementation) is used to grow crystals of the ternary compound $AgIn_{11}S_{17}$. The kinetic coefficients are measured, and photosensitive structures based on the grown crystals are fabricated for the first time. The photoelectric parameters of solid-state surface-barrier structures and photoelectrochemical cells are determined, the band gap for the compound $AgIn_{11}S_{17}$ is estimated, and the features of interband transitions in this compound are discussed. It is shown that the structures developed can be used in photodetectors of natural optical radiation. *© 2004 MAIK "Nauka/Interperiodica".*

1. INTRODUCTION

Detailed studies of systems of I–III–VI compounds yielded results that concerned not only the well-known I–III–VI_2 compounds but also a number of new I–III_n–VI_m ternary semiconductor phases (here, the n and m subscripts are natural numbers) [1–5]. An analysis of interaction in these phases showed that variations in their composition gives rise to a stability region for positionally ordered phases, in which case a variation in the subscripts n and m brings about the formation of new semiconductor compounds [5]. The new substances, along with I–III–VI_2 compounds, may turn out to be promising materials in solving problems of contemporary electronics and photoelectronics based on solar-energy conversion.

In this paper, we report the results of studying the physical properties of the new semiconductor compound $AgIn_{11}S_{17}$ and structures based on this compound.

2. EXPERIMENTAL

Crystals of the ternary compound $AgIn_{11}S_{17}$ were grown by planar crystallization of the melt (the horizontal Bridgman–Stockbarger method). The metallic components (silver and indium of 99.9999% purity), which were placed in a quartz boat, and sulfur (of 99.99999% purity) were positioned in different parts of an evacuated quartz cell. The amount of sulfur was in excess over the stoichiometry, which was necessary to ensure that the sulfur-vapor pressure above the formed melt was 1.5–2.0 atm. The cell was installed in a two-zone horizontal furnace with independently controlled temperatures in each of the zones. The temperature of the zone with metallic components was maintained at a level of ~1380 K. The temperature of the zone with sulfur was increased at a rate of 50 K/h to a temperature of 700 K; this temperature was then maintained for 2 h in order to ensure that the reaction between silver, indium, and sulfur proceeded. In order to ensure that this reaction was completed, we increased the temperature of this zone to ~800K at the same rate and again kept the samples at this temperature for 1 h. We then carried out planar recrystallization by lowering the melt temperature to 1000 K at a rate of ~3 K/h; homogenizing annealing of the crystals formed was then performed for 300 h at the above temperature. The grown crystals had a large-block structure; the dimensions of the individual blocks were $15 \times 8 \times 5$ mm^3.

The composition of the grown crystals was determined from the results of chemical analysis using the methods suggested in [8–10]. The content of elements in the crystals obtained ([Ag] : [In] : [S] = 3.54 : 37.78 : 58.68 at %, respectively) is in satisfactory agreement with the specified composition in the starting charge ([Ag] : [In] : [S] = 3.45 : 37.83 : 58.72 at %). The distribution of elements over the crystal length was uniform within the experimental accuracy.

The structure and parameters of a unit cell of the crystals obtained were determined using X-ray analysis. X-ray measurements were carried out using a DRON-3M diffractometer, CuK_α radiation, and a Ni filter. The diffraction patterns measured for different parts of the crystal corresponded to the cubic structure of the spinel type with the unit-cell parameter $a = 10.797 \pm 0.002$ Å.

According to the thermoelectric-power sign, the $AgIn_{11}S_{17}$ crystals had n-type conductivity; the resistivity was $\rho \approx (2–5) \times 10^{-2}$ Ω cm, the charge-carrier concentration $n \approx (3–5) \times 10^{18}$ cm^{-3}, and the electron

Table 1. Photoelectric properties of a surface-barrier structure based on the compound $AgIn_{11}S_{17}$ (T = 300 K)

Structure	R_0, Ω	$\hbar\omega_{max}$, eV	φ_b, eV	δ, eV	S_u^{max}, V/W
$In/AgIn_{11}S_{17}$	75	1.57	0.82	0.6	0.02

mobility $\mu_n \approx 30$–40 cm^2/(V s) at T = 300 K for samples cut from different parts of the ingot.

3. RESULTS AND DISCUSSION

As a result of studying contact phenomena in the grown $AgIn_{11}S_{17}$ crystals, we found that the contact of thin layers of metallic indium ($d \approx 1$–3 μm) with a natural-cleavage surface exhibits rectifying and photovoltaic properties. The parameters of the $In/AgIn_{11}S_{17}$ surface-barrier structures fabricated for the first time are listed in Table 1. Measurements of steady-state current–voltage (I–V) characteristics showed that the aforementioned structures feature rectification, with the conducting direction corresponding to the negative polarity of external bias voltage applied to the semiconductor. The rectification factor (K) in these structures, which is defined as the ratio between the forward and reverse currents at a voltage $U \approx 0.5$ V, was found to be relatively small (K = ~5). The forward portion of the I–V characteristics for the structures under consideration is governed by the following law at $U > 0.3$ V:

$$U = U_0 + IR_0. \quad (1)$$

The value of residual resistance R_0 for the structures under investigation is listed in Table 1; the cutoff voltage was $U \approx 0.4$ V.

If these structures were illuminated, we observed a photovoltaic effect; the positive photovoltage was observed at the barrier contact, which is consistent with the rectification direction. The largest value of the voltage photosensitivity (S_u^{max}) for the best surface-barrier structures is listed in Table 1. The highest photovoltage for the $In/AgIn_{11}S_{17}$ barrier structures obtained is attained when the indium-contact side of these structures is illuminated.

In Fig. 1, we show the spectral dependence of relative quantum efficiency of photoconversion $\eta(\hbar\omega)$ for an $In/AgIn_{11}S_{17}$ structure at T = 300 K when the barrier-contact side of the structure is illuminated. It can be seen that the dependence $\eta(\hbar\omega)$ for the structures under consideration features a maximum at photon energy $\hbar\omega_{max}$. A rapid increase in photosensitivity begins at photon energy $\hbar\omega \approx 0.9$ eV; the long-wavelength edge of photosensitivity spectra follows Fowler's law [11] (Fig. 2) and may be related to photoemission. Extrapolation of the dependence $\eta^{1/2}(\hbar\omega)$ to zero makes it possible to determine the potential-barrier height φ_b for $In/AgIn_{11}S_{17}$ structures. The value of φ_b for these structures is listed in Table 1.

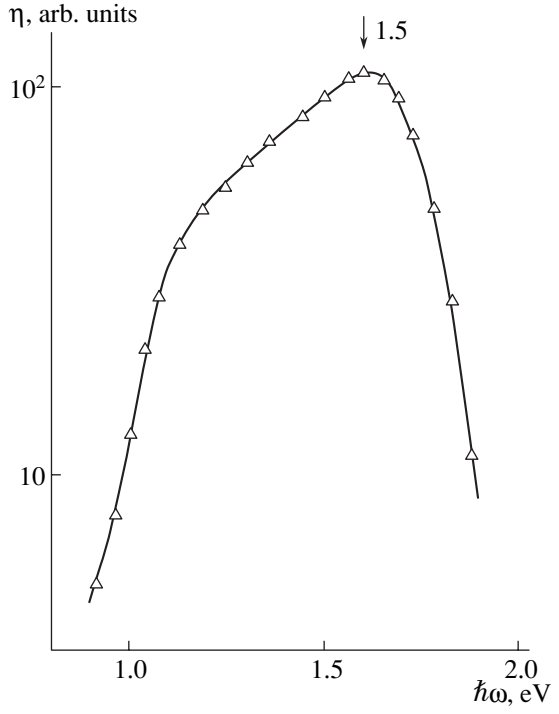

Fig. 1. Spectral dependence of the relative quantum efficiency of photoconversion for an $In/AgIn_{11}S_{17}$ structure at 300 K. The barrier-contact side of the structure was illuminated.

We should also note the second special feature of the spectral dependence $\eta(\hbar\omega)$ for the surface-barrier structure under consideration: a fairly sharp short-wavelength falloff of photosensitivity is observed when either the barrier-contact or the crystal side of the structures is illuminated. Our research showed that the energy position of the short-wavelength falloff in $In/AgIn_{11}S_{17}$ structures is virtually independent of the direction of illumination. This circumstance suggests that the barriers under consideration do not ensure the suppression of surface recombination in photogenerated electron–hole pairs; apparently, this recombination is responsible for the short-wavelength falloff of η at $\hbar\omega > \hbar\omega_{max}$.

The full width of the $\eta(\hbar\omega)$ spectra at their half-heights (δ) is listed in Table 1. It can be seen that the photosensitivity spectrum normalized to the number of incident photons is of the wide-band type for structures based on the ternary compound $AgIn_{11}S_{17}$.

The feasibility of fabricating photoelectrochemical cells, along with solid-state surface-barrier structures, based on $AgIn_{11}S_{17}$ crystals was also studied [12, 13]. Distilled water with the addition of NaCl was used as the electrolyte; this electrolyte was brought into direct contact with the cleaved surface of crystals provided with an ohmic contact. In order to isolate the electrolyte

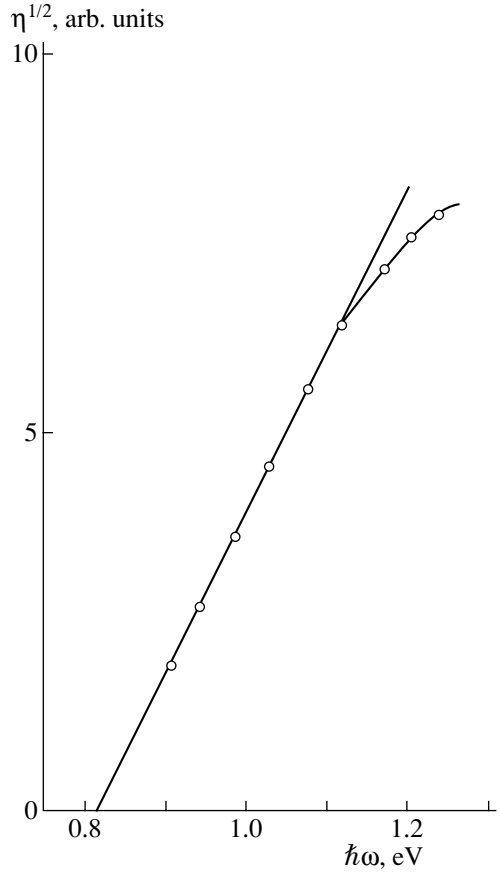

Fig. 2. The dependence $\eta^{1/2} = f(\hbar\omega)$ for an $In/AgIn_{11}S_{17}$ structure at 300 K.

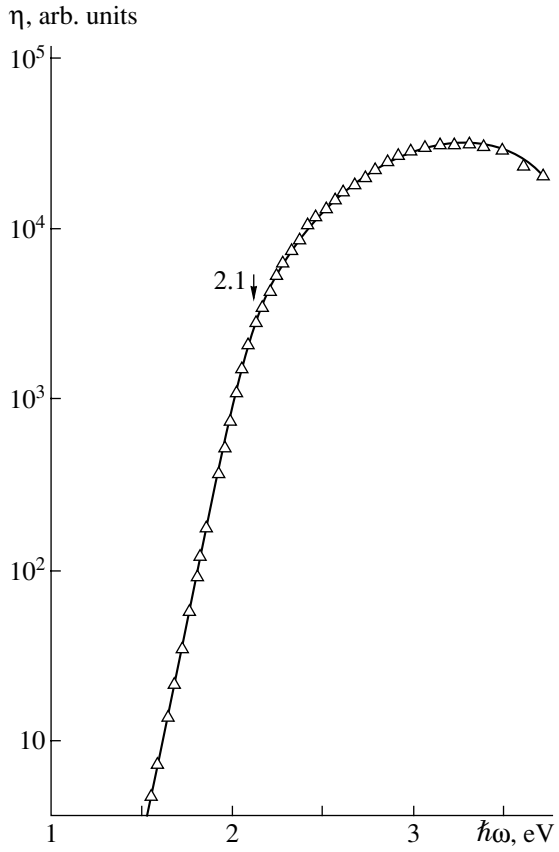

Fig. 3. Spectral dependence of the relative quantum efficiency of photoconversion for $H_2O/AgIn_{11}S_{17}$ cells at 300 K. The electrolyte side of the structure was illuminated.

from the ohmic contact, this contact was coated with an insulating varnish. A sharpened platinum conductor was used as the counterelectrode in the photoelectrochemical cell. The photosensitivity of $H_2O/AgIn_{11}S_{17}$ photoelectrochemical cells was measured with modulated ($f \approx 20$ Hz) illumination of the counterelectrode side of the structure; nonpolarized radiation was used for the illumination [13]. The electric-current rectification ($K \approx 20$ at $U \approx 10$ V) and the photovoltaic-effect were larger in all the fabricated photoelectrochemical-cell structures than in the $In/AgIn_{11}S_{17}$ surface-barrier structure. It should also be noted that no degradation in the photoelectric parameters of the fabricated photoelectrochemical cells was observed.

The $\eta(\hbar\omega)$ spectra typical of the fabricated photoelectrochemical cells when the electrolyte side of these cells was exposed to nonpolarized light are shown in Fig. 3. It can be seen that the spectrum shown in Fig. 3 differs considerably from the spectrum of the surface-barrier structure formed on the basis of the same crystals (Fig. 1). Indeed, an almost exponential increase in the dependence $\eta = f(\hbar\omega)$ is observed in the region $\hbar\omega < 2$ eV for the $H_2O/AgIn_{11}S_{17}$ photoelectrochemical cells. This increase can be related to the slope S, which is defined as

$$S = \Delta(\ln\eta)/\Delta(\hbar\omega). \quad (2)$$

The absence of a pronounced short-wavelength falloff of η is the main difference between the photosensitivity spectra obtained for photoelectrochemical cells based on $AgIn_{11}S_{17}$ crystals and the spectra for the surface-barrier solid-state structures considered above. This suggests that the efficiency of separation and collection of photogenerated electron–hole pairs in the semiconductor/electrolyte barriers is much higher than that in the solid-state structures of $In/AgIn_{11}S_{17}$. The spectral range of the highest photosensitivity $\hbar\omega_{max}$ for photoelectrochemical cells is listed in Table 2. The val-

Table 2. Photoelectric properties of an $H_2O/AgIn_{11}S_{17}$ structure and the energies of the band-to-band transitions for the compound $AgIn_{11}S_{17}$ at 300 K

Structure	$\hbar\omega_{max}$, eV	δ, eV	S, eV^{-1}	S_u^{max}, V/W	E_g^{in}, eV	E_g^{dir}, eV
$H_2O/AgIn_{11}S_{17}$	3–3.4	~1.2	12	1900	1.83	2.48

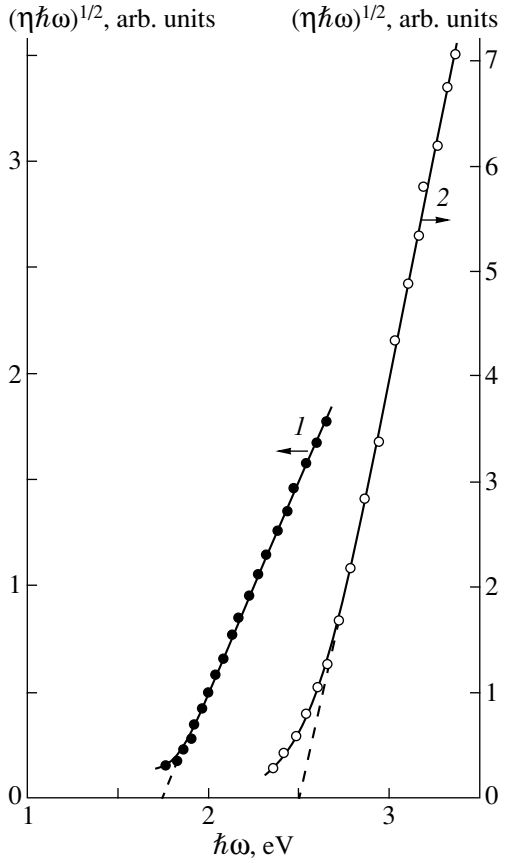

Fig. 4. The dependences (*1*) $(\eta\hbar\omega)^{1/2} = f(\hbar\omega)$ and (*2*) $(\eta\hbar\omega)^2 = f(\hbar\omega)$ for $H_2O/AgIn_{11}S_{17}$ cells at 300 K.

ues of δ and S_u^{max} determined from the $\eta(\hbar\omega)$ spectra for these cells were found to be much larger than those for the surface-barrier structures (Table 1).

In Fig. 4, we show the spectral dependences $\eta(\hbar\omega)$ for photoelectrochemical cells; these dependences are plotted in the coordinates of $(\eta\hbar\omega)^{1/2} = f(\hbar\omega)$ and $(\eta\hbar\omega)^2 = f(\hbar\omega)$. Assuming that these dependences are controlled by band-to-band absorption and taking into account the existing theory [14], we may evaluate the features of the interband transitions and the band gap for the ternary compound $AgIn_{11}S_{17}$. It can be seen that the ascending portion of photosensitivity dependence in the region of longer wavelengths for photoelectrochemical cells can be linearized in the coordinates $(\eta\hbar\omega)^{1/2} = f(\hbar\omega)$. This circumstance allows us to assume that the long-wavelength edge of $\eta(\hbar\omega)$ is controlled by indirect band-to-band transitions in the ternary compound $AgIn_{11}S_{17}$; the extrapolation $(\eta\hbar\omega)^{1/2} \longrightarrow 0$ can be used to determine the band gap E_g^{in} for these transitions. The values of E_g^{in} are listed in Table 2. It can also be seen from Fig. 4 that the shorter wavelength portion of the photosensitivity spectrum for the photoelectrochemical cell obeys the square-law dependence $(\eta\hbar\omega)^2 = f(\hbar\omega)$. Therefore, we may relate this special feature to the onset of direct band-to-band transitions; the extrapolation $(\eta\hbar\omega)^2 \longrightarrow 0$ makes it possible to estimate the energy of direct interband transitions (E_g^{dir}) for the compound under consideration. The results of this estimation are listed in Table 2.

4. CONCLUSION

To summarize, we fabricated for the first time photosensitive $In/AgIn_{11}S_{17}$ Schottky barriers and photoelectrochemical $H_2O/AgIn_{11}S_{17}$ cells based on crystals of the ternary compound $AgIn_{11}S_{17}$; the photoelectric properties of these structures were studied. Conclusions were drawn about the nature of the band-to-band transitions in the compound under consideration; the band gap was evaluated. It was shown that the aforementioned structures can be used as selective and wideband photodetectors of natural optical radiation.

REFERENCES

1. I. V. Bodnar', T. L. Kushner, V. Yu. Rud', *et al.*, Zh. Prikl. Spektrosk. **69**, 519 (2002).
2. C. Rincon, S. M. Wasim, G. Marin, and R. Marques, in *Abstracts of 13th ICTMC* (Paris, 2002), p. 83.
3. S. M. Wasim, G. Marin, C. Rincon, *et al.*, in *Abstracts of 13th ICTMC* (Paris, 2002), p. 205.
4. N. M. Gasanly, A. Serpengurel, A. Audinly, *et al.*, J. Appl. Phys. **85**, 3198 (1999).
5. S. B. Tsang, S. H. Wei, A. Zunger, and H. Katayama-Yochida, Phys. Rev. B **57**, 9642 (1998).
6. J. L. Shay and J. H. Wernick, *Ternary Chalcopyrite Semiconductors: Growth, Electronic Properties and Applications* (Pergamon, New York, 1975).
7. *Copper Indium Diselenide for Photovoltaic Applications*, Ed. by T. J. Coutts, L. L. Kazmerskii, and S. Wagner (Elsevier, Amsterdam, 1986).
8. N. N. Ishchenko, L. G. Starobinets, and L. I. Ganago, Izv. Akad. Nauk BSSR, Ser. Khim. Nauk, No. 5, 132 (1977).
9. L. G. Starobinets, N. N. Ishchenko, and L. I. Ganago, Izv. Akad. Nauk BSSR, Ser. Khim. Nauk, No. 1, 111 (1988).
10. P. P. Kish and S. T. Orlovskiĭ, Zh. Anal. Khim. **17**, 1057 (1962).
11. T. S. Moss, G. J. Burrell, and B. Ellis, *Semiconductor Opto-Electronics* (Butterworths, London, 1973; Mir, Moscow, 1976).
12. Yu. Ya. Gurevich and Yu. V. Pleskov, *Photoelectrochemistry of Semiconductors* (Nauka, Moscow, 1976).
13. Yu. V. Rud' and M. Tairov, Fiz. Tekh. Poluprovodn. (Leningrad) **21**, 615 (1987) [Sov. Phys. Semicond. **21**, 377 (1987)].
14. J. I. Pankove, *Optical Processes in Semiconductors* (Prentice Hall, Englewood Cliffs, N.J., 1971; Mir, Moscow, 1973).

Translated by A. Spitsyn

Semiconductors, Vol. 38, No. 2, 2004, pp. 169–174. Translated from Fizika i Tekhnika Poluprovodnikov, Vol. 38, No. 2, 2004, pp. 172–178.

ELECTRONIC AND OPTICAL PROPERTIES OF SEMICONDUCTORS

Magnetic Properties of Germanium-Doped Cadmium Telluride

Yu. V. Shaldin*^, I. Warchulska, and Yu. M. Ivanov***

**Shubnikov Institute of Crystallography, Russian Academy of Sciences, Leninskiĭ pr. 59, Moscow, 117333 Russia*
^e-mail: graimo@aha.ru
***International Laboratory of High Magnetic Fields and Low Temperatures, 53-421 Wrozlaw, Poland*
Submitted February 10, 2003; accepted for publication April 29, 2003

Abstract—The considerable contribution of van Vlek paramagnetism, which is caused by the presence of charged interstitial Te atoms and donor–acceptor pairs of the $V_{Te}Ge_i$ type, to the total magnetic susceptibility of CdTe:Ge in the temperature range 4.2–300 K is revealed. The presence of a special feature in the $\chi(T)$ dependence at 50 K is caused by a variation in the charge state of interstitial Te_i atoms, whose contribution starts to compete with a diamagnetic contribution induced by motion of vacancies along closed hexahedral ring-shaped trajectories. In fields as high as 0.15 T, magnetic hysteresis, which is caused by the orientation of magnetic clusters in the external field, is observed. © *2004 MAIK "Nauka/Interperiodica".*

1. INTRODUCTION

The preparation of CdTe-based material with fairly high resistivity, which is necessary for the development of active elements of various practical devices [1, 2], is a rather complex but very urgent problem in materials science of semiconductors [3]. Undoubtedly, a solution to this problem should be based on quite clear notions about the real structure of CdTe. The necessary variations in the real structure of CdTe could be attained by doping. In some cases, these variations are basic; i.e., the response of defects and their complexes with the impurity introduced to the external, for example, magnetic field is comparable with the magnetic susceptibility of the host crystal. It seems to us that this possibility of using magnetic methods for the investigation of imperfect semiconductors was originally noted by Kröger [4].

Magnetic properties of imperfect CdTe crystals doped with Al, In, Ga, Au, Cu, and Cl were investigated in a rather wide temperature range [5–7]. Measurements showed a considerable contribution of van Vlek polarization paramagnetism to the effective magnetic susceptibility χ. This contribution is comparable with the magnetic susceptibility itself of a nominally pure CdTe sample. Recent investigations of In- and Cl-doped samples revealed two facts [7]. First, the transition of the samples to the paramagnetic state at $T < 50$ K occurs due to an abrupt increase in the contribution of gas of paramagnetic defects, and, second, the ensembles of donor–acceptor pairs (DAPs), the exchange interaction between which leads to the effects of magnetic saturation, exist in the samples. However, no direct measurements of magnetization curves for all the objects listed were carried out. Such an omission is astonishing, since the initial samples should be inhomogeneous both electrically and magnetically. The procedures for investigating the inhomogeneity of semiconductors in the electric field have already been developed [8, 9]. However, the problem of investigating the magnetic inhomogeneity of CdTe, which is caused by nonmagnetic impurities, has not even been stated.

In contrast with, for example, the impurity atoms of Groups III and VII of the periodic table, the behavior of Ge atoms in II–VI compounds is not so obvious. A similar situation was considered by Madelung with respect to III–V compounds [10] and may be generalized as applied to CdTe. We believe that the realization of three possible variants is most probable: (i) Ge impurity atoms are incorporated only into the Cd sublattice, i.e., behave as donors and lead to an increase in resistivity; (ii) Ge impurity atoms are localized at two neighboring sites and form neutral DAPs; and (iii) impurity atoms are distributed statistically over interstitials with all the resulting consequences.

According to the resistivity measurements [11], the first variant is realized in *p*-CdTe when the Ge concentration is no higher than 5×10^{16} cm^{-3}. A further increase in the impurity content causes no increase in the sample resistivity. It may turn out that, with a further increase in the Ge concentration, the DAPs arising in the bulk of single crystals are grouped into clusters due to exchange interaction. These clusters are randomly oriented along the crystallographic directions and possess a nonzero magnetic moment.

Below, we will present the magnetization curves in the fields from 0.05 to 0.425 T at temperatures of 4.2, 77.5, and 295 K, as well as the magnetic susceptibilities of the grown Ge-doped CdTe samples.

2. EXPERIMENTAL

To investigate the magnetic properties of Ge-doped CdTe, we chose crystals that were grown by the Obreimov–Shubnikov technique with the use of a self-seed-

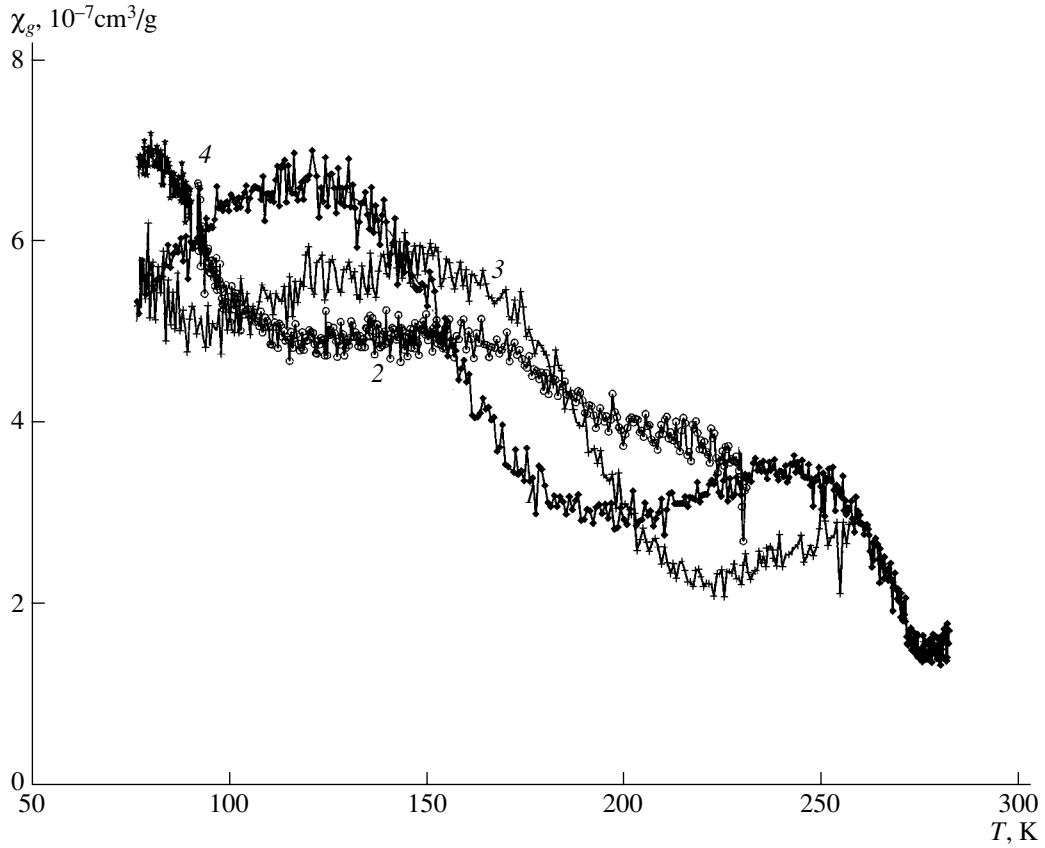

Fig. 1. Temperature dependences of the magnetic susceptibility for CdTe:Ge. Samples were cooled in the absence of a field to (*1*) 77.3 K, (*2*) 4.2 K in 24 h, and (*3*) 4.2 K in 48 h. The field was switched on at 77.3 K. (*4*) The part of the dependence when the field was switched on at 4.2 K measured in 240 h. All measurements are carried out in the mode of increasing temperature.

ing procedure under a partial pressure of Cd of about one atmosphere [12–14]. A specific feature of the growth procedure was that an unconventional method of controlling the partial pressure of Cd vapor above the melt was used. This method provides better reproducibility of the composition of the single crystals grown. A furnace charge of purity "Extra" of the Svetlovodsk plant of pure metals was used as an initial material. Our technology enabled us to obtain single crystals with a small deviation from stoichiometry with respect to Te and without precipitates. The crystals had a rather high optical quality; namely, transmission in the range 2–25 μm amounted to about 60%, and the absorption coefficient at a wavelength of 10.6 μm was equal to about 10^{-3} cm^{-1}. The crystals were doped by adding a corresponding alloy to the melt. This method made it possible to obtain CdTe with a Ge concentration in the range from 7.2×10^{14} to 1.9×10^{17} cm^{-3}. The initial samples had *p*-type conductivity. Their dark resistivity varied from 10^4 (for nominally pure CdTe) to 5×10^8 Ω cm due to doping.

The magnetization curves of the CdTe:Ge samples and their magnetic susceptibility were measured by the Faraday method [15] in a magnetic field as high as 0.425 T. All measurements were carried out for oriented samples of $2.5 \times 2.7 \times 3.5$ mm^3 in size weighing no more than 0.3 g. A Cahn-1000 Electrobalance was used as the recording device. The samples were oriented along the cleavage planes, and the longest sample edge corresponded to the ⟨001⟩ direction. The samples were placed in a Cu container, which was suspended on a Kevlar filament in the bulk of a He flow-through cryostat. The sample temperature was measured using a gold–Chromel thermocouple and was set by a thermal controller. The setup sensitivity for the sample weight mentioned was 5×10^{-8} g^{-1}. Since we could not determine accurately the orientation of the sample, the data given below should be considered as averaged over the (110) plane. The magnetization was measured at 4.2, 77.5, and 293 K in a field ranging from 0.05 to 0.425 T. The magnetic field was switched on only after attaining the lowest starting temperature. The specific features of the experimental setup used provided no way of varying the field direction and carrying out measurements starting from $H = 0$.

The magnetic susceptibility was measured in a field of 0.3 T in the temperature range 4.2–293 K. In the measurement technique chosen, the samples were cooled to low temperatures in the absence of a field.

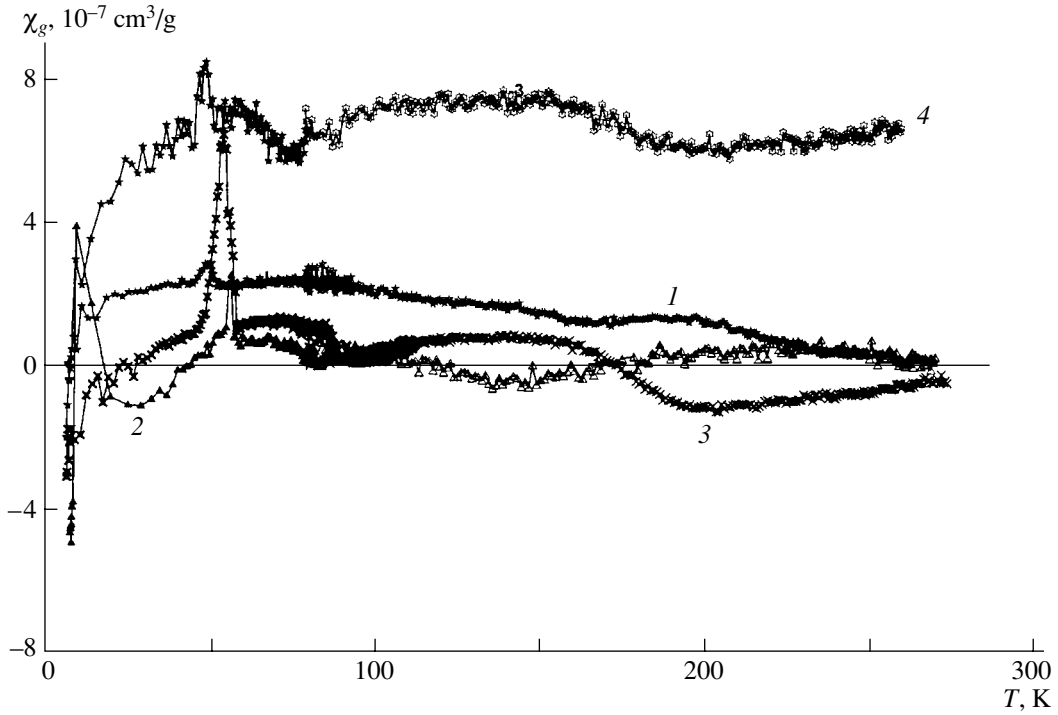

Fig. 2. Temperature dependences of the magnetic susceptibility for CdTe samples with Ge concentrations equal to (*1*) 0, (*2*) 5×10^{15}, (*3*) 3×10^{16}, and (*4*) 2×10^{17} cm^{-3}.

Under such conditions, the static magnetic susceptibility features time dependence, and its behavior is irreversible [15]. Since similar (nonergodic) behavior is caused mainly by the actual structure of the samples, we attempted to estimate the contribution of these processes to the summary measurement error. For this purpose, we measured the magnetic susceptibility as a function of time in a temperature range where the T dependence is insignificant (Fig. 1). It follows from the data presented that solid-state chemical reactions proceed in the sample bulk [3]. These reactions are accompanied by athermic diffusion of a defect due to, for example, the diamagnetoelectric effect [16] and cause variation in the charge state of the samples with all the ensuing consequences. It follows from the experimental data that the main behavioral tendency of χ is retained whereas the spread of values reaches ±15%.

3. RESULTS AND DISCUSSION

The experimental temperature dependences of magnetic susceptibility and magnetization curves of the CdTe:Ge samples in a magnetic field are shown in Figs. 2 and 3. The data presented differ drastically from the results [5–7]. In [5, 6], the χ magnitudes for the CdTe:Ge samples were practically independent of temperature, and, with increasing Ge concentration, these magnitudes decreased due to van Vlek paramagnetism. However, Shaldin [7] found that the In and Cl doping impurities lead to behavioral anomalies of effective values of $\chi(T)$. This effect is attributed to the existence of magnetic clusters and, in some cases, to the transition of the samples to the paramagnetic state at $T < 50$ K. Such variation in the experimental data should be attributed primarily to the specific features of the defect structure in CdTe single crystals grown by various methods.

When analyzing the experimental data, we follow [5–7] and rely on the fact that the effective values of the magnetic susceptibility of CdTe:Ge are controlled by the diamagnetic susceptibility of nominally pure CdTe χ^d itself and by the magnetic contribution of certain defects $\Delta\chi^p$, which depends on T and H:

$$\chi = \chi^d + \Delta\chi^p(T, H).$$

The value given in [5–7] and equal to $-(35.0 \pm 3.5) \times 10^{-8}$ cm^3/g may be apparently accepted as χ^d. Assuming that χ^d is practically independent of both T and H [15, 17], the difference between χ and χ^d should be considered as the contribution of the defect subsystem of crystals, which is a function of temperature and the magnetic field. At $T = 300$ K, the $\Delta\chi^p$ magnitude is as large as $\sim 10^{-6}$ cm^3/g; i.e., the contribution of defects exceeds the χ^d value (in magnitude) by a factor of almost 3 (Fig. 2).

To the first approximation, three temperature regions should be separated out in the experimental dependence. The first range at $T < 20$ K features an abrupt decrease in the magnitude and the reversal of the sign of χ. In the second T range from 20 to 70 K, the

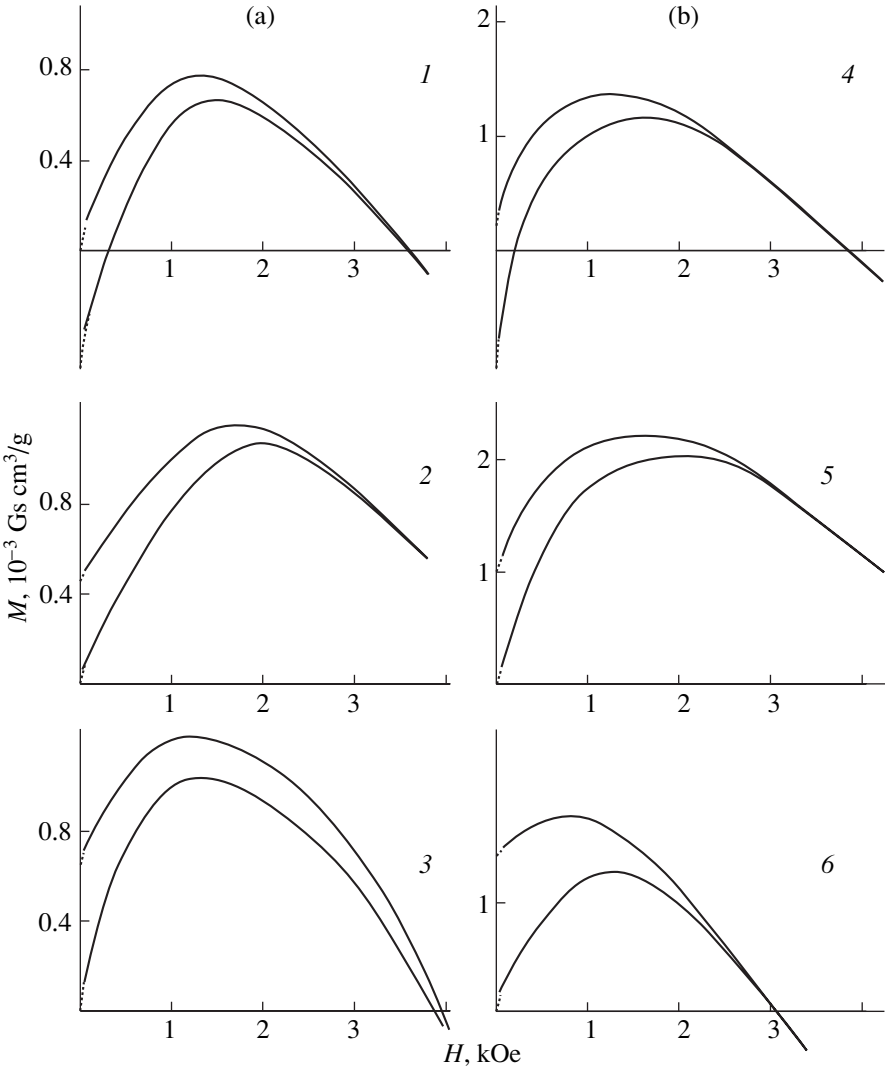

Fig. 3. Field dependences of magnetization of (a) nominally pure and (b) Ge-doped CdTe at temperatures T = (*1*, *4*) 295, (*2*, *5*) 77, and (*3*, *6*) 4.2 K.

dependence is nonmonotonic. Finally, in the third region at $T > 70$ K, the magnetic susceptibility is practically monotonic and, as a rule, positive. Thus, judging from the behavior of χ, at least three possible mechanisms of variations in the magnetic susceptibility exist in doped CdTe with allowance made for intrinsic defects. Therefore, when discussing these mechanisms, we will consider the following possibilities: (i) the samples contain charged Cd vacancies [18], which are filled by Ge during doping with the subsequent formation of ($Ge_{Cd}V_{Cd}$), and (ii) not only impurity atoms but also Te atoms are present at the octahedral sites of the structure (Fig. 4).

The specific feature of crystals with a sphalerite structure is the anisotropic distribution of valence electrons over the bonds. In this case, the nonadditive contribution to the total susceptibility of van Vlek paramagnetism arises in addition to Langevin precession diamagnetism [17]. The existence of intrinsic defects and their associations with Ge in CdTe, under specific conditions, leads to the emergence of local electric fields. This phenomenon is accompanied by the removal of (the linear by field) anisotropic degeneracy of electron levels in the Brillouin zone [19] and by admixing a part of the orbital momentum of the ground state to that of the excited state. The structural deformation at uncharged DAPs may additionally contribute to the local fields due to the piezoelectric effect.

At the first stage, Ge-doping of CdTe samples leads to the formation of uncharged DAPs of the $V_{Cd}Ge_{Cd}$ type. As was reported by Panchuk *et al.*, for a Ge concentration of more than approximately 5×10^{16} cm^{-3}, the incorporation of Ge is accompanied by an increase in resistivity [11]. According to our data, this is also accompanied by an insignificant variation in magnetic susceptibility of doped single crystals at T = 300 K

(Fig. 2). With a further increase in the impurity concentration, resistivity is practically independent of the impurity content, whereas the total magnetic susceptibility at $T = 300$ K substantially increases with the magnitude (Fig. 2). These facts may be interpreted as the result of Ge incorporation into the interstices with the subsequent variation in their charge states when the electroneutrality condition for the unit volume is satisfied. Such a process is accompanied by the emergence of local fields and, therefore, leads to an increase in the contribution of van Vlek paramagnetism.

With decreasing temperature in the range 70–20 K, the charge state of interstitial Te inevitably varies from Te_i'' to Te_i' and then to the neutral state due to the localization of holes at impurity centers. For samples with various Ge contents, the process goes with various rates. This fact manifests itself most clearly in the CdTe sample with an impurity concentration of about 5×10^{16} cm^{-3} (Fig. 3, curve *3*). A similar anomaly at the same temperature is observed for PbTe:In crystals [20], thus confirming the presence of ionized Te atoms at the interstices of CdTe.

For all Ge-doped CdTe samples, an abrupt change of the total susceptibility occurs in the region $T < 20$ K and, as a result, the χ sign is reversed. A similar phenomenon was observed for In-doped $Pb_{1-x}Sb_xTe$ crystals [20] and for $Cd_{1-x}Zn_xTe$ samples [21]. Therefore, there are reasons to assume that this result is mainly associated with the localization of carriers at donors and acceptors, which form cyclic ringlike associations in a sphalerite structure. Similar formations are inherent in the molecules of aromatic compounds, which possess a clearly pronounced anisotropy of magnetic susceptibility [17].

Hexahedral fragments are an example of such rings in a sphalerite structure. These fragments form a cellular (honeycomb-like) structure in the (110) planes (Fig. 5). Excluding the extreme case when H lies in the (110) plane, eddy currents are induced in the cells under the effect of a magnetic field. According to the Lenz rule, the direction of these currents leads to the emergence of the magnetic field, which compensate the external effect. Thus, an additional diamagnetic moment arises, which considerably exceeds the magnetic moment of individual atoms. The fact that dissipation proceeds in this temperature range is confirmed by test measurements of the real and imaginary parts of the magnetic susceptibility of the CdTe:Ge sample with a Ge concentration of 5×10^{15} cm^{-3} (Fig. 6). We are continuing research into the details of this phenomenon.

Additional information on the magnetic properties of the Ge-doped samples may be gained from the investigation of magnetization curves (Fig. 3). The existence of hysteresis, which is also observed for other samples, first of all, points to the irreversibility of magnetization of imperfect CdTe crystals. We assume that the magnetization is mainly associated with the orientation of magnetic clusters in an external magnetic field. By analogy with ferromagnets, the samples investigated in a strong field tend to the stable state with a minimum of corresponding thermodynamic potential. For a weak field, numerous metastable states, which correspond to the potential minima, exist in actual CdTe samples. The transitions between the potential minima are complicated due to high potential barriers that exceed kT. The variations in the external effects affect the conditions for thermodynamic equilibrium. However, in contrast to ferromagnets, the irreversibility of magnetization is caused only by the sizes of structural imperfections (clusters) with an arbitrary orientation of axes of easy magnetization. Thus, the magnetization depends on the shape of the defect formations and their orientation with respect to the crystallographic directions. In magnetic fields higher than 0.25 T, the samples gradually transform into the diamagnetic state, which is accompanied by magnetization saturation. In this region of magnetic fields, the derivative $\partial M/\partial T$ for all samples is practically constant and independent of the concentration of a doping impurity.

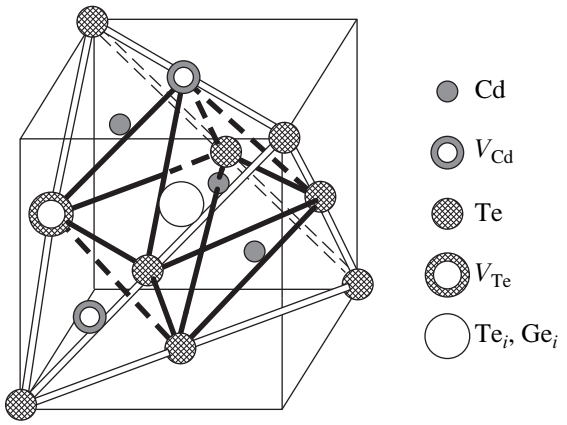

Fig. 4. Fragment of the structure of impurity-containing CdTe with structural defects.

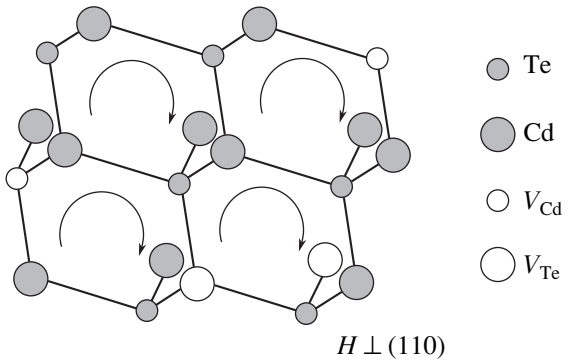

Fig. 5. Projection of a fragment of the CdTe structure on the (110) plane. Arrows show the direction of carrier motion under the effect of a magnetic field.

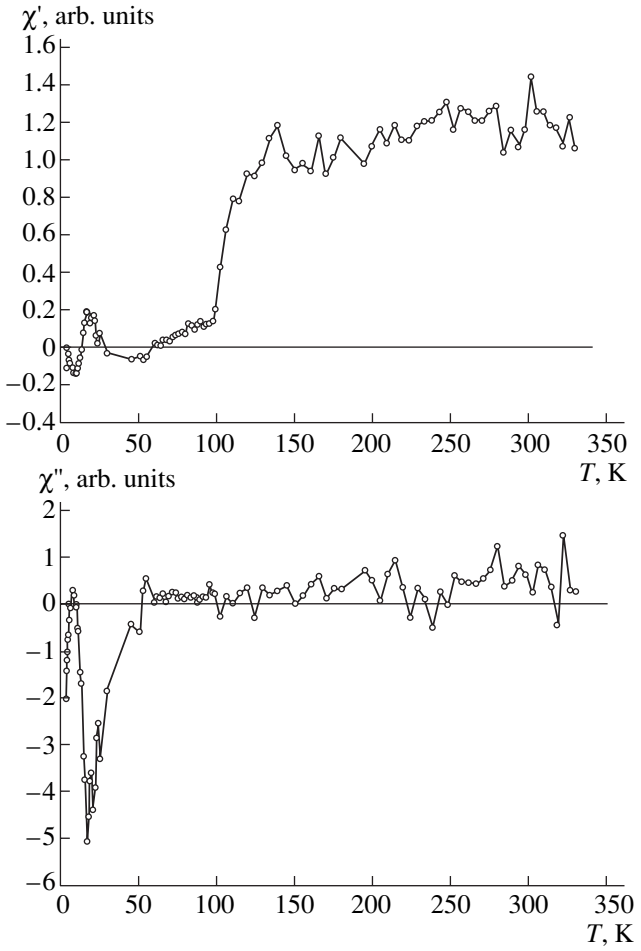

Fig. 6. Temperature dependences of the real (χ') and imaginary (χ'') parts of magnetic susceptibility of CdTe:Ge for a Ge concentration of 5×10^{15} cm^{-3}. Measurements are carried out using an EXA Oxford Inst. magnetometer, 1000 Hz, 20 Oe.

4. CONCLUSION

The results presented apparently point to the potential of magnetic methods for the investigation of an actual crystal structure. The role of interstitial Te in the formation of summary magnetic susceptibility is shown with a high degree of confidence for the first time. Further steps should be taken to develop theoretical approaches to the description of the defect subsystem in crystals.

REFERENCES

1. M. Hage-Ali and P. Siffert, Semicond. Semimet. **43**, 291 (1995).
2. E. Rzepka, Y. Marfaing, M. Cuniot, and R. Triboulet, Mater. Sci. Eng. B **16**, 262 (1993).
3. *Physics of II–VI Compounds*, Ed. by A. N. Georgobiani and M. K. Sheĭnkman (Nauka, Moscow, 1986), Chap. 3, p. 72.
4. F. A. Kröger, *Chemistry of Imperfect Crystals* (Academic, New York, 1964; Mir, Moscow, 1969).
5. V. I. Ivanov-Omskii, B. T. Kolomiets, V. K. Ogorodnikov, and Yu. V. Rud', Phys. Status Solidi A **13**, 61 (1972).
6. R. D. Ivanchuk, E. S. Nikonyuk, A. V. Savitskiĭ, and I. F. Snitsko, Fiz. Tekh. Poluprovodn. (Leningrad) **11**, 2046 (1977) [Sov. Phys. Semicond. **11**, 1202 (1977)].
7. Yu. V. Shaldin, Neorg. Mater. **37**, 670 (2001).
8. Yu. V. Shaldin and D. A. Belogurov, Fiz. Tekh. Poluprovodn. (Leningrad) **6**, 934 (1972) [Sov. Phys. Semicond. **6**, 807 (1972)].
9. N. A. Klimenko, V. K. Komar', V. P. Migal', and D. P. Nalivaĭko, Fiz. Tekh. Poluprovodn. (St. Petersburg) **35**, 139 (2001) [Semiconductors **35**, 135 (2001)].
10. O. Madelung, *Physics of III–V Compounds* (Wiley, New York, 1964; Mir, Moscow, 1967), Chap. 5, p. 257.
11. O. Panchuk, A. Savitsky, P. Fochuk, *et al.*, J. Cryst. Growth **197**, 607 (1999).
12. Yu. M. Ivanov, Neorg. Mater. **34**, 1062 (1998).
13. Yu. M. Ivanov, J. Cryst. Growth **194**, 309 (1998).
14. P. Hosch, Ju. M. Ivanov, and E. Belas, J. Cryst. Growth **184–185**, 1039 (1998).
15. R. M. White, *Quantum Theory of Magnetism*, 2nd ed. (Springer, Berlin, 1983; Mir, Moscow, 1985), Chap. 3, p. 79.
16. Yu. V. Shaldin, Fiz. Tverd. Tela (St. Petersburg) **37**, 1555 (1995) [Phys. Solid State **37**, 844 (1995)].
17. S. V. Vonsovskiĭ, *Magnetism* (Nauka, Moscow, 1971; Wiley, New York, 1974), Chap. 12.
18. R. Parmenter, Phys. Rev. **100**, 573 (1955).
19. T. Taguchi and B. Ray, Prog. Cryst. Growth Charact. **6**, 103 (1983).
20. A. Vasil'ev, T. Voloshok, J. Warchulska, and H. Kageyama, J. Phys. Soc. Jpn. **70**, 22 (2001).
21. M. Kh. Rabadanov, Yu. V. Shaldin, I. Varchulska, and V. K. Komar', in *Abstracts of X National Conference on Crystal Growth* (Moscow, 2002), p. 86.

Translated by N. Korovin

Semiconductors, Vol. 38, No. 2, 2004, pp. 175–181. Translated from Fizika i Tekhnika Poluprovodnikov, Vol. 38, No. 2, 2004, pp. 179–185.

ELECTRONIC AND OPTICAL PROPERTIES OF SEMICONDUCTORS

Nonlinearity of the Piezoresistive Effect in Polycrystalline Silicon Films

V. A. Gridchin and V. M. Lubimsky*

Novosibirsk State Technical University, Novosibirsk, 630092 Russia

**e-mail: lubvlm@ngs.ru*

Submitted March 3, 2003; accepted for publication May 13, 2003

Abstract—Piezoresistive properties of polycrystalline silicon films are described phenomenologically using elastoresistance and piezoresistance tensors in the quadratic approximation. Formulas are derived for calculating the second-order piezoresistance coefficients for some textures of polysilicon films in terms of the second-order piezoresistance coefficients for single-crystal silicon. Satisfactory agreement between the experimental and calculated piezoresistance coefficients is obtained in the region of heavy doping. © *2004 MAIK "Nauka/Interperiodica".*

1. INTRODUCTION

Piezoresistive properties of polycrystalline silicon films were reported in a number of publications [1–13]; either the strain-sensitivity coefficients or the piezoresistance coefficients were determined in the linear approximation with respect to the strain or stress. There are several models that satisfactorily explain the piezoresistive properties of polycrystalline silicon films. These models are based on the following assumptions: (i) the crystallites in the film have an arbitrary orientation so that the film is isotropic or the film features a texture; (ii) a strain or stresses are totally transferred to the film from the substrate; and (iii) the electrical properties of the heavily doped films are controlled by crystallites, in which case the contribution of barriers can be ignored. The coefficients of elasticity, strain sensitivity, and piezoelastoresistance in conditions of heavy doping of polycrystalline silicon (polysilicon) films are calculated using the procedure for averaging [2–13].

The nonlinearity of piezoresistive properties of *p*-type polysilicon films was discussed by Gridchin *et al.* [14]. Experimental data on the longitudinal and transverse coefficients of strain sensitivity were determined in the quadratic approximation; the values of these coefficients obtained using the procedure for averaging for the ⟨110⟩ texture were reported.

The aim of this study was to describe phenomenologically the piezoresistive properties of polysilicon films using elastoresistance and piezoresistance tensors in the quadratic approximation.

2. THEORY

The suggested theory of piezoresistive properties of polysilicon films is based on the following assumptions: (i) the polysilicon films are either isotropic or feature a texture with the axis that is perpendicular to the film surface; (ii) the film is much thinner than the substrate, so that the strain in the substrate is completely transferred to the film; (iii) the crystallite sizes along the axis perpendicular to the film plane are equal to the film thickness (the columnar approximation); (iv) the variation in the resistance of the film when it is subjected to deformation (stress) is caused only by the variation in the resistivity of crystallites (the grain boundaries only contribute to the film resistance and thus affect the strain-sensitivity or piezoresistance coefficients); and (v) the procedure suggested by Voigt [15] is used to calculate the mean values of the elastoresistance and elastic-constant tensor components for polysilicon films. In the case of textures, the mean values are calculated using integration with respect to the angle in the film plane [6].

The relative variation in resistivity ($\left(\frac{\Delta\rho_{ij}}{\langle\rho\rangle}\right)$) under the effect of strain (ε_{kl}) or stress (T_{mn}) is expressed in the quadratic approximation in terms of the piezoresistance coefficients (π_{ijmn}, π_{ijmnst}) or elastoresistance coefficients (m_{ijkl}, m_{ijklpr}), which are the tensors of the second and sixth ranks; i.e.,

$$\frac{\Delta\rho_{ij}}{\langle\rho\rangle} = m_{ijkl}\cdot\varepsilon_{kl} + m_{ijklpr}\cdot\varepsilon_{kl}\cdot\varepsilon_{pr}$$
$$= \pi_{ijmn}\cdot T_{mn} + \pi_{ijmnst}\cdot T_{mn}\cdot T_{st}.$$

The tensors $\pi_{ijmnst}(m_{ijklpr})$ are symmetric with respect to permutation of the second and third pairs of indices and to permutation within the pairs:

$$\pi_{ijnmst} = \pi_{jimnst} = \pi_{ijnmst} = \pi_{ijmnts} = \pi_{ijstmn}.$$

If the nonlinearity of elastic properties is disregarded in comparison with the nonlinearity of the

piezoresistive effect, the tensors m_{ijkl}, m_{ijklpr} and π_{ijmn}, π_{ijmnst} are related to each other via the elastic-constant tensor (C_{mnkl}) or the tensor of elastic-compliance coefficients (S_{klmn}); i.e.,

$$\pi_{ijmn} = m_{ijkl} \cdot S_{klmn}, \quad \pi_{ijmnst} = m_{ijklpr} \cdot S_{klmn} \cdot S_{prst},$$
$$m_{ijkl} = \pi_{ijmn} \cdot C_{mnkl}, \quad m_{ijklpr} = \pi_{ijmnst} \cdot C_{mnkl} \cdot C_{prst}.$$

The tensors π_{ijmn}, π_{ijmnst}, m_{ijkl}, m_{ijklpr}, C_{mnkl}, and S_{klmn} can be written in terms of the matrices π_{in}, m_{ik}, m_{ikp}, C_{nk}, and S_{kn}.

The coefficients $m_{\lambda\mu\nu}$ and $\pi_{\lambda\mu\nu}$ are related to the components of the tensors by the following conversion rules: $m_{\lambda\mu\nu} = m_{ijklpr}$ ($ij \longleftrightarrow \lambda = 1, \ldots, 6$; $kl \longleftrightarrow \mu = 1, \ldots, 6$; $pr \longleftrightarrow \nu = 1, \ldots, 6$); i.e., we have

$$\pi_{\lambda\mu\nu} = \left\{ \begin{array}{l} \pi_{ijmnst} (ij \longleftrightarrow \lambda = 1, \ldots, 6; \\ mn \longleftrightarrow \mu = 1, 2, 3;\ st \longleftrightarrow \nu = 1, 2, 3) \\ 2\pi_{ijmnst} (ij \longleftrightarrow \lambda = 1, \ldots, 6; \\ mn \longleftrightarrow \mu = 1, 2, 3;\ st \longleftrightarrow \nu = 4, 5, 6) \\ 2\pi_{ijmnst} (ij \longleftrightarrow \lambda = 1, \ldots, 6; \\ mn \longleftrightarrow \mu = 4, 5, 6;\ st \longleftrightarrow \nu = 1, 2, 3) \\ 4\pi_{ijmnst} (ij \longleftrightarrow \lambda = 1, \ldots, 6; \\ mn \longleftrightarrow \mu = 4, 5, 6;\ st \longleftrightarrow \nu = 4, 5, 6) \end{array} \right\}.$$

The structure of polycrystalline silicon films grown on oxidized silicon substrates depends on the conditions of growth; crystallites in these films are either arbitrarily oriented (isotropic films) or have an arbitrary orientation in the film plane but exhibit certain orientation in the direction perpendicular to the film plane (textures). French and Evans [10] reported the typical axes of the textures. These axes correspond to the crystallographic directions [100], [110], [111], [113], and [331].

The textures belong to one of the five limiting symmetry groups [16]. An analysis of the symmetry elements of polycrystalline silicon films with the [100], [110], [111], [113], and [331] axes shows that these films belong to the ∞/mm limiting symmetry group.

Isotropic films of polycrystalline silicon belong to the $\infty\infty m$ limiting symmetry group.

For the symmetry class ∞/mm, the matrices $C_{nk}(S_{kn})$ and $\pi_{in}(m_{ik})$ have five (C_{11}, C_{12}, C_{13}, C_{33}, and C_{44}) and seven (π_{11}, π_{12}, π_{13}, π_{31}, π_{32}, π_{33}, and π_{44}) independent elements, respectively [16].

For the class ∞mm, the number of independent components is equal to three ($C_{13} = C_{23} = C_{12}$, $C_{33} = C_{11}$; $S_{13} = S_{23} = S_{12}$, $S_{33} = S_{11}$; $m_{13} = m_{23} = m_{31} = m_{32} = m_{12}$, $m_{33} = m_{11}$; $\pi_{13} = \pi_{23} = \pi_{31} = \pi_{32} = \pi_{12}$, $\pi_{33} = \pi_{11}$) for matrices $C_{nk}(S_{kn})$ and $\pi_{in}(m_{ik})$ and is equal to four (π_{111}, π_{112}, π_{122}, and π_{123}) for matrices $\pi_{ins}(m_{ikp})$ [16].

It is appropriate to determine experimentally the piezoresistance coefficients, whereas it is more convenient to perform the procedure for averaging in terms of strains and elastoresistance coefficients.

The resistivity of polysilicon film in the situation where the size of the interface between crystallites is much less than the width of the charged layer can be written as [17, 18]

$$\rho_i = \rho_{bi}\frac{2w}{L} + \rho_{ci}\left(1 - \frac{2w}{L}\right),$$

where ρ_{bi} is the barrier resistivity, ρ_{ci} is the resistivity of the crystallite, $2w$ is the width of the charged region, and L is the size of the crystallite.

Assuming that the barriers do not contribute to the piezoresistive effect, we obtain

$$\left\langle \frac{\Delta\rho_i}{\langle\rho\rangle} \right\rangle = \left(1 - \frac{2w}{L}\right)\frac{\langle\Delta\rho_{ci}\rangle}{\langle\rho\rangle} = \left(1 - \frac{2w}{L}\right)\frac{\langle\rho_c\rangle}{\langle\rho\rangle}\frac{\langle\Delta\rho_{ci}\rangle}{\langle\rho_c\rangle}.$$

Assuming also that the piezoresistive effect in polysilicon films is related only to the variation in the resistivity of the crystallites, we can express the mean values of relative variations in resistivity in the film plane as

$$\frac{\langle\Delta\rho_{ci}\rangle}{\langle\rho_c\rangle} = \frac{\varepsilon_1}{\omega}\int m'_{i1}d\Omega + \frac{\varepsilon_2}{\omega}\int m'_{i2}d\Omega + \frac{1}{\omega}\int m'_{i3}\varepsilon'_3 d\Omega + \frac{\varepsilon_1^2}{\omega}\int m'_{i11}d\Omega + \frac{\varepsilon_2^2}{\omega}\int m'_{i22}d\Omega + \frac{1}{\omega}\int m'_{i33}\varepsilon'^2_3 d\Omega + \frac{2\varepsilon_1\varepsilon_2}{\omega}\int m'_{i12}d\Omega + \frac{2\varepsilon_1}{\omega}\int m'_{i13}\varepsilon'_3 d\Omega + \frac{2\varepsilon_2}{\omega}\int m'_{i23}\varepsilon'_3 d\Omega + \frac{\varepsilon_6^2}{\omega}\int m'_{i66}d\Omega,$$

$$\frac{\langle\Delta\rho_{c6}\rangle}{\langle\rho_c\rangle} = \frac{\varepsilon_6}{\omega}\int m'_{66}d\Omega + \frac{2\varepsilon_1\varepsilon_6}{\omega}\int m'_{616}d\Omega + \frac{2\varepsilon_2\varepsilon_6}{\omega}\int m'_{626}d\Omega + \frac{\varepsilon_6}{\omega}\int m'_{636}\varepsilon'_3 d\Omega,$$

where m'_{ik} and m'_{ikp} are the elastoresistance coefficients for single-crystal silicon; these coefficients are written for the substrate axes.

In the case of textures, $\omega = 2\pi$ and Ω is the angle in the film plane. For an isotropic film, $\omega = 8\pi^2$ and $d\Omega = \sin\theta d\theta d\varphi d\phi$, where θ, φ, and ϕ are the Eulerian angles.

Taking into account that the strains ε_1, ε_2, and ε_6 in the substrate plane are completely transferred to the film, we can express the stresses T'_n in a crystallite along the substrate axes as

$$T'_1 = C'_{11} \cdot \varepsilon_1 + C'_{12} \cdot \varepsilon_2 + C'_{13} \cdot \varepsilon'_3,$$
$$T'_2 = C'_{21} \cdot \varepsilon_1 + C'_{22} \cdot \varepsilon_2 + C'_{23} \cdot \varepsilon'_3,$$
$$T_3 = T'_3 = C'_{31} \cdot \varepsilon_1 + C'_{32} \cdot \varepsilon_2 + C'_{33} \cdot \varepsilon'_3,$$
$$T'_6 = C'_{66} \cdot \varepsilon_6,$$

where ε_3' are the strains of the crystallites written for the substrate axes and C_{nk}' are the elastic constants of the crystallites written for the substrate axes.

We then obtain $\varepsilon_3' = \dfrac{T_3 - C_{31}' \cdot \varepsilon_1 - C_{32}' \cdot \varepsilon_2}{C_{33}'}$ and $\langle \varepsilon_3 \rangle = \dfrac{1}{\omega}\int \varepsilon_3' d\Omega$.

The stresses T_3 in the direction perpendicular to the surface plane are identical in all crystallites. For the plane stress, $T_3 = 0$.

As follows from consideration of the relative variation in resistivity in a certain direction at an angle relative to the substrate axes, the equalities

$$\langle m_{13}^p \varepsilon_3 \rangle = \langle m_{23}^p \varepsilon_3 \rangle, \quad \langle m_{113}^p \varepsilon_3 \rangle = \langle m_{223}^p \varepsilon_3 \rangle,$$
$$\langle m_{123}^p \varepsilon_3 \rangle = \langle m_{213}^p \varepsilon_3 \rangle,$$
$$\langle m_{133}^p \varepsilon_3^2 \rangle = \langle m_{233}^p \varepsilon_3^2 \rangle, \quad \langle m_{313}^p \varepsilon_3 \rangle = \langle m_{323}^p \varepsilon_3 \rangle,$$

should be valid; using these equalities, we determined that

$$\langle m_{13}^p \rangle = \frac{\langle m_{13}^p \varepsilon_3 \rangle + \langle m_{23}^p \varepsilon_3 \rangle}{2\langle \varepsilon_3 \rangle},$$

$$\langle m_{113}^p \rangle = \frac{\langle m_{113}^p \varepsilon_3 \rangle + \langle m_{223}^p \varepsilon_3 \rangle}{2\langle \varepsilon_3 \rangle},$$

$$\langle m_{123}^p \rangle = \frac{\langle m_{123}^p \varepsilon_3 \rangle + \langle m_{213}^p \varepsilon_3 \rangle}{2\langle \varepsilon_3 \rangle},$$

$$\langle m_{113}^p \rangle = \frac{\langle m_{113}^p \varepsilon_3^2 \rangle + \langle m_{233}^p \varepsilon_3^2 \rangle}{2\langle \varepsilon_3^2 \rangle},$$

$$\langle m_{313}^p \rangle = \frac{\langle m_{313}^p \varepsilon_3 \rangle + \langle m_{323}^p \varepsilon_3 \rangle}{2\langle \varepsilon_3 \rangle}.$$

For textures with crystallites' symmetry axes that are perpendicular to the film axis and correspond to a symmetry whose order is less than threefold, $\langle m_{636}^p \rangle = \langle m_{663}^p \rangle = \dfrac{\langle m_{636}^p \varepsilon_3 \rangle}{\langle \varepsilon_3 \rangle}$ only in the case of plane stress.

Then,

$$\frac{\langle \Delta\rho_{ci} \rangle}{\langle \rho_c \rangle} = \langle m_{i1}^p \rangle \varepsilon_1 + \langle m_{i2}^p \rangle \varepsilon_2 + \langle m_{i3}^p \rangle \langle \varepsilon_3 \rangle + \langle m_{i11}^p \rangle \varepsilon_1^2$$
$$+ \langle m_{i22}^p \rangle \varepsilon_2^2 + \langle m_{i33}^p \rangle \langle \varepsilon_3 \rangle^2 + 2\langle m_{i12}^p \rangle \varepsilon_1 \varepsilon_2$$
$$+ 2\langle m_{i13}^p \rangle \varepsilon_1 \langle \varepsilon_3 \rangle + 2\langle m_{i23}^p \rangle \varepsilon_2 \langle \varepsilon_3 \rangle + \langle m_{i66}^p \rangle \varepsilon_6^2,$$

$$\frac{\langle \Delta\rho_{c6} \rangle}{\langle \rho_c \rangle} = \langle m_{66}^p \rangle \varepsilon_6 + 2\langle m_{616}^p \rangle \varepsilon_1 \varepsilon_6$$
$$+ 2\langle m_{626}^p \rangle \varepsilon_2 \varepsilon_6 + 2\langle m_{636}^p \rangle \langle \varepsilon_3 \rangle \varepsilon_6,$$
$$i = 1, 2, 3.$$

The piezoresistance coefficients of polysilicon films are defined as

$$\langle \pi_{in}^p \rangle = \langle m_{ik}^p \rangle \langle S_{kn}^p \rangle, \quad \langle \pi_{ins}^p \rangle = \langle m_{ikp}^p \rangle \langle S_{kn}^p \rangle \langle S_{ps}^p \rangle.$$

In the table, we list the second-order piezoresistance coefficients for isotropic and textured polysilicon films with the textures under consideration; these coefficients are expressed in terms of the corresponding coefficient for single-crystal silicon. When calculating the quantity π_{ins}', we used the values of S_{kn}^p reported in [13].

3. DISCUSSION

The procedure for averaging used by us automatically leads to the fulfillment of requirements of symmetry for the coefficients of elastoresistance and piezoresistance: $\langle m_{222}^p \rangle = \langle m_{111}^p \rangle$, $\langle m_{212}^p \rangle = \langle m_{112}^p \rangle$, $\langle m_{213}^p \rangle = \langle m_{123}^p \rangle$, $\langle m_{323}^p \rangle = \langle m_{313}^p \rangle$, $\langle m_{322}^p \rangle = \langle m_{311}^p \rangle$, $\langle m_{266}^p \rangle = \langle m_{166}^p \rangle$, $\langle \pi_{222}^p \rangle = \langle \pi_{111}^p \rangle$, $\langle \pi_{211}^p \rangle = \langle \pi_{122}^p \rangle$, $\langle \pi_{223}^p \rangle = \langle \pi_{113}^p \rangle$, $\langle \pi_{212}^p \rangle = \langle \pi_{112}^p \rangle$, $\langle \pi_{213}^p \rangle = \langle \pi_{123}^p \rangle$, $\langle \pi_{233}^p \rangle = \langle \pi_{133}^p \rangle$, $\langle \pi_{323}^p \rangle = \langle \pi_{313}^p \rangle$, $\langle \pi_{322}^p \rangle = \langle \pi_{311}^p \rangle$, $\langle \pi_{266}^p \rangle = \langle \pi_{166}^p \rangle$, and $\langle \pi_{626}^p \rangle = \langle \pi_{616}^p \rangle$.

Taking into account the symmetry, the following relations are valid for isotropic films:

$$\langle \pi_{144}^p \rangle = \frac{1}{2}(\langle \pi_{122}^p \rangle - \langle \pi_{123}^p \rangle),$$

$$\langle \pi_{155}^p \rangle = \frac{1}{4}(\langle \pi_{111}^p \rangle - 2\langle \pi_{112}^p \rangle + \langle \pi_{122}^p \rangle),$$

$$\langle \pi_{414}^p \rangle = \frac{1}{2}(\langle \pi_{112}^p \rangle - \langle \pi_{123}^p \rangle),$$

$$\langle \pi_{424}^p \rangle = \frac{1}{4}(\langle \pi_{111}^p \rangle - \langle \pi_{122}^p \rangle),$$

$$\langle \pi_{456}^p \rangle = \frac{1}{8}(\langle \pi_{111}^p \rangle - 2\langle \pi_{112}^p \rangle - \langle \pi_{122}^p \rangle + 2\langle \pi_{123}^p \rangle).$$

The following conclusions are valid for all textured and isotropic films:

(i) Homogeneous strain ($\varepsilon = \varepsilon_1 = \varepsilon_2 = \varepsilon_3$) does not affect the symmetry of crystallites and does not lead to

The piezoresistance coefficients of polysilicon films

	Texture					
	⟨100⟩	⟨110⟩	⟨111⟩	⟨113⟩	⟨331⟩	Isotropy
$\langle \pi^p_{111} \rangle$	$.6250\pi_{111} + .2500\pi_{112} + .1250\pi_{122} + .7830\pi_{661} + .3065\pi_{166}$	$.09375\pi_{123} + .3906\pi_{111} + .1719\pi_{122} + .3438\pi_{112} + .2936\pi_{441} + 1.077\pi_{661} + .1150\pi_{144} + .4215\pi_{166} + .4598\pi_{456}$	$.0556\pi_{123} + .2222\pi_{122} + .4444\pi_{112} + .2778\pi_{111} + .5450\pi_{166} + 1.392\pi_{661} + .1740\pi_{441} + .0681\pi_{144} + .2725\pi_{456}$	$.04620\pi_{123} + .3216\pi_{112} + .1608\pi_{122} + .4715\pi_{111} + .2266\pi_{456} + .0567\pi_{144} + .3943\pi_{166} + .1447\pi_{441} + 1.007\pi_{661}$	$.3568\pi_{111} + .3750\pi_{112} + .1875\pi_{122} + .0807\pi_{123} + .2527\pi_{441} + 1.174\pi_{661} + .3958\pi_{456} + .4598\pi_{166} + .0989\pi_{144}$	$.1714\pi_{122} + .3429\pi_{112} + .4286\pi_{111} + .0571\pi_{123} + .1790\pi_{441} + 1.074\pi_{661} + .0701\pi_{144} + .2803\pi_{456} + .4204\pi_{166}$
$\langle \pi^p_{112} \rangle$	$.1250\pi_{111} + .7500\pi_{112} + .1250\pi_{122} - .3065\pi_{166}$	$.07813\pi_{111} + .2188\pi_{123} + .5938\pi_{112} + .1094\pi_{122} + .2936\pi_{441} + .0979\pi_{661} - .0383\pi_{144} - .1916\pi_{166} - .1533\pi_{456}$	$.2778\pi_{123} + .1111\pi_{122} + .5556\pi_{112} + .0556\pi_{111} - .1362\pi_{166} + .1740\pi_{661} + .3480\pi_{441} - .0681\pi_{144} - .2725\pi_{456}$	$.1349\pi_{123} + .6544\pi_{112} + .1164\pi_{122} + .0943\pi_{111} - 0.1087\pi_{456} - .0272\pi_{144} - .2312\pi_{166} + .1765\pi_{441} + .0694\pi_{661}$	$.0714\pi_{111} + .5830\pi_{112} + .1101\pi_{122} + .2355\pi_{123} + .3082\pi_{441} + .1212\pi_{661} - .1899\pi_{456} - .1750\pi_{166} - .0475\pi_{144}$	$.1143\pi_{122} + .6286\pi_{112} + .0857\pi_{111} + .1714\pi_{123} + .2237\pi_{441} + .0895\pi_{661} - .0350\pi_{144} - .1401\pi_{456} - .2102\pi_{166}$
$\langle \pi^p_{122} \rangle$	$.1250\pi_{111} + .2500\pi_{112} + .6250\pi_{122} - .7830\pi_{661} + .3065\pi_{166}$	$.0781\pi_{111} + .2188\pi_{112} + .4844\pi_{122} + .2188\pi_{123} - .0979\pi_{441} - .4894\pi_{661} + .2682\pi_{144} + .2682\pi_{166} - .1533\pi_{456}$	$.2778\pi_{123} + .4444\pi_{122} + .2222\pi_{112} + .0556\pi_{111} - .1362\pi_{166} + .1740\pi_{661} + .3480\pi_{441} - .0681\pi_{144} - .2725\pi_{456}$	$.1349\pi_{123} + .2329\pi_{112} + .5379\pi_{122} + .0943\pi_{111} - .1087\pi_{456} + .1654\pi_{144} + .2856\pi_{166} - .0694\pi_{441} - .5906\pi_{661}$	$.0714\pi_{111} + .2201\pi_{112} + .4730\pi_{122} + .2355\pi_{123} - .1212\pi_{441} - .4470\pi_{661} - 1899\pi_{456} + .2699\pi_{166} + .2888\pi_{144}$	$.5143\pi_{122} + .2286\pi_{112} + .0857\pi_{111} + .1714\pi_{123} - .0895\pi_{441} - .5369\pi_{661} + .2102\pi_{144} - .1401\pi_{456} + .2803\pi_{166}$
$\langle \pi^p_{123} \rangle$	$.2500\pi_{112} + .7500\pi_{123} - .3915\pi_{441}$	$.03125\pi_{111} + .3750\pi_{112} + .2187\pi_{122} + .3750\pi_{123} - .4894\pi_{441} + .1958\pi_{661} - .2299\pi_{144} - .0766\pi_{166} + .3065\pi_{456}$	$.2778\pi_{123} + .2778\pi_{122} + .3889\pi_{112} + .0556\pi_{111} - .1362\pi_{166} - .3480\pi_{661} - .4350\pi_{441} - .2725\pi_{144} + .5450\pi_{456}$	$.5195\pi_{123} + .3234\pi_{112} + .1349\pi_{122} + .0222\pi_{111} + .2174\pi_{456} - .1382\pi_{144} - .0543\pi_{166} - .4371\pi_{441} - .1388\pi_{661}$	$.0387\pi_{111} + .3783\pi_{112} + .2356\pi_{122} + .3475\pi_{123} - .4711\pi_{441} - .2425\pi_{661} + .3797\pi_{456} - .0949\pi_{166} - .2413\pi_{144}$	$.1714\pi_{122} + .3429\pi_{112} + .0286\pi_{111} + .4571\pi_{123} - .4474\pi_{441} - .1790\pi_{661} - .1752\pi_{144} + .2803\pi_{456} - .0701\pi_{166}$
$\langle \pi^p_{113} \rangle$	$.7500\pi_{112} + .2500\pi_{123} - .3915\pi_{441}$	$.0937\pi_{111} - .0766\pi_{144} - .2230\pi_{166} - .3065\pi_{456} + .1563\pi_{122} + .1250\pi_{123} + .6250\pi_{112} + .0979\pi_{441} + .1958\pi_{661}$	$.1667\pi_{111} + .5000\pi_{112} + .1667\pi_{122} + .1667\pi_{123} + .2610\pi_{441} - .4087\pi_{166}$	$.0665\pi_{111} - .0295\pi_{144} - .1631\pi_{166} + .1867\pi_{123} + .2547\pi_{441} + .0905\pi_{122} + .6563\pi_{112} - .1179\pi_{456} + .0753\pi_{661}$	$.1395\pi_{123} - .0515\pi_{144} - .2848\pi_{166} + .1526\pi_{441} + .1161\pi_{111} + .5863\pi_{112} + .1581\pi_{122} + .1315\pi_{661} - .2059\pi_{456}$	$.1143\pi_{122} + .6286\pi_{112} + .0857\pi_{111} + .1714\pi_{123} + .2237\pi_{441} + .0895\pi_{661} - .0350\pi_{144} - .1401\pi_{456} - .2102\pi_{166}$
$\langle \pi^p_{133} \rangle$	π_{122}	$.1250\pi_{111} + .3065\pi_{144} + .3065\pi_{166} + .3750\pi_{122} + .2500\pi_{123} + .2500\pi_{112} - .7830\pi_{661}$	$.2725\pi_{144} - .5450\pi_{456} - .6960\pi_{661} + .1111\pi_{111} + .4444\pi_{112} + .2222\pi_{122} + .2222\pi_{123} - .3480\pi_{441} + .5450\pi_{166}$	$.0684\pi_{111} + .1677\pi_{144} + .2174\pi_{166} + .1367\pi_{123} - .0635\pi_{441} + .6176\pi_{122} + .1773\pi_{112} - .0995\pi_{456} - .4283\pi_{661}$	$.2388\pi_{123} + .2928\pi_{144} + .3797\pi_{166} - .1110\pi_{441} + .1194\pi_{111} + .3097\pi_{112} + .3321\pi_{122} - .7480\pi_{661} - .1738\pi_{456}$	$.5143\pi_{122} + .2286\pi_{112} + .0857\pi_{111} + .1714\pi_{123} - .0895\pi_{441} - .5369\pi_{661} + .2102\pi_{144} - .1401\pi_{456} + .2803\pi_{166}$
$\langle \pi^p_{166} \rangle$	$.2039\pi_{111} - .4078\pi_{112} + 2039\pi_{122} + .5000\pi_{166}$	$.1274\pi_{111} - .2549\pi_{112} + .1784\pi_{122} - .0510\pi_{123} + .2500\pi_{456} + .4375\pi_{166} + .1596\pi_{661} - .1596\pi_{441} + .1875\pi_{144}$	$.0906\pi_{111} - .1812\pi_{112} + .1812\pi_{122} - .0906\pi_{123} + .4444\pi_{166} + .2838\pi_{661} - .2838\pi_{441} + .2222\pi_{144} + .2222\pi_{456}$	$.1538\pi_{111} - .3076\pi_{112} + .1899\pi_{122} - .0362\pi_{123} + .1367\pi_{456} + .1127\pi_{144} + .4658\pi_{166} - .1132\pi_{441} + .1132\pi_{661}$	$.1164\pi_{111} - .2328\pi_{112} + .1795\pi_{122} - .0631\pi_{123} - .1977\pi_{441} + .1977\pi_{661} + .2388\pi_{456} + .4403\pi_{166} + .1968\pi_{144}$	$.1398\pi_{111} - .2796\pi_{112} + .1864\pi_{122} - .0466\pi_{123} - .1460\pi_{441} + .1460\pi_{661} + .1429\pi_{144} + .1714\pi_{456} + .4571\pi_{166}$

Table. (Contd.)

	Texture					
	⟨100⟩	⟨110⟩	⟨111⟩	⟨113⟩	⟨331⟩	Isotropy
$\langle \pi^p_{311} \rangle$	$.7500\pi_{112} + .2500\pi_{123} + .3065\pi_{144}$	$.1250\pi_{123} + .0938\pi_{111} + .3125\pi_{112} + .4688\pi_{122} + .1533\pi_{144} + .3832\pi_{166} - .3065\pi_{456} - .1958\pi_{441} - .5873\pi_{661}$	$.1667\pi_{123} + .3333\pi_{122} + .3333\pi_{112} + .1667\pi_{111} + .4087\pi_{166} - 1.044\pi_{661} + .2044\pi_{144}$	$.1867\pi_{123} + .1811\pi_{112} + .5657\pi_{122} + .0665\pi_{111} + .0753\pi_{441} + .2289\pi_{144} - .1179\pi_{456} - .4165\pi_{661} + .2220\pi_{166}$	$.1161\pi_{111} + .3162\pi_{112} + .4282\pi_{122} + .1395\pi_{123} - .1315\pi_{441} - .7274\pi_{661} - .2059\pi_{456} + .3878\pi_{166} + .1710\pi_{144}$	$.5143\pi_{122} + .2286\pi_{112} + .0857\pi_{111} + .1714\pi_{123} - .0895\pi_{441} - .5369\pi_{661} + .2102\pi_{144} - .1401\pi_{456} + .2803\pi_{166}$
$\langle \pi^p_{312} \rangle$	$.2500\pi_{122} + .7500\pi_{123} - .3065\pi_{144}$	$.3750\pi_{123} + .0312\pi_{111} + .4375\pi_{122} + .1562\pi_{122} - .1533\pi_{144} - .0766\pi_{166} + .3065\pi_{456} - .5873\pi_{441} - .1958\pi_{661}$	$.2778\pi_{123} + .1111\pi_{122} + .5556\pi_{112} + .0556\pi_{111} - .1362\pi_{166} - .3480\pi_{661} - .6960\pi_{441} - .0681\pi_{144} + .5450\pi_{456}$	$.5195\pi_{123} + .2697\pi_{112} + .1886\pi_{122} + .0222\pi_{111} - .3530\pi_{441} - .2041\pi_{144} + .2174\pi_{456} - .1388\pi_{661} - .0544\pi_{166}$	$.0387\pi_{111} + .4710\pi_{112} + .1427\pi_{122} + .3475\pi_{123} - .6164\pi_{441} - .2425\pi_{661} + .3797\pi_{456} - .0949\pi_{166} - .1276\pi_{144}$	$.1714\pi_{122} + .3429\pi_{112} + .0286\pi_{111} + .4571\pi_{123} - .4474\pi_{441} - .1790\pi_{661} - .1752\pi_{144} + .2803\pi_{456} - .0701\pi_{166}$
$\langle \pi^p_{313} \rangle$	π_{112}	$.2500\pi_{123} + .1250\pi_{111} + .5000\pi_{112} + .1250\pi_{122} - .3065\pi_{166} + .3915\pi_{441}$	$.2222\pi_{123} + .2222\pi_{122} + .4444\pi_{112} + .1111\pi_{111} - .2725\pi_{166} + .3480\pi_{661} + .1740\pi_{441} - .1362\pi_{144} - .5450\pi_{456}$	$.1367\pi_{123} + .7062\pi_{112} + .0887\pi_{122} + .0684\pi_{111} + .1824\pi_{441} - .0249\pi_{144} - .0995\pi_{456} + .0635\pi_{661} - .1677\pi_{166}$	$.1194\pi_{111} + .4870\pi_{112} + .1548\pi_{122} + .2388\pi_{123} + .3185\pi_{441} + .1110\pi_{661} - .1738\pi_{456} - .2928\pi_{166} - .0434\pi_{144}$	$.1143\pi_{122} + .6286\pi_{112} + .0857\pi_{111} + .1714\pi_{123} + .2237\pi_{441} + .0895\pi_{661} - .0350\pi_{144} - .1401\pi_{456} - .2102\pi_{166}$
$\langle \pi^p_{333} \rangle$	π_{111}	$.2500\pi_{111} + .5000\pi_{112} + .2500\pi_{122} + 1.566\pi_{661} + .6131\pi_{166}$	$.2222\pi_{123} + .2222\pi_{122} + .4444\pi_{112} + .1111\pi_{111} + .5450\pi_{166} + 1.090\pi_{456} + 1.392\pi_{661} + .6960\pi_{441} + .2725\pi_{144}$	$.0406\pi_{123} + .2735\pi_{112} + .1367\pi_{122} + .5492\pi_{111} + .1271\pi_{441} + 0497\pi_{144} + .1990\pi_{456} + .8565\pi_{661} + .3353\pi_{166}$	$.2127\pi_{111} + .4776\pi_{112} + .2388\pi_{122} + .0709\pi_{123} + .2219\pi_{441} + 1.496\pi_{661} + .3475\pi_{456} + .5857\pi_{166} + .0869\pi_{144}$	$.1714\pi_{122} + .3429\pi_{112} + .4286\pi_{111} + .0571\pi_{123} + .1790\pi_{441} + 1.074\pi_{661} + .0701\pi_{144} + .2803\pi_{456} + .4204\pi_{166}$
$\langle \pi^p_{366} \rangle$	0	0	0	$.0362\pi_{111} - .0723\pi_{112} + .3076\pi_{122} - .2714\pi_{123} + .2264\pi_{441} + .3531\pi_{144} - .2735\pi_{456} - .2264\pi_{661} + .2254\pi_{166}$	$.06313\pi_{111} - .1263\pi_{112} + .2328\pi_{122} - .1697\pi_{123} + .3955\pi_{441} - .3955\pi_{661} - .4776\pi_{456} + .3936\pi_{166} + .2435\pi_{144}$	0
$\langle \pi^p_{661} \rangle$	$.1596\pi_{111} - .1596\pi_{122} + .5000\pi_{661}$	$.5000\pi_{661} + .1958\pi_{456} + .0489\pi_{166} - .0489\pi_{144} - .0399\pi_{123} - .0998\pi_{122} + .0399\pi_{112} + .0998\pi_{111} + .1250\pi_{441}$	$.5556\pi_{661} + .1740\pi_{456} + .0870\pi_{166} - .0870\pi_{144} - .0710\pi_{123} - .0710\pi_{122} + .0710\pi_{112} + .0710\pi_{111} + .1111\pi_{441}$	$.1204\pi_{111} + .0283\pi_{112} + .5101\pi_{661} - .1204\pi_{122} - .0283\pi_{123} - .0347\pi_{144} + .0347\pi_{166} + .1071\pi_{456} + .0684\pi_{441}$	$- .0606\pi_{144} + .0606\pi_{166} + .0494\pi_{112} + .0911\pi_{111} + .5177\pi_{661} - .0911\pi_{122} - .0494\pi_{123} + .1870\pi_{456} + .1194\pi_{441}$	$.1342\pi_{456} - .0365\pi_{123} + .1095\pi_{111} + .0365\pi_{112} - .0447\pi_{144} - .1095\pi_{122} + .0447\pi_{166} + .5143\pi_{661} + .0857\pi_{441}$
$\langle \pi^p_{636} \rangle$	$.3193\pi_{112} - .3193\pi_{123} + .5000\pi_{441}$	$.2500\pi_{661} - .3915\pi_{456} - .0979\pi_{166} + .0979\pi_{144} - .1596\pi_{123} - .0399\pi_{122} + .1596\pi_{112} + .0399\pi_{111} + .3750\pi_{441}$	$.2222\pi_{661} - .3480\pi_{456} - .1740\pi_{166} + .1740\pi_{144} - .0710\pi_{123} - .0710\pi_{122} + .0710\pi_{112} + .0710\pi_{111} + .4444\pi_{441}$	$.0283\pi_{111} + .2125\pi_{112} + .1367\pi_{661} - .0283\pi_{122} - .2125\pi_{123} + .0694\pi_{144} - .0694\pi_{166} - .2141\pi_{456} + .4418\pi_{441}$	$.1212\pi_{144} - .1212\pi_{166} + .1328\pi_{112} + .0494\pi_{111} + .2388\pi_{661} - .0494\pi_{122} - .1329\pi_{123} - .3740\pi_{456} + .3983\pi_{441}$	$- .2685\pi_{456} - .1824\pi_{123} + .0365\pi_{111} + .1824\pi_{112} + .0895\pi_{144} - .0365\pi_{122} - .0895\pi_{166} + .1714\pi_{661} + .4286\pi_{441}$

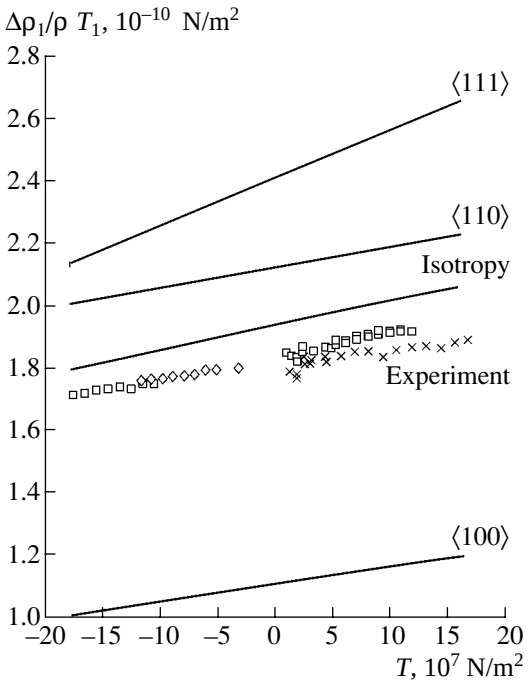

Fig. 1. Dependences of the relative variation in longitudinal resistivity (per unit stress) on the stress.

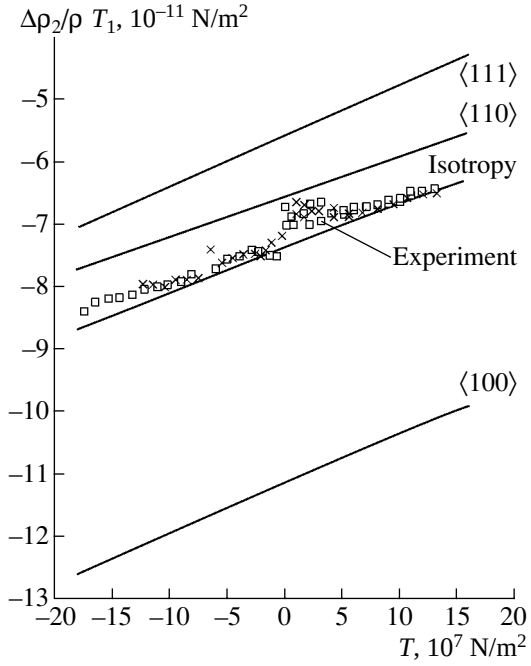

Fig. 2. Dependences of the relative variation in transverse resistivity (per unit stress) on the stress.

a great piezoresistive effect nor to pronounced nonlinearity ($m_{111} \approx m_{122} \approx m_{112} \approx m_{123} \approx 0$); i.e.,

$$\frac{\langle \Delta\rho_{c1}\rangle}{\langle \rho_c\rangle} = (\langle m^p_{11}\rangle + \langle m^p_{12}\rangle + \langle m^p_{13}\rangle)\varepsilon + (\langle m^p_{111}\rangle + \langle m^p_{122}\rangle + \langle m^p_{133}\rangle + 2\langle m^p_{112}\rangle + 2\langle m^p_{113}\rangle + 2\langle m^p_{123}\rangle)\varepsilon^2 = (m_{11} + 2m_{12})\varepsilon + (m_{111} + 2m_{122} + 4m_{112} + 2m_{123})\varepsilon^2.$$

(ii) Hydrostatic pressure ($T = T_1 = T_2 = T_3$) does not affect the symmetry of crystallites and also does not lead to a great piezoresistive effect nor to pronounced nonlinearity; i.e.,

$$\frac{\langle \Delta\rho_{c1}\rangle}{\langle \rho_c\rangle} = (\langle \pi^p_{11}\rangle + \langle \pi^p_{12}\rangle + \langle \pi^p_{13}\rangle)T + (\langle \pi^p_{111}\rangle + \langle \pi^p_{122}\rangle + \langle \pi^p_{133}\rangle + 2\langle \pi^p_{112}\rangle + 2\langle \pi^p_{113}\rangle + 2\langle \pi^p_{123}\rangle)T^2 = (\pi_{11} + 2\pi_{12})T + (\pi_{111} + 2\pi_{122} + 4\pi_{112} + 2\pi_{123})T^2$$

($\pi_{111} \approx \pi_{122} \approx \pi_{112} \approx \pi_{123} \approx 0$) [19].

In Figs. 1 and 2, we show the experimental and calculated dependences of relative variations in resistivity per unit stress $\left(\left(\frac{\langle \Delta\rho_i\rangle}{\langle \rho\rangle T_j}\right)\right)$ on stresses in polysilicon films at room temperature. In calculations, the second-order piezoresistance coefficients for single-crystal silicon were taken from [19], where the corresponding values were reported for three doping levels with the accuracy of determination indicated. Experimental data on the relative variation in the resistivity in relation to stresses were taken from [14]. The films had a ⟨110⟩ texture, with a possible contribution from the isotropic component. The dopant concentration in the polysilicon films was 7×10^{19} cm^{-3} [14] and differed from those reported in [19]. Therefore, the following values of the second-order piezoresistance coefficients were used in the calculations: $\pi_{111} = \pi_{112} = \pi_{122} = \pi_{123} = 0$, $\pi_{661} = -3 \times 10^{-20}$ Pa^{-2}, $\pi_{166} = 55 \times 10^{-20}$ Pa^{-2}, $\pi_{144} = -28 \times 10^{-20}$ Pa^{-2}, $\pi_{441} = 12 \times 10^{-20}$ Pa^{-2}, and $\pi_{456} = -20 \times 10^{-20}$ Pa^{-2}. It can be seen from Figs. 1 and 2 that, both for the longitudinal and transverse effects, the slopes of the straight lines are almost the same for the ⟨100⟩ and ⟨110⟩ textures and for isotropic films. For the ⟨110⟩ texture and an isotropic film, a satisfactory agreement between experimental and calculated dependences is observed.

4. CONCLUSIONS

(i) We described phenomenologically the piezoresistive properties of polycrystalline silicon films in the quadratic approximation using elastoresistance and piezoresistance tensors and taking into account the symmetry of crystallites in the films.

(ii) The equalities relating the averaged second-order coefficients of piezoresistance and elastoresistance are valid for all the textured and isotropic films under consideration; these equalities follow from the symmetry requirements.

(iii) A satisfactory agreement between experimental and calculated dependences of relative variations in

resistivity (per unit stress) on the stress for polysilicon films at room temperature in the region of heavy doping is observed.

REFERENCES

1. V. Mosser, J. Suski, J. Goss, and E. Obermeir, Sens. Actuators A **28**, 113 (1991).
2. J. Suski, V. Mosser, and J. Goss, Sens. Actuators **17**, 405 (1989).
3. J. Suski, V. Mosser, and G. Le Roux, in *Proceedings of Electrochemical Society Conference, San Diego, CA, USA* (1986), p. 331.
4. E. Obermeir, Ph.D. Thesis (Univ. of Munich, 1983).
5. P. H. French and A. G. R. Evans, Sens. Actuators **7**, 135 (1985).
6. D. Shubert, W. Jenschke, T. Uhlig, and F. M. Schmidt, Sens. Actuators **11**, 145 (1987).
7. V. A. Gridchin, V. M. Lubimsky, and M. P. Sarina, Sens. Actuators A **49**, 67 (1995).
8. P. H. French and A. G. R. Evans, Electron. Lett. **24**, 999 (1984).
9. T. Toriyama, Y. Yokoyama, and S. Sugiyama, Sens. Mater. **12**, 473 (2000).
10. P. H. French and A. G. R. Evans, Solid-State Electron. **32**, 1 (1989).
11. M. Le Berre, M. Lemiti, D. Barbier, *et al.*, Sens. Actuators A **46–47**, 166 (1995).
12. W. Vanden Bossche and J. R. Mollinger, Sens. Actuators A **62**, 475 (1997).
13. V. A. Gridchin and V. M. Lyubimskiĭ, Mikroélektronika (2003) (in press).
14. V. A. Gridchin, V. M. Lubimsky, and M. P. Sarina, in *Proceedings of Measurement'97* (Smolenice, 1997), p. 74.
15. W. Voigt, *Lehrbuch der Kristallphysik* (Teubner, Leipzig, 1910).
16. Yu. I. Sirotin and M. P. Shaskol'skaya, *Fundamentals of Crystal Physics* (Nauka, Moscow, 1975).
17. N. C. C. Lu, L. Gerzberg, C. Y. Lu, and J. D. Meindl, IEEE Trans. Electron Devices **28**, 818 (1981).
18. D. M. Kim, A. N. Khondker, S. S. Ahmed, and R. R. Shah, IEEE Trans. Electron Devices **31**, 480 (1984).
19. K. Matsuda, Y. Kanda, K. Yamamura, and K. Suzuki, Jpn. J. Appl. Phys. **29**, L1941 (1990).

Translated by A. Spitsyn

Semiconductors, Vol. 38, No. 2, 2004, pp. 182–184. Translated from Fizika i Tekhnika Poluprovodnikov, Vol. 38, No. 2, 2004, pp. 186–189.

ELECTRONIC AND OPTICAL PROPERTIES OF SEMICONDUCTORS

Impurity States of Tin in $Bi_2Te_{3-x}Se_x$ ($x = 0.06, 0.12$) Solid Solutions

M. K. Zhitinskaya*, S. A. Nemov*, T. E. Svechnikova, and E. Müller*****

**St. Petersburg State Polytechnical University, St. Petersburg, 195251 Russia*

***Baikov Institute for Metallurgy and Materials Science, Russian Academy of Sciences, Moscow, 117334 Russia*

****German Aerospace Center, Institute of Materials Research, D-51170 Cologne, Germany*

Submitted May 19, 2003; accepted for publication May 21, 2003

Abstract—The conductivity σ_{11} and Seebeck (S_{11}), Hall (R_{321}), and Nernst–Ettingshausen (Q_{123}) coefficients have been studied in Sn-doped $Bi_2Te_{3-x}Se_x$ ($x = 0.06, 0.12$) solid solutions in the temperature range 77–400 K. The homogeneity of the crystals was studied with a micro-thermal probe at room temperature. Specific features associated with resonance states were observed in the temperature dependences of kinetic coefficients. The data indicate the presence of impurity states of Sn on the background of the valence band. High electrical homogeneity and improved distribution of components throughout the bulk are observed in solid solutions with the Fermi level stabilized at the energy level of Sn impurity states. *© 2004 MAIK "Nauka/Interperiodica".*

1. INTRODUCTION

$Bi_2Te_{3-x}Se_x$ solid solutions are efficient materials for thermoelectric devices. These compounds belong to crystals of a trigonal crystal system with a strong anisotropy of physical properties. In real growth conditions, even the best single crystals of this compound contain multiple heterogeneities, which impair the technical characteristics of thermoelectric devices. Therefore, the search for new ways of homogenizing crystals with the aim of improving their thermoelectric properties is a problem of current practical relevance.

A new untraditional area of research to improve thermoelectric characteristics is to use the unusual properties of crystals with resonant states of Sn in the valence band of Bi_2Te_3. As shown in [1–5], resonant states of Sn considerably modify the electrical properties of Bi_2Te_3 crystals. In particular, the presence of these states improves the electrical homogeneity of the crystals [5]. However, for practical use, the effect of Sn atoms on the thermoelectric properties of Bi_2Te_3-based solid solutions must be investigated.

We have investigated the effect of Sn atoms on the physical properties of single crystals of *p*-$Bi_2Te_{3-x}Se_x$ solid solutions. The following kinetic coefficients were studied: conductivity σ_{11} and Seebeck (S_{11}), Hall (R_{321}), and Nernst–Ettingshausen (Q_{123}) coefficients in the temperature range 77–400 K. The distribution of the Seebeck coefficient over the surface of a crystal was measured with a microthermal probe.

2. EXPERIMENTAL

Samples were grown by the Czochralski technique with the liquid phase replenished from a floating crucible [6]. Since the crystal structure of Bi_2Te_3 and its solid solutions is complex, special procedures were developed for the appropriate choice of growth parameters (pulling velocity, seed and crucible, speed of rotation, temperature gradient at the crystallization front) in order to ensure the fabrication of perfect crystals. Single crystals were grown in the [1010] direction, normal to the principal crystal axis C_3. The stock was composed of Bi, Te, and Sn of 99.9999% purity. The sample composition was described by the formula $Bi_{2-y}Sn_yTe_{3-x}Se_x$ with $x = 0.06$ and 0.12; $y = 0$ and 0.01 ($y = 0.01$ corresponds to atomic concentration of 6×10^{19} cm^{-3}). The tin content was determined by plasma atomic-absorption spectroscopy. Samples for electrical measurements were cut at a distance of 70–90 mm from the end of an ingot. The perfection of single crystals was monitored by X-ray diffraction topography.

Independent components of kinetic tensors were measured: conductivity σ_{11} and Seebeck (S_{11}), Hall (R_{321}), and Nernst–Ettingshausen (Q_{123}) coefficients. In this notation, axis C_3 corresponds to crystal trigonal axis C_3. The subscripts of the coefficients indicate the direction of the measured electric field (first), that of the current or temperature gradient (second), and that of the magnetic field (third). In studying the Hall and Nernst–Ettingshausen effects, we have applied special methods to minimize the parasitic nonisothermal components of the effects, which might otherwise make a significant contribution to the total measured effect in thermoelectric materials.

It is known that the Seebeck coefficient is sensitive to fluctuations of the carrier density. Therefore, the character of the carrier spatial distribution can be judged from the microthermoelectric power measured at multiple points on the crystal's surface. The thermoelectric power distribution over the surface of $Bi_{2-y}Sn_yTe_{3-x}Se_x$ single

crystals was studied using a microprobe method described in [7]. The method uses a temperature difference of 3–5 K. The relative error in the thermoelectric power is less than 1%. The technique of studying the local Seebeck coefficient using a scanning thermal probe was derived as a method for monitoring and characterizing the distribution of electrically active components in V–VI semiconductor compounds. The principal advantages of this technique are the simplicity of the measuring process and the high resolution.

3. RESULTS AND DISCUSSION

The obtained experimental data on the transport phenomena show that the tin doping of $Bi_{2-y}Sn_yTe_{3-x}Se_x$ not only changes the numerical values of all the kinetic coefficients, but modifies the character of their temperature dependences (Figs. 1a–1d). The specific features observed in the electrical properties of crystals are as follows.

1. Temperature dependences of the Hall coefficient R_{321} (Fig. 1b) change from "conventional," for undoped solid solutions (curves *1*, *2*), to strongly decreasing as the temperature rises, for Sn-doped samples (curves *4*, *5*).

2. Temperature dependences of the Seebeck coefficient S_{11} for Sn-doped samples are more gently sloping than for undoped samples. It is also seen in Fig. 1c that Sn doping raises the Seebeck coefficient at $T < 200$ K and at $T > 380$ K.

3. In Sn-doped samples, the Hall and Nernst mobilities of holes in the cleavage plane, μ_H and μ_N, are considerably reduced in the range from liquid nitrogen temperature to 200 K (μ_N was determined from $Q_{123}e/k$ (Fig. 1d); here, k is the Boltzmann constant).

The specifics of the experimental data on kinetic effects in the $Bi_{2-y}Sn_yTe_{3-x}Se_x$ solid solutions under study can be attributed to resonant impurity states of Sn on the background of the valence band, similar to those in Sn-doped p-Bi_2Te_3. These states are partially filled with electrons. The occupancy of impurity states changes with increasing temperature, which results in the modification of the temperature dependences of the Seebeck and Hall coefficients as compared with undoped solid solutions. In terms of this model, the decrease in the Hall and Nernst mobilities μ_H and μ_N can be related to additional scattering of holes in the band of Sn states (similar to resonant scattering of holes in PbTe on Tl impurities [8]).

If a peak of resonant states exists in the valence band, effects related to pinning of the Fermi level ε_F are to be expected. In this context, we have studied the distribution of thermoelectric power over the surface of $Bi_{2-y}Sn_yTe_{3-x}Se_x$ single crystals using a micro-thermal probe. The results are shown in Fig. 2. The comparison of data obtained for undoped and Sn-doped $Bi_2Te_{2.94}Se_{0.06}$ and $Bi_{1.99}Sn_{0.01}Te_{2.94}Se_{0.06}$ solid solutions (Fig. 2a, 2b), as well as $Bi_2Te_{2.88}Se_{0.12}$ and $Bi_{1.99}Sn_{0.01}Te_{2.88}Se_{0.12}$ (Fig. 2c, 2d), shows that, in

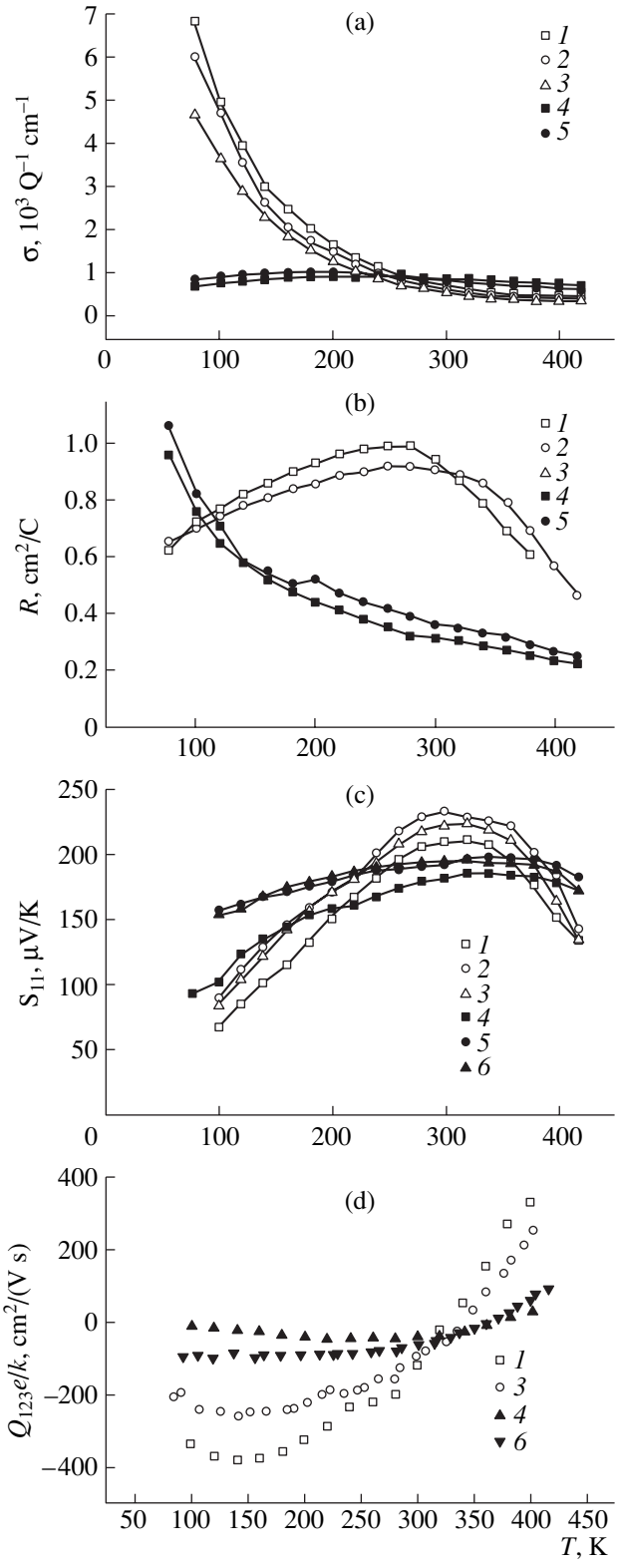

Fig. 1. Temperature dependences of kinetic coefficients: (a) conductivity σ_{11} and (b) Hall (R_{321}), (c) Seebeck (S_{11}), and (d) Nernst–Ettingshausen ($Q_{123}e/k$) coefficients for undoped samples: (*1*) Bi_2Te_3, (*2*) $Bi_2Te_{2.94}Se_{0.06}$, and (*3*) $Bi_2Te_{1.88}Se_{0.12}$; (*4*–*6*) for samples doped with 1 at % tin.

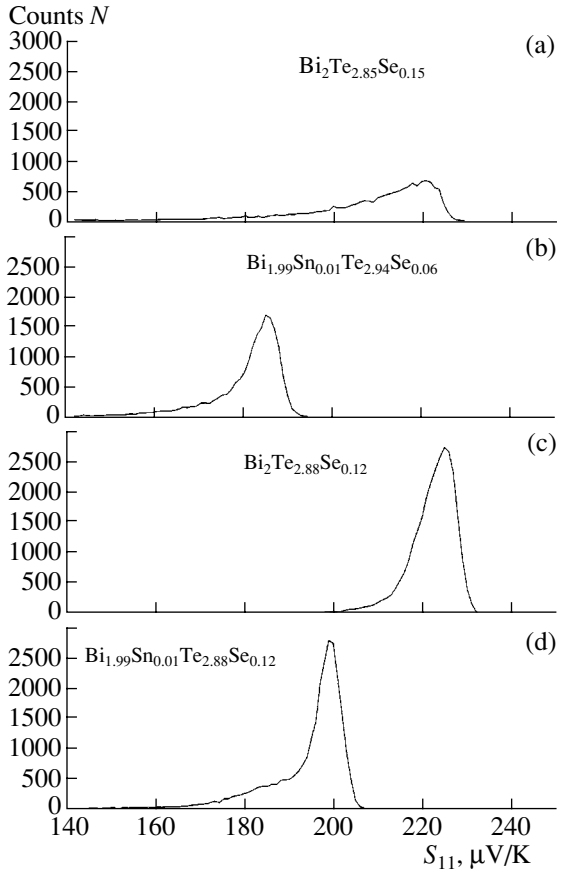

Fig. 2. Distribution of counts N in measurements of the Seebeck coefficient for undoped samples of (a) $Bi_2Te_{2.94}Se_{0.06}$ and (c) $Bi_2Te_{2.88}Se_{0.12}$; (b, d) for samples doped with 1 at % tin.

doped samples, the fluctuations of thermoelectric power are considerably weaker, and the distribution of thermoelectric power is narrowed.

It is worth noting that, as a rule, the introduction of ordinary dopants in semiconductors results in a considerable increase in thermoelectric power fluctuations, related to random distribution of impurities. However, in the case of doping with impurities producing resonant states, such as Sn in Bi_2Te_3 [3, 5] or Tl and In in PbTe [6], crystals are evidently homogenized. The point is that, as mentioned above, resonant states are only partially filled with electrons and, when electrically active intrinsic defects, donors or acceptors, are formed, these states are either additionally filled or partially depleted. If the amount of intrinsic defects or additional impurities is less than that of the introduced tin, the Fermi level remains stabilized within the peak of resonant states. It is this fact that is the reason for the higher homogeneity of the crystals in question.

This conclusion was confirmed by X-ray fluorescence microanalysis of the uniformity of distribution of the basic elements Bi and Te in these crystals [9]. Doping with Sn does not induce any noticeable nonuniformity in the elemental distribution; on the contrary, it reduces the composition fluctuations for base elements.

Further, X-ray photoelectron spectroscopy of $Bi_2Te_{2.94}Se_{0.06}$, $Bi_2Te_{2.88}Se_{0.12}$, $Bi_{1.99}Sn_{0.01}Te_{2.94}Se_{0.06}$, and $Bi_{1.99}Sn_{0.01}Te_{2.88}Se_{0.12}$ single crystals has shown that doping with Sn raises the electron density near the Fermi level [9]; the effect was similar to that observed in doping bismuth telluride with tin [4].

4. CONCLUSION

Experimental data on the kinetic effects in the $Bi_{2-y}Sn_yTe_{3-x}Se_x$ solid solutions studied indicate the presence of resonant states of Sn impurity on the background of the valence band.

$Bi_{2-y}Sn_yTe_{3-x}Se_x$ single crystals exhibit a high homogeneity of electrical properties. The Seebeck coefficient, which is sensitive to fluctuations in the charge density, features a high stability even with an enhanced content of Sn impurity.

REFERENCES

1. V. A. Kulbachinskii, N. B. Brandt, P. A. Cheremnykh, *et al.*, Phys. Status Solidi B **150**, 237 (1988).
2. G. T. Alekseeva, P. P. Konstantinov, V. A. Kutasov, *et al.*, Fiz. Tverd. Tela (St. Petersburg) **38**, 2998 (1996) [Phys. Solid State **38**, 1639 (1996)].
3. M. K. Zhitinskaya, S. A. Nemov, and T. E. Svechnikova, Fiz. Tverd. Tela (St. Petersburg) **40**, 1428 (1998) [Phys. Solid State **40**, 1297 (1998)].
4. I. V. Gasenkova, M. K. Zhitinskaya, S. A. Nemov, and T. E. Svechnikova, Fiz. Tverd. Tela (Leningrad) **41**, 1969 (1999) [Phys. Solid State **41**, 1805 (1999)].
5. M. K. Zhitinskaya, S. A. Nemov, T. E. Svechnikova, *et al.*, Fiz. Tekh. Poluprovodn. (St. Petersburg) **34**, 1417 (2000) [Semiconductors **34**, 1363 (2000)].
6. T. E. Svechnikova, S. N. Chizhevskaya, and N. V. Polikarpova, Izv. Akad. Nauk SSSR, Neorg. Mater. **23**, 1128 (1987).
7. P. Reinshaus, H. Sussmann, M. Bohm, *et al.*, in *Proceedings of 2nd Symposium on Thermoelectrics: Materials, Processing Techniques and Applications* (Dresden, 1994), p. 90.
8. I. V. Gasenkova, V. A. Chubarenko, E. A. Tyavlovskaya, and T. E. Svechnikova, Fiz. Tekh. Poluprovodn. (St. Petersburg) **37**, 661 (2003) [Semiconductors **37**, 636 (2003)].
9. V. I. Kaĭdanov, S. A. Nemov, and Yu. I. Ravich, Fiz. Tekh. Poluprovodn. (St. Petersburg) **26**, 201 (1992) [Sov. Phys. Semicond. **26**, 113 (1992)].

Translated by D. Mashovets

Semiconductors, Vol. 38, No. 2, 2004, pp. 185–188. Translated from Fizika i Tekhnika Poluprovodnikov, Vol. 38, No. 2, 2004, pp. 190–193.

ELECTRONIC AND OPTICAL PROPERTIES OF SEMICONDUCTORS

Observation of the Bose Condensation of Cooper Pairs in $(Pb_{1-x}Sn_x)_{1-z}In_zTe$ Semiconductor Solid Solutions

S. A. Nemov*, P. P. Seregin*, V. P. Volkov*, N. P. Seregin, and D. V. Shamshur*****

**St. Petersburg Polytechnical University, ul. Politekhnicheskaya 29, St. Petersburg, 195251 Russia*

***Institute for Analytical Instrumentation, Russian Academy of Sciences, Rizhskiĭ pr. 26, St. Petersburg, 198103 Russia*

****Ioffe Physicotechnical Institute, Russian Academy of Sciences, ul. Politekhnicheskaya 26, St. Petersburg, 194021 Russia*

Submitted June 9, 2003; accepted for publication June 18, 2003

Abstract—Emission Mössbauer spectroscopy based on the isotope $^{73}As(^{73}Ge)$ is used to ascertain that the superconducting phase transition in $(Pb_{1-x}Sn_x)_{1-z}In_zTe$ solid solutions (the phase-transition temperature ~4 K) is accompanied by an increase in the electron density at cationic sites, whereas this density at anionic sites remains unchanged. © *2004 MAIK "Nauka/Interperiodica".*

The phase transition of semiconductors to the superconducting state typically occurs at temperatures of 0.1–0.5 K [1]; in this respect, $(Pb_{1-x}Sn_x)_{1-z}In_zTe$ semiconductor solid solutions are an exception since the critical temperature for these solutions is $T_c \approx 4$ K [2].

According to the Bardeen–Cooper–Schrieffer (BCS) theory, the phenomenon of superconductivity is attributed to the formation of a Bose condensate of Cooper pairs; the distribution of electron density at the lattice sites is different at temperatures lower and higher than the temperature of transition to the superconducting state [3]. A promising approach to studying the properties of the Bose condensate consists in using the Mössbauer effect to gain insight into characteristics of superconducting materials: in principle it is possible to detect the process of condensation of Cooper pairs by measuring the temperature dependence of the centroid S in the Mössbauer spectra [4]. However, attempts to detect the formation of Cooper pairs and their Bose condensation both in conventional (of the Nb_3Sn type [5]) and high-temperature (of the $YBa_2Cu_3O_7$ type [6]) superconductors by measuring the temperature dependence of the centroid in the Mössbauer spectra of ^{119}Sn and ^{57}Fe failed; this was attributed to the low resolution of Mössbauer spectroscopy based on these isotopes. In this context, it was suggested that emission Mössbauer spectroscopy based on a ^{67}Zn probe be used in order to determine the variation in the electron density in the course of a superconducting transition [4]. However, it was shown that the observed variation in the electron density at the ^{67}Zn nuclei depended on the phase-transition temperature T_c. This circumstance leads to certain problems in the observation of variations in the electron density using EMS based on the isotope ^{67}Zn in superconductors with a phase-transition temperature below 20 K [7].

Taking the above into account, EMS based on the isotope ^{73}Ge [8] was suggested for studying the Bose condensation of Cooper pairs in materials of the $(Pb_{1-x}Sn_x)_{1-z}In_zTe$ type; the resolution of this isotope is at least 2000 times greater than that provided by the isotopes ^{57}Fe and ^{119}Sn. In Fig. 1, we illustrate the formation of the Mössbauer ^{73}Ge level as a result of radioactive decay of the parent ^{73}As isotope: electron capture by the parent ^{73}As nucleus is accompanied by emission of a neutrino. Calculations show that the recoil energy for the daughter ^{73}Ge atoms does not exceed the recoil energy for atoms at the conventional lattice sites. Thus, one may expect that the radioactive transmutation does not bring about a displacement of germanium atoms from conventional lattice sites. Consequently, the parameters of the ^{73}As (^{73}Ge) emission Mössbauer spectra should be sensitive to the state of ^{73}Ge atoms localized in either cationic or anionic sublattices.

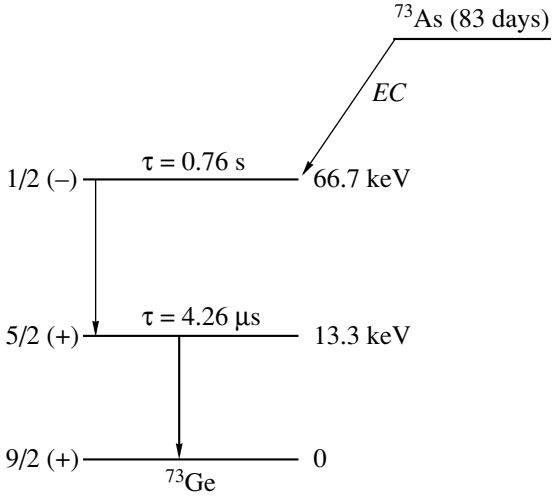

Fig. 1. Schematic representation of ^{73}As decay.

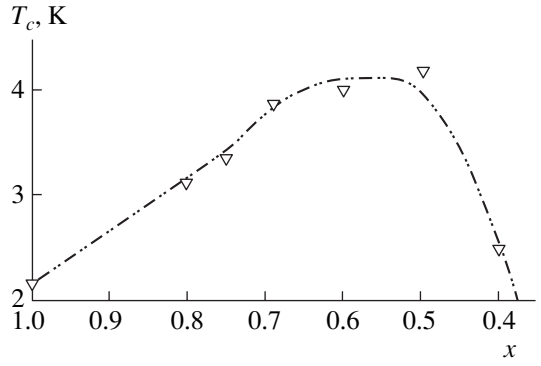

Fig. 2. Dependence of the superconducting-transition temperature T_c on the composition of the $(Pb_{1-x}Sn_x)_{0.84}In_{0.16}Te$ solid solution.

The radioactive isotope ^{73}As was obtained using the $^{74}Ge(p, 2n)^{73}As$ reaction, whereas the method based on the large difference between the volatilities of arsenic and parent atoms was used to separate the carrier-free ^{73}As agent. To this end, a germanium film that was irradiated with protons and contained ~98% ^{74}Ge isotope was aged for three months (in order to reduce the content of radioactive ^{74}As isotope in the film) and was finally installed in an evacuated quartz cell; the cell's end containing the target was then heated to 900 K for 5 h in a tubular furnace. After the cell was opened, ~80% of ^{73}As atoms were adsorbed at the inner wall of the quartz cell, and the carrier-free ^{73}As preparation was removed using a nitric acid solution.

In Fig. 2, we show the dependence of the temperature that corresponds to the superconducting phase transition on the composition (x) of the $(Pb_{1-x}Sn_x)_{0.84}In_{0.16}Te$ solid solutions. Taking into account this dependence, we chose two compounds to study: $(Pb_{0.4}Sn_{0.6})_{0.84}In_{0.16}Te$ and $(Pb_{0.5}Sn_{0.5})_{0.84}In_{0.16}Te$; these compounds were transformed into the superconducting state at $T_c \approx 4.2$ K. The $(Pb_{0.4}Sn_{0.6})_{0.97}In_{0.03}Te$ solid solution was chosen as the control sample; this solid solution remained in the normal state at a temperature as low as 2 K. The Mössbauer sources were prepared by the diffusion-induced doping of polycrystalline $(Pb_{1-x}Sn_x)_{1-z}In_zTe$ samples with the radioactive isotope ^{73}As in quartz cells for 10 h at 500°C; the concentration of arsenic impurity atoms did not exceed 10^{16} cm^{-3}. For such a low impurity concentration, one should not expect changes in the value of T_c; as a result, the control experiments showed that the aforementioned diffusion-inducing annealing did not appreciably affect the value of T_c for the $(Pb_{0.4}Sn_{0.6})_{0.84}In_{0.16}Te$ and $(Pb_{0.5}Sn_{0.5})_{0.84}In_{0.16}Te$ samples.

The Mössbauer spectra of ^{73}As (^{73}Ge) were measured using a commercial SM-2201 spectrometer in the conventional configuration of transmission. The absorbers were either single-crystal ^{73}Ge (to detect the spectra for a ^{73}Ge probe in the anionic sublattice) or $^{73}GeTe$ (to detect the spectra for a ^{73}Ge probe in the cationic sublattice). All the absorbers were enriched with the isotope ^{73}Ge by ~90%.

The Mössbauer spectra of the $(Pb_{0.4}Sn_{0.6})_{0.84}In_{0.16}Te$:$^{73}As$, $(Pb_{0.5}Sn_{0.5})_{0.84}In_{0.16}Te$:$^{73}As$, and $(Pb_{0.4}Sn_{0.6})_{0.97}In_{0.03}Te$:$^{73}As$ sources in the temperature range 2–297 K are represented by individual lines. It is significant that the width of the spectra considerably exceeds the natural width of the spectral line for ^{73}Ge ($G_{exp} \approx 50$ μm/s for the spectra measured using the GeTe absorber, and $G_{exp} \approx 100$ μm/s for the spectra measured using the Ge absorber). In the case of the $^{73}GeTe$ absorber, the broadening of the spectrum is mainly caused by a distortion of the cubic symmetry in the local surroundings of germanium atoms in the GeTe lattice.

The spectra obtained using the ^{73}Ge absorber should be attributed to the $^{73}Ge^0$ centers in the anionic sublattice of the $(Pb_{1-x}Sn_x)_{1-z}In_zTe$ solid solutions (lead atoms are found in the close vicinity of these centers); the $^{73}Ge^0$ atoms are formed as a result of decay of ^{73}As atoms that reside in the anionic sublattice of $(Pb_{1-x}Sn_x)_{1-z}In_zTe$. The spectrum obtained with the $^{73}GeTe$ absorber should be attributed the $^{73}Ge^{2+}$ centers in the cationic sublattice of $(Pb_{1-x}Sn_x)_{1-z}In_zTe$ (tellurium atoms are nearest neighbors of these centers); the $^{73}Ge^{2+}$ atoms are formed as a result of a decay of ^{73}As atoms that reside in the cationic sublattice of $(Pb_{1-x}Sn_x)_{1-z}In_zTe$. Thus, we may conclude that arsenic impurity atoms in the $(Pb_{1-x}Sn_x)_{1-z}In_zTe$ can be found in both anionic and cationic sublattices. It is noteworthy that such behavior is characteristic in general of Group V impurities in lead chalcogenides [9, 10].

As mentioned above, it is necessary to measure the temperature dependence of the centroid S of the Mössbauer spectrum in order to detect the Bose condensation of Cooper pairs using Mössbauer spectroscopy; this dependence has the following form at a constant pressure P:

$$\left(\frac{\delta S}{\delta T}\right)_P = \left(\frac{\delta I}{\delta \ln V}\right)_T \left(\frac{\delta \ln V}{\delta T}\right)_P + \left(\frac{\delta D}{\delta T}\right)_P + \left(\frac{\delta I}{\delta T}\right)_V. \quad (1)$$

The first term in formula (1) accounts for the dependence of isomer shift I on the volume V, the second term represents the second-order Doppler shift D, and the third term describes the temperature dependence of the isomer shift I. It is the third term that accounts for the variation in the electron density at the Mössbauer nuclei as the host crystal is transformed into the superconducting state [11]; i.e.,

$$I = \alpha \Delta |\Psi(0)|^2. \quad (2)$$

Here, $\Delta|\Psi(0)|^2$ is the difference between electron densities at the nuclei under investigation in two samples and α is a constant that depends on the nuclear parameters of the isotope employed.

As can be seen from Figs. 3 and 4, the experimental temperature dependence of the centroid S of the spec-

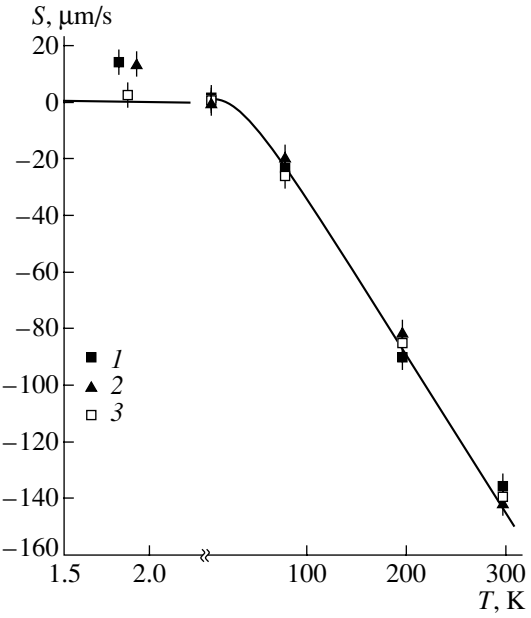

Fig. 3. Temperature dependences of the centroid S of Mössbauer spectra for ^{73}Ge at cationic sites in (*1*) $(Pb_{0.4}Sn_{0.6})_{0.84}In_{0.16}Te$, (*2*) $(Pb_{0.5}Sn_{0.5})_{0.84}In_{0.16}Te$, and (*3*) $(Pb_{0.4}Sn_{0.6})_{0.97}In_{0.03}Te$ solid solutions; the variations were measured relative to their values at 4.2 K. The solid line represents the theoretical temperature dependence of S for the case of the second-order Doppler shift at $\theta = 130$ K.

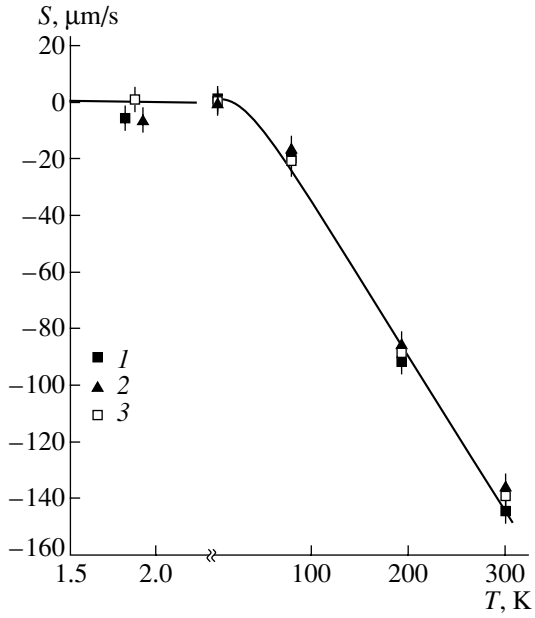

Fig. 4. Temperature dependences of the centroid S of Mössbauer spectra for ^{73}Ge at anionic sites in the (*1*) $(Pb_{0.4}Sn_{0.6})_{0.84}In_{0.16}Te$, (*2*) $(Pb_{0.5}Sn_{0.5})_{0.84}In_{0.16}Te$, and (*3*) $(Pb_{0.4}Sn_{0.6})_{0.97}In_{0.03}Te$ solid solutions; the variations were measured relative to their values at 4.2 K. The solid line represents the theoretical temperature dependence of S in the case of the second-order Doppler shift at $\theta = 130$ K.

trum that corresponds to the ^{73}Ge probe in the cationic and anionic sublattices of the $(Pb_{0.4}Sn_{0.6})_{0.97}In_{0.03}Te$:^{73}As solid solution coincides with the theoretical temperature dependence of the second-order Doppler shift in the temperature range 2–297 K; this theoretical dependence is given by [11]

$$\left(\frac{\delta D}{\delta T}\right)_P = -\frac{3kE_0}{2Mc^2}F\left(\frac{T}{\theta}\right), \qquad (3)$$

where k is the Boltzmann constant, E_0 is the energy of isomeric transition, M is the mass of the probe nucleus, c is the speed of light in free space, θ is the Debye temperature, and $F(T/\theta)$ is the Debye function. Agreement between theory and experiment is ensured if Debye temperatures determined from measurements of the heat capacity [12] are used.

As can be seen from Fig. 3, the dependence $S(T)$ for the spectra that correspond to the ^{73}Ge probe in the cationic sublattice of superconducting $(Pb_{1-x}Sn_x)_{1-z}In_zTe$ solid solutions is also accounted for by the second-order Doppler shift (3) at $T > T_c$; however, in the temperature region $T < T_c$, the value of S depends on temperature more strongly than follows from formula (3). Evidently, we should take into account the temperature dependence of the isomer shift in expression (1): the transition to the superconducting state is accompanied by an increase in the electron density at the ^{73}Ge nuclei in the cationic sublattice.

A different situation occurs in the case of a ^{73}Ge probe in the anionic sublattice of superconducting $(Pb_{1-x}Sn_x)_{1-z}In_zTe$ solid solutions. As can be seen from Fig. 4, the experimental temperature dependence of the spectrum centroid S virtually coincides in this case with the theoretical temperature dependence of the second-order Doppler shift in the temperature range 2–297 K. Consequently, for ^{73}Ge atoms in the anionic sublattice, a variation in the electron density at ^{73}Ge nuclei is not observed as a result of the transition of the compound to the superconducting state; at least, this variation cannot be detected using Mössbauer spectroscopy on the basis of the isotope ^{73}Ge. Similar behavior was observed in the emission Mössbauer spectra of ^{67}Cu(^{67}Zn) in high-temperature superconductors based on copper metal oxides; i.e., a variation in the electron density formed by the Bose condensate of the Cooper pairs for crystals that contained two structurally nonequivalent sites for copper atoms was found to be different for these sites. This behavior was interpreted as proof of the spatial nonuniformity of the Bose condensate of Cooper pairs [7]. Evidently, spatial nonuniformity of the Bose condensate (the variation in the electron density in the transition from the normal state to the superconducting state is much larger for the cationic sublattice than for the anionic sublattice) also occurs for lattices of $(Pb_{1-x}Sn_x)_{1-z}In_zTe$ solid solutions.

This study was supported by the Russian Foundation for Basic Research, project no. 02-02-17306.

REFERENCES

1. M. Cohen, G. Gladstone, M. A. Jensen, and J. R. Schrieffer, in *Superconductivity*, Ed. by R. Parks (Marcel Dekker, New York, 1969; Mir, Moscow, 1972).
2. R. V. Parfeniev, D. V. Shamshur, and M. F. Shakhov, J. Alloys Compd. **219**, 313 (1995).
3. J. R. Schrieffer, *Theory of Superconductivity* (Benjamin, New York, 1964; Nauka, Moscow, 1970).
4. N. P. Seregin and P. P. Seregin, Zh. Éksp. Teor. Fiz. **118**, 1421 (2000) [JETP **91**, 1230 (2000)].
5. J. S. Shier and R. D. Taylor, Phys. Rev. **174**, 346 (1968).
6. Y. Wu, S. Pradhan, and P. Boolchand, Phys. Rev. Lett. **67**, 3184 (1991).
7. N. P. Seregin, Fiz. Tverd. Tela (St. Petersburg) **45**, 12 (2003) [Phys. Solid State **45**, 11 (2003)].
8. S. A. Nemov, P. P. Seregin, Yu. V. Kozhanova, *et al.*, Fiz. Tverd. Tela (St. Petersburg) **45**, 1938 (2003) [Phys. Solid State **45**, 2036 (2003)].
9. S. A. Nemov, P. P. Seregin, S. M. Irkaev, and N. P. Seregin, Fiz. Tekh. Poluprovodn. (St. Petersburg) **37**, 279 (2003) [Semiconductors **37**, 263 (2003)].
10. S. A. Nemov and P. A. Osipov, Fiz. Tekh. Poluprovodn. (St. Petersburg) **35**, 731 (2001) [Semiconductors **35**, 700 (2001)].
11. D. L. Nagy, in *Mössbauer Spectroscopy of Frozen Solutions*, Ed. by A. Vértes and D. L. Nagy (Akadémiai Kiadó, Budapest, 1990; Mir, Moscow, 1998).
12. Yu. I. Ravich, B. A. Efimova, and I. A. Smirnov, *Semiconducting Lead Chalcogenides* (Nauka, Moscow, 1968; Plenum, New York, 1970).

Translated by A. Spitsyn

Semiconductors, Vol. 38, No. 2, 2004, pp. 189–191. Translated from Fizika i Tekhnika Poluprovodnikov, Vol. 38, No. 2, 2004, pp. 194–196.

ELECTRONIC AND OPTICAL PROPERTIES OF SEMICONDUCTORS

Substitutional 3*d* Impurities in Cubic Silicon Carbide

I. I. Parfenova

St. Petersburg State Electrotechnical University, St. Petersburg, 197376 Russia

e-mail: SiC.Me@eltech.ru; iparf@hotbox.ru

Submitted March 11, 2003; accepted for publication June 26, 2003

Abstract—The transition-metal impurities that replace silicon atoms in silicon carbide are studied using the semiempirical tight-binding method. It is shown that exchange-induced splitting affects the arrangement of levels and leads to the fulfillment of Hund's rules for the main impurities. The effective impurity charge is found to depend only slightly on the corresponding charge state. Calculated energy levels are compared with relevant experimental data. © *2004 MAIK "Nauka/Interperiodica".*

1. INTRODUCTION

The behavior of a number of 3*d* transition-metal impurities in semiconductors, in particular, silicon [1–3] and III–V semiconductors (GaP [2, 4], GaAs [3, 5, 6], and InP [4]), were studied intensively in the 1980s (see the comprehensive reviews [7, 8]). The transition-metal impurities in silicon carbide have been considered in only a few papers [9–12], and the authors of these studies disagreed concerning both the site occupied by the impurity and the energy structure of the impurity states. In addition, the charge state of impurities was not considered [9–12], which complicated the interpretation of experimental data. In this paper, the results of studying the 3*d* substitutional impurities in silicon carbide in the context of a semiempirical tight-binding model are reported.

2. A MODEL FOR CALCULATION

A small cluster consisting of an impurity atom, four nearest carbon atoms, and 12 silicon atoms as the next-nearest neighbors was considered. The formation of such a cluster was envisaged as a removal of the central silicon atom resulting in the formation of a vacancy and the subsequent accommodation of an impurity atom at this site. In this simple model, the *d* states with *e* symmetry do not interact with the vacancy and have the energy E_d. Energies of other states of the impurity were determined by diagonalizing a matrix of the type

$$\begin{bmatrix} E_s & 0 & V_{2s} & 0 \\ 0 & E_d & 0 & V_{2d} \\ V_{2s} & 0 & E_{va} & 0 \\ 0 & V_{2d} & 0 & E_{vt} \end{bmatrix}, \quad (1)$$

where E_s and E_d are the energies of the *s* and *d* orbitals of a transition-metal atom; E_{va} and E_{vt} are the energies of the vacancy states with symmetries a_1 and t_2, respectively; and V_{2s} and V_{2d} represent potentials of interaction between the above states. It was assumed that redistribution of the electronic charge of ligands and variation in the electron occupancy of the *d* impurity orbitals brought about a linear shift of the energies of the vacancy and *d* orbitals. It was also assumed that there was a linear dependence of this shift on the electron occupancy. Taking into account the multiple-electron interactions and using the approach suggested by

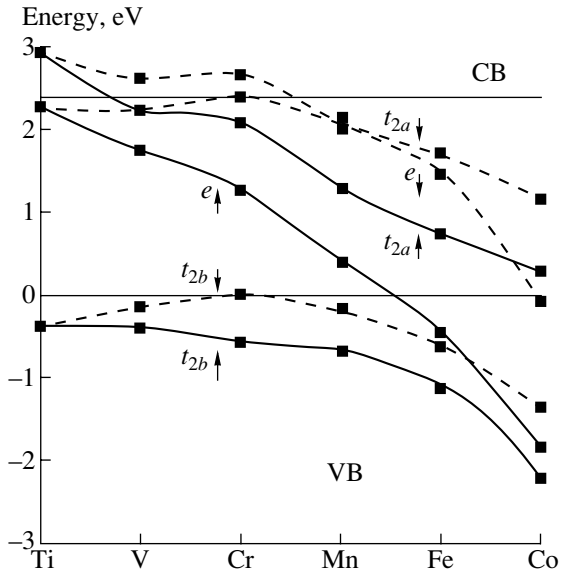

Spin-polarized energy levels of 3*d* impurities in 3*C* SiC. The energy is reckoned from the top of the valence band. The lines are drawn to make it easier to trace the shift of states: the solid lines represent states with the spin oriented upward, while the dashed lines represent states with the spin oriented downward. The bonding (~–5 eV) and antibonding (~11 eV) states formed by the a_1 states of the vacancy and 4*s* states of transition metal are not shown. The notation CB stands for the conduction band, and VB stands for the valence band.

1063-7826/04/3802-0189$26.00 © 2004 MAIK "Nauka/Interperiodica"

Energies of impurity levels and total spin S for transition-metal impurities in cubic silicon carbide

Transition metal	S		Energy, eV			
			$e\uparrow$	$e\downarrow$	$t_{2a}\uparrow$	$t_{2a}\downarrow$
Ti^{2+}	*	1	1.195	1.745	2.316	2.593
Ti^{+}	*	1/2	1.798	2.027	2.645	2.761
Ti^{0}	*	0	2.283	2.283	2.937	2.937
Ti^{-}	*	1/2	3.163	3.685	3.597	3.860
Ti^{2-}	*	1	4.421	5.466	4.718	5.246
V^{2+}	*	1/2	0.501	0.818	1.710	1.870
V^{+}	*	0	1.070	1.070	1.977	1.977
V^{0}	*	1/2	1.742	2.251	2.374	2.631
V^{-}	*	1	2.505	3.524	2.930	3.443
V^{2-}	max	3/2	3.378	4.821	3.670	4.397
Cr^{2+}	*	0	−0.080	−0.080	1.403	1.403
Cr^{+}	*	1/2	0.619	1.190	1.709	1.996
Cr^{0}	*	1	1.274	2.417	2.085	2.660
Cr^{-}	max	3/2	1.784	3.305	2.426	3.192
Cr^{2-}	max	2	2.533	4.561	3.014	4.036
Mn^{2+}	*	1/2	−0.587	0.076	0.857	1.190
Mn^{+}	*	1	0.053	1.380	1.110	1.776
Mn^{0}	max	3/2	0.400	2.036	1.287	2.108
Mn^{-}	max	2	0.813	2.873	1.520	2.554
Mn^{2-}	max	5/2	1.382	4.061	1.901	3.246
Fe^{2+}	*	1	–1.072	0.377	0.495	1.222
Fe^{+}	max	3/2	−0.771	0.873	0.617	1.442
Fe^{+}	min	1/2	−0.270	0.545	0.781	1.145
Fe^{0}	max	2	−0.441	1.466	0.754	1.710
Fe^{0}	min	0	0.422	0.422	1.122	1.122
Fe^{-}	max	5/2	−0.063	2.227	0.921	2.069
Fe^{-}	min	1/2	0.823	1.282	1.373	1.603
Fe^{2-}	max	2	0.958	3.121	1.491	2.576
Co^{2+}	min	1/2	–1.352	–0.599	0.208	0.586
Co^{+}	min	0	−0.569	−0.569	0.479	0.479
Co^{0}	min	1/2	−0.253	0.075	0.634	0.799
Co^{-}	max	2	−0.375	1.205	0.613	1.405
Co^{2-}	*	3/2	0.592	2.056	1.133	1.867

* Only a single configuration is possible; the notation max (min) corresponds to the situation where a configuration with maximal (minimal) spin exists.

Picoli *et al.* [13], the energies of the above states were written as

$$\begin{aligned} E_{d\uparrow} &= E_{d0} + U_d(n_d - n_{d0}) - J(n_{d\uparrow} - n_{d\downarrow})/2, \\ E_{d\downarrow} &= E_{d0} + U_d(n_d - n_{d0}) + J(n_{d\uparrow} - n_{d\downarrow})/2, \\ E_v &= E_{v0} + U_v(n_v - n_{v0}), \end{aligned} \qquad (2)$$

where n_d and n_v are the occupancies of the d orbitals and the vacancy states; U_d and U_v are the average Coulomb energies for the d electrons and the dangling bonds of the vacancy, respectively; J is the mean exchange integral for electron–electron interaction between two different d orbitals [3]; and the arrows denote the states with opposite spins.

The screening effects for an uncharged defect were taken into account assuming that the cluster was neutral. For an impurity in the charge state q, the net charge was assumed to be equal to q/ε, where ε is the permittivity.

The problem was solved self-consistently in the tight-binding approximation using the Harrison parameters [14] for the elements of matrix (1). The atomic energies corresponded to the Herman–Skillman scheme, and the electron configuration s^1d^{n-1} was assumed. The quantity U_v was evaluated using the data reported by Zywietz *et al.* [15] for a Si vacancy in silicon carbide and was assumed to be equal to 0.2 eV, which is much smaller than the value of U_d (5–6 eV [14]).

Estimation of the lattice relaxation around an impurity atom shows that the displacements are positive for Ti (0.095 Å), V (0.055 Å), and Cr (0.080 Å) and are negative for Mn (–0.008 Å), Fe (–0.06 Å), and Co (–0.002 Å). The magnitudes of these displacements are smaller than 0.01 nm, and the corresponding variations in energies are less than the calculation accuracy. Therefore, the crystal-lattice relaxation and the Jahn–Teller effect were disregarded.

3. DISCUSSION

The figure illustrates the results of calculations for neutral impurities; the results for other charged states are listed in the table. Similarly to the situation in Si and III–V semiconductors, levels e and t_{2b} correspond to atomic orbitals perturbed by the crystal field (strong localization), whereas levels t_{2a} are related to the states of the vacancy (weak localization). For elements with comparatively small atomic numbers, the levels t_{2b} are pinned in the valence band. At least one of the e levels penetrates into the band gap after Co (as in III–V compounds) in the Co–Fe–Mn–Cr–V–Ti series rather than after Fe (as in Si); however, level e is not occupied. Starting with Cr, levels t_{2a} penetrate the conduction band, which contradicts the claim [8] that these states are pinned in the band gap.

The exchange interaction is most pronounced at the midposition in the 3d series of elements. Level $e_\downarrow$ intersects level $t_{2a\uparrow}$ twice (in the vicinity of V and between Fe and Co), which results in the fulfillment of Hund's rule for main impurities. It should be noted that levels $e_\downarrow$ and $t_{2a\uparrow}$ are virtually degenerate for vanadium. If the charge state of impurity varies from (2+) to (2–), level $e_\downarrow$ intersects sequentially levels $t_{2a\uparrow}$ and $t_{2a\downarrow}$, which makes the configurations with smaller spin preferential for some of the charge states. This situation is realized for Co and Fe in SiC.

When the formal charge of impurity changes by unity, the effective charge of transition-metal atoms increases by only 0.25–0.20. For example, the electron occupancy of a Cr atom changes insignificantly (from 4.81 to 5.60) when Cr^{2+} is replaced by Cr^{2-}, which is consistent with the data for GaP:Cr (0.2–0.3) and GaAs:Cr (0.08–0.28). This behavior is ensured by the electron density redistribution that involves resonance levels in the valence band.

The energies of the levels are reckoned from the top of the valence band and are determined from experimental data. These energies were determined only for Ti (3.09–3.13 eV or 2.27–2.31 eV for the –/0 level and 1.73–1.90 eV for the 0/+ level) and for Cr (3.08–3.11 eV for the 2–/– level, 2.47–2.49 eV for the –/0 level, and 0.53–0.63 eV for the +/2+ level) [16–18]. The calculated values are in satisfactory agreement with experimental data.

ACKNOWLEDGMENTS

This study was supported by the Russian Foundation for Basic Research, project no. 01-03-33175.

REFERENCES

1. L. K. Ermakov, Fiz. Tekh. Poluprovodn. (Leningrad) **12**, 1230 (1978) [Sov. Phys. Semicond. **12**, 732 (1978)].
2. V. A. Singh and A. Zunger, Phys. Rev. B **31**, 3729 (1985).
3. C. Delerue, M. Lannoo, and G. Allan, Phys. Rev. B **39**, 1669 (1989).
4. L. K. Ermakov, V. F. Masterov, and B. E. Samorukov, Fiz. Tekh. Poluprovodn. (Leningrad) **18**, 2092 (1984) [Sov. Phys. Semicond. **18**, 1304 (1984)].
5. M. P. Il'in and V. F. Masterov, Fiz. Tekh. Poluprovodn. (Leningrad) **11**, 1470 (1977) [Sov. Phys. Semicond. **11**, 864 (1977)].
6. V. F. Masterov, Fiz. Tekh. Poluprovodn. (Leningrad) **18**, 3 (1984) [Sov. Phys. Semicond. **18**, 1 (1984)].
7. V. F. Masterov, Fiz. Tekh. Poluprovodn. (Leningrad) **12**, 625 (1978) [Sov. Phys. Semicond. **12**, 363 (1978)].
8. A. Zunger, Solid State Phys. **39**, 275 (1986).
9. P. Deak, A. Gali, and J. Miro, Mater. Sci. Forum **264–268**, 279 (1998).
10. K. O. Barbosa, W. V. Machado, and L. V. C. Assali, Physica B (Amsterdam) **308–310**, 726 (2001).
11. V. A. Gubanov, C. Boekema, and C. Y. Fong, Appl. Phys. Lett. **78**, 216 (2001).
12. N. I. Medvedeva, É. I. Yur'eva, and A. L. Ivanovskiĭ, Fiz. Tekh. Poluprovodn. (St. Petersburg) **36**, 805 (2002) [Semiconductors **36**, 781 (2002)].
13. G. Picoli, A. Chomette, and M. Lannoo, Phys. Rev. B **30**, 7138 (1984).
14. W. A. Harrison, *Elementary Electronic Structure* (World Sci., Singapore, 1999).
15. A. Zywietz, J. Furthmüller, and F. Bechstedt, Phys. Rev. B **59**, 15166 (1999).
16. A. A. Lebedev, Fiz. Tekh. Poluprovodn. (St. Petersburg) **33**, 129 (1999) [Semiconductors **33**, 107 (1999)].
17. K. F. Dombrowski, U. Kaufmann, M. Kunzer, *et al.*, Appl. Phys. Lett. **65**, 1811 (1994).
18. J. Grillenberger, N. Achtziger, and G. Pasold, Mater. Sci. Forum **389–393**, 573 (2002).

Translated by A. Spitsyn

Semiconductors, Vol. 38, No. 2, 2004, pp. 192–196. Translated from Fizika i Tekhnika Poluprovodnikov, Vol. 38, No. 2, 2004, pp. 197–201.

ELECTRONIC AND OPTICAL PROPERTIES OF SEMICONDUCTORS

The Nature of Low-Temperature Hysteresis of Hopping Magnetoresistance in Compensated Ge:Ga in the Vicinity of the Metal–Insulator Transition

S. V. Egorov*, A. G. Zabrodskiĭ, and R. V. Parfen'ev

Ioffe Physicotechnical Institute, Russian Academy of Sciences, St. Petersburg, 194021 Russia

**e-mail: Sergey.V.Egorov@mail.ioffe.ru*

Submitted June 30, 2003; accepted for publication July 1, 2003

Abstract—Earlier, the authors described the hysteresis in hopping magnetoresistance in neutron-transmutation-doped Ge:Ga. This effect, accompanied by an abrupt drop in resistivity of ~10% upon reversal of the sample's magnetization, depends on the Ga concentration and is observed at temperatures no higher than 0.7 K. The present study shows that the abrupt change in resistivity results from a momentary heating of the sample. A model is suggested according to which heat is released when the magnetization of holes localized in the Ga impurity band is reversed. The results of calculation are compared with experimental data. © *2004 MAIK "Nauka/Interperiodica".*

1. INTRODUCTION

Earlier [1], we described a new effect of hysteresis of the hopping magnetoresistance, which was observed in a set of samples of neutron-transmutation-doped Ge:Ga with the compensation $K = 0.3$ at temperatures below 0.7 K. The samples were in the insulating state, with variable-range-hopping conduction via states in the Coulomb gap in the Ga-acceptor band. The effect was maximum at the Ga concentration $N_{Ga} \approx 4 \times 10^{16}$ cm^{-3}, whereas the metal–insulator transition occurs at $N_C = 1.85 \times 10^{17}$ cm^{-3} [2]. The goal of the present study was to reveal the nature of the observed hysteresis of the hopping magnetoresistance.

2. EXPERIMENTAL MANIFESTATION OF THE EFFECT

The observed hysteresis of the hopping magnetoresistance $\rho(H)$ is accompanied by characteristic abrupt changes associated with the reversal of the sample's magnetization in the critical magnetic field H_C. The field H_C was determined for different samples from the maximum in the derivative $d\rho/dH$. Typical values of H_C were 600–850 Oe, and they varied only slightly as the impurity concentration changed. Figure 1 shows typical magnetoresistance curves for samples on the insulator side of the metal–insulator transition at $H \parallel [111]$. If we follow the change in the magnetic field (shown by the arrows), it can be seen that, after the field sign is changed, the curve shows an abrupt drop in the sample resistivity by ~10% in fields $H \approx H_C$ (points *3*, *6*), with subsequent relaxation to its equilibrium value (portions *3–4*, *6–1*). Note that the magnitude of the abrupt change in magnetoresistance, $\Delta\rho$, increases as the magnetization field increases.

As can be seen in Fig. 2, which shows how the magnitude of this change, which is associated with the hysteresis, depends on the impurity concentration, the relative change $\Delta\rho/\rho(0)$ is maximum at $N_{Ga} = 0.45N_C$. No abrupt change in resistivity is observed on the metallic side.

The hysteresis effect with an abrupt drop in the sample's resistance in the field H_C may be related to the heating of the sample when the magnetization is reversed. Since it is exponentially dependent on temperature, the activated resistivity is a good sensor of the sample temperature. A specific quantity of heat is released when the magnetization of the sample is reversed, and its resistance falls abruptly. The subsequent relaxation portion of the $\rho(H)$ dependence corre-

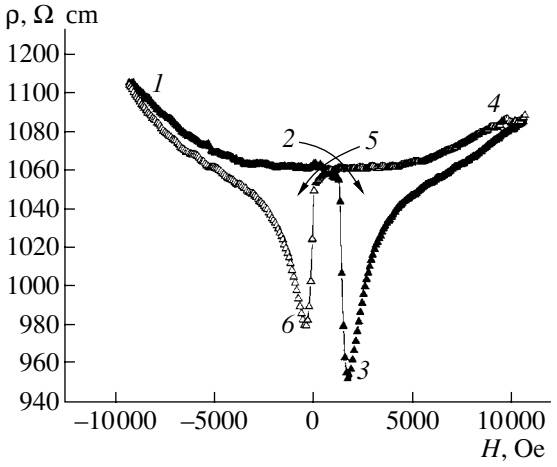

Fig. 1. Hysteresis of the magnetoresistance of sample *2*; $T = 0.45$ K and the magnetic field variation rate was 3.6 kOe/min. Arrows indicate the direction of variation.

1063-7826/04/3802-0192$26.00 © 2004 MAIK "Nauka/Interperiodica"

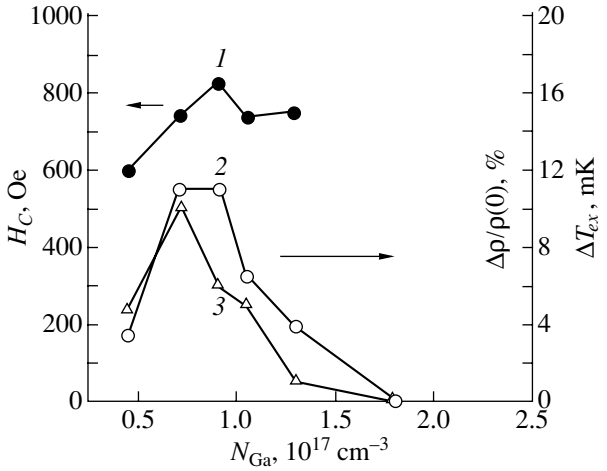

Fig. 2. Parameters characterizing the hysteresis: (*1*) critical field H_C; (*2*) experimentally determined change in temperature of Ge:Ga samples; (*3*) relative abrupt change in the resistance.

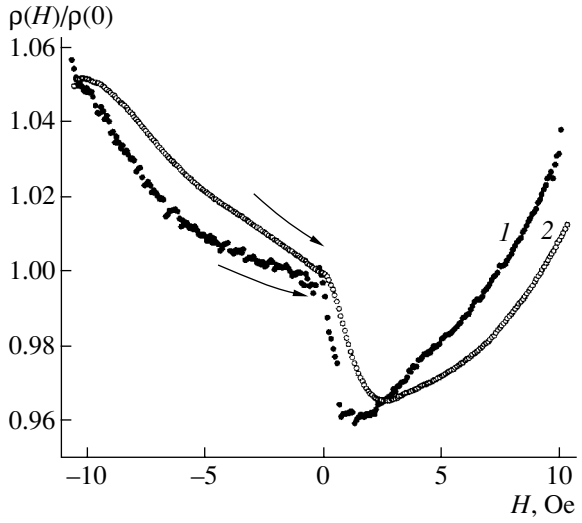

Fig. 3. Magnetoresistance of sample *2*: (*1*) exposed and (*2*) heat-insulated; T = 0.45 K.

sponds to the cooling of the sample to the temperature of a cryostat.

The thermal nature of the abrupt changes in resistance was confirmed by comparing the magnetoresistance curves of an exposed Ge sample with those for a sample placed in a heat-insulating stearin sheath. Figure 3 illustrates the results of this experiment. Compared to the curve for the exposed sample, the curve for a heat-insulated sample demonstrates a slower decrease in ρ and a longer relaxation to the equilibrium value. The explanation is that the stearin sheath raises the thermal resistance between the sample and the thermostat and, consequently, decreases the rates of the heating and cooling processes, which is manifested in the fact that the change in magnetoresistance becomes less abrupt. In an additional experiment, the rate of the magnetic field sweep near point *A*, at which the resistance is at a minimum, was reduced by a factor of 50 (Fig. 4). In this case, the relaxation portion of the magnetoresistance curve (intervals *3–4*, *6–1* in Fig. 1) transformed to a vertical line *AB*, which describes the relaxation to the equilibrium value of the magnetoresistance in a nearly constant field.

3. EXPERIMENTAL DETERMINATION OF THE MAIN PARAMETERS OF THE EFFECT

The change in temperature, ΔT_{ex}, which corresponds to the reduction of resistance in the critical magnetic field, can be determined from the temperature dependence of the sample resistance (Table 1). The dependence of ΔT_{ex} on Ga concentration is shown in Fig. 2, along with data on the magnitude of the abrupt change in magnetoresistance. The maxima in both dependences coincide. As noted below, the localization of magnetic moments and their interaction are necessary conditions for the observation of the effect. Because of this circumstance, the maximum effect is reached on the insulator side near the metal–insulator transition.

The release of a certain quantity of heat, ΔQ, within the sample corresponds to the temperature change ΔT_{ex}; this heat can be estimated based on the heat balance equation for the system including the sample and the thermostat. This quantity of heat is spent to heat the sample and the ambient cooling agent, liquid ^{3}He:

$$\Delta Q = \Delta Q_{\mathrm{Ge}} + \Delta Q_{^3\mathrm{He}}. \quad (1)$$

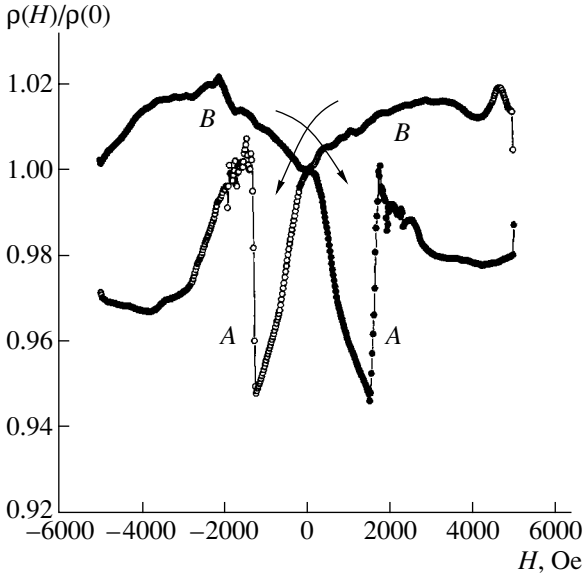

Fig. 4. Magnetoresistance of sample *2*. Arrows indicate the direction of the variation in magnetic field. The variation rate was 3.6 kOe/min. At point *A*, at which the resistance is at a minimum, the rate was reduced by a factor of 50; at point *B*, it is raised again to 3.6 kOe/min.

Table 1

	N_{Ga}, 10^{16} cm^{-3}	T_{ex}, K	$\|\Delta\rho\|/\rho$, %	H_C, Oe	$(\Delta T)_{ex}$, mK	$\left(\frac{\Delta Q}{m}\right)_{ex}$, 10^{-10} J g^{-1}
1	4.5	0.45	4.75	600	3.4	1.9
2	7.1	0.46	10	740	11	6.4
3	9.1	0.4	6	830	11	3.9
4	10.5	0.44	5	740	6.5	3.3
5	13.5	0.43	1	750	3.9	1.9
6	17.8	0.43	0	–	–	–

The relation between the terms on the right-hand side depends on the rate of heat transfer between the sample and the liquid ^{3}He, which is defined by the Kapitsa thermal resistance. As can be seen in Fig. 1, the short leading edge of the resistance "pulse" corresponds to sample heating, and its extended trailing edge, to sample cooling. Therefore, it can be concluded that the heat exchange between the sample and ^{3}He is considerably slower than the process of sample heating. As a result, the second term in (1) can be disregarded, and the following formula can be written for the specific quantity $\Delta Q/m_{Ge}$:

$$\Delta Q/m_{Ge} \approx \Delta Q_{Ge}/m_{Ge} = C_{Ge}(T_{ex})\Delta T_{ex}, \qquad (2)$$

where $C_{Ge}(T_{ex})$ is the isobaric specific heat of Ge at the temperature of the experiment; $C_{Ge}(T_{ex}) = C_{Ge}(1\text{ K})T^3$; $C_{Ge}(1\text{ K})$, the isobaric specific heat of Ge at $T = 1$ K; $C_{Ge}(1\text{ K}) = 6 \times 10^{-7}$ J g^{-1} K^{-1} [3]; and m_{Ge}, the mass of the sample. The values of $\Delta Q/m_{Ge}$ thus obtained are listed in Table 1.

4. QUANTITATIVE DESCRIPTION OF THE OBSERVED ABRUPT CHANGES IN MAGNETORESISTANCE

As is well known [4, 5], the resistivity of neutron-transmutation-doped Ge:Ga follows, in the mode of variable-range-hopping, the law

$$\rho = \rho_0 \exp(T_0/T)^{1/2}, \qquad (3)$$

Table 2

	N_{Ga}, 10^{16} cm^{-3}	T_0, K	a, Å	g_0, 10^{26} eV^{-3} cm^{-3}
1	4.49	62	77.2	3.13
2	7.14	34.2	123	4.61
3	9.07	20.07	160.2	10.3
4	10.5	13.8	183.5	21.1
5	13.5	5.1	274	126
6	17.8	0.93	611.4	1870

where the characteristic parameter T_0 is given by

$$T_0 = \frac{A}{g_0^{1/3} a}. \qquad (4)$$

Here a is the localization radius of a hole on Ga impurity; g_0, the factor in the expression for the density of states in a parabolic Coulomb gap

$$g = g_0(E - E_F)^2; \qquad (5)$$

and E_F, the Fermi energy. In terms of the Efros–Shklovsky Coulomb gap model, the coefficient $g_0 = \kappa^3/e^6$, where κ is the dielectric constant, e is the elementary charge, and the constant $A = 2.8$. According to experimental data in [5], the Coulomb gap in moderately compensated Ge:Ga is anomalously narrow, with the coefficient g_0 about two orders of magnitude higher than that which follows from the single-electron theory by Efros and Shklovsky [4]. According to [5], this anomalous narrowing of the gap is related to multielectron correlations in hopping. It is well known (see, e.g., [5]) that magnetoresistance in the mode of variable-range-hopping via the Coulomb gap states is described by the relation

$$\ln\left(\frac{\rho(H)}{\rho(0)}\right) = 0.0015\frac{e^2 a^4 H^2}{c^2 \hbar^2}\left(\frac{T_0}{T}\right)^{3/2}, \qquad (6)$$

where c is the speed of light and $\hbar$ is the reduced Planck constant.

Experimental dependences $\rho(T)$ allow one to determine the parameter T_0 (see (3)). Then, using Eq. (6), the radius a of hole localization on an impurity can be determined from the dependence of resistivity on the magnetic field. After that, the parameter g_0, which determines the density of localized states in a parabolic Coulomb gap, can be found from Eq. (4). The data thus obtained are listed in Table 2; they show that the Coulomb gap collapses when the insulator–metal transition is approached, owing to the divergence of the dielectric constant.

We will now show that the source of heat released in the sample is indeed the reversal of magnetization of the system of interacting localized magnetic moments of holes. The magnetic interaction between the local-

ized holes accounts for the stability of the configuration of magnetic dipoles when the sign of the magnetic field is reversed and the field increases to its critical value H_C. In the field H_C, the system of dipoles is reoriented. This leads to a release of heat, which reduces the resistivity of the sample.

To perform a quantitative analysis of this model, we consider the splitting of the ground state of a shallow Ga acceptor in a magnetic field. According to [6], the shallow acceptor state is split in crystals of tetrahedral symmetry in the magnetic field into four states with quantum numbers –3/2, –1/2, 1/2, and 3/2. It is also stated in [6] that in fields below 10 kOe the term in the Hamiltonian, quadratic in H (diamagnetic shift), can be disregarded, and the acceptor levels in the magnetic field parallel to the [111] axis take the form

$$E_{\pm\frac{3}{2}} = \pm\frac{1}{2}\left[\frac{9}{4}\left(2g_1 + \frac{23}{6}g_2\right)^2 + 2g_2^2\right]^{\frac{1}{2}}\mu_0 H, \qquad (7)$$

$$E_{\pm\frac{1}{2}} = \pm\frac{1}{2}\left(g_1 + \frac{13}{4}g_2\right)\mu_0 H, \qquad (8)$$

where μ_0 is the Bohr magneton and the g-factor components (g_1 = –1.15 and g_2 = 0.45) originate from the degeneracy of the valence band. According to Eq. (7), the energy distance between the states with quantum numbers 3/2 and –3/2 is as high as 0.062 meV in the strongest fields (~10 kOe), which is about twice the kT at the temperature of the experiment (0.4 K). This causes an uneven population of quantum states with different magnetic moments and brings about the magnetization of the ensemble of localized holes

$$M = \mu_0\sum_m mN_m, \qquad (9)$$

where m is the magnetic quantum number and N_m is the occupancy of the corresponding state. Then, the Boltzmann distribution of carriers over states is assumed:

$$N_m = N_0\exp(-\Delta E/kT), \qquad (10)$$

where N_0 is the occupancy of the ground state and ΔE is the energy spacing between the state with the quantum number m and the ground state with m = 3/2.

To calculate the occupancies of magnetic states, the normalization requirement must be found. Note that not all the impurity band states are localized in the vicinity of the metal–insulator transition. Only the states in the Coulomb gap can be considered localized with certainty, and it is these states that contribute to the sum (9). Therefore, the normalization requirement in question has the form

$$\sum_m N_m = \int_{E_{\min}}^{E_{\max}} g_0(E - E_F)^2 dE = g_0\frac{\Delta^3}{12}, \qquad (11)$$

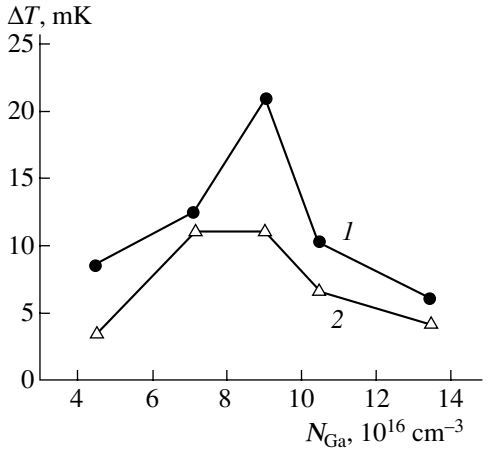

Fig. 5. Change in sample temperature, ΔT, corresponding to the abrupt change in magnetoresistance: (*1*) ΔT_{calc} and (*2*) ΔT_{ex}.

where $E_{\min}$ and $E_{\max}$ are determined from the conditions $E_{\max} = E_F + \Delta/2$, $E_{\min} = E_F - \Delta/2$, and Δ is the Coulomb gap width.

The parameter Δ can be determined by equating the density of states at the edges of the Coulomb gap to the average density of states in the impurity band $g_0\Delta^2/4 = N_{Ga}/w$, where $w = e^2N_D^{1/3}/\varepsilon$ is the width of the impurity band, with the Coulomb gap disregarded; ε is the static dielectric constant of Ge, equal to 16 [3]. The occupancies calculated by Eqs. (10) and (11) for the temperature of experiment T_{ex} are listed in Table 3.

The heat released within the sample is calculated under the assumption that the magnetization in the initial field of 10 kOe is approximately retained when the field decreases, changes its sign, and starts to grow up to the critical value H_C at which the reversal of magnetization occurs. At this point, the magnetization changes by 2M, and the corresponding specific energy $\Delta Q_{calc}/m_{Ge}$ released in a sample is given by

$$\Delta Q_{calc}/m_{Ge} = 2\frac{V}{m}MH_C = 2\frac{MH_C}{d}, \qquad (12)$$

where V and m_{Ge} are the volume and mass of the sample, d = 5.23 g/cm^3 is the density of Ge, and the corresponding abrupt change in temperature equals

$$\Delta T_{calc} = \frac{\Delta Q_{calc}}{m_{Ge}C(T_{ex})} = \frac{2MH_C}{dC(T_{ex})}. \qquad (13)$$

The calculated values of $\Delta Q_{calc}/m_{Ge}$ and ΔT_{calc} are listed in Table 3.

Figure 5 compares the thus calculated ΔT_{calc} with the experimental ΔT_{ex}. As can be seen, the coincidence is adequate. In particular, the calculation accounts for the observed maximum in the magnitude of the effect in the range of concentrations N = 0.4–0.5N_C. Thus, it is shown that the reversal of magnetization of an ensem-

Table 3

N_{Ga}, 10^{16} cm^{-3}	4.5	7.1	9.1	10.5	13.5
g_0, 10^{26} eV cm^{-3}	3.13	4.61	10.3	21.1	126
w, meV	2.14	2.5	2.71	2.84	3.09
Δ, meV	0.52	0.50	0.36	0.26	0.12
$\frac{g_0}{12}\Delta^3$, 10^{15} cm^{-3}	3.62	4.74	4.03	3.26	1.71
T_{ex}, K	0.45	0.46	0.4	0.44	0.43
$N_{+3/2}$, 10^{15} cm^{-3}	1.70	2.21	2.03	1.53	0.805
$N_{+1/2}$, 10^{15} cm^{-3}	0.966	1.27	1.06	0.87	0.456
$N_{-1/2}$, 10^{15} cm^{-3}	0.606	0.803	0.6172	0.546	0.286
$N_{-3/2}$, 10^{15} cm^{-3}	0.344	0.461	0.321	0.310	0.162
M(10 kOe), 10^7 eV G^{-1} cm^{-3}	1.285	1.650	1.61	1.180	0.631
H_C, Oe	600	740	830	740	750
$C(T_{ex})$, 10^{-8} J g^{-1} K^{-1}	5.47	5.84	3.84	5.11	4.77
$\left(\frac{\Delta Q}{m}\right)_{calc}$, 10^{-10} J g^{-1}	4.64	7.35	8.07	5.26	2.85
$(\Delta T)_{calc}$, mK	8.5	12.6	21	10.3	6.0

ble of localized holes in the impurity band can indeed be a reason for the experimentally observed abrupt changes in magnetoresistance that accompany hysteresis in moderately compensated Ge:Ga magnetized in the field $H \gg H_C$.

It remains unclear why the carriers oriented by the magnetic field retain their orientation when the magnetic field decreases to zero, changes its sign, and further grows to H_C. We believe that a ferromagnetic ordering of spins occurs in the hole ensemble in the vicinity of the metal–insulator transition. This is the fundamental difference between *p*-type material with a strong spin–orbit coupling and *n*-type material, in which, according to ESR data [7], a local antiferromagnetic ordering is observed near the metal–insulator transition.

ACKNOWLEDGMENTS

The authors are grateful to N.S. Averkiev for valuable discussions and to A.V. Chernyaev for assistance in the experiment.

This study was supported by the Russian Foundation for Basic Research (project nos. 00-15-96750 and 01-02-17813).

REFERENCES

1. A. G. Andreev, S. V. Egorov, A. G. Zabrodskiĭ, *et al.*, Fiz. Tekh. Poluprovodn. (St. Petersburg) **34**, 796 (2000) [Semiconductors **34**, 768 (2000)].
2. A. G. Zabrodskii, A. G. Andreev, and S. V. Egorov, Phys. Status Solidi B **205**, 61 (1998).
3. *Physical Quantities. Handbook*, Ed. by I. S. Grigor'ev and E. Z. Meĭlikhov (Énergoatomizdat, Moscow, 1991).
4. B. I. Shklovskiĭ and A. L. Éfros, *Electronic Properties of Doped Semiconductors* (Nauka, Moscow, 1979; Springer, Berlin, 1984).
5. A. G. Zabrodskiĭ and A. G. Andreev, Pis'ma Zh. Éksp. Teor. Fiz. **58**, 809 (1993) [JETP Lett. **58**, 756 (1993)].
6. N. S. Averkiev, V. M. Asnin, Yu. N. Lomasov, *et al.*, Fiz. Tverd. Tela (Leningrad) **23**, 3117 (1981) [Sov. Phys. Solid State **23**, 1815 (1981)].
7. A. I. Veĭnger, A. G. Zabrodskiĭ, T. V. Tisnek, and E. N. Mokhov, Fiz. Tekh. Poluprovodn. (St. Petersburg) **46**, 874 (2003) [Semiconductors **37**, 846 (2003)].

Translated by D. Mashovets

Semiconductors, Vol. 38, No. 2, 2004, pp. 197–201. Translated from Fizika i Tekhnika Poluprovodnikov, Vol. 38, No. 2, 2004, pp. 202–206.

SEMICONDUCTOR STRUCTURES, INTERFACES, AND SURFACES

Structures Based on Cu(Ag)In_nS_m Semiconductor Compounds

I. V. Bodnar'*^, V. A. Polubok*, V. Yu. Rud', Yu. V. Rud'***, and M. S. Serginov*****

**Belarussian State University of Informatics and Radioelectronics, Minsk, 220072 Belarus*

^e-mail: chemzav@gw.bsuir.unibel.by

***St. Petersburg State Polytechnical University, St. Petersburg, 195251 Russia*

e-mail: rudvas@spbstu.ru

****Ioffe Physicotechnical Institute, Russian Academy of Sciences, Politekhnicheskaya ul. 26, St. Petersburg, 194021 Russia*

Submitted April 15, 2003; accepted for publication April 22, 2003

Abstract—Crystals of $CuIn_7S_{11}$, $CuIn_{11}S_{17}$, and $AgIn_{11}S_{17}$ compounds are grown by planar crystallization. Measurements of the Hall coefficient and electrical conductivity are used to determine the conductivity type, resistivity, electron density, and the Hall mobility of charge carriers, which made it possible to classify the substances obtained as semiconductors. Photosensitive structures based on the compounds grown are fabricated for the first time. Photoelectric parameters of solid-state surface-barrier structures and photoelectrochemical cells obtained are determined, the features of band-to-band transitions are discussed, and the band gap of new semiconductors is estimated. It is shown that the structures developed can be used in photodetectors of natural optical radiation. © *2004 MAIK "Nauka/Interperiodica".*

1. INTRODUCTION

Detailed investigations of interaction in I–III–VI systems, in addition to the rather well-known I–III–VI_2 compounds, yielded data on the existence of a number of new semiconductor phases. These phases have the general formula I–III_n–VI_m, where *n* and *m* are natural numbers [1–5]. Such phases provide an efficient way to control the properties of semiconductors by varying the ratio between atoms of a specified nature. Theoretical analysis of interaction in these systems has shown that the regions of stability of positionally ordered phases emerge as the composition is varied when new semiconductor compounds with their own *n* and *m* indices are formed [5]. Such substances, similarly to I–III–VI_2 compounds [6, 7], may be promising for solving problems of modern optoelectronics and solar power engineering.

In this study, which is part of this new area of research, the problem of obtaining new I–II_n–VI_m semiconductor compounds is solved for the first time. The physical properties of these compounds are investigated, and the methods for fabrication of photosensitive structures based on them are suggested.

2. EXPERIMENTAL

Crystals of the ternary compounds $CuIn_7S_{11}$, $CuIn_{11}S_{17}$, and $AgIn_{11}S_{17}$ were grown by planar crystallization of a melt (a horizontal variant of the Bridgman–Stockbarger method). Metal components, namely, Cu (Ag) and In (of 99.9999% purity) in a quartz boat, and S (of 99.99999% purity) were placed in different parts of an evacuated quartz cell. Sulfur was taken in excess relative to stoichiometry, which is necessary to provide the vapor pressure over the melt up to 2.0 atm. The cell was placed in a two-zone horizontal furnace with independently controlled heaters. The temperature of the zone with metal components was kept in the range 1370–1400 K, depending on the compound. The temperature of the zone with S was increased at a rate of 50 K/h to 700 K and maintained for 2 h. During this period, the reaction between Cu (Ag), In, and S occurred. To complete the reaction, the temperature of this zone was increased at the same rate to ≈800 K and again maintained for 1 h. Then the melt was subjected to directional crystallization by decreasing the temperature at a rate of 2–3 K/h to 1000 K. At this temperature, homogenizing thermal treatment of the crystals grown was carried out for 300 h. The crystals grown consisted of large grains with a single grain as large as $15 \times 8 \times 5$ mm.

The composition of the crystals grown was determined using chemical analysis according to procedures suggested in [8–10]. Our results are shown in Table 1.

It can be seen that the calculated and experimental data are in quite satisfactory agreement. The distribution of elements along the crystal is uniform within the limits of the measurement error.

The structure and unit-cell parameters of the crystals grown were determined using X-ray powder diffraction analysis, which was carried out using a DRON-3M diffractometer (CuK_α radiation, Ni filter). The X-ray powder diffraction patterns recorded from various parts of the crystal corresponded to a cubic structure of the spinel type.

Table 1. Results of chemical analysis of the compounds $CuIn_7S_{11}$, $CuIn_{11}S_{17}$, and $AgIn_{11}S_{17}$

Compound	Cu, at %		Ag, at %		In, at %		S, at %	
	I	II	I	II	I	II	I	II
$CuIn_7S_{11}$	5.27	5.30	–	–	36.84	36.52	57.85	58.18
$CuIn_{11}S_{17}$	3.45	3.39	–	–	37.93	38.10	58.62	58.51
$AgIn_{11}S_{17}$	3.45	3.54	–	–	37.93	37.78	58.62	58.68

Note: The data in columns I correspond to calculation; in columns II, to experiment.

Table 2. Electrical properties of crystals of the I–III_n–VI_m compounds

Compound	Conductivity type	T = 300 K			T = 77 K		
		ρ, Ω · cm	n, cm^{-3}	μ, $cm^2/(V \cdot s)$	ρ, Ω · cm	n, cm^{-2}	μ, $cm^2/(V \cdot s)$
$CuIn_7S_{11}$	*n*	0.4	4×10^{17}	40	2	2×10^{17}	20
$CuIn_{11}S_{17}$	*n*	38	5×10^{15}	40	4×10^3	3×10^{14}	5
$AgIn_{11}S_{17}$	*n*	2×10^{-2}	4×10^{18}	30	–	–	–

3. RESULTS AND DISCUSSION

Investigations of kinetic coefficients were carried out using homogeneous samples cut from the crystals obtained (the samples were shaped like rectangular parallelepipeds with average dimensions $1 \times 2 \times 10$ mm); constant weak electric and magnetic fields were used. Nonrectifying contacts were fabricated by welding thin (~100 μm) platinum wires to the samples under an electric discharge. Typical results of measurements are given in Table 2. It can be seen that all the crystals grown by us are of *n*-type conductivity. Their resistivity and carrier concentration vary over a rather wide range. A decrease in the Hall electron mobility as the temperature decreases to 77 K, which was observed for $CuIn_7S_{11}$ and $CuIn_{11}S_{17}$ (Table 2), apparently indicates that the carrier scattering is determined by static defects. It follows from the correlation between free electron concentrations for $CuIn_7S_{11}$ and $CuIn_{11}S_{17}$ at T = 300 and 77 K that the electrical properties of these compounds are determined by thermal excitation of electrons from defect levels. The electrical properties of the new compounds with the general formula I–III_n–VI_m grown by us are given in Table 2. In general, these properties indicate that one can vary *n* and *m* values (based on the example of $CuIn_nS_m$ and $AgIn_nS_m$ systems) in order to control the electrical properties of semiconductors that have constituent atoms of the same nature.

Table 3. Photoelectric properties of the surface-barrier structures based on the I–III_n–VI_m compounds at T = 300 K

Compound	R_0, Ω	$\hbar\omega^m$, eV	φ, eV	δ, eV	S_u^m, V/W
$In/CuIn_7S_{11}$	160	1.23	0.82	0.27	1.0
$In/CuIn_{11}S_{17}$	800	1.24	0.82	0.26	0.1
$In/AgIn_{11}S_{17}$	75	1.57	0.82	0.60	2

When investigating the contact phenomena of the semiconductors obtained with *n*-type conductivity, we found rectifying and photovoltaic properties of the interface between thin layers of metal In (d = 1–3 μm) and the natural cleaved surface of the I–III_n–VI_m crystals. The parameters of the originally fabricated In/(I–III_n–VI_m) surface-barrier structures are given in Table 3. The measurements of steady-state current–voltage (I–V) characteristics showed that the $In/CuIn_7S_{11}$, $In/CuIn_{11}S_{17}$, and $In/AgIn_{11}S_{17}$ structures possess rectifying properties. The forward direction corresponds to a negative polarity of the external bias applied to the crystals mentioned. The rectification factor (K) for these structures, which was determined as the ratio between the forward and reverse currents, was low (2–5) for voltages $U \approx 0.5$ V. The forward portion of the I–V characteristic for $U > 0.3$ V usually follows the law

$$U = U_0 + IR. \quad (1)$$

The residual resistances R_0 for the structures fabricated are given in Table 3. The cutoff voltages are U_0 = 0.2–0.4 V.

When these structures are illuminated, a photovoltaic effect with a positive photovoltage polarity at the barrier contact is observed, which is consistent with the direction of rectification. The highest magnitudes of the voltaic photosensitivity S_u^m for the best surface-barrier structures are given in Table 3. In the In/(I–III_n–VI_m) barriers obtained, the highest photovoltage is observed when the In-barrier contact side of these structures is illuminated.

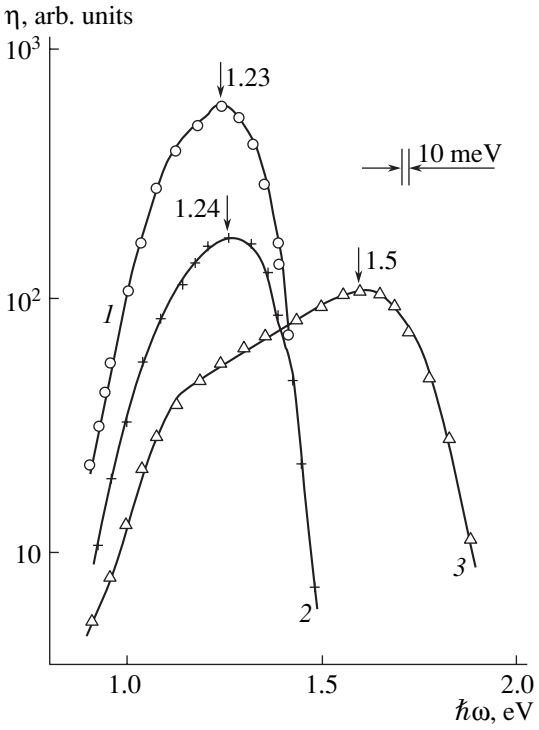

Fig. 1. Spectral dependences of the relative quantum efficiency of photoconversion for the structures (*1*) $In/CuIn_7S_{11}$, (*2*) $In/CuIn_{11}S_{17}$, and (*3*) $In/AgIn_{11}S_{17}$ at 300 K. The barrier-contact side of the structures was illuminated.

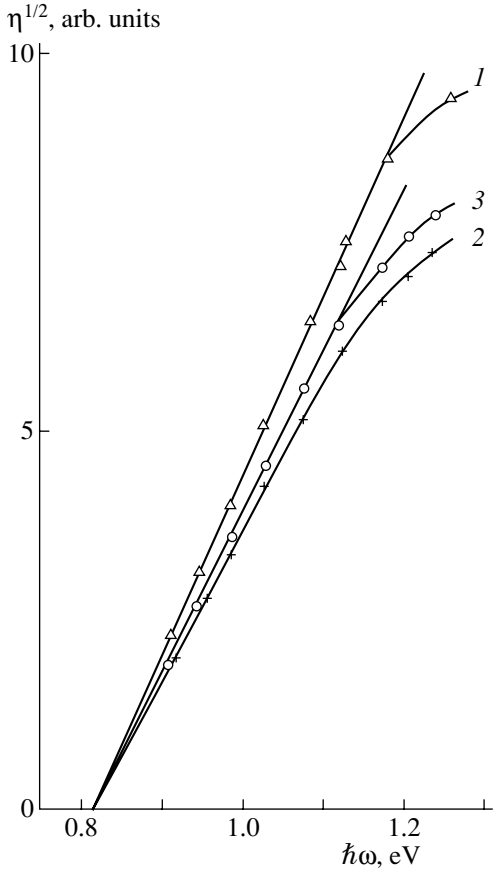

Fig. 2. Dependences $\eta^{1/2} - \hbar\omega$ for the $In/Cu(Ag)In_nS_m$ surface-barrier structures at T = 300 K. The notation of the curves corresponds to Fig. 1.

The spectral dependences of the relative quantum efficiency of photoconversion $\eta(\hbar\omega)$ for the $In/(I–III_n–VI_m)$ structures at T = 300 K when they are illuminated from the barrier contact side are shown in Fig. 1. It can be seen that the spectral dependences $\eta(\hbar\omega)$ for these structures are represented by peaked curves. A rapid increase in the photosensitivity for the structures fabricated starts with the photon energy $\hbar\omega \approx 0.9$ eV, and the long-wavelength edge of these spectra for $\hbar\omega < 1.1$ eV (Fig. 2) follows Fowler's law [11]. Therefore, this edge may be attributed to photoemission. Extrapolation of the $\eta^{1/2}(\hbar\omega)$ dependences to zero ($\eta \approx 0$) enables us to determine the energy barrier height (φ_B) for the $In/(I–III_n–VI_m)$ structures. This height turned out to be practically independent of the atomic composition of semiconductors used for the fabrication of barrier structures (Table 3). The cause of this special feature remains to be clarified, and this requires additional research.

A second specific feature of the surface-barrier structures obtained should also be noted: the existence of an abrupt short-wavelength falloff of photosensitivity, which manifests itself when the structures are illuminated both from the barrier contact side and from the crystal side. The measurements carried out showed that, for crystal wafers ≈0.1 mm thick, the energy position of a short-wavelength falloff of η for the $In/(I–III_n–VI_m)$ structures obtained is almost independent of the illumination geometry. This circumstance enables us to assume that the barriers obtained do not provide the suppression of the effect of the surface recombination of photogenerated pairs, which is apparently responsible for the short-wavelength falloff of η at $\hbar\omega > \hbar\omega^m$.

The fullwidth at a half-maximum δ of the $\eta(\hbar\omega)$ spectra is also given in Table 3. It can be seen that the photosensitivity spectra with the broadest bands are characteristic of $In/AgIn_{11}S_{17}$ structures. Along with the solid-state surface-barrier structures based on the new semiconductor compounds, the possibility of fabricating photoelectrochemical cells was also investigated [12, 13]. Distilled water with an NaCl additive was used as the electrolyte. The water was in direct contact with the cleaved surface of the $I–III_n–VI_m$ crystals, which were provided with a nonrectifying contact. In order to isolate the electrolyte from the nonrectifying contact, the latter was coated with insulating lacquer. A sharpened Pt conductor was used as the counter electrode of the photoelectrochemical cell. The measurements of photosensitivity of the $H_2O/(I–III_n–VI_m)$ cells were carried out in modulated illumination ($f \approx 20$ Hz) with nonpolarized radiation from the counter-electrode side

Table 4. Photoelectric properties of the $H_2O/I–III_n–VI_m$ structures and energies of the band-to-band transitions for the $I–III_n–VI_m$ compounds at $T = 300$ K

Structures	$\hbar\omega$, eV	δ, eV	S_u, eV	S_u^m, V/W	E_g^{in}, eV	E_g^{dir}, eV
$H_2O/CuIn_7S_{11}$	2.4–2.8	~1.8	21	8000	1.36	1.74
$H_2O/CuIn_{11}S_{17}$	2.8–3.6	>1.1	19	5000	1.37	2.23
$H_2O/AgIn_{11}S_{17}$	3.0–3.4	~1.2	12	1900	1.83	2.48

[12]. All the photoelectrochemical cells obtained featured both higher rectification of the electric current ($K \approx 20$ for $U \approx 10$ V at $T = 300$ K) compared with the solid-state structures based on the same crystals and a photovoltaic effect. A comparison of Tables 3 and 4 shows that the highest voltaic photosensitivity of the photoelectrochemical cell is three to four orders of magnitude higher than that of $In/(I–III_n–VI_m)$ surface-barrier structures. In this case, the absence of any degradation of photoelectric parameters of the photoelectrochemical cell should be noted. Figure 3 shows the spectral dependences of the relative quantum efficiency of photoconversion $\eta(\hbar\omega)$ for photoelectrochemical cells $H_2O/(I–III_n–VI_m)$ when they are illuminated from the electrolyte side. It can be seen that these spectra differ substantially from similar spectra for the $In/(I–III_n–VI_m)$ surface-barrier structures (Fig. 1). In fact, instead of a short-wavelength falloff of η, an almost exponential increase in the photosensitivity emerges in the $H_2O/(I–III_n–VI_m)$ photoelectrochemical cells. This

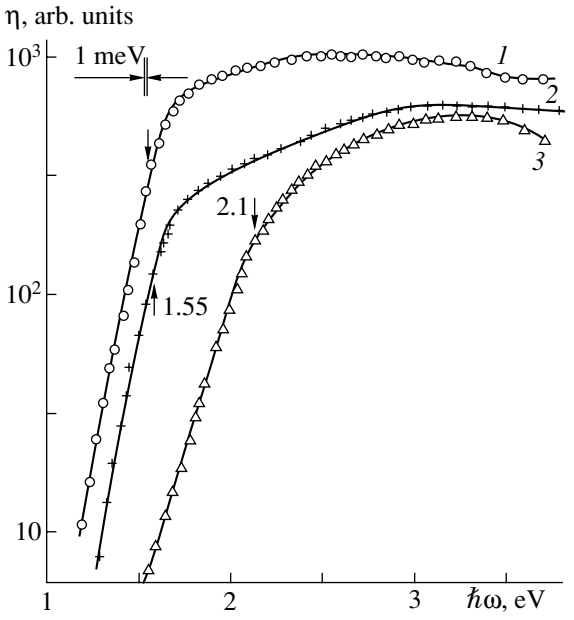

Fig. 3. Spectral dependences of the relative quantum efficiency of photoconversion for the $H_2O/Cu(Ag)In_nS_m$ cells at 300 K. Illumination was from the electrolyte side. The photoelectrode substance was (*1*) $CuIn_7S_{11}$, (*2*) $CuIn_{11}S_{17}$, and (*3*) $AgIn_{11}S_{17}$. To exclude overlapping, the curves are shifted in parallel with the ordinate axis.

increase corresponds to the slope S, which is determined from the relationship

$$S = \delta(\ln\eta)/\delta(\hbar\omega). \quad (2)$$

Table 4 shows that the slope of the long-wavelength increase in the photosensitivity spectra is higher for the photoelectrochemical cells fabricated from the $CuIn_nS_m$ crystals than for the cells fabricated based on the crystals of the compound $AgIn_{11}S_{17}$. Based on the slope magnitude according to [14], we may conclude that an exponential increase in η in the case of $CuIn_7S_{11}$- and $CuIn_{11}S_{17}$-based cells may point to direct band-to-band transitions. The lower value $S \approx 12$ eV^{-1} for the $AgIn_{11}S_{17}$-based cells may be attributed to pseudodirect band-to-band transitions, which are known for a series of II–IV–V_2 semiconductors with the chalcopyrite lattice [15].

A pronounced short-wavelength falloff of η is absent in the photosensitivity spectra originally obtained for the $I–III_n–VI_m$-based photoelectrochemical cells. This should be considered as the main difference between these spectra and those considered for the surface-barrier solid-state structures. The spectral range of highest photosensitivity for the photoelectrochemical cells obtained is given in Table 4. The value of δ for the $H_2O/(I–III_n–VI_m)$ cells estimated from the $\eta(\hbar\omega)$ spectra is much larger than for the surface-barrier structures. This fact, along with the high values of S_u^m, gives grounds to assume that the efficiency of separation and collection of photogenerated pairs for the semiconductor/electrolyte barriers is much higher than for the $In/(I–III_n–VI_m)$ solid-state structures.

Spectral dependences $\eta(\hbar\omega)$ for the $H_2O/(I–III_n–VI_m)$ photoelectrochemical cells plotted in the coordinates $(\eta\hbar\omega)^{1/2} – \hbar\omega$ and $(\eta\hbar\omega)^2 – \hbar\omega$ are shown in Fig. 4. Assuming that these dependences are mainly determined by the processes of band-to-band absorption, we can evaluate the character of band-to-band transitions and the band gap for the compounds under consideration based on the existing theory [16]. It can be seen from Fig. 4 that a long-wavelength increase in photosensitivity of photoelectrochemical cells (curves *1–3*) is linearized in the coordinates $(\eta\hbar\omega)^{1/2} – \hbar\omega$. This enables us to assume that the long-wavelength edge of $\eta(\hbar\omega)$ is governed by indirect band-to-band transitions in the $I–III_n–VI_m$ crystals. Accordingly, the band gap for indirect optical transitions (Eg^{in}) can be estimated from

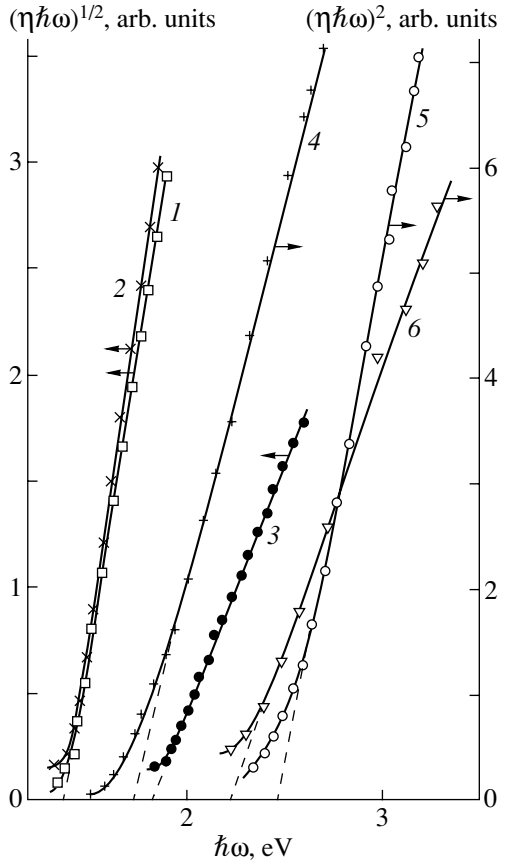

Fig. 4. Dependences (*1–3*) $(\eta\hbar\omega)^{1/2} - \hbar\omega$ and (*4–6*) $(\eta\hbar\omega)^2 - \hbar\omega$ for the $H_2O/Cu(Ag)In_nS_m$ cells at 300 K. The photoelectrode substance was (*1*, *4*) $CuIn_7S_{11}$, (*2*, *5*) $CuIn_{11}S_{17}$, and (*3*, *6*) $AgIn_{11}S_{17}$.

the extrapolation $(\eta\hbar\omega)^2 \longrightarrow 0$. The results of this estimation are given in Table 4. It should be noted that the energy position of the short-wavelength falloff in the $\eta(\hbar\omega)$ spectra for the surface-barrier structures agrees satisfactorily with the value of Eg^{in} for the corresponding compounds (Table 4). Therefore, the short-wavelength falloff of $\eta(\hbar\omega)$ may be associated with an increase in the optical absorption of the incident radiation due to the emergence of indirect band-to-band transitions in the I–III_n–VI_m compounds.

It can be also seen from Fig. 4 that the short-wavelength part of the photosensitivity spectra for the photoelectrochemical cells follows the square law $(\eta\hbar\omega)^2 - \hbar\omega$. Therefore, we may associate this specific feature with the emergence of direct band-to-band transitions. Accordingly, the energy of direct band-to-band transitions (Eg^{dir}) for these compounds could be estimated from the extrapolation $(\eta\hbar\omega)^2 \longrightarrow 0$. The results of this estimation are given in Table 4.

4. CONCLUSION

We ascertained for the first time that photosensitive Schottky barriers and photoelectrochemical cells can be fabricated using the crystals of I–III_n–VI_m ternary compounds. The photoelectric properties of these structures were investigated, a conclusion was drawn concerning the character of band-to-band transitions in the electron spectrum of these materials, and their band gap was estimated. It was shown that new photosensitive structures can be used as selective and broadband photodetectors of natural radiation.

REFERENCES

1. I. V. Bodnar', T. L. Kushner, V. Yu. Rud', *et al.*, Zh. Prikl. Spektrosk. **69**, 519 (2002).
2. C. Rincon, S. M. Wasim, G. Marin, and R. Marques, in *Abstracts of 13th ICTMC* (Paris, 2002), p. 83.
3. S. M. Wasim, G. Marin, C. Rincon, *et al.*, in *Abstracts of 13th ICTMC* (Paris, 2002), p. 205.
4. N. M. Gasanly, A. Serpengurel, A. Audinly, *et al.*, J. Appl. Phys. **85**, 3198 (1999).
5. S. B. Tsang, S. H. Wei, A. Zunger, and H. Katayama-Yochida, Phys. Rev. B **57**, 9642 (1998).
6. J. L. Shay and J. H. Wernick, *Ternary Chalcopyrite Semiconductors: Growth, Electronic Properties and Applications* (Pergamon, New York, 1975).
7. *Copper Indium Diselenide for Photovoltaic Applications*, Ed. by T. J. Coutts, L. L. Kazmerskii, and S. Wagner (Elsevier, Amsterdam, 1986).
8. N. N. Ishchenko, L. G. Starobinets, and L. I. Ganago, Izv. Akad. Nauk BSSR, Ser. Khim. Nauk, No. 5, 132 (1977).
9. L. G. Starobinets, N. N. Ishchenko, and L. I. Ganago, Izv. Akad. Nauk BSSR, Ser. Khim. Nauk, No. 1, 111 (1988).
10. P. P. Kish and S. T. Orlovskiĭ, Zh. Anal. Khim. **17**, 1057 (1962).
11. T. S. Moss, G. J. Burrell, and B. Ellis, *Semiconductor Opto-Electronics* (Butterworths, London, 1973; Mir, Moscow, 1976).
12. Yu. Ya. Gurevich and Yu. V. Pleskov, *Photoelectrochemistry of Semiconductors* (Nauka, Moscow, 1976).
13. Yu. V. Rud' and M. Tairov, Fiz. Tekh. Poluprovodn. (Leningrad) **21**, 615 (1987) [Sov. Phys. Semicond. **21**, 377 (1987)].
14. A. Shileika, Surf. Sci. **37**, 730 (1973).
15. V. D. Prochukhan and Yu. V. Rud', Fiz. Tekh. Poluprovodn. (Leningrad) **12**, 209 (1978) [Sov. Phys. Semicond. **12**, 121 (1978)].
16. J. I. Pankove, *Optical Processes in Semiconductors* (Prentice Hall, Englewood Cliffs, N.J., 1971; Mir, Moscow, 1973).

Translated by N. Korovin

Semiconductors, Vol. 38, No. 2, 2004, pp. 202–208. Translated from Fizika i Tekhnika Poluprovodnikov, Vol. 38, No. 2, 2004, pp. 207–212.

LOW-DIMENSIONAL SYSTEMS

Phonon Scattering of Quasi-Two-Dimensional Electrons in GaAs/$Al_xGa_{1-x}As$ Superlattices

S. I. Borisenko

Siberian Kuznetsov Physicotechnical Institute, pl. Revolyutsii 1, Tomsk, 634050 Russia

e-mail: sib@elefot.tsu.ru

Submitted March 12, 2003; accepted for publication May 19, 2003

Abstract—Longitudinal and transverse electron mobilities in the lower miniband of a GaAs/$Al_{0.35}Ga_{0.65}As$ superlattice are calculated for the case of scattering by long-range potential of polar-optical phonons at $T = 300$ K. Partial contributions to the mobility and effective relaxation time of different vibrational modes are analyzed. The dependences of the mobility and effective relaxation time for scattering by both polar-optical and acoustic phonons on the width of the superlattice quantum wells and on the temperature are studied. The calculation is performed using the linearized Boltzmann equation. The scalar potential of polar optical phonons is calculated in the model of dielectric continuum. © *2004 MAIK "Nauka/Interperiodica".*

1. INTRODUCTION

It is well known that, in GaAs/$Al_xGa_{1-x}As$ superlattices (SLs) composed of semiconductors with ionic bonding, the main contribution to charge carrier scattering by lattice vibrations at room temperature comes from scattering by the long-range potential of polar optical phonons. This scattering mechanism and related mobility for structures with isolated quantum wells (QWs) were analyzed in numerous papers that dealing with both the problem in general [1–9] and its specific aspects [10–14]. However, there are practically no publications that address this problem for SLs consisting of QWs [15–17]. Up to now the analysis of charge-carrier mobility in SLs, which is governed by scattering by polar optical phonons, has encountered considerable difficulties, owing to the complex form of the vibrational spectrum of the long-range potential for polar optical phonons in SLs and to the inelastic character of scattering.

In this paper, using a unified approach, we calculate the longitudinal and transverse mobilities of nondegenerate electron gas in the lowest miniband of a symmetric GaAs/$Al_{0.35}Ga_{0.65}As$ SL in which both the QW width a and the potential-barrier thickness b are equal to 5 nm. The calculation of the mobility and effective relaxation time at $T = 300$K is carried out taking into account electron scattering by the long-range potential of polar optical phonons. We analyze partial contributions to the mobility and effective relaxation time of different vibrational modes of the long-range potential of polar optical phonons. We also study the dependences of the mean effective relaxation time and mobility for scattering by polar-optical and acoustic phonons on the width of QWs in an SL and on the temperature. The calculation of the effective relaxation time was carried out using the linearized Boltzmann equation. The scalar potential of polar optical phonons was calculated in the model of dielectric continuum.

2. METHOD OF CALCULATION

We calculated the longitudinal and transverse (with respect to the symmetry axes of the SL) mobilities using the linearized Boltzmann equation. Taking inelastic scattering by phonons into account, we calculated the nonequilibrium part of the distribution function $g(\mathbf{k})$; as a result, we obtained

$$g(\mathbf{k}) = e\frac{\partial f_0}{\partial \varepsilon}\sum_i \tau_i(\mathbf{k})E_i v_i(\mathbf{k}), \qquad (1)$$

where $\tau_i(\mathbf{k})$ are the desired functions, which are referred to as the effective relaxation time and generally depend on the wave vector $\mathbf{k}$; $f_0(\varepsilon)$ is the equilibrium Fermi–Dirac distribution function; $\mathbf{E}$ is the electric field vector; $\mathbf{v}(\mathbf{k}) = \nabla_k\varepsilon/\hbar$ is the electron velocity;

$$\varepsilon(\mathbf{k}) = \frac{\hbar^2 k_\perp^2}{2m_\perp} + \frac{\Delta}{2}[1 - \cos(k_z d)] \qquad (2)$$

is the electron energy in the lowest miniband of the SL in the tight-binding approximation; $\mathbf{k}_\perp = (k_x, k_y, 0)$ is the wave vector normal to the symmetry axis of the SL; $m_\perp$ is the transverse effective mass, whose value is close to that of the electron effective mass for the material of the QW; m_a is the width of the lower miniband of the SL; and d is the SL period.

The effective relaxation time was calculated by numerically solving the linearized Boltzmann equation; for a quasi-two-dimensional (quasi-2D) electron

gas (i.e., for $\Delta < k_0T$), the solution has the following form taking into account Eqs. (1) and (2) [17]:

$$\tau_\perp(\varepsilon) = \tau_0(\varepsilon)\left\{\sum_{\mathbf{k}'}[w_{\mathbf{k}'\mathbf{k}} + f_0(\varepsilon)(w_{\mathbf{k}\mathbf{k}'} - w_{\mathbf{k}'\mathbf{k}})] \times \frac{f_0'(\varepsilon')\mathbf{k}_\perp\mathbf{k}_\perp'}{f_0'(\varepsilon)k_\perp^2}\tau_\perp(\varepsilon') + 1\right\}, \quad (3)$$

$$\tau_\parallel(\varepsilon) = \tau_0(\varepsilon)\left\{\sum_{\mathbf{k}'}[w_{\mathbf{k}'\mathbf{k}} + f_0(\varepsilon)(w_{\mathbf{k}\mathbf{k}'} - w_{\mathbf{k}'\mathbf{k}})] \times \frac{f_0'(\varepsilon')\sin(k_z'd)}{f_0'(\varepsilon)\sin(k_zd)}\tau_\parallel(\varepsilon') + 1\right\}. \quad (4)$$

Here,

$$\tau_0^{-1}(\varepsilon) = \sum_{\mathbf{k}'}\{w_{\mathbf{k}\mathbf{k}'} + f_0(\varepsilon')(w_{\mathbf{k}'\mathbf{k}} - w_{\mathbf{k}\mathbf{k}'})\}, \quad (5)$$

τ_0 is the total electron lifetime in the state with the wave vector $\mathbf{k}$,

$$w_{\mathbf{k}\mathbf{k}'} = w^{\pm}_{\mathbf{k}\mathbf{k}'} + w^{\pm}_{\mathbf{k}'\mathbf{k}},$$
$$w^{\pm}_{\mathbf{k}\mathbf{k}'} = w(\mathbf{q})\left(N_\omega + \frac{1}{2} \pm \frac{1}{2}\right)\delta_{\mathbf{k}', \mathbf{k}\mp\mathbf{q}}\delta(\varepsilon' - \varepsilon \pm \hbar\omega) \quad (6)$$

is the probability of scattering by phonons with energy $\hbar\omega$, N_ω is the number of phonons given by the Bose–Einstein function, $\tau_\perp(\varepsilon) = \tau_x(\varepsilon) = \tau_y(\varepsilon)$, $\tau_\parallel(\varepsilon) = \tau_z(\varepsilon)$, and $\varepsilon = \varepsilon(\mathbf{k}_\perp) = \dfrac{\hbar^2k_\perp^2}{2m_a}$. It should be noted that, in the quasi-2D approximation, the functions τ_i in the effective relaxation time and the function τ_0 depend only on the energy of transverse electron motion. Taking into account inelastic scattering by polar optical phonons [the probability of this scattering is given by Eq. (6)] and other scattering mechanisms described by the relaxation times $\tau_{j\perp}(\varepsilon)$ and $\tau_{j\parallel}(\varepsilon)$ and integrating with respect to the wave vector $\mathbf{k}'$, we can write Eqs. (3) and (4) in functional form as

$$\tau_i(\varepsilon) = \tau_{0i}(\varepsilon)\{G_i^+(\varepsilon)\tau_i(\varepsilon + \hbar\omega) + G_i^-(\varepsilon)\tau_i(\varepsilon - \hbar\omega) + 1\}, \quad (7)$$

where (see Appendix I)

$$\tau_{0i}^{-1}(\varepsilon) = \tau_0^{-1}(\varepsilon) + \sum_j \tau_{ji}^{-1}(\varepsilon). \quad (8)$$

It is well known that, for III–V semiconductors in the dielectric continuum approximation [16], the modes corresponding to long-range potential of polar optical phonons can be divided into two types, according to the character of the scalar potential dependence on the coordinate along the SL axis. These modes are referred to as guided, or G modes, and interfacial, or I modes. The infinite number of guided modes are degenerate in a frequency that assumes two values equal to the frequencies of longitudinal polar-optical phonons of the original semiconductor components of the QW ω_{La} and of the potential barrier ω_{Lb}. The amplitudes of G modes of frequency ω_{La} are nonzero only inside the QW, whereas the amplitudes of modes with frequency ω_{Lb} are nonzero only within the potential barriers. Therefore, one may speak of G modes of QWs and of potential barriers. The interfacial vibrations have four modes, whose frequencies are close to the frequencies of longitudinal and transverse polar-optical phonons of the original semiconductors and have dispersion in the wave vector. In contrast to guided modes, the amplitudes of I modes are defined over the entire SL period. The probability of electron scattering by the G and I modes of the long-range potential was calculated using the approximate envelope wave function taken in the form of the Bloch sum containing the ground state wave functions of infinitely deep QWs,

$$\psi = \psi_{\mathbf{k}}(\mathbf{r}) = \sqrt{\frac{d}{V}}e^{i\mathbf{k}_\perp\mathbf{r}_\perp}\sum_n e^{ik_zdn}\varphi(z - dn), \quad (9)$$

where

$$\varphi(z) = \begin{cases}\sqrt{\dfrac{2}{a}}\cos\left(\dfrac{\pi}{a}z\right) & |z| \le \dfrac{a}{2},\\ 0 & |z| > \dfrac{a}{2}.\end{cases} \quad (10)$$

In this approximation for the total probability of scattering by all symmetric QW G modes of frequency $\omega_G = \omega_{La}$, the function $w(\mathbf{q})$ in Eq. (6) can be analytically written as

$$w_G(\mathbf{q}) = w_G(q_\perp) = \frac{1}{8}C_{PO}\frac{\pi\alpha(4 + \alpha^2)(8 + 3\alpha^2) - 64\tanh(aq_\perp/2)}{\alpha^3(4 + \alpha^2)^2}, \quad (11)$$

where

$$C_{PO} = \frac{e^2ad\omega_{La}}{\pi^2\varepsilon_0\varepsilon_a^*V},$$

$\alpha = aq_\perp/\pi$, a is the QW width, $1/\varepsilon^* = 1/\varepsilon_\infty - 1/\varepsilon_s$, and V is the SL volume. The subscript a specifies the semiconductor material of the QW.

Partial relaxation times averaged over energies for nondegenerate electrons interacting with the G and I modes of the scalar potential of polar optical phonons at $T = 300$ K

Relaxation time	G	I_1	I_2	I_3	I_4	Σ	V
$\langle\tau_\perp\rangle$, ps	1.8	920	170	1.2	3.3	0.58	0.30
$\langle\tau_\parallel\rangle$, ps	2.4	1500	95	0.95	3.0	0.53	0.30

Note: Σ is the total relaxation time for scattering by all modes of polar optical phonons and V is the relaxation time for scattering by bulk phonons.

For scattering by I modes of frequency $\omega = \omega_\lambda(\mathbf{q})$, the function $w(\mathbf{q})$ is given by

$$w_I(\mathbf{q}) = 16C_{PO}\frac{|1+\vartheta(\mathbf{q})|^2\sinh(aq_\perp/2)}{\alpha^3(4+\alpha^2)^2}\frac{\omega_{La}c_{aL}^2}{\omega c_a^2}$$
$$\times\left\{\sinh(aq_\perp)+\frac{1}{4}e^{dq_\perp}\sinh(bq_\perp)\frac{\rho_{\mu b}c_b^2}{\rho_{\mu a}c_a^2}\right.$$
$$\left.\times\left|e^{-aq_\perp}\left(1-\frac{\varepsilon_a}{\varepsilon_b}\right)+\vartheta\left(1+\frac{\varepsilon_a}{\varepsilon_b}\right)\right|^2\right\}^{-1}, \quad (12)$$

where

$$c_i^2 = c_i^2(\omega) = \frac{\varepsilon_0\varepsilon_{\infty i}(\omega_{Li}^2-\omega_{Ti}^2)}{\rho_{\mu i}(\omega^2-\omega_{Ti}^2)^2},$$
$$\varepsilon_i = \varepsilon_i(\omega) = \varepsilon_{\infty i}\frac{\omega_{Li}^2-\omega^2}{\omega_{Ti}^2-\omega^2}, \quad (13)$$
$$c_{aL}^2 = c_a^2(\omega_{La}), \quad \frac{1}{\rho_{\mu i}} = \Omega\left(\frac{1}{m_{Ai}}+\frac{1}{m_{Bi}}\right),$$

Ω is the volume of the unit cell of the original III–V semiconductor (it is assumed to be the same for the QW and for the potential barrier); m_A and m_B are the masses of the atoms in the unit cell; ω_T and ω_L are the frequencies of the transverse and longitudinal optical phonons in the original semiconductors; $\vartheta = \vartheta_\lambda(\mathbf{q})$ is a dimensionless complex function (see Appendix II); and the subscript i assumes two values: a for the QW and b for the potential barrier.

Taking into account the Umklapp processes and using the approximation of the bulk phonon spectrum, we obtain the following expression for $w(\mathbf{q})$ [17]:

$$w(\mathbf{q}) = \frac{a}{\pi d}C_{PO}\sum_n\frac{\sin^2(\pi x_n)}{x_n^2(1-x_n^2)^2}\frac{1}{[\alpha^2+4x_n^2]}. \quad (14)$$

Here,

$$x_n = \frac{a}{2\pi}\left(q_z+\frac{2\pi}{d}n\right), \quad -\frac{N_z}{2}\le n<\frac{N_z}{2},$$

and N_z is the number of SL periods. Elastic scattering by acoustic phonons was described using an isotropic relaxation time calculated by the expression [17]

$$\tau_\perp(\varepsilon) = \tau_\parallel(\varepsilon) = \tau = \frac{2}{3}\frac{ac_L\hbar^3}{m_aD_c^2k_0T}, \quad (15)$$

where $c_L = c_{11}+\frac{2}{5}(c_{12}+2c_{44}-c_{11})$ is the averaged value of the elastic modulus for longitudinal acoustic vibrations in the bulk semiconductor approximation for the phonon spectrum and D_c is the deformation-potential constant for the edge of the conduction band. In the model of effective relaxation time and in the quasi-2D approximation for the electron gas in the SL, the longitudinal and transverse mobilities were calculated from the expressions [17]

$$\mu_\perp = e\langle\tau_\perp\rangle/m_\perp, \quad \mu_\parallel = e\langle\tau_\parallel\rangle/\langle m_\parallel\rangle. \quad (16)$$

Here, $\langle\tau_\perp\rangle$, $\langle\tau_\parallel\rangle$, and $\langle m_\parallel\rangle$ are the energy-averaged functions of effective time for transverse and longitudinal relaxation and electron longitudinal effective mass in the lowest miniband,

$$\langle\tau_\perp\rangle = \frac{\rho_c}{n}\int_0^\infty\left(-\frac{\partial f_0}{\partial\varepsilon}\right)\tau_\perp(\varepsilon)\varepsilon d\varepsilon,$$
$$\langle\tau_\parallel\rangle = [1-\exp(-n/N_c)]^{-1}\int_0^\infty\left(-\frac{\partial f_0}{\partial\varepsilon}\right)\tau_\parallel(\varepsilon)\varepsilon d\varepsilon, \quad (17)$$

$$\frac{1}{\langle m_\parallel\rangle} = \frac{\Delta\rho_c}{4m_\parallel n}[1-\exp(-n/N_c)], \quad (18)$$

where $\rho_c = m_\perp/\pi d\hbar^2$ is the 2D density of states in the lower conduction miniband, $N_c = k_0T\rho_c$ is the effective density of states, and $m_\parallel = 2\hbar^2/\Delta^2d^2$ is the longitudinal effective mass at the bottom of the miniband. For a nondegenerate electron gas ($n \ll N_c$), the expression for the longitudinal effective mass averaged over energy assumes a simple form:

$$\frac{1}{\langle m_\parallel\rangle} = \frac{\Delta}{k_0Tm_\parallel}. \quad (19)$$

3. ANALYSIS OF THE RESULTS OF NUMERICAL CALCULATION

The longitudinal and transverse effective relaxation times and mobility of quasi-2D nondegenerate electron gas in the lowest miniband of a $GaAs/Al_{0.35}Ga_{0.65}As$ SL were calculated for the following values of the parameters: $a = 5$ nm, $b = 5$ nm, $m_\perp = m_a = 0.066m_0$, $\hbar\omega_{La} = 36.23$ meV, $\hbar\omega_{Ta} = 33.27$ meV, $\varepsilon_{sa} = 13.18$, $\varepsilon_{\infty a} = 10.82$, $\hbar\omega_{Lb} = 34.11$ meV, $\hbar\omega_{Tb} = 32.89$ meV, $\varepsilon_{sb} = 12.06$, and $\varepsilon_{\infty b} = 9.82$ [18]. According to the calculations of the energy spectrum of the conduction band taking into account the Kane nonparabolicity [19], this SL has a

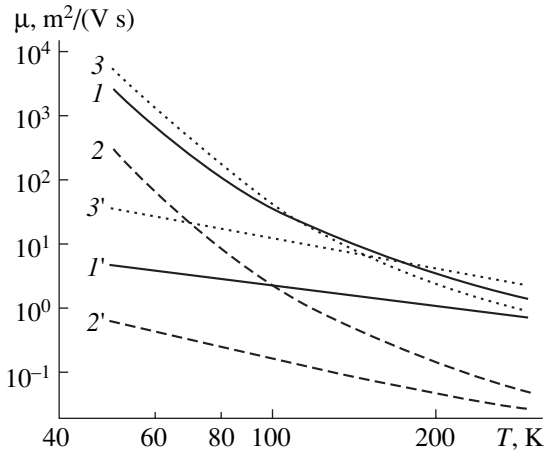

Fig. 1. Temperature dependence of the electron mobility μ for scattering by (*1*–*3*) polar optical phonons and (*1*'–*3*') acoustic phonons; (*1*, *1*') transverse mobility; (*2*, *2*') longitudinal mobility; and (*3*, *3*') the data for GaAs.

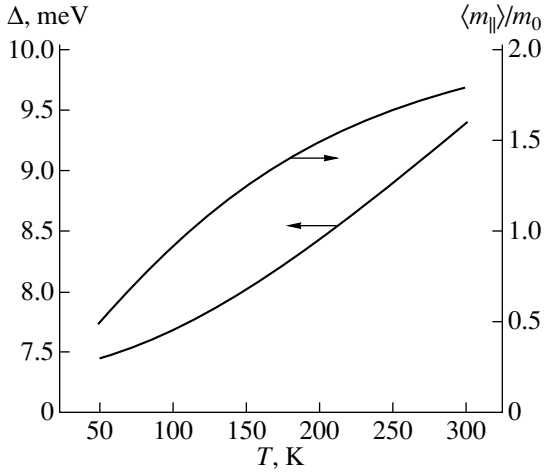

Fig. 2. Temperature dependences of the miniband width Δ and of the average longitudinal electron effective mass $\langle m_{\|} \rangle$.

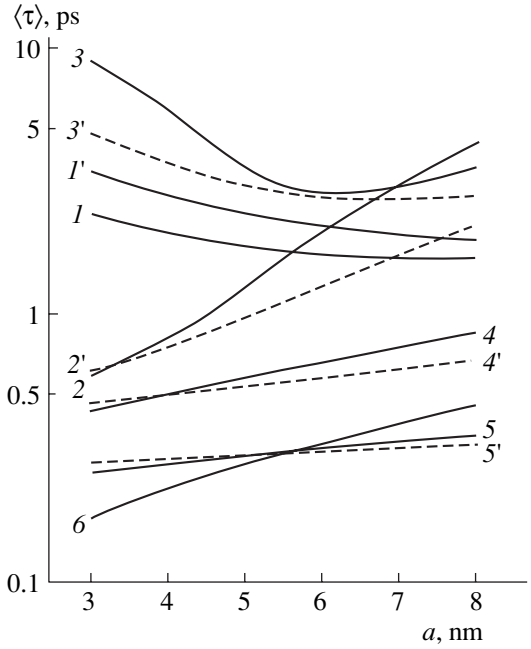

Fig. 3. Mean electron effective relaxation time $\langle \tau \rangle$ as a function of the QW width at T = 300K for scattering by the modes of polar optical phonons: (*1*, *1*') G mode; (*2*, *2*') I_3 mode; (*3*, *3*') I_4 mode; (*4*, *4*') relaxation time for scattering by all modes of polar optical phonons (Σ); (*5*, *5*') relaxation time for scattering by bulk phonons (V); (*6*) scattering by acoustic phonons; (*1*–*5*) transverse relaxation time; and (*1*'–*5*') longitudinal relaxation time.

single miniband in a QW at 300 K. The second miniband lies at the height of the potential barrier with an energy of 260 meV and is separated from the first miniband by 150 meV. An SL with such parameters can be used as a photodetector of infrared radiation with a wavelength of about 7 μm. The width of the lower miniband Δ at this temperature is 9.4 meV. For an SL with doped QWs with an electron density of 10^{14} cm^{-3}, the reduced Fermi level is $-8.9k_0T$, and the average longitudinal effective mass calculated by Eq. (19) is $1.8m_0$. The effective times of longitudinal and transverse relaxation due to scalar potential of polar optical phonons were calculated by numerically solving Eqs. (7) using the sweep method and taking into account all I modes and the even G modes of the QW. Energy conservation in scattering was accounted for in the approximation $\omega_\lambda(\mathbf{q}) \approx \omega_{La}$, since the calculations show that the dispersion of I frequencies and the difference between the frequencies of the interfacial modes are much smaller than k_0T. In the table, we list the partial effective relaxation times averaged over the energies and the mobilities controlled by the scattering by all the even G modes of the QW and by the four I modes, calculated at T = 300 K. It follows from the table that the electron scattering by polar optical phonons for the SL under consideration at room temperature has a mixed character because of the scattering by the interfacial I_3 I_4 modes and by symmetric guided G modes of the QW. The total relaxation time (Σ) due to mixed scattering by all modes of the scalar potential of polar optical phonons is almost two times greater than the value obtained in the approximation of bulk (V) phonon spectrum [17] and is also greater than the effective relaxation time for scattering by polar optical phonons in the bulk GaAs [20]; the latter time is equal to 0.39 ps. In Fig. 1 we plot the temperature dependence of the mobility calculated by Eqs. (16)–(19) for scattering by polar-optical and acoustic phonons. When calculating the mobility, we took into account the temperature dependence of the miniband width, which, according to Eqs. (18) and (19), is related to the temperature dependence of the longitudinal effective mass (see Fig. 2). It can be seen from Fig. 1 that the scattering by acoustic phonons is the main mechanism of electron scattering by lattice vibrations in an SL in the entire temperature region

below 300 K, whereas in pure GaAs at room temperature scattering by polar optical phonons (curve *3*) is more important than scattering by acoustic phonons (curve *3*').

In Fig. 3, the average effective relaxation time $\langle\tau\rangle$ for scattering of electrons by polar optical phonons is shown as a function of the QW width. The calculations were carried out for T = 300K and for potential barrier thickness b = 5 nm. It follows from Fig. 3 that the average effective times $\langle\tau_\perp\rangle$ of longitudinal relaxation and $\langle\tau_\parallel\rangle$ of transverse relaxation, with allowance for total scattering by polar optical phonons, increase with the QW width (curves *4*, *4*'). The rate of increase in $\langle\tau_\perp\rangle$ is higher than in $\langle\tau_\parallel\rangle$, which gives rise to an increase in the anisotropy of the effective relaxation time. For small QW widths, the main contribution to scattering comes from the interfacial modes I_3 (curves *2*, *2*'). With increasing QW width, symmetric G modes of the QW begin to play the major role in the scattering by polar optical phonons.

4. CONCLUSIONS

From the numerical analysis of the results obtained for the SLs under consideration, we may draw the following conclusions. (i) The reconstruction of the scalar potential of polar optical phonons in an SL in the model of dielectric continuum results in weaker scattering compared to the approximation of the bulk phonon spectrum. (ii) The relative role of scattering by acoustic phonons at room temperature compared to scattering by polar optical phonons is greater in SLs than in bulk GaAs. (iii) Generally, scattering by polar optical phonons has a mixed character due to scattering by symmetric G modes of a QW and by interfacial modes with frequencies close to the frequencies of longitudinal polar optical phonons in bulk semiconductors that form the QW and potential-barrier regions.

APPENDIX I

The functions of the transverse energy appearing in functional equation (7) have the following form:

$$G_i^\pm(\varepsilon) = \left\{N_\omega + \frac{1}{2} \mp \frac{1}{2} \pm f_0(\varepsilon \pm \hbar\omega)\right\} \times \frac{f_0'(\varepsilon \pm \hbar\omega)}{f_0'(\varepsilon)} S_i^\pm(\varepsilon), \quad \text{(A.I.1)}$$

where

$$S_\perp^\pm(\varepsilon) = \frac{V}{(2\pi)^3}\int d\mathbf{k}' w(\mathbf{q}) \times \frac{\mathbf{k}_\perp'\mathbf{k}_\perp}{k_\perp^2}\delta_{\mathbf{k}',\,\mathbf{k}\pm\mathbf{q}}\delta(\varepsilon' - \varepsilon \mp \hbar\omega), \quad \text{(A.I.2)}$$

$$S_\parallel^\pm(\varepsilon) = \frac{V}{(2\pi)^3}\int d\mathbf{k}' w(\mathbf{q}) \times \frac{\sin(k_z'd)}{\sin(k_z d)}\delta_{\mathbf{k}',\,\mathbf{k}\pm\mathbf{q}}\delta(\varepsilon' - \varepsilon \mp \hbar\omega). \quad \text{(A.I.3)}$$

In the quasi-2D approximation, taking into account that the function $w(\mathbf{q})$ is even and periodic in q_z,

$$w\left(\mathbf{q}_\perp, q_z \pm \frac{2\pi}{d}n\right) = w(\mathbf{q}_\perp, q_z), \quad \text{(A.I.4)}$$

we obtain the following expressions for $S(\varepsilon)$:

$$S_\perp^\pm(\varepsilon) = \frac{V}{(2\pi)^3}\int d\mathbf{k}_\perp' w_\perp(\mathbf{q}_\perp) \times \frac{\mathbf{k}_\perp'\mathbf{k}_\perp}{k_\perp^2}\delta_{\mathbf{k}_\perp',\,\mathbf{k}_\perp\pm\mathbf{q}_\perp}\delta(\varepsilon' - \varepsilon \mp \hbar\omega), \quad \text{(A.I.5)}$$

$$S_\parallel^\pm(\varepsilon) = \frac{V}{(2\pi)^3}\int d\mathbf{k}_\perp' w_\parallel(\mathbf{q}_\perp) \times \delta_{\mathbf{k}_\perp',\,\mathbf{k}_\perp\pm\mathbf{q}_\perp}\delta(\varepsilon' - \varepsilon \mp \hbar\omega), \quad \text{(A.I.6)}$$

where

$$w_\perp(\mathbf{q}_\perp) = 2\int_0^{\pi/2} w(\mathbf{q})dq_z, \qquad w_\parallel(\mathbf{q}_\perp) = 2\int_0^{\pi/d} w(\mathbf{q})\cos(q_z d)dq_z. \quad \text{(A.I.7)}$$

APPENDIX II

According to the dielectric continuum model [16], the scalar potential of polar optical phonons in a SL for the G and I modes in normal coordinates has the form

$$V(\mathbf{r}) = \sum_{\lambda\mathbf{q}}\left(\frac{\hbar}{2\omega_{\lambda\mathbf{q}}\rho_\mu(z)}\right)^{1/2} \times [a_\lambda^+(-\mathbf{q}) + a_\lambda(\mathbf{q})] f_{\lambda\mathbf{q}}(z)e^{i\mathbf{q}_\perp\mathbf{r}_\perp}, \quad \text{(A.II.1)}$$

where $\rho_\mu(z)$ is the specific reduced mass of the atoms in a unit cell and λ is the vibrational mode number. The function $f(z)$ satisfying the Bloch theorem with the SL period d is a solution to the Poisson equation

$$\nabla\varepsilon(z)\nabla\frac{1}{\sqrt{\rho_\mu(z)}}f(z)e^{i\mathbf{q}_\perp\mathbf{r}_\perp} = 0, \quad \text{(A.II.2)}$$

where

$$\varepsilon(z) = \varepsilon(z + dm) = \varepsilon_\infty\frac{\omega_L^2 - \omega^2}{\omega_T^2 - \omega^2}$$

is the high-frequency permittivity for III–V semiconductors. For interfacial vibrations whose frequencies do not coincide with the longitudinal optical-phonon frequency of the bulk spectrum in semiconductors of the QW and of the potential barrier, the function $f(z)$ is a solution to the equation

$$\frac{d}{dz}f(z) = q_\perp^2 f(z). \quad \text{(A.II.3)}$$

Over the SL period with the origin at the QW center, this function has the following form:

$$f(z) = \begin{cases} A_1 e^{q_\perp z} + B_1 e^{-q_\perp z}, & -a/2 \le z < a/2; \\ A_2 e^{q_\perp z} + B_2 e^{-q_\perp z}, & -d/2 \le z < -a/2; \\ A_3 e^{q_\perp z} + B_3 e^{-q_\perp z}, & a/2 \le z < d/2. \end{cases} \quad \text{(A.II.4)}$$

The unknown amplitudes in (A.II.4) satisfy the system of linear equations that follow from the boundary conditions for the scalar potential and for the normal component of the electric field at the heterointerfaces. The condition for nontrivial solution of this system leads to the following secular equation for the frequencies of interfacial vibrations:

$$\cosh(aq_\perp)\cosh(bq_\perp) + \frac{1}{2}\left(x + \frac{1}{x}\right)\sinh(aq_\perp)\sinh(bq_\perp) = \cos(dq_z), \quad \text{(A.II.5)}$$

where

$$x = x(\omega) = \varepsilon_a(\omega)/\varepsilon_b(\omega). \quad \text{(A.II.6)}$$

Equation (A.II.5) with respect to x is a second-degree algebraic equation; its roots can be found analytically; i.e.,

$$x_{1,2} = w \pm \sqrt{w^2 - 1}, \quad \text{(A.II.7)}$$

where

$$w = \frac{\cos(dq_z) - \cosh(aq_\perp)\cosh(bq_\perp)}{\sinh(aq_\perp)\sinh(bq_\perp)}.$$

According to Eq. (A.II.6), two frequencies correspond to each of the roots:

$$\omega_{1,2}^2 = u \pm \sqrt{u^2 - \frac{\varepsilon_{\infty a}\omega_{La}^2\omega_{Tb}^2 - \varepsilon_{\infty b}\omega_{Lb}^2\omega_{Ta}^2 x}{\varepsilon_{\infty a} - \varepsilon_{\infty b}x}}, \quad \text{(A.II.8)}$$

where

$$u = \frac{\varepsilon_{\infty a}(\omega_{La}^2 + \omega_{Tb}^2) - \varepsilon_{\infty b}(\omega_{Lb}^2 + \omega_{Ta}^2)x}{2(\varepsilon_{\infty a} - \varepsilon_{\infty b}x)}.$$

Using (A.II.4) and (A.II.6), we can write the function $\vartheta = \vartheta_\lambda(\mathbf{q})$ in Eq. (10) as

$$\vartheta = \vartheta_\lambda(\mathbf{q}) = \frac{B_1}{A_1} = \frac{(e^{idq_z} + e^{aq_\perp})(e^{bq_\perp} - 1)x - (e^{idq_z} - e^{aq_\perp})(e^{bq_\perp} + 1)}{(e^{idq_z}e^{aq_\perp} + 1)(e^{bq_\perp} - 1)x + (e^{idq_z}e^{aq_\perp} - 1)(e^{bq_\perp} + 1)}. \quad \text{(A.II.9)}$$

The solution of the system of linear equations for amplitudes in the potential barrier region yields

$$B_2 = B_3 e^{-(q_\perp + iq_z)d}, \quad A_2 = A_3 e^{(q_\perp - iq_z)d}; \quad \text{(A.II.10)}$$

$$A_3 = \sqrt{\frac{\rho_{\mu b}}{\rho_{\mu a}}}\left\{\frac{1+x}{2}A_1 + \frac{1-x}{2}B_1 e^{-aq_\perp}\right\},$$
$$B_3 = \sqrt{\frac{\rho_{\mu b}}{\rho_{\mu a}}}\left\{\frac{1-x}{2}A_1 e^{aq_\perp} + \frac{1+x}{2}B_1\right\}. \quad \text{(A.II.11)}$$

After introducing the normal coordinates, we can write the expression for the normalized amplitude A_1 in the form of an analytical function,

$$A_1 = \sqrt{\frac{d}{q_\perp V}}\left\{4c_a^2\sinh(aq_\perp) + c_b^2 e^{dq_\perp}\sinh(bq_\perp)\frac{\rho_{\mu b}}{\rho_{\mu a}} \times \left|e^{-aq_\perp}\left(1 - \frac{\varepsilon_a}{\varepsilon_b}\right) + \vartheta\left(1 + \frac{\varepsilon_a}{\varepsilon_b}\right)\right|^2\right\}^{-1/2}. \quad \text{(A.II.12)}$$

For symmetric guided QW G modes with frequency ω_{La} and number $m = 2n + 1$, the normalized function $f_{m\mathbf{q}}(z)$ in formula (A.II.1) for the scalar potential has the form (over an SL period)

$$f_{m\mathbf{q}}(z) = \begin{cases} \sqrt{\frac{2ad}{c_{aL}^2 V}}\cos\left(\frac{\pi}{a}mz\right)/[(aq_\perp)^2 + (m\pi)^2]^{1/2}, & |z| \le \frac{a}{2}; \\ 0, & \frac{a}{2} < |z| < \frac{d}{2}. \end{cases} \quad \text{(A.II.13)}$$

It should be noted that, for the case of guided modes, the function $f_{m\mathbf{q}}(z)$ does not depend on the longitudinal component of the wave vector and rapidly decreases with increasing m.

In the approximation of the spectrum of bulk polar optical phonons, the function $f(z)$ has a single branch and, according to formula (A.II.1), can be written as

$$f_{\mathbf{q}}(z) = -i\sqrt{\frac{\rho_\mu(z)}{\varepsilon_0\varepsilon^*(z)V}}\frac{\omega_L(z)}{q}\exp(iq_z z). \quad \text{(A.II.14)}$$

REFERENCES

1. B. K. Ridley, Phys. Rev. B **39**, 5282 (1989).
2. G. Q. Hai, F. M. Peeters, and J. T. Devreese, Phys. Rev. B **48**, 4666 (1993).
3. G. Q. Hai, F. M. Peeters, and J. T. Devreese, Phys. Rev. B **62**, 10572 (2000).
4. V. V. Bondarenko and F. F. Sizov, Phys. Low-Dimens. Semicond. Struct., Nos. 8–9, 123 (1995).
5. D. N. Mirlin and A. V. Rodina, Fiz. Tverd. Tela (St. Petersburg) **38**, 3201 (1996) [Phys. Solid State **38**, 1749 (1996)].
6. X. Zianni, C. D. Simserides, and G. P. Triberis, Phys. Rev. B **55**, 16324 (1997).
7. C. R. Bennett, M. A. Amato, N. A. Zakhleniuk, *et al.*, J. Appl. Phys. **83**, 1499 (1998).
8. B. A. S. Camacho, Phys. Status Solidi B **220**, 53 (2000).
9. J. Pozela, A. Namajunas, K. Pozela, and V. Juciene, Physica E (Amsterdam) **5**, 108 (1999).
10. Z. Yisong, Lu Tianquan, Liu Jiang, and Su Wenhui, Semicond. Sci. Technol. **12**, 1235 (1997).
11. M. Alcalde Augusto and Weber Gerald, Phys. Rev. B **56**, 9619 (1997).
12. Duan Wenhui, Zhu Jia-Lin, Gu Bing-Lin, and Wu Jian, Solid State Commun. **114**, 101 (2000).
13. K. Pozela, Fiz. Tekh. Poluprovodn. (St. Petersburg) **35**, 1361 (2001) [Semiconductors **35**, 1305 (2001)].
14. D. R. Anderson, N. A. Zakhleniuk, M. Babiker, *et al.*, Phys. Rev. B **63**, 245313 (2001).
15. G. J. Warren and P. N. Butcher, Semicond. Sci. Technol. **1**, 133 (1986).
16. I. Dharssi and P. N. Butcher, J. Phys.: Condens. Matter **2**, 119 (1990).
17. S. I. Borisenko, Fiz. Tekh. Poluprovodn. (St. Petersburg) **36**, 861 (2002) [Semiconductors **36**, 808 (2002)].
18. *Landolt–Börnstein, Numerical Data and Functional Relationships in Science and Technology*, Ed. by O. Madelung (Springer, Berlin, 1987), New Ser. III, Vol. 22a.
19. S. I. Borisenko and G. F. Karavaev, Fiz. Tekh. Poluprovodn. (St. Petersburg) **32**, 607 (1998) [Semiconductors **32**, 544 (1998)].
20. S. I. Borisenko, Fiz. Tekh. Poluprovodn. (St. Petersburg) **35**, 313 (2001) [Semiconductors **35**, 298 (2001)].

Translated by I. Zvyagin

Semiconductors, Vol. 38, No. 2, 2004, pp. 209–212. Translated from Fizika i Tekhnika Poluprovodnikov, Vol. 38, No. 2, 2004, pp. 213–217.

LOW-DIMENSIONAL SYSTEMS

Effect of In and Al Content on Characteristics of Intrinsic Defects in GaAs-Based Quantum Dots

T. V. Bezyazychnaya*, V. M. Zelenkovskiĭ*, G. I. Ryabtsev, and M. M. Sobolev*****

**Institute of Physicoorganic Chemistry, National Academy of Sciences of Belarus, Minsk, 220072 Belarus*

***Stepanov Institute of Physics, National Academy of Sciences of Belarus, Minsk, 220072 Belarus*

****Ioffe Physicotechnical Institute, Russian Academy of Sciences, St. Petersburg, 194021 Russia*

e-mail: m.sobolev@mail.ioffe.ru

Submitted May 19, 2003; accepted for publication May 20, 2003

Abstract—The effect of In and Al on the properties of the As_{Ga} defect complex (arsenic substituted for gallium at a crystal lattice site) in GaAs-based quantum dots (QDs) was investigated using the nonempirical quantum-chemical SCF–MO–LCAO technique. It is shown that an As_{Ga} defect can exist in stable and metastable states. Raising the indium or aluminum content in QD enhances the probability of As_{Ga} defect formation in the stable state; in case of In introduction, this effect is manifested more strongly. The activation energy of the transition between stable and metastable states varies between 0.886 and 2.049 eV, depending on the QD stoichiometry. The formation of an As_{Ga} defect gives rise to two deep levels in the band gap. *© 2004 MAIK "Nauka/Interperiodica".*

1. INTRODUCTION

The formation of In(GaAs) quantum dots (QD) by self-organized growth is accompanied by the generation of structural defects, which can affect the characteristics of optoelectronic devices with quantum-confined active layers [1–6]. One of these defects is an intrinsic defect designated in the literature as *EL2* [5, 7, 8]. It is observed in both doped and undoped GaAs, and its concentration can be high.

In the literature there is no unanimous opinion about not only the atomic composition of the *EL2* defect, but also its influence on the electronic and optical properties of crystals. It is pointed out that *EL2* exhibits thermal and optical metastability associated with the structural reconstruction of the defect [9, 10]. It is assumed that the defect is an As_{Ga} complex (an As atom substitutes for Ga at a crystal lattice site) and its aggregations with other defects in GaAs [11–13]. It has been suggested [14] that the metastability of an *EL2* defect may be related to the transfer of an As atom from the lattice site normally occupied by the Ga atom to an interstice, with the formation of a complex including As_{Ga} and a Ga vacancy. The influence of the content of impurity atoms capable of entering into the composition of GaAs-based QDs on the *EL2* characteristics has not been studied.

This paper is devoted to studying the influence of In and Al content on the properties of an As_{Ga} defect in GaAs-based QDs. The process of defect formation was investigated using the nonempirical quantum-chemical SCF–MO–LCAO approach (the self-consistent field method, which represents each molecular orbital as a linear combination of atomic orbitals). The computer simulation was performed in the cluster approximation; i.e., a limited fragment was cut from the crystal lattice, with the initial positions of atoms corresponding to their positions at the sites of an actual lattice.

2. CALCULATION PROCEDURE

The parameters of the As_{Ga} defect were calculated using the GAMESS software package [15, 16]. The basis set MINI was used, which enables one to calculate the energy of chemical bonds and intermolecular interactions in crystalline compounds quite precisely [17]. A 26-atom fragment of crystal lattice of a GaAs-based QD was chosen as a cluster model (Fig. 1). The dangling bonds at the cluster boundary were satisfied with hydrogen (30 atoms); this excluded distortions of the electronic structure related to the effect of unpaired electrons on the cluster surface. The boundary hydrogen atoms make it possible to approximately take into account the interface between the QD and the matrix in the modeling.

To model an intrinsic point defect As_{Ga}, a Ga atom at the lattice site (in the center of the cluster) was replaced by an As atom. The length of the Ga–As bond in the cluster was chosen as 2.44 Å, so that the lattice constant was matched with the lattice constant of bulk GaAs crystal, 5.65 Å. The effect of In or Al content on the characteristics of such a defect was simulated by replacing a part of the Ga atoms by Al or In atoms in a specific percentage amount (from 10 to 40%).

To calculate the defect structure, a full gradient optimization of the cluster geometrical parameters (bond lengths, valence and torsion angles) within the first

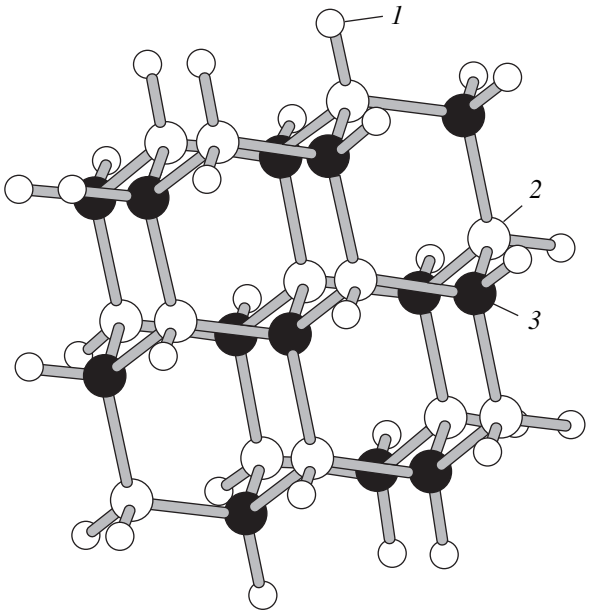

Fig. 1. A model of a 26-atom GaAs cluster. Atoms: (*1*) H, (*2*) Ga, and (*3*) As.

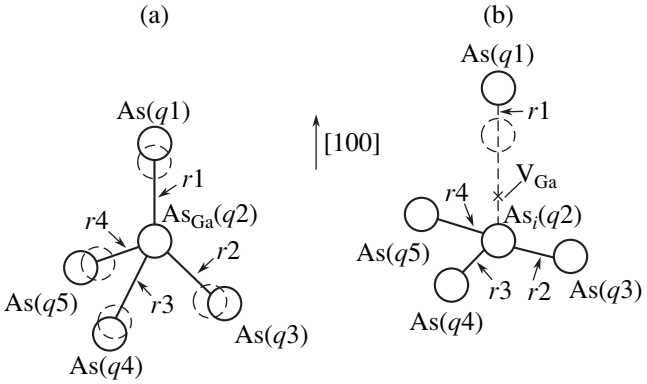

Fig. 2. The structure of an As_{Ga} defect as obtained in the calculation of GaAs, $Al_{1-x}Ga_xAs$, and $In_{1-x}Ga_xAs$ clusters: (a) stable, (b) metastable state.

coordination sphere was done. This approach allows one to determine the crystal lattice relaxation in the defect region, taking account of the crystal field of the environment.

3. RESULTS AND DISCUSSION

The calculation of the parameters of GaAs clusters containing Al and In allowed us to reveal two minima, which differ in energy, on the potential energy surface of the system. It appeared that they correspond to two relatively stable structural states of the As_{Ga} defect in the cluster, which hereinafter we will refer to as "stable" and "metastable." Similar defect structures were discussed in [18] for the case of undoped GaAs.

Figure 2 shows the structures corresponding to stable and metastable states of an As_{Ga} defect, and Table 1 lists interatomic distances r and charges q on atoms incorporated into clusters: GaAs, $Al_{0.1}Ga_{0.9}As$, $Al_{0.2}Ga_{0.8}As$, $Al_{0.4}Ga_{0.6}As$, $In_{0.1}Ga_{0.9}As$, $In_{0.2}Ga_{0.8}As$, and $In_{0.4}Ga_{0.6}As$.

As is seen in Fig. 2, the lattice structure in the vicinity of the defect is distorted when an As atom is substituted for Ga at the lattice site. When the stable state is formed, all the As_{Ga}–As bonds are slightly elongated compared to the Ga–As bond, symmetrically in all directions (Fig. 2a, Table 1). After relaxation of the nearest environment, the As_{Ga} atom remains at the lattice site owing to the lower strength of the As_{Ga}–As bond in comparison with the Ga–As bond. In the metastable state of an As_{Ga} defect, three As atoms remain in their places, and the fourth, which has a lowered coordination number, is shifted toward the plane in which the three Ga atoms bonded to it lie (Fig. 2b, Table 1). The As atom replacing Ga is shifted toward the interstice and is located just below the plane containing three As atoms bonded to it. The metastable state of an As_{Ga} defect can be considered as a complex comprising a Ga vacancy V_{Ga} and an interstitial As atom.

The analysis of the distribution of charge on atoms in a GaAs cluster that models the defect-free lattice shows that an As atom at a site is charged negatively ($-0.32\bar{e}$). This means that an As atom accepts part of the electron density from Ga atoms. In the metastable state of an As_{Ga} defect, the charge on the As atom is virtually zero ($q2 = +0.06\bar{e}$, Table 1), with As in a trivalent state typical of its covalent molecular compounds.

With the formation of a defect, the distribution of charges in a cluster is modified. In the stable state of an As_{Ga} defect, the As atom is at the lattice site; it forms four As–As bonds. As is seen in Table 1, in this case the As atom accepts a considerable positive charge $q2 = +0.35\bar{e}$; in other words, a large part of the electron density is transferred from the As_{Ga} atom to neighboring atoms. This redistribution of the electron density can give rise to deep donor levels in the energy gap of (Al,Ga)As crystal; they can be related to the *EL2* defect [5, 7, 8].

One should note that the total charge of an As_{Ga} defect is nearly the same for stable and metastable states, but its distributions between the atoms in the defect region are substantially different in different states. The addition of Al or In atoms to a GaAs lattice does not significantly change the charges on atoms and the structural parameters of the defect, neither in the stable nor in the metastable state (Table 1). At the same time, the energy parameters of an As_{Ga} defect are noticeably modified when the content of aluminum or indium in a GaAs lattice increases.

The difference between the energies of stable and metastable state ΔE and the activation energy E_a of the transition from the stable to the metastable state of an

Table 1. Interatomic distances and atomic charges in relation to Al and In content for stable and metastable states of an As_{Ga} defect in GaAs, $Al_xGa_{1-x}As$, and $In_xGa_{1-x}As$

Compound	Stable state								
	interatomic distances, Å				atomic charges, elementary charge units				
	r^1	r^2	r^3	r^4	q^1	q^2	q^3	q^4	q^5
GaAs	2.60	2.59	2.60	2.59	–0.48	+0.35	–0.38	–0.39	–0.39
$Al_{0.1}Ga_{0.9}As$	2.60	2.59	2.60	2.60	–0.49	+0.35	–0.38	–0.39	–0.39
$Al_{0.2}Ga_{0.8}As$	2.60	2.59	2.60	2.60	–0.49	+0.35	–0.38	–0.40	–0.39
$Al_{0.4}Ga_{0.6}As$	2.60	2.59	2.60	2.60	–0.49	+0.35	–0.40	–0.40	–0.39
$In_{0.1}Ga_{0.9}As$	2.60	2.56	2.61	2.56	–0.40	+0.35	–0.38	–0.40	–0.50
$In_{0.2}Ga_{0.8}As$	2.63	2.54	2.55	2.55	–0.42	+0.35	–0.41	0.37	–0.51
$In_{0.4}Ga_{0.6}As$	2.63	2.54	2.53	2.58	–0.42	+0.36	–0.40	–0.40	–0.52
Metastable state									
GaAs	3.46	2.43	2.43	2.43	–0.50	+0.06	–0.24	–0.36	–0.24
$Al_{0.1}Ga_{0.9}As$	3.46	2.43	2.43	2.43	–0.50	+0.06	–0.24	–0.38	–0.24
$Al_{0.2}Ga_{0.8}As$	3.46	2.43	2.43	2.43	–0.50	+0.06	–0.24	–0.26	–0.24
$Al_{0.4}Ga_{0.6}As$	3.46	2.43	2.43	2.43	–0.50	+0.06	–0.26	–0.26	–0.38
$In_{0.1}Ga_{0.9}As$	3.48	2.41	2.40	2.40	–0.50	+0.06	–0.23	–0.40	–0.24
$In_{0.2}Ga_{0.8}As$	3.50	2.40	2.39	2.39	–0.51	+0.06	–0.23	–0.40	–0.27
$In_{0.4}Ga_{0.6}As$	3.49	2.40	2.39	2.38	–0.51	+0.07	–0.29	–0.27	–0.40

Table 2. The difference between the energies of stable and metastable state ΔE and the activation energy E_a of the transition from the stable to the metastable state of an As_{Ga} defect with different Al or In content in GaAs, $Al_xGa_{1-x}As$, and $In_xGa_{1-x}As$

	GaAs	$Al_{0.1}Ga_{0.9}As$	$Al_{0.2}Ga_{0.8}As$	$Al_{0.4}Ga_{0.6}As$	$In_{0.1}Ga_{0.9}As$	$In_{0.2}Ga_{0.8}As$	$In_{0.4}Ga_{0.6}As$
ΔE, eV	0.70	0.71	0.73	0.74	0.85	0.88	0.90
E_a, eV	1.05	1.86	1.86	0.97	2.05	0.89	1.84

As_{Ga} defect are listed in Table 2 for different Al or In content in GaAs, $Al_xGa_{1-x}As$, and $In_xGa_{1-x}As$. The quantity ΔE characterizes the relative probability of the formation of structures corresponding to stable and metastable defect states in the crystal. As follows from Table 2, the rise of Al or In content raises the probability that an As_{Ga} defect will occur in a stable state. This effect is manifested more strongly when In atoms are introduced into the crystal.

To estimate E_a, the structures of the corresponding transition states were calculated. These structures were defined based on the conjectured path of As atom transfer from a site to an interstice (stable to metastable state of the defect), taking the lattice symmetry into account. Figure 3 shows schematically the displacement of an As atom from the lattice site to an interstice, which corresponds to the transition of a defect from the stable to the metastable state. For each of the clusters that model different In or Al content in the lattice, the calculations revealed on the potential energy surfaces extremal points corresponding to the structures in which the As atom lies in the plane of the three As atoms bonded to it. The activation energy E_a was determined as the difference between the total energies of the cluster at the extremal point (transition state) and in the stable state.

It is seen from Table 2 that the introduction of In or Al into a GaAs crystal lattice raises the activation energy of the transition between the stable and the metastable state of the defect. The nonmonotonic dependence of E_a on In content may indicate the influence of In distribution in the crystal to the activation energy. To obtain better estimation of the E_a dependence on In content, is seems necessary to raise the number of atoms in clusters. For an Al content of 10–20%, the activation energy remains virtually unchanged. At the same time, the activation energy sharply decreases at 40% Al, which may indicate a considerable modification of energy characteristics of the crystal lattice in the defect region.

The limited size of the clusters used in the study give no way of describing precisely the band structure of the materials under study. Nevertheless, the contribution of an As_{Ga} defect to the electronic structure of the cluster was estimated based on the calculated eigenenergies and eigenvectors of the corresponding molecular orbitals. It appeared that this defect gives rise to two deep

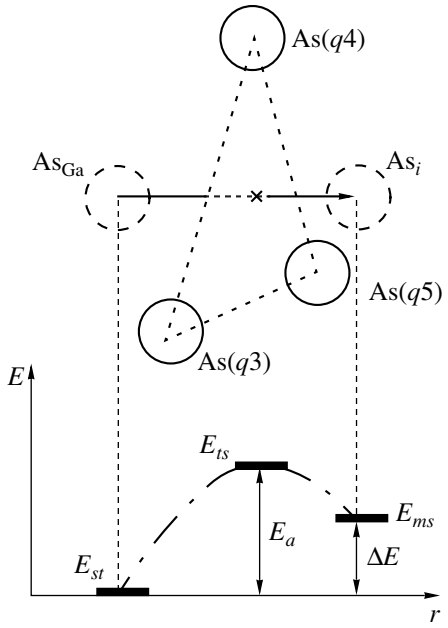

Fig. 3. Schematics of the defect transition from stable (As_{Ga}) to metastable ($As_i + V_{Ga}$) state: E_{st} is the total energy of the cluster in the stable state; E_{ts}, the energy of the transition state; E_{ms}, the total energy of a metastable state. The sign × marks the position of the As atom corresponding to the transition state.

levels in the band gap, which qualitatively agrees with the results of [14]. According to our estimates, the positions of these levels in respect to the top of the valence band in undoped GaAs are $E_{S1} = 0.40$ eV, $E_{S2} = 1.26$ eV for the stable and $E_{M1} = 0.23$ eV, $E_{M2} = 1.32$ eV for the metastable state. The addition of In or Al only slightly affects the positions of E_{S1}, E_{S2}, and E_{M1} levels, whereas the energy E_{M2} decreases by 0.26 eV. At a 40% In/Al content, only one level E_{M1} appears in the metastable state of a As_{Ga} defect.

4. CONCLUSION

The effect of In and Al content on the properties of As_{Ga} defects in GaAs-based QDs has been investigated using the nonempirical quantum-chemical SCF–MO–LCAO technique. It is shown that a As_{Ga} defect can exist in stable or metastable states, which differ in their structural, electronic, and energy characteristics. Increasing the In or Al content enhances the probability that the As_{Ga} defect will form in the stable state; this effect is manifested more strongly in the case of In introduction into a QD. The activation energy of the transition between the stable and the metastable state varies between 0.886 and 2.049 eV, depending on the QD stoichiometry. The formation of an As_{Ga} defect gives rise to two deep levels in the band gap, whose positions are also dependent on the introduction of In or Al.

ACKNOWLEDGMENTS

This study was supported in part by the program SCOPES (Scientific Cooperation between Eastern Europe and Switzerland) 2000–2003 (project no. 7 SUP JO62392), the scientific program “Physics of Solid-State Nanostructures,” and the Russian Foundation for Basic Research (project no. 00-03-16703).

The authors are grateful to A. L. Gurskiĭ for valuable discussion.

REFERENCES

1. M. Sugawara, K. Mukai, and H. Shoji, Appl. Phys. Lett. **71**, 2791 (1997).
2. Zh. I. Alferov, Fiz. Tekh. Poluprovodn. (St. Petersburg) **32**, 3 (1998) [Semiconductors **32**, 1 (1998)].
3. Zhao Zhen, D. A. Bedarev, B. V. Volovik, *et al.*, Fiz. Tekh. Poluprovodn. (St. Petersburg) **33**, 91 (1999) [Semiconductors **33**, 80 (1999)].
4. M. M. Sobolev, I. V. Kochnev, V. M. Lantratov, *et al.*, Physica B (Amsterdam) **273–274**, 959 (1999).
5. M. M. Sobolev, I. V. Kochnev, V. M. Lantratov, *et al.*, Fiz. Tekh. Poluprovodn. (St. Petersburg) **34**, 200 (2000) [Semiconductors **34**, 195 (2000)].
6. M. M. Sobolev, I. V. Kochnev, V. M. Lantratov, and N. N. Ledentsov, Fiz. Tekh. Poluprovodn. (St. Petersburg) **35**, 1228 (2001) [Semiconductors **35**, 1175 (2001)].
7. G. M. Martin, Appl. Phys. Lett. **39**, 747 (1981).
8. G. A. Baraff and M. Schluter, Phys. Rev. B **35**, 6154 (1987).
9. A. Chantre and D. Bois, Phys. Rev. B **31**, 7979 (1985).
10. J. J. Van Kooten, G. A. Waller, and C. A. J. Ammerlaan, Phys. Rev. B **30**, 4564 (1984).
11. J. F. Wager and J. A. Van Vechten, Phys. Rev. B **35**, 2330 (1987).
12. G. A. Baraff and M. Schluter, Phys. Rev. Lett. **55**, 2340 (1985).
13. H. J. Von Bardeleben, D. Stieveard, D. Deresmes, *et al.*, Phys. Rev. B **34**, 7192 (1986).
14. J. Dabrovskii and M. Scheffler, Phys. Rev. B **40**, 10391 (1989).
15. M. W. Schmidt, K. K. Baldridge, J. A. Boatz, *et al.*, J. Comput. Chem. **14**, 1347 (1993); A. A. Granovsky, http://classic.chem.msu.su/gran/gamess/index.html.
16. M. Dupuis, J. D. Watts, H. O. Villar, and G. J. B. Hurst, Comput. Phys. Commun. **52**, 415 (1989).
17. S. Huzinaga, J. Andzelm, M. Klobukowski, E. Radzio-Andzelm, Y. Sakai, and H. Tatewaki, *Gaussian Basis Sets for Molecular Calculations* (Elsevier, Amsterdam, 1984).
18. D. J. Chadi and K. J. Chang, Phys. Rev. Lett. **60**, 2187 (1988).

Translated by D. Mashovets

Semiconductors, Vol. 38, No. 2, 2004, pp. 213–216. Translated from Fizika i Tekhnika Poluprovodnikov, Vol. 38, No. 2, 2004, pp. 218–221.

LOW-DIMENSIONAL SYSTEMS

Normal-Incidence Responsivity of MOCVD-Grown Multiple Quantum Well Structures

V. B. Kulikov*^, G. H. Avetisyan*, L. M. Vasilevskaya*, I. D. Zalevskiĭ, I. V. Budkin**, and A. A. Padalitsa****

**Pulsar State Unitary Research and Production Enterprise, Moscow, 105187 Russia*

^e-mail: vladimir_kulikov@mtu-net.ru

***Sigm Plus Co. Ltd., Moscow, 109377 Russia*

Submitted April 15, 2003; accepted for publication May 22, 2003

Abstract—Recently, the MOCVD method has been increasingly used in the fabrication of multiple quantum well (MQW) devices, along with MBE technology. The authors' experience in working with MQW photodetectors shows several differences between the devices grown by MOCVD and their MBE-grown analogues. These are the stronger asymmetry of the current–voltage characteristic and high responsivity under normal incidence of light without special input units. The authors believe that these distinctions are due to specific features of the epitaxy process. The results of an experimental study of MQW photodetectors are presented, and the correlation between their properties and the structural features related to MOCVD is discussed. © *2004 MAIK "Nauka/Interperiodica".*

1. INTRODUCTION

Until recently, in the published experimental studies of photoconductivity in structures with multiple quantum wells (MQW), these structures have been MBE-grown. Our experience in studying MOCVD-grown MQW structures shows that the photoconductivity of these structures is characterized by several specific features compared with those grown by MBE. These features are the stronger asymmetry of the current–voltage (*I–V*) characteristic and high responsivity under normal incidence of light without special input units. We believe that these features are related to differences in the technologies of MQW growth.

We present the results of an experimental study of MQW photodetectors produced by MOCVD and discuss their correlation with specific features of MQWs that are caused by the epitaxy method.

2. SAMPLES

The structures under study were grown by MOCVD on semi-insulating ⟨100⟩ GaAs substrates at a pressure of 65 mm Hg and a temperature of ~700°C. The MQW structures comprised 50 heterostructure periods with 50 Å-thick GaAs QWs and 450 Å-thick $Al_xGa_{1-x}As$ (x = 024) barrier layers. The wells were doped with Si to a concentration of 10^{18} cm^{-3}. The top and bottom contact layers, which were 0.5 and 1 μm thick, respectively, were doped to a concentration exceeding 10^{18} cm^{-3}.

Experimental photoresistors were fabricated in the form of mesa structures 400×400 μm^2 in size from the grown structures by chemical etching. No special light input devices, such as diffraction gratings, were used. Ohmic contacts were fabricated by the deposition of Au:Ge alloy through the photoresist mask and explosive treatment of the deposited layer and its subsequent firing-in. The contacts thus obtained were covered with Ti and Al layers.

3. EXPERIMENTAL RESULTS

In the experimental investigations of the photoresistors, *I–V* characteristics at different temperatures and responsivity spectra were measured and the dependences of the absolute responsivity at the peak of the spectrum and the noise current on bias were determined. The data obtained were used to calculate the photoelectric gain and the detectivity of the photoresistors as functions of bias and temperature. The responsivity spectra were recorded using a special stand based on an MDR-41 monochromator. The absolute responsivity was measured with a source of modulated light in which a model absolute black body with a temperature of 573 K served as the emitter. The modulation frequency was 1200 Hz. The signals and noises of the photoresistors were measured using a narrow-band amplifier with a resonance frequency of 1200 Hz and bandwidth of 200 Hz. During measurements, the samples under study were placed in a pumped liquid nitrogen cryostat, which enabled the samples to be cooled to 60 K. A cooled diaphragm mounted in front of the sample limited the field of view to an angle of ~25°.

Figure 1 shows the *I–V* characteristics of a photoresistor protected from the background illumination by a cold screen. The right portions of the *I–V* characteristics (positive bias) were obtained with the top contact of

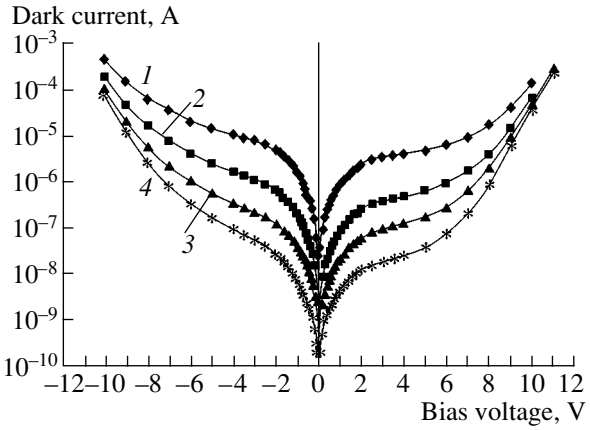

Fig. 1. *I–V* characteristics of MQW photoresistors at temperatures of (*1*) 78, (*2*) 70, (*3*) 65, and (*4*) 60 K.

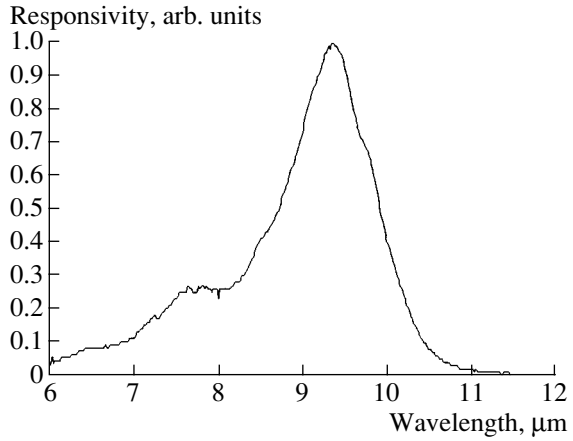

Fig. 2. Responsivity spectrum of MQW photoresistors.

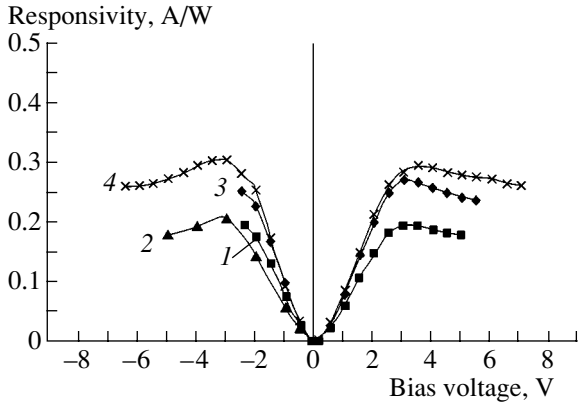

Fig. 3. Absolute responsivity of MQW photoresistors at the peak of the spectrum as a function of bias. Curve numbers as in Fig. 1.

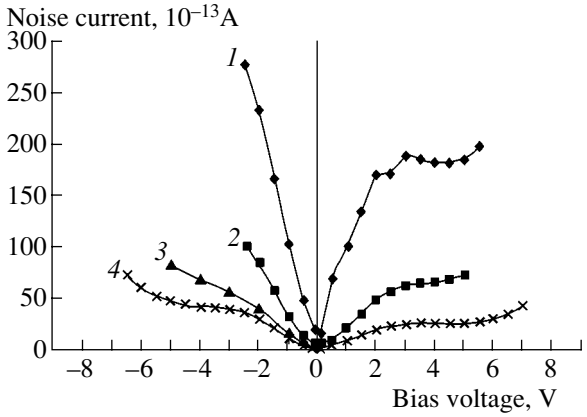

Fig. 4. Noise current in MQW photoresistors as a function of bias. Curve numbers as in Fig. 1.

the photoresistor negative, i.e., with the direction of field coinciding with the direction of growth of an MQW structure. The *I–V* characteristics of the studied samples were distinctly asymmetrical. Note that higher responsivity is observed with the top contact positive at the same bias magnitude.

Figure 2 shows the responsivity spectrum recorded with the top contact of a photoresistor positive. The shape of the spectrum and the position of its peak do not change significantly as the temperature varies within the range 60–77 K, or bias, within 1–4 V.

Figure 3 shows the absolute responsivity of a photoresistor at the peak of the spectrum as a function of bias for both bias polarities and different temperatures. The dependences were calculated considering the coefficient of utilization of light emitted by the absolutely black body, which was calculated by numerical integration of the responsivity spectrum (Fig. 2). Along with the asymmetry of these dependences, it is worth noting the magnitude of responsivity, which is several tenths of A/W. Such a high responsivity was obtained in photoresistors without special devices for inputting light normally incident onto the front surface of a photoresistor. Figure 4 shows the dependences of noise current I_n on bias for both bias polarities at different temperatures. Based on these curves and using the known relation $I_n = (4eI_d g\Delta f)^{1/2}$ (here e is the elementary charge; I_d, the dark current; g, the photoelectric gain; Δf, the frequency band in which noise is recorded), we calculated the dependences of photoelectric gain on bias, which are shown in Fig. 5. The g value lies in the limits 0.5–0.6, which is typical of photoresistors based on MBE-grown structures and is an indication that the barrier layers in the samples under study are of fair quality.

Figure 6 shows the dependences of photoresistor detectivity $D^*_{\lambda\max}$ on bias at different temperatures. The value of $D^*_{\lambda\max}$ was calculated based on the data obtained in measurements of the absolute responsivity and noise current (Figs. 3, 4).

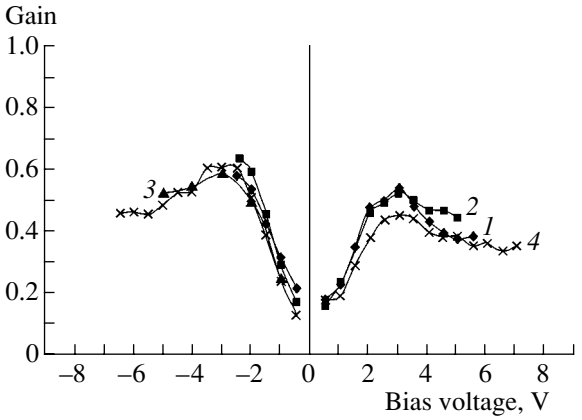

Fig. 5. Photoelectric gain of MQW photoresistors as a function of bias. Curve numbers as in Fig. 1.

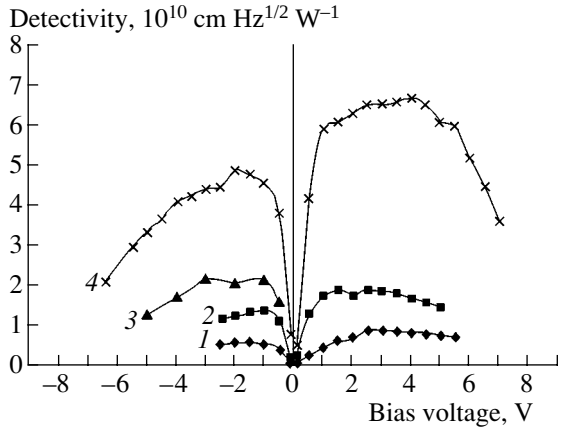

Fig. 6. Detectivity of MQW photoresistors as a function of bias. Curve numbers as in Fig. 1.

4. DISCUSSION OF RESULTS

Based on the data obtained, we conclude that our structures contain QWs that are not symmetrical. The last assertion can be made, albeit based on the fact that *I–V* characteristics and responsivity dependences on bias are asymmetrical. Similar results were obtained for MBE-grown MQW structures with wells that are intentionally fabricated asymmetrical [1]. It was also shown in [1] that, for the same magnitude of applied bias, in the case when the external field is directed toward a sharper interface of an asymmetric well higher responsivity and higher currents are observed than in the opposite case. The asymmetry of the well interfaces can induce a difference in the coefficients of the above-barrier reflection of carriers and, consequently, a difference in the photoelectric gain at opposite bias polarities. Taking these data into account in the analysis of dependences shown in Figs. 1 and 3, we can assume that the initial barrier interfaces (i.e., the interfaces between a QW and a barrier layer at the start of its growth) are less abrupt than the final ones.

Now we turn to the anomalously high responsivity under normal incidence of light without special input devices. It is known that the responsivity depends on two factors: photoelectric gain g and quantum efficiency η. As mentioned above, g is not anomalously high. An estimate of η from the relation for the photoresistor responsivity $R_{\lambda\max} = (e/h\nu)\eta g$, where $h\nu$ is the photon energy, gave η of more than 8%. Considerably smaller η is obtained in standard MBE-grown MQW photoresistors under normal incidence of light. The high quantum efficiency also reflects on detectivity, which was found to be unexpectedly high in comparison with the values typical of MQW structures without light input devices (Fig. 6). A noticeable increase in the quantum yield in MBE-grown MQW photoresistors under normal incidence of light was achieved when the structures were grown on substrates with an orientation at which the effective mass tensor has nonzero off-diagonal elements. This means that the momentum of an electron interacting with the in-plane electric field of an electromagnetic wave in QW has a nonzero component normal to the layers of an MQW structure [2]. In our case, all the substrates on which MQW structures were grown had ⟨100⟩ orientation, which should not lead to the effect discussed above. The high responsivity under normal incidence of light in our MQW structures might be explained by the influence of the lateral surface of the photoresistor mesa as a kind of prism functioning as an input device. However, estimates based on comparison of the lateral and front surface areas of the mesa show that the observed responsivity of several tenths of A/W can only be achieved if the lifetime of nonequilibrium carriers in MQW exceeds 10^{-8} s or the quantum yield is higher than 100%. Noise measurements failed to confirm either of these assumptions. Note also that the back side of the photoresistor substrates, which might scatter signal light and serve as an input device in the case of inappropriate treatment, was polished.

To explain the result obtained, we stress the following fact. A weak absorption of radiation under normal incidence is usually observed in MBE-grown MQW structures. These structures best conform to the model of rectangular symmetrical wells, which underlies the theory of the effect. However, no theory of this kind has been developed for nonrectangular asymmetrical wells. Meanwhile, as shown in [3], a deviation of the shape of the well from symmetrical may strongly affect the polarization dependence of light absorption in an MQW structure. A strong deviation of the real shape of QWs from the classical model is possible in MOCVD-grown MQW structures. The asymmetry in the sharpness of the well–barrier interfaces can be caused by specific features of the MOCVD process. MOCVD is characterized by a higher pressure of the gas reagents. Their viscosity is higher than in MBE, which can give rise to long transient processes in switching between gas flows, and, consequently, to stronger deviations of the shape of the well from rectangular and symmetrical. Furthermore, as mentioned above, MOCVD is per-

formed at above 700°C. At these temperatures, the diffusion of silicon, the standard dopant for wells, becomes significant [4]; i.e., the impurity distribution profile is not localized within the well upon termination of growth, regardless of the initial position of the doping region. In other words, the impurity is present both in the wells and in barrier layers in all the structures under study, irrespective of the place where it is introduced. As a result, when it is cooled to cryogenic temperatures the impurity within the barrier layers will be ionized, because electrons will pass to levels in the wells, and a built-in field will appear at the well–barrier interfaces. Approximate estimates show that this field value may be as high as 10^5 V/cm. Such a field could deform the initially rectangular and symmetrical well and, as a result, lead to considerable absorption of normally incident light. The possibility of such an influence of the electric field on mechanisms of light absorption in MQW structures was discussed in [4] and [5]. This effect will be much weaker in MBE-grown MQW structures, because in this case the central part of the well is usually doped, and the impurity has no time to diffuse into barriers at growth temperatures of ~500°C.

The conclusions based on the above analysis of reasons for the anomalously high responsivity and other specific features of MOCVD-grown MQW photoresistors are preliminary conjectures. Further study is necessary to clarify the real reasons for the effects discussed.

5. CONCLUSION

Characteristics of MOCVD-grown MQW photodetectors were studied. The analysis of the experimental *I–V* characteristics, dependences of the absolute responsivity on bias, and responsivity spectra give grounds to assume that wells in MQW structures are asymmetrical. An unexpected result was the high responsivity of MQW photoresistors under normal incidence of light without any special devices for light input. The possible reasons for the observed effects were analyzed. Further study is necessary to establish their physical nature and obtain detailed information about the structural features of MOCVD-grown MQW devices.

REFERENCES

1. A. Brandel, A. Fraenkel, E. Finkman, *et al.*, Semicond. Sci. Technol. **8**, S412 (1993).
2. Y. Zhang, N. Baruh, and W. I. Wang, Electron. Lett. **29** (2), 213 (1993).
3. W. E. Hagston, T. Stirner, and F. Rasul, J. Appl. Phys. **89**, 1087 (2001).
4. D. G. Deppe and N. Holonyak, J. Appl. Phys. **64** (12), R93 (1988).
5. A. Ya. Shik, Fiz. Tekh. Poluprovodn. (Leningrad) **20**, 1598 (1986) [Sov. Phys. Semicond. **20**, 1002 (1986)].

Translated by D. Mashovets

Semiconductors, Vol. 38, No. 2, 2004, pp. 217–220. Translated from Fizika i Tekhnika Poluprovodnikov, Vol. 38, No. 2, 2004, pp. 222–225.

LOW-DIMENSIONAL SYSTEMS

Energy Structure of A^+ Centers in Quantum Wells

N. S. Averkiev, A. E. Zhukov, Yu. L. Ivanov, P. V. Petrov, K. S. Romanov*, A. A. Tonkikh, V. M. Ustinov, and G. E. Tsyrlin

Ioffe Physicotechnical Institute, Russian Academy of Sciences, Politekhnicheskaya ul. 26, St. Petersburg, 194021 Russia

**e-mail: const@stella.ioffe.ru*

Submitted June 18, 2003; accepted for publication June 30, 2003

Abstract—Hole states localized at acceptors in quantum wells are considered within the zero-range potential model. The dispersion equation for holes is analytically derived taking into account the complex structure of the valence band of symmetry Γ_8. The results obtained are compared with the experimental dependences of the binding energy of holes localized at A^+ centers on the quantum-well width, and good agreement with the theoretical results is demonstrated. © *2004 MAIK "Nauka/Interperiodica".*

1. INTRODUCTION

Quantum structures containing impurities are extensively studied not only in view of their promising applications but also because they have some new physical properties. Indeed, both the potential of impurities and the structure potential affect an electron or a hole localized at a defect in a quantum well. In this case, the structure potential, which diminishes the carrier-localization region, increases the kinetic energy of a carrier and leads to its delocalization in the well plane. The impurity potential may also include several terms. These are, primarily, the Coulomb part of the potential (for charged centers) and the short-range part arising from the mismatch between the impurity and lattice atoms. In this context, the problem of determining the binding energy and the wave function of a carrier localized at a defect in a quantum well becomes rather intricate and dependent on the chemical nature of the defect. In principle, the dependence of the carrier binding energy on the well parameters and the defect type makes it possible to identify impurities; for this purpose, it is necessary to have the theoretical and experimental dependences of the defect binding energy on the heterostructure parameters.

In [1–3], we experimentally studied the binding energy and the characteristic size of the wave function for A^+ centers in quantum wells of different width. Theoretical analysis of shallow Coulomb acceptors in rectangular quantum wells was performed in [4–6], and the hole binding energies were calculated numerically for specific structures.

The aim of this paper is to calculate the spectrum of an acceptor or an A^+ center in a quantum well within the zero-range potential method, which yields analytical expressions for binding energies and wave functions. It is shown that the results of the calculations are in good agreement with the experimental data [1, 2].

2. THEORY

In the zero-range potential model, the potential of a defect is described by modifying the Schrödinger equation for a free particle. Namely, solutions to the Schrödinger equation in the absence of attractive potential, which decay at infinity, are constructed. The attractive potential is taken into account by introducing the boundary condition that determines the asymptotic behavior of the spherically symmetric part of the wave function near a defect [7],

$$\bar{\psi}|_{r\to 0} = C\left(\frac{1}{r} - \alpha\right) + o(r), \qquad (1)$$

where $\bar{\psi}$ is the angle-averaged wave function and α is the coefficient describing the short-range potential.

In the case of a bulk semiconductor, where the valence band has Γ_8 symmetry, the wave function of the ground state of a hole bound at the zero-range potential also has Γ_8 symmetry. Thus, the wave function of the ground state can be divided into a spherically symmetric part and a part containing second-order spherical harmonics; the radial component of the asymmetric part remains almost constant at $r \longrightarrow 0$. Therefore, when studying the acceptor states in cubic semiconductors, we must substitute the angle-averaged wave function ψ into boundary condition (1).

At the same time, in terms of the zero-range potential method, the wave function for the donor ground state in a bulk semiconductor has only a spherically symmetric part. Therefore, one can simply use the wave function ψ in the boundary condition (1), e.g., as in [8].

The coefficient α depends on both the defect charge and the chemical properties of the defect and the properties of the quantum-well material. In the zero-range potential approach, this coefficient is a problem parameter. In this study, the parameter α was determined from the best fit of the energy level position for the bulk material to the experimental value and then used in the

calculation of the energy-level position for the quantum well.

Thus, in the zero-range potential method, the Schrödinger equation can be written as

$$H_0\psi(\mathbf{r}) = E\psi(\mathbf{r}) + V\delta(\mathbf{r}-\mathbf{r}_0)\Psi_0,$$

where H_0 is the Luttinger Hamiltonian, Ψ_0 is an arbitrary constant spinor, and $\mathbf{r}_0$ is the position vector of a defect. In the spherically symmetric approximation,

$$H_0 = \frac{1}{m_0}\left[\left(\gamma_1 + \frac{5}{2}\gamma\right)\frac{\hat{p}^2}{2} - \gamma(\hat{\mathbf{p}}\mathbf{J})\right],$$

where γ and γ_1 are the Luttinger parameters, m_0 is the free electron mass, and $\mathbf{J}$ are the matrices of the 3/2 momentum.

It is convenient to perform calculations using a mixed coordinate–momentum representation. We choose the system of coordinates in which the *OX* and *OY* axes lie in the plane of the quantum well and the *OZ* axis is perpendicular to the well plane. For convenience, we place the origin of coordinates at the center of the well. Then, the Schrödinger equation in the mixed representation has the form

$$H_0\psi(\mathbf{q}, z) = E\psi(\mathbf{q}, z) + V\delta(z-z_0)\Psi_0, \qquad (2)$$

where $\mathbf{q}$ is the two-dimensional wave vector in the well plane and z_0 is the defect coordinate. The experiments were performed with samples in which defects were located at the centers of the wells. Hence, we consider hereinafter only the case $z = 0$.

Since the Hamiltonian commutes with the time reversal operator, it is convenient to use the Hopfield method to find the wave function. In this method, system of four equations (2) is reduced to the system of two equations

$$\begin{cases} (H_{11}-E)\psi_{\frac{3}{2}} + \left(H_{13} - H_{12}\dfrac{H_{43}}{H_{42}}\right)\psi_{-\frac{1}{2}} = A\delta(z), \\ H_{31}\psi_{\frac{3}{2}} + (H_{33}-E)\psi_{-\frac{1}{2}} = C\delta(z), \end{cases} \qquad (3)$$

where A and C are the constant components of the spinor ψ_0; $\psi_{\frac{3}{2}}$ and $\psi_{-\frac{1}{2}}$ are the components of the wave function corresponding to the 3/2 and –1/2 projections of the momentum, respectively; and E is counted from the bottom of the band gap.

We find the wave function for either of the two regions of the quantum well separated by the plane $z = 0$. The matching at $z = 0$ is performed using the boundary conditions obtained by integrating the equations of system (3) over the z coordinate in the interval (–0; +0). At the well boundaries, the hole wave function is set equal to 0 since we are considering the case of an infinitely deep well.

The calculations show that, after averaging over the azimuthal angle, the hole wave function has the form

$$\psi(q, z) = \begin{pmatrix} A\psi_{\frac{3}{2}}(q, z) \\ C\psi_{-\frac{1}{2}}(q, z) \end{pmatrix}. \qquad (4)$$

Here, the components $\psi_{\frac{3}{2}}$ and $\psi_{-\frac{1}{2}}$ are given by the formulas

$$\begin{cases} \psi_{\frac{3}{2}} = \sinh\left(\lambda_+\left(\dfrac{a}{2} - |z|\right)\right)(3\lambda_+^2 + \kappa_+^2)/(\lambda_+\cosh(a\lambda_+/2)) \\ + \sinh\left(\lambda_-\left(\dfrac{a}{2} - |z|\right)\right)(3\kappa_-^2 - 3\lambda_-^2)/(\lambda_-\cosh(a\lambda_-/2)), \\ \psi_{-\frac{1}{2}} = \sinh\left(\lambda_+\left(\dfrac{a}{2} - |z|\right)\right)(3\kappa_+^2 - 3\lambda_+^2)/(\lambda_+\cosh(a\lambda_+/2)) \\ + \sinh\left(\lambda_-\left(\dfrac{a}{2} - |z|\right)\right)(\kappa_-^2 + 3\lambda_-^2)/(\lambda_-\cosh(a\lambda_-/2)), \end{cases} \qquad (5)$$

where a is the well width, $\lambda_\pm = \sqrt{\kappa_\pm^2 + q^2}$, $\kappa_+ = \sqrt{-2Em_h}$, $\kappa_- = \sqrt{-2Em_l}$, and m_l and m_h are the effective masses of light and heavy holes, respectively. At $E < 0$, the coefficients $\kappa_\pm$ are real and, at $E > 0$, they are purely imaginary.

To find the energy levels and the coefficients A and C, we have to use boundary condition (1), which characterizes the potential. Therefore, the components $\psi_{\frac{3}{2}}$ and $\psi_{-\frac{1}{2}}$ should be transformed into the coordinate representation and then averaged over the polar angle. It is rather difficult to find analytical expressions for these functions but, in order to calculate the energy levels, we only need to know the asymptotic behavior of these functions at $r \longrightarrow 0$. Specifically, we must know the behavior of the first two terms in the expansion in r, i.e., the coefficients at $1/r$ and 1. The parameter α in boundary condition (1) is equal to the ratio of these coefficients averaged over the azimuthal angle.

First, we find the most important term at $r \longrightarrow 0$. We then subtract its Fourier transform from the initial function and find the next term.

It can be seen that the combinations ($A = 1$, $C = 0$) and ($A = 0$, $C = 1$) determine the eigenstates of the system. The two energies correspond to the two wave func-

tions. The energies of the two states are determined by the equations

$$\alpha = \left(\kappa_+^2 \ln(2\cosh(a\kappa_+/2)) + 3\kappa_-^2 \ln(2\cosh(a\kappa_-/2)) - a\frac{3}{2}\int_{\kappa_+}^{\kappa_-} \lambda^2 \tanh(a\lambda/2)d\lambda\right)/(a(\kappa_+^2 + \kappa_-^2)),$$

$$\alpha = \left(3\kappa_+^2 \ln(2\cosh(a\kappa_+/2)) + \kappa_-^2 \ln(2\cosh(a\kappa_-/2)) + a\frac{3}{2}\int_{\kappa_+}^{\kappa_-} \lambda^2 \tanh(a\lambda/2)d\lambda\right)/(a(\kappa_+^2 + \kappa_-^2)). \quad (6)$$

Thus, in order to evaluate the position of the level corresponding to the defect-bound state, we find the coefficient α from the value of the binding energy. In the case of bulk material, we use Eqs. (6) to find α at $a \longrightarrow \infty$, and then the energies are determined from the same equations at finite values of a. It should be noted that, in real experiments, the energy of the transition between the localized level and the first level of heavy holes in the quantum well ($E_{hh} = \pi^2\hbar^2/(2m_h a^2)$) is measured rather than the binding energy.

3. RESULTS AND DISCUSSION

We performed experiments with the samples prepared by molecular-beam epitaxy and selectively doped with beryllium; the bulk hole concentration in GaAs amounted to 1×10^{17} cm^{-3}.

Each sample represented a set of ten GaAs quantum wells separated by 20-nm $Al_{0.35}Ga_{0.65}As$ barriers; the well width varied from 7 to 18 nm. Stable A^+ centers were formed in quantum wells by the so-called double selective doping method; i.e., both quantum wells and barriers were simultaneously doped. Such an impurity distribution leads to the capture of holes localized at acceptors in the barrier regions by acceptors in quantum wells, i.e., to the formation of A^+ centers.

Photoluminescence spectra were measured from the samples immersed directly in liquid helium. A glass optical fiber was used to feed light from a He–Ne laser to a sample and to output a luminescence signal. The radiation was recorded by a diffraction spectrometer and a photomultiplier in the photon-counting mode.

Excess electrons and holes excited by the pump light, interacting with neutral acceptors, may form both bound excitons and A^+ centers. A typical photoluminescence spectrum of the structures studied [3] contains a peak due to the emission from A^+ centers and a peak due to the recombination of excitons bound at neutral acceptors. The heights of these peaks linearly depend on the pump intensity. To separate the luminescence peaks and find their exact positions, the spectra were smoothed and approximated by Gaussian functions.

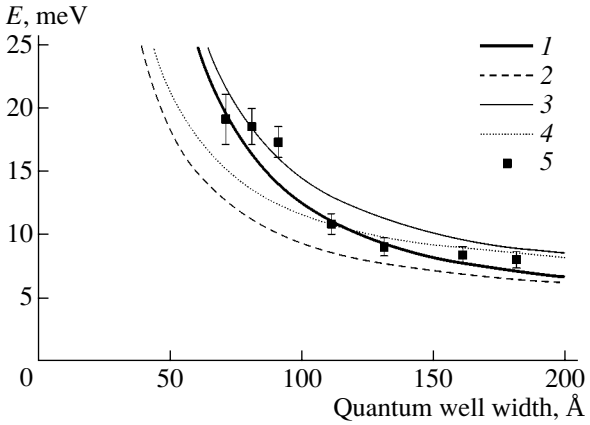

Fig. 1. Calculated binding energies of the ground (E_1) and excited (E_2) states of the A^+ center as functions of the well width, corresponding to hole-binding energies for the bulk material equal to 5 and 7 meV. The details of the experiment are described in the text. The dependences of E_1 correspond to a bulk binding energy of (*1*) 5 and (*3*) 7 meV; the dependences of E_2 correspond to a bulk binding energy of (*2*) 5 and (*4*) 7 meV; (*5*) experimental data.

These peaks were identified by studying the temperature dependence of the photoluminescence. This technique is based on the fact that the peak of bound excitons rapidly disappears with an increase in temperature due to the low binding energy of excitons localized at neutral centers, whereas the intensity of radiative free-electron–A^+-center transitions decreases only slightly. The activation energy of A^+ centers was determined by summing the energy difference between the emission peaks of A^+ centers and the peaks of bound excitons with the binding energy of an exciton localized at a neutral acceptor (the latter is known from the literature).

The accuracy of the measurements was affected by the following factors: the dependence of the binding energy on the position of the impurity center in the well (which is especially strong for narrow wells); the deviations of the parameters of the grown structures from the specified values; and the instrumental errors. The largest error is related to the deviation of the width of a grown quantum well from the specified value. This error was estimated by multiplying the derivative of the A^+-center energy with respect to the well width by the characteristic deviation of the well size. The value of the total error is indicated in Fig. 1.

Figure 1 shows the hole ionization energies for the ground and excited levels calculated using Eqs. (6) for different values of the parameter α. In the case of a bulk material, the parameter α is related to the binding energy as follows:

$$\alpha = \sqrt{-2E}\frac{(\gamma_1 + 2\gamma)^{-3/2} + (\gamma_1 - 2\gamma)^{-3/2}}{(\gamma_1 + 2\gamma)^{-1} + (\gamma_1 - 2\gamma)^{-1}}.$$

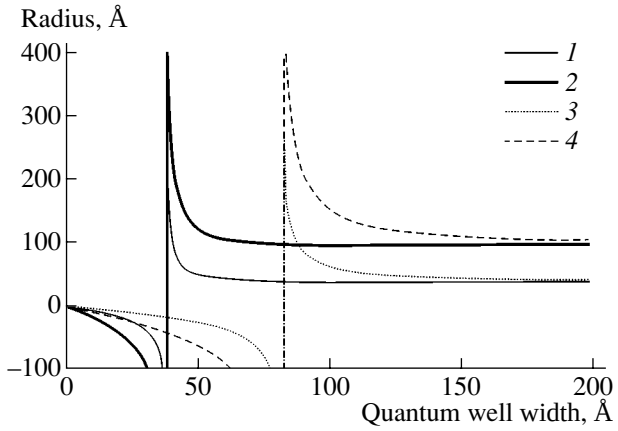

Fig. 2. Dependences of the characteristic size of the wave function of an A^+ center on the well width for the (*1*, *2*) ground and (*3*, *4*) excited states corresponding to a bulk binding energy of 5 meV. (*1*, *3*) $1/\kappa_+$, (*2*, *4*) $1/\kappa_-$.

Here, γ and γ_1 are the Luttinger parameters for the material considered.

The curves in Fig. 1 refer to the following values of the binding energies for the bulk material: $E_1 = 5$ meV and $E_2 = 7$ meV. As can be seen, the results of the calculation are in good agreement with experiment. Figure 2 shows the dependences of the characteristic sizes of the hole wave function ($1/\kappa_+$ and $1/\kappa_-$) on the well width for the ground and excited states, at ionization energy $E = 5$ meV. The fact that κ_+ and κ_- are negative at some values of the well width indicates that the decay of the wave function obeys the power rather than exponential law.

In [2] we estimated the size of an A^+ center by analyzing the hopping conductivity. According to our calculations [1, 2], the characteristic size of the wave function in quantum wells is 100 Å. This result is consistent with the data of [2] (80 Å).

4. CONCLUSIONS

In this study, we showed that the model of the A^+ center with a zero-range potential describes well the experimental data and makes it possible to take into account the chemical nature of an impurity.

ACKNOWLEDGMENTS

This work was supported in part by grants from the Russian Foundation for Basic Research; INTAS; the European Office of Aerospace Research and Development; ISTC (grant no. 2206); the programs of the Ministry of Industry, Science, and Technology of the Russian Federation; the programs of the Presidium and the Department of Physics of the Russian Academy of Sciences; and the Foundation for the Support of Russian Science.

REFERENCES

1. Yu. L. Ivanov, P. V. Petrov, A. A. Tonkikh, *et al.*, Fiz. Tekh. Poluprovodn. (St. Petersburg) **37**, 1114 (2003) [Semiconductors **37**, 1090 (2003)].
2. N. V. Agrinskaya, Yu. L. Ivanov, V. M. Ustinov, and D. A. Poloskin, Fiz. Tekh. Poluprovodn. (St. Petersburg) **35**, 571 (2000) [Semiconductors **35**, 550 (2000)].
3. Yu. L. Ivanov, N. V. Agrinskaya, P. V. Petrov, *et al.*, Fiz. Tekh. Poluprovodn. (St. Petersburg) **36**, 993 (2002) [Semiconductors **36**, 929 (2002)].
4. W. T. Masselink, Y.-C. Chang, and H. Morkoc, Phys. Rev. B **28**, 7373 (1983).
5. V. I. Belyavskiĭ, M. V. Gol'dfarb, and Yu. V. Kopaev, Fiz. Tekh. Poluprovodn. (St. Petersburg) **31**, 1095 (1997) [Semiconductors **31**, 936 (1997)].
6. V. Ya. Aleshkin, B. A. Andreev, V. I. Gavrilenko, *et al.*, Fiz. Tekh. Poluprovodn. (St. Petersburg) **34**, 582 (2000) [Semiconductors **34**, 563 (2000)].
7. V. I. Perel' and I. N. Yassievich, Zh. Éksp. Teor. Fiz. **82**, 237 (1982) [Sov. Phys. JETP **55**, 143 (1982)].
8. A. A. Pakhomov, K. V. Khalipov, and I. N. Yassievich, Fiz. Tekh. Poluprovodn. (St. Petersburg) **30**, 1387 (1996) [Semiconductors **30**, 730 (1996)].

Translated by I. Zvyagin

Semiconductors, Vol. 38, No. 2, 2004, pp. 221–224. Translated from Fizika i Tekhnika Poluprovodnikov, Vol. 38, No. 2, 2004, pp. 226–229.

LOW-DIMENSIONAL SYSTEMS

TEM Study of the Formation and Modification of Nanocrystalline Si Inclusions in *a*-Si:H Films

V. P. Afanasiev*, A. S. Gudovskikh*, A. Z. Kazak-Kazakevich*, A. P. Sazanov*, I. N. Trapeznikova^, and E. I. Terukov****

**St. Petersburg State Electrotechnical University, St. Petersburg, 197376 Russia*

***Ioffe Physicotechnical Institute, Russian Academy of Sciences, St. Petersburg, 194021 Russia*

^e-mail: trapez@mail.ioffe.ru

Submitted June 20, 2003; accepted for publication June 30, 2003

Abstract—Transmission electron microscopy has been used to investigate the formation and modification of the nanocrystalline silicon (*nc*-Si) phase in thin *a*-Si:H films. The films were produced by three different methods: plasmochemical deposition of *a*-Si:H, cyclic plasmochemical deposition with intermediate annealing of layers 10–20 nm in thickness in hydrogen plasma, and plasmochemical deposition of *a*-Si:H with the annealing of 40-nm-thick films in hydrogen plasma. In the films produced by cyclic deposition with intermediate annealing in hydrogen plasma and subsequent thermal treatment at 750°C for 30 min, the size of nanocrystallites does not exceed the thickness of a layer deposited in a cycle. In contrast, in uniform films with similar thermal treatment, crystallites may be as large as 1 μm or more. Models that account for the effects observed are suggested. These models are validated by calculating profiles of hydrogen diffusion in *a*-Si:H film after annealing in hydrogen plasma and thermal treatment in vacuum. © *2004 MAIK "Nauka/Interperiodica".*

1. INTRODUCTION

Films of amorphous hydrogenated silicon (*a*-Si:H) with nanocrystalline (*nc*-Si) inclusions nowadays attract considerable attention [1–6]. This interest is due to the high photosensitivity of *a*-Si:H⟨*nc*-Si⟩ films compared with homogeneous hydrogenated films [1–4]. It is assumed that nanocrystalline inclusions partially relieve mechanical stresses in an amorphous matrix, thus opening the way to formation of less a strained network with a lower concentration of weak bonds, which is less subject to degradation. The great interest in films containing nanocrystalline inclusions is also related to the possibility of designing efficient light emitters in the visible range [5–6]. However, mechanisms of the influence of the size and volume fraction of nanocrystalline inclusions on the stability and photoelectric and luminescent properties of films still remain unclear. Up to now, the processes of nanocrystallite nucleation and growth in amorphous *a*-Si:H films are poorly understood, which means that one cannot control the size and volume fraction of nanocrystalline inclusions and thereby optimize the structure and properties of *a*-Si:H⟨*nc*-Si⟩ films for various applications. This is because the theory of nanocrystallite formation in an amorphous matrix is still in its infancy [7, 8], and the technology of *nc*-Si formation is based on experimental data that depend on the equipment used.

Earlier [4, 9], we demonstrated the successful use of a cyclic method for fabricating *a*-Si:H⟨*nc*-Si⟩ films with improved photosensitivity and stability. The method consists in periodic alternation of cycles of deposition of *a*-Si:H thin films and their annealing in hydrogen plasma. A structural study of the films by transmission electron microscopy (TEM) revealed that they have a clearly pronounced layered structure with interlayer spacing corresponding to the thickness of a layer deposited in a single cycle (dark regions in the cross-sectional TEM micrograph, Fig. 1). Bright stripes correspond to *a*-Si:H regions that appear during the annealing in hydrogen plasma and are characterized by a higher concentration of hydrogen. These regions also

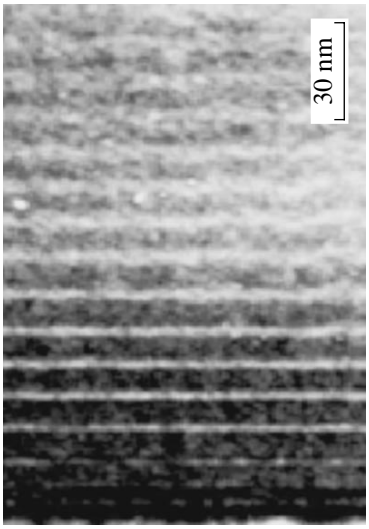

Fig. 1. Cross-sectional TEM image of *a*-Si:H film produced by cyclic deposition.

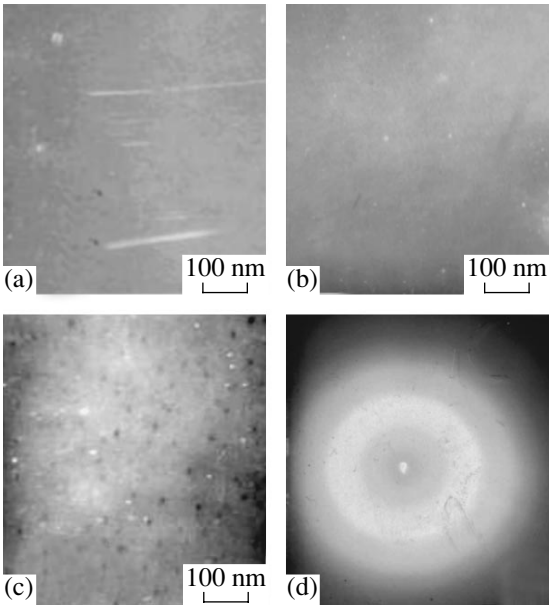

Fig. 2. TEM images of *a*-Si:H films produced in modes (a) 1, (b) 2, and (c) 3; (d) electron diffraction pattern of these films.

contain crystalline Si inclusions with an average size of 4.5 nm and a volume fraction below 1% [9]. Based on the analysis of the experimental data, we suggested a model according to which hydrogen diffuses, during annealing in hydrogen plasma in a deposition cycle, to a depth smaller than the thickness of the layer deposited in the preceding cycle. The alternation of deposition and annealing results in a nonuniform distribution of hydrogen and, consequently, leads to variation in the energy gap E_g across the film thickness. Therefore, *a*-Si:H films are graded band-gap structures with alternating hydrogen-rich and hydrogen-lean layers with band gaps that are wider and narrower, respectively.

This paper presents the results of a TEM study of how *nc*-Si inclusions are formed in *a*-Si:H films produced by plasmochemical deposition, cyclic plasmochemical deposition with intermediate annealing of 10- to 25-nm-thick layers, and plasmochemical deposition with annealing of 40-nm-thick films in hydrogen plasma, and how the film structure is modified by subsequent thermal treatment.

2. SAMPLE FABRICATION AND EXPERIMENTAL PROCEDURE

Cyclic plasmochemical deposition of *a*-Si:H films onto NaCl substrates fixed on a rotating substrate-holder drum was performed in a diode HF (13.56 MHz) system with a substrate temperature of 250°C, discharge power of 40 W, substrate-holder rotational velocity of 4 rpm, and gas mixture (80% Ar + 20% SiH_4) pressure of 25 Pa. The substantiation of the selected deposition mode and the specifics of *a*-Si:H film fabrication in a Kont vacuum system can be found elsewhere [10, 11]. The annealing of layers in hydrogen plasma was done at the same temperature of 250°C with an HF discharge power of 150 W and a gas mixture (80% Ar + 20% H_2) pressure of 25 Pa.

Films produced in three different modes were studied:

(1) films of about 40 nm in thickness produced by continuous plasmochemical deposition for 6 min (without annealing in hydrogen plasma);

(2) layered films produced by cyclic deposition (plasmochemical deposition of each of three 12-nm-thick layers for 2 min, annealing of each layer in hydrogen plasma for 3 min) [2];

(3) films of 40 nm in thickness produced by continuous 6-min plasmochemical deposition and annealed in hydrogen plasma for 12 min.

An EM-125 electron microscope with 100 kV accelerating voltage was used in TEM and microdiffraction studies of the film's structure. Films were deposited onto single-crystal NaCl then transposed to a copper grid in distilled water. *a*-Si:H⟨*nc*-Si⟩ films on grids were annealed for 30 min in vacuum at temperatures of 450 and 750°C.

3. RESULTS AND DISCUSSION

The results of the structural studies of the as-grown films produced in modes 1–3 are as follows. Films obtained in mode 1 were single-phase amorphous (Fig. 2a).

Layered films (mode 2) contained a small (<1%) volume fraction of nanocrystalline inclusions 10 nm in size (Fig. 2b). Films produced in mode 3 contained *nc*-Si with crystallites 4–5 nm in size; their volume fraction was several percent (Fig. 2c). The electron diffraction patterns (Fig. 2d) of all the films were similar, which indicates the domination of the amorphous phase in the films and the small size of the crystallites (no more than 10 nm).

To validate the suggested model of nonuniform distribution of hydrogen across the thickness of a layered film (mode 2), we have calculated theoretically the hydrogen concentration profile in *a*-Si:H films after the annealing in hydrogen plasma in conditions of cyclic deposition (250°C for 30 s). In the calculation of hydrogen diffusion, experimental data on the diffusion coefficient from plasma and a solid source [12, 13] were used. The calculated diffusion profile (Fig. 3) shows that, during the annealing in plasma, hydrogen diffuses to a depth of about 3 nm, which is much smaller than the thickness of a layer deposited in a cycle.

To determine the variation in the hydrogen distribution across the film thickness in the course of film growth and after thermal treatment in vacuum, we calculated the diffusion of hydrogen from a finite solid source, with effusion disregarded. Figure 4 shows the calculated profiles of hydrogen distribution prior to annealing and after thermal treatment in vacuum for 5 h

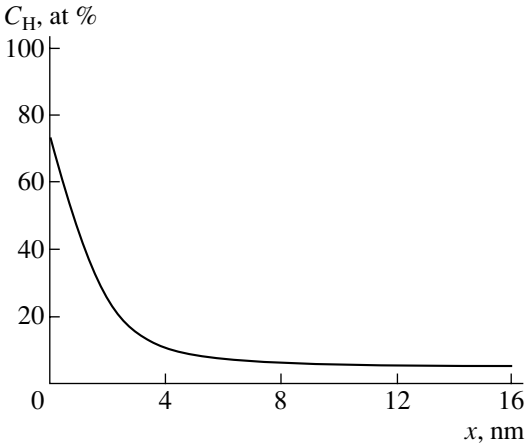

Fig. 3. Distribution of hydrogen concentration away from the surface of *a*-Si:H film annealed in hydrogen plasma. $E_d = 0.5$ eV, $D_0 = 4 \times 10^{11}$ cm^2 s^{-1}, $t = 30$ s, and $T = 250$°C.

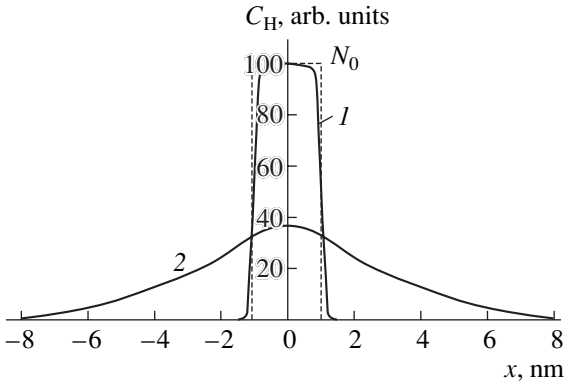

Fig. 4. Concentration profiles of hydrogen strongly bound with silicon (*1*) after annealing in the deposition conditions and (*2*) after thermal treatment at 450°C for 1h ($E_d = 1.9$ eV, $D_0 = 10^{-4}$ cm^2 s^{-1}).

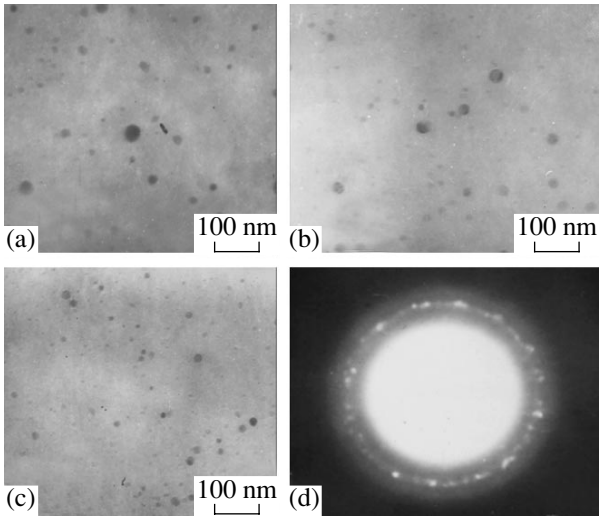

Fig. 5. TEM images of *a*-Si:H films after their thermal treatment at 450°C in vacuum: films grown in modes (a) 1, (b) 2, and (c) 3; (d) electron diffraction pattern of these films.

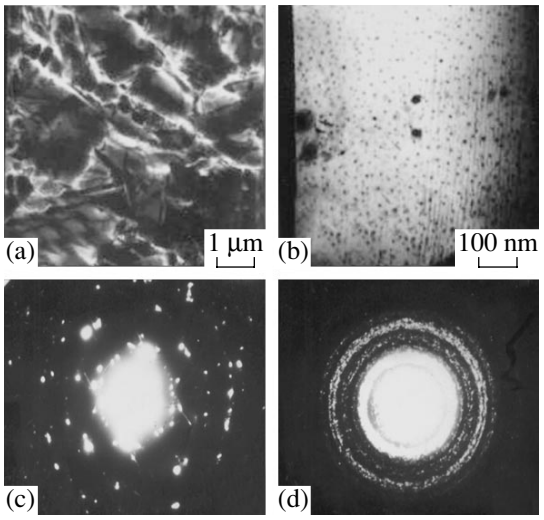

Fig. 6. TEM images of *a*-Si:H films produced in modes (a) 1 and (b) 2 after their thermal treatment at 750°C in vacuum; (c, d) electron diffraction patterns of these films.

at 250°C and for 1 h at 450°C. The calculation shows that the initial distribution remains virtually unchanged after the annealing for 5 h at 250°C (i.e., in deposition conditions). After 1-h annealing at 450°C, the hydrogen concentration profile is partially broadened; however, the nonuniform distribution of hydrogen, strongly bound to Si, across the *a*-Si:H film thickness is still retained. It is likely that the formation and growth of nanocrystallites in a homogeneous *a*-Si:H film during vacuum annealing proceeds more effectively, whereas in layered films, the growth of nanocrystals is limited by interfaces with increased content of hydrogen between the layers.

This approach was confirmed experimentally. After being annealed at 450°C, nanocrystallites 10–20 nm in size that occupy several percent of volume are formed in films of type 1 (Fig. 5a). In films of type 2, the amount of crystallites increases to 10% of volume, and their size, to 10–15 nm (Fig. 5b). In films of type 3, the size of *nc*-Si also increases to 10–15 nm (Fig. 5c).

Raising the temperature of thermal treatment in vacuum further demonstrated that, after treatment at 750°C, the structures of the annealed films produced in modes 1 and 2 differ dramatically (Fig. 6). The film produced by continuous plasmochemical deposition is polycrystalline and consists of rather coarse (1 μm and more) crystallites (Fig. 6a). Analysis of electron diffraction patterns shows a predominance of crystallites with the normal-to-surface orientation of the [111] axis in polycrystalline silicon films. At the same time, the

film produced with an intermediate annealing in hydrogen plasma contains nanocrystallites with a typical size of 10–15 nm (Fig. 6b). After thermal treatment at 750°C, the content of the crystalline phase becomes virtually 100% in both cases.

Thus, the average size of crystallites in layered films after thermal treatment in vacuum at 750°C does not exceed the thickness of a layer deposited in a single cycle. This creates novel opportunities for controlling the size and volume fraction of nanocrystalline Si inclusions, which can be used in the fabrication of luminescent films.

4. CONCLUSIONS

(1) Annealing in hydrogen plasma initiates the formation of nanocrystalline inclusions in *a*-Si:H films, with their size and concentration depending on the conditions of film growth. Cyclic deposition of films causes a nonuniform distribution of hydrogen across the film thickness and stimulates the formation of nanocrystallites.

(2) Calculations of hydrogen diffusion in *a*-Si:H films show that only partial smearing of the layered structure occurs during thermal treatment at 450°C, while the nonuniformity of the hydrogen distribution is retained. The growth of nanocrystallites in layered structures after thermal treatment at 750°C in a vacuum is limited by interfaces with increased hydrogen concentration, so their average size does not exceed the thickness of layers deposited in a single cycle.

(3) An intense crystallization of silicon is observed after the annealing of homogeneous *a*-Si:H films at 750°C for 30 min; as a result, a polycrystalline structure is formed, with the crystallite size exceeding 1 μm. The annealing of layered *a*-Si:H films in the same conditions raises the volume content of the nanocrystalline phase to virtually 100%, with an insignificant increase in the size of crystallites (up to 10–15 nm).

ACKNOWLEDGMENTS

This study was supported by the program of the Russian Ministry of Education “Fundamental Studies in the Natural Sciences” (project no. T02-022-1424).

REFERENCES

1. C. Longeaud, J. P. Kleider, P. Roca i Cabarrocas, *et al.*, J. Non-Cryst. Solids **227–230**, 96 (1998).
2. V. P. Afanas’ev, A. S. Gudovskikh, O. I. Kon’kov, *et al.*, Fiz. Tekh. Poluprovodn. (St. Petersburg) **34**, 495 (2000) [Semiconductors **34**, 477 (2000)].
3. I. A. Kurova, N. A. Ormont, E. I. Terukov, *et al.*, Fiz. Tekh. Poluprovodn. (St. Petersburg) **35**, 367 (2001) [Semiconductors **35**, 353 (2001)].
4. V. P. Afanas’ev, A. S. Gudovskikh, V. N. Nevedomskiĭ, *et al.*, Fiz. Tekh. Poluprovodn. (St. Petersburg) **36**, 238 (2002) [Semiconductors **36**, 230 (2002)].
5. X.-N. Liu, S. Njng, L.-C. Wang, *et al.*, J. Appl. Phys. **78**, 6193 (1995).
6. T. Toyama, Y. Kotani, A. Shimode, and H. Okamoto, Mater. Res. Soc. Proc. **557**, 469 (1999).
7. T. Itoh, K. Yamamoto, K. Ushikoshi, *et al.*, J. Non-Cryst. Solids **266–269**, 201 (2000).
8. Y. He, C. Yin, G. Cheng, *et al.*, J. Appl. Phys. **75**, 797 (1994).
9. V. P. Afanasjev, A. S. Gudovskikh, J. P. Kleider, *et al.*, J. Non-Cryst. Solids **299–302**, 1070 (2002).
10. V. P. Afanas’ev, A. A. Lyanguzov, and A. P. Sazanov, Peterb. Zh. Élektron., No. 2, 7 (1995).
11. V. P. Afanas’ev, A. S. Gudovskikh, A. P. Sazanov, *et al.*, Izv. Vyssh. Uchebn. Zaved., Mater. Élektron. Tekh., No. 4, 29 (1999).
12. P. V. Santos and W. B. Jackson, Phys. Rev. B **46**, 4595 (1992).
13. W. B. Jackson and C. C. Tsai, Phys. Rev. B **45**, 6564 (1992).

Translated by D. Mashovets

Semiconductors, Vol. 38, No. 2, 2004, pp. 225–231. Translated from Fizika i Tekhnika Poluprovodnikov, Vol. 38, No. 2, 2004, pp. 230–236.

LOW-DIMENSIONAL SYSTEMS

Spectroscopy of Excitonic Polaritons in Strained II–VI Semiconductor Structures with Wide Quantum Wells

S. A. Markov, R. P. Seisyan*, and V. A. Kosobukin

Ioffe Physicotechnical Institute, Russian Academy of Sciences, Politekhnicheskaya ul. 26, St. Petersburg, 194021 Russia

**e-mail: rseis@ffm.pti.spb.su*

Submitted May 19, 2003; accepted for publication July 2, 2003

Abstract—Excitonic polaritons in $ZnSe/ZnS_xSe_{1-x}$ quantum wells, whose width exceeds the Bohr radius of exciton, were investigated. From the reflection and transmission optical spectra measured at 2 K, the spectra of optical density with several exciton absorption peaks were obtained by excluding the modulating effect of the Fabry–Perot interference. A method of transfer matrices, which makes allowance for the existence of two excitonic resonances in the quantum well that feature spatial dispersion and have almost identical frequencies, is developed as applied to exciton–polariton transport in the structures under investigation. Excitons involving heavy and light holes, whose subbands are split due to the strain emerging because of the lattice mismatch between constituent semiconductors, were considered as the aforementioned resonances. It is shown that two series of peaks in the absorption spectra belong to the levels of dimensional quantization of heavy and light excitons in a wide quantum well. By fitting the theoretical spectra to the experimental spectra, the effective exciton parameters are determined. *© 2004 MAIK "Nauka/Interperiodica".*

1. INTRODUCTION

The properties of excitons in quantum wells (QWs) depend heavily on the ratio between the Bohr exciton radius a_B and the well width a. If $a \gtrsim a_B$, we will refer to QWs as narrow, and, if $a_B \ll a$, we will refer to them as wide. The quantization of carriers (electrons and/or holes) that form quasi-two-dimensional excitons is characteristic of a narrow QW [1]. For a wide QW, exciton properties remain largely the same as for corresponding bulk semiconductor, but the motion of the exciton as a whole is quantized [2, 3]. In this case, the effects of spatial dispersion, which consist in the existence of additional waves of light and the need to consider additional boundary conditions with allowance made for exciton polarization, play a substantial role [3]. The theoretical investigation of excitonic polaritons in wide QWs (and in thin films [3–5]) started many years ago [1, 2]. However, the number of experimental studies remains relatively small. In this context, let us note the investigation of GaAs-based structures with a = 150–600 nm [6, 7] or CdTe-based structures with a = 5–100 nm [8]. For structures with wide QWs based on II–VI semiconductors, which possess a large strength of the excitonic oscillator, research on electromagnetic transport is of great practical relevance. However, this research has so far been very limited in scale. [8, 9].

The purpose of this study was to investigate experimentally the excitonic polaritons in periodic structures that contain a small number of wide II–VI QWs. The reflection and transmission spectra were measured for $ZnSe/ZnS_xSe_{1-x}$ heterostructures that included several identical supercells with ZnSe QWs. To interpret the spectra of the II–VI structures, a variant of the transfer-matrix method is developed taking into account the existence of two excitonic resonances with nearly equal frequencies; each of these resonances has inherent parameters of spatial dispersion. Based on this theory, the dispersion relation and optical spectra of $ZnSe/ZnS_xSe_{1-x}$ structures are calculated. It is shown that the peaks in the absorption spectra are related to the dimensional quantization of excitons that involve light and heavy holes.

2. THEORY

A specific feature of ZnSe, similarly to many other cubic II–VI semiconductors with a zinc blende structure, is the existence of twofold degeneracy at the center of the Brillouin zone of subbands of heavy (J = 3/2) and light (J = 1/2) holes [10]. As a result of this, free excitons involving heavy (h) and light (l) holes should exist in bulk semiconductors with degenerate hole subbands [11]. It was shown theoretically that, due to splitting of the exciton into heavy and light excitons with allowance made for weak exchange interaction, three branches of excitonic polaritons emerge in the case of ZnSe [12, 13]. Their existence was confirmed experimentally [14, 15]. It is important that the existence of two additional branches of excitonic polaritons call for the use of two additional boundary conditions [12, 13] rather than one condition, as usual [3–5].

These specific features of the exciton structure are important if $a_B \ll a$; i.e., they should appear in quite wide QWs. For strained II–VI heterostructures, the

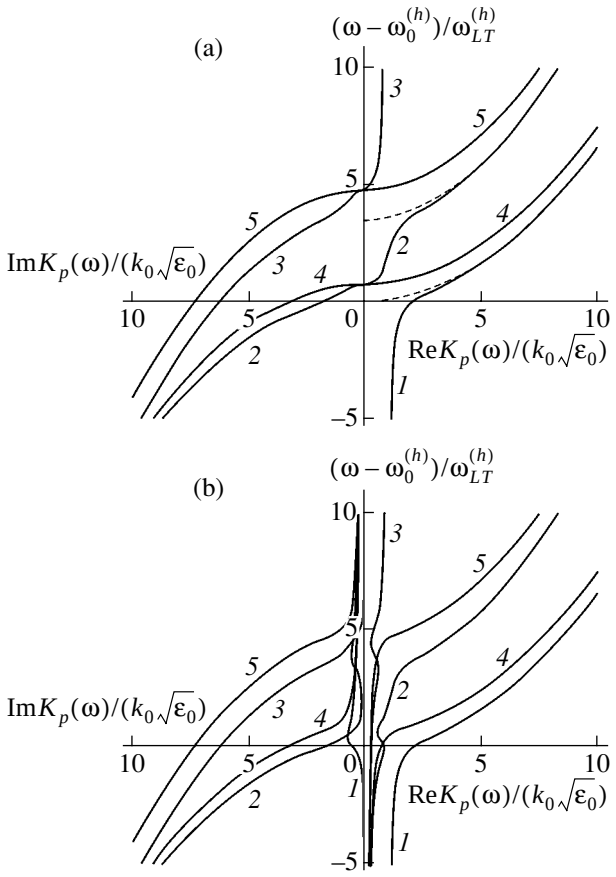

Fig. 1. $\mathrm{Im}K_p(\omega)/(k_0\sqrt{\varepsilon_0})$ and $\mathrm{Re}K_p(\omega)/(k_0\sqrt{\varepsilon_0})$ versus $(\omega - \omega_0^{(h)})/\omega_{LT}^{(h)}$ for bulk exciton polaritons in a semiconductor with two exciton resonances $\omega_0^{(h)}$ and $\omega_0^{(l)} = \omega_0^{(h)} + \Delta_e/\hbar$ for dimensionless damping parameter Γ/ω_{LT} equal to (a) 0 and (b) 2/3. Computations were carried out with the parameters $\Gamma^{(h)} = \Gamma^{(l)} = \Gamma$, $\omega_{LT}^{(h)} = \omega_{LT}^{(l)} = \omega_{LT}$, $\hbar\omega_{LT} = 1.5$ meV, $M^{(h)} = 0.7m_0$, $M^{(l)} = 0.5m_0$, and $\varepsilon_0 = 9.1$ in formula (1) and $\Delta_e = 3.53\hbar\omega_{LT}$, which corresponds to ZnSe with the components of the uniaxial strain $e_{xx} = e_{yy} = -10^{-3}$. Numbers *1*, *2*, and *3* indicate the branches p of transverse excitonic polaritons, and numbers *4* and *5* indicate the branches of longitudinal excitons. The dispersion relation for free excitons is represented by dashed lines.

uniaxial strain, which is caused by the lattice mismatch between the QW and barrier layers, may be the cause of exciton splitting [1]. Thus, due to the compression (tension) of the crystal lattice during the pseudomorphous growth of the heterostructure, the lattice symmetry varies in strained semiconductor layers. The valence band is shifted as a whole, the subbands of light and heavy holes are split at the center of the Brillouin zone, and the effective masses of electrons and holes vary. It follows from estimations of the variation in band parameters [16] that the energy of splitting of heavy and light excitons, which is denoted below as Δ_e, is determined mainly by the splitting of hole subbands if strains are small. Since the relative energy positions of subbands of heavy and light holes depend on the strain sign [10], Δ_e may generally be of both signs. The reason is that the crystal lattice of one of the components of the heterostructure is compressed in the growth direction, whereas the crystal lattice of the other component is stretched. Henceforth, the strain splitting Δ_e, as well as the parameters of heavy and light excitons, are introduced phenomenologically, and their experimental determination is one of the purposes of this study.

We will take into account the existence of two electron resonances, which have almost the same energies, for each wide QW using the following dielectric function of the QW material:

$$\varepsilon(\omega, K) = \varepsilon_0\left(1 + \sum_{j=1}^{2}\frac{2\omega_{LT}^{(j)}\omega_0^{(j)}}{(\omega_0^{(j)})^2 - \omega^2 + \frac{\hbar K^2}{M^{(j)}}\omega_0^{(j)} - i\omega\Gamma^{(j)}}\right) = \varepsilon_0 + \sum_{j=1}^{2}\chi^{(j)}(\omega, K), \quad (1)$$

where ω is the frequency, K is the magnitude of the wave vector, and ε_0 is the background permittivity. In our case, the index of the exciton resonance j takes the values $j = 1$ for an exciton with a heavy hole (h) and $j = 2$ for an exciton with a light hole (l) (usually, only a single resonance mode is considered [2–7]). For an exciton of the jth type, $\omega_0^{(j)}$ is the resonance frequency, $\omega_{LT}^{(j)}$ is the frequency of the longitudinal–transverse splitting, $\Gamma^{(j)}$ is the damping parameter, and $M^{(j)}$ is the translation mass of the exciton. Taking into account (1), the solutions of equations

$$(K/k_0)^2 = \varepsilon(\omega, K), \quad (2)$$

$$\varepsilon(\omega, K) = 0, \quad (3)$$

($k_0 = \omega/c$ and c is the speed of light in free space) determine the dispersion branches $K_p(\omega)$ of excitonic polaritons in the QW material. Of these branches, three (p = 1, 2, 3) are related to the transverse modes that satisfy Eq. (2) and two (p = 4, 5) are related to the longitudinal modes that satisfy Eq. (3). As an example, the dispersion branches $\mathrm{Re}K_p/(k_0\sqrt{\varepsilon_0})$ and their damping $\mathrm{Im}K_p/(k_0\sqrt{\varepsilon_0})$ for the case when the strain-induced splitting $|\omega_0^{(l)} - \omega_0^{(h)}| = |\Delta_e|/\hbar$ is comparable with $\omega_{LT}^{(j)}$ are shown in Fig. 1. Note that the dispersion branches were calculated previously with allowance made for the exchange splitting of this quantity [13]. It is significant that, in the case of two close exciton resonances, the number of normal waves of each type at a frequency specified is greater by unity than the number of normal waves existing in the case of a single resonance [3–5].

Let us consider the propagation of excitonic polaritons in periodic structures with wide resonance QWs. For this purpose, we will generalize the transfer-matrix method [17] to the case of two exciton resonances that exist in the QW and have nearly equal energies. We will assume that the monochromatic electromagnetic wave (polariton) propagates in the heterostructure along its growth axis z normally to QWs. Within the nth barrier layer ($z_{n-1} + a < z < z_n$) with the permittivity ε_b, the electric field of the transverse wave is given by

$$\mathbf{E}(z, \omega) = \mathbf{e}_y[U_n e^{ik(z-z_n)} + W_n e^{-ik(z-z_n)}], \quad (4)$$

where $\mathbf{e}_y$ is the unit vector of polarization and $k = k_0\sqrt{\varepsilon_b}$. Constants appearing in expression (4) for the field on both sides of the nth QW, which occupies the region $0 < z - z_{n-1} < a$, are related to each other by the transfer matrix $\hat{\Lambda}$:

$$\begin{pmatrix} U_n \\ W_n \end{pmatrix} = \hat{\Lambda}\begin{pmatrix} U_{n-1} \\ W_{n-1} \end{pmatrix}. \quad (5)$$

Inside the nth wide QW, the electric field is expressed by the formula

$$\mathbf{E}(z, \omega) = \mathbf{e}_y \sum_{p=1}^{3} [u_n^{(p)} e^{iK_p(z-z_n^-)} + w_n^{(p)} e^{-iK_p(z-z_n^+)}], \quad (6)$$

where $z_n^- = z_n$ and $z_n^+ = z_n + a$. The contributions of excitons with the heavy and light holes to the total polarization field $\mathbf{P} = \mathbf{P}^{(h)} + \mathbf{P}^{(l)}$ that are induced by field (6) have the form

$$4\pi P^{(j)}(z, \omega) = \sum_{p=1}^{3} \chi^{(j)}(\omega, K_p) \times [u_n^{(p)} e^{iK_p(z-z_n^-)} + w_n^{(p)} e^{-iK_p(z-z_n^+)}]. \quad (7)$$

Both fields (6) and (7) include transverse modes with p = 1–3, whose dispersion relation $K_p(\omega)$ is determined by Eq. (2).

In order to find the matrix $\hat{\Lambda}$, electric field (6) should be matched to the field of type (4) at the boundaries of the QW using the Maxwell boundary conditions and additional boundary conditions with allowance made for exciton polarization (7). Two poles $\omega_0^{(h)}$ and $\omega_0^{(l)}$ of function (1) exist (three solutions to Eq. (2)). As a result, one additional Pekar boundary condition $\mathbf{P} = 0$ for the total polarization is insufficient to define the constants in expressions (4) and (6). We overcome this difficulty by representing the total polarization as the sum of contributions made by two exciton resonances $\mathbf{P} = \mathbf{P}^{(h)} + \mathbf{P}^{(l)}$, for each of which we specify its own Pekar boundary condition:

$$\mathbf{P}^{(j)}(z)\big|_{\text{QW boundary}} = 0. \quad (8)$$

Such a generalization of additional boundary conditions, which is the simplest possible generalization in the case of two exciton resonances (compare [13]), was previously applied to bulk excitonic polaritons in InP subjected to uniaxial tensile stress [18].

The transfer matrix obtained from the boundary conditions is expressed via the coefficients of reflection r and transmission t of light by a single QW in the following way:

$$\hat{\Lambda} = \frac{1}{t}\begin{pmatrix} (t^2 - r^2)e^{ikb} & r \cdot e^{ikb} \\ -r \cdot e^{-ikb} & e^{-ikb} \end{pmatrix}. \quad (9)$$

The form of these coefficients is determined by the excitonic structure of the QWs. In this case, we have

$$r = \frac{1 - \rho^2 + \tau^2}{(1+\rho)^2 - \tau^2}, \quad t = \frac{2\tau}{(1+\rho)^2 - \tau^2}, \quad (10)$$

where $1 + t = r$. Here,

$$\rho = \mathbf{F} \cdot \mathbf{s}, \quad \tau = \mathbf{G} \cdot \mathbf{s}, \quad (11)$$

and each of vectors $\mathbf{F}$ and $\mathbf{G}$ have three components (p = 1, 2, 3)

$$F_p = i\sqrt{\varepsilon_p/\varepsilon_b}/\tan(K_p a), \quad G_p = i\sqrt{\varepsilon_p/\varepsilon_b}/\sin(K_p a), \quad (12)$$

where $\varepsilon_p \equiv \varepsilon(\omega, K_p)$. The vector $\mathbf{s}$ is determined in terms of the vector product

$$\mathbf{s} = \boldsymbol{\chi}^{(h)} \times \boldsymbol{\chi}^{(l)} / \|\boldsymbol{\chi}^{(h)} \times \boldsymbol{\chi}^{(l)}\|, \quad (13)$$

where the components of vectors $\boldsymbol{\chi}^{(j)}$ are the quantities $\chi_p^{(j)} = \chi^{(j)}(\omega, K_p)$ that appear in expression (1) and are calculated for $K_p(\omega)$ with p = 1–3; the notation $\|\mathbf{v}\| = \sum_{p=1}^{3} v_p$ ($\mathbf{v}$ is an arbitrary vector) is used in the denominator of expression (13).

Excitonic polaritons propagate through a periodic structure (a superlattice with the period $d = a + b$, $z_n = nd$) that consists of N identical QWs. In the absence of transfer of an exciton between the wells, the dispersion relation for the polariton with the wave number q in terms of transfer matrix (9) has the form $\cos(qd) = (\Lambda_{11} + \Lambda_{22})/2$ [17]; hence

$$\cos(qd) = \frac{1}{2t}[(t^2 - r^2 + 1)\cos(kb) + i(t^2 - r^2 - 1)\sin(kb)]. \quad (14)$$

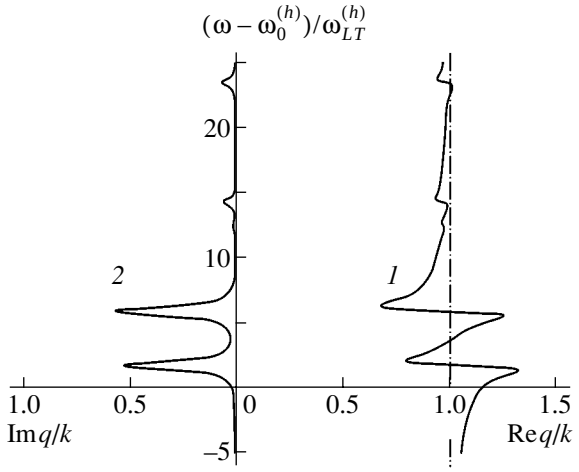

Fig. 2. (*1*) Req/k and (*2*) Imq/k versus $(\omega - \omega_0^{(h)})/\omega_{LT}^{(h)}$ for excitonic polaritons propagating along the axis of the $ZnSe/ZnS_xSe_{1-x}$ superlattice, which consists of $N = 15$ ZnSe quantum wells of $a = 15$ nm ($d = 30$ nm) in width. Calculations were carried out with the same parameters as for Fig. 1.

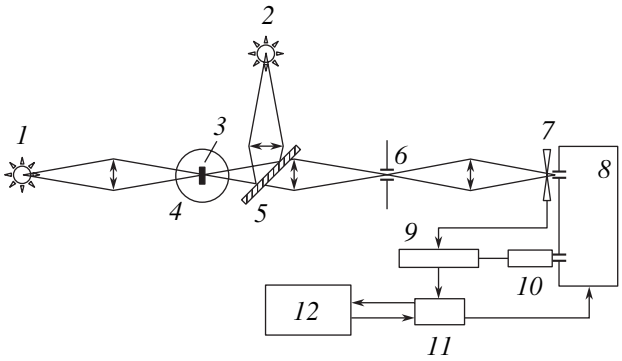

Fig. 3. Experimental layout: (*1*, *2*) lamps, (*3*) sample, (*4*) cryostat, (*5*) semitransparent plate, (*6*) crossed slits, (*7*) modulator, (*8*) monochromator, (*9*) amplifier, (*10*) photomultiplier, (*11*) coupling facility, and (*12*) computer.

The quantities Req/k and Imq/k are shown in Fig. 2. The condition $\hbar(\omega_0^{(l)} - \omega_0^{(h)}) = \Delta_e > 0$ is taken into account during the calculation. This condition means that the built-in strain in the samples under investigation leads to the compression of the ZnSe layers in the lateral plane. The peaks of the damping parameter Imq/k correspond to the polaritonic special features in the Req/k dependence. These special features are associated with the energy levels of dimensional quantization of excitons in QWs

$$\hbar\omega_l^{(j)} = \hbar\omega_0^{(j)} + \frac{(\pi\hbar)^2}{2M^{(j)}a^2}l^2, \qquad (15)$$

with $l = 1, 2, \ldots$, which correspond to boundary conditions (8).

Using expression (9) for the transfer matrix and the previous results [17], we express the energy coefficients of reflection and transmission for the structure consisting of N identical equidistantly positioned QWs in the following way:

$$R_N = \left|\frac{r\sin(qdN)}{t\sin(qd(N-1)) - e^{-ikb}\sin(qdN)}\right|^2, \qquad (16)$$

$$T_N = \left|\frac{t\sin(qd)}{t\sin(qd(N-1)) - e^{-ikb}\sin(qdN)}\right|^2, \qquad (17)$$

where $q(\omega)$ is determined by Eq. (14). Based on formulas (16) and (17), we define the optical density D_N and the effective absorption coefficient α_N of the finite-length structure by the formula [19]

$$D_N = \alpha_N a = -\ln\left(\frac{T_N}{1-R_N}\right). \qquad (18)$$

Formulas (16)–(18) define the theoretical spectral quantities that should be compared with the experimental data.

3. RESULTS AND DISCUSSION

To carry out the experiment, the structures with a small number N of wide ZnSe QWs and ZnS_xSe_{1-x} barrier layers with equal widths $a = b$ ($d = 2a$ is the period of the structure) were grown by molecular-beam epitaxy. The structures were grown on an (001) GaAs substrate at 295 K. Due to the growth conditions chosen, the quality of QWs in the structures under investigation was fairly high. After the substrate was etched off chemically, the samples comprised thin films 0.5–0.8 μm thick. Using samples in a free state enabled us to avoid stresses other than those induced by the lattice mismatch between the QWs and barriers. Optical experiments were carried out for three samples with the following parameters: (I) $a = 15$ nm and $N = 15$, (II) $a = 30$ nm and $N = 9$, and (III) $a = 60$ nm and $N = 10$.

The experimental layout is shown in Fig. 3. In the experiment, the reflection and transmission spectra were measured independently with the normal incidence of light on the film. The light from lamp *1* was focused on sample *3* in He cryostat *4*. After passing through the sample, the light was collected on crossed slits *6*, which enabled us to select a part of the image. Then the light passed through modulator *7* and was focused on the input slit of monochromator *8*. From the output slit of the monochromator, the signal was directed to photoelectric multiplier *10* with an operating wavelength range of 300–800 nm. Then, the electrical signal passed through the amplifier and coupling facility *11* and was fed to computer *12* for processing. As can be seen from Fig. 3, the reflection spectrum was recorded from the sample side that was opposite to the side illuminated during measurements of the reflection spectrum. After passing through the lens, the light from

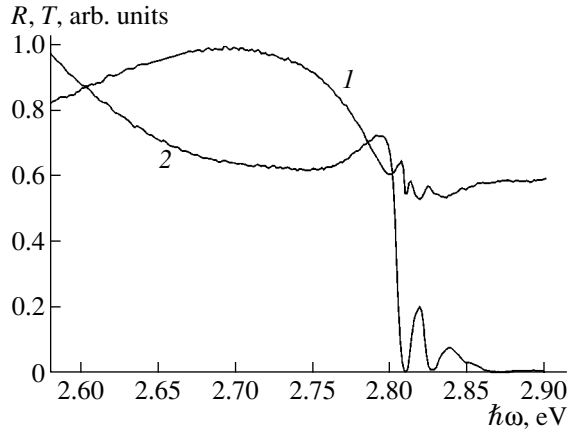

Fig. 4. Spectra of (*1*) reflection and (*2*) transmission measured at $T \approx 2$ K for sample I with $N = 15$ and $a = b = 15$ nm. For convenience, the spectra are normalized to unity.

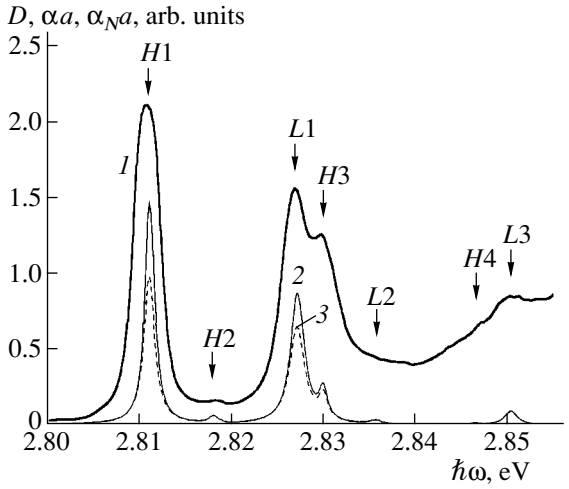

Fig. 5. (*1*) Spectra of optical density D measured at $T \approx 2$ K for sample I with $N = 15$ and $a = b = 15$ nm and calculated dimensionless absorption coefficients (*2*) $\alpha_N a$ for the supercell with $N = 15$ and (*3*) αa for the single quantum well with $N = 1$ and $a = 15$ nm. The peak positions corresponding to the levels of dimensional quantization of excitons of heavy ($H1$, $H2$, …) and light ($L1$, $L2$, …) holes are indicated.

lamp *2* fell on semitransparent plate *5* and on sample *3* after being reflected from the plate. After being reflected from the sample, the light again passed through semitransparent plate *5* and followed the same path as during measurements of the transmission spectra. The highest signal-to-noise ratio was provided by the choice of the voltage supplied to the photomultiplier and by cooling the latter with the vapor of boiling liquid nitrogen. The measurements were carried out with the width of the monochromator slit set at 50–200 μm, which corresponded to an optical width of a slit of 0.3–1.0 Å (0.2–0.5 meV). The instrument-related lineshape had a half-width of 0.2 meV.

The quality of the optical spectra measured was substantially different for various samples. Figure 4 shows the most clearly pronounced spectra of reflection R and transmission T measured for normal incidence of light on sample I and normalized to unity for convenience. In the resonance region of these spectra, Fabry–Perot oscillations caused by the finite thickness of the structure are clearly seen. It should be noted that the interference peak in the reflection spectrum corresponds to the interference minimum in the transmission spectrum. To obtain a spectrum of optical density (absorption coefficient) free of the modulation effect of Fabry–Perot interference, the measured spectra of reflection R and transmission T were processed. The optical density was calculated from the formula [20]

$$D = -\ln\left(\frac{-(1-R)(1-R_b) + \sqrt{(1-R)^2(1-R_b)^2 + 4R_bT^2}}{2R_bT}\right), \tag{19}$$

where $R_b = (\sqrt{\varepsilon_b} - 1)^2/(\sqrt{\varepsilon_b} + 1)^2$ is the reflectance of light from a semi-infinite medium with the permittivity ε_b.

In Fig. 5, curve *1* represents the experimental spectrum of optical density calculated from formula (19) using the spectra shown in Fig. 4. The experimental spectrum in Fig. 5 is compared with the theoretical spectrum $\alpha_N a$ calculated from formulas (16)–(18) with the parameters corresponding to sample I ($N = 15$) and to a single QW ($N = 1$). The parameters of excitons of the ZnSe QW in function (1) were calculated by fitting theoretical spectrum (18) to experimental spectrum (19) so that the peak positions coincided and their shape was similar. The absorption coefficient in Fig. 5, which was calculated from formula (18), features many peaks,

Fitted values of parameters obtained for the $ZnSe/ZnS_xSe_{1-x}$ sample ($N = 15$, $a = 15$ nm)

$\hbar\omega_0^{(h)}$, eV	$\hbar\omega_0^{(l)}$, eV	$M^{(h)}/m_0$	$M^{(l)}/m_0$	$\hbar\omega_{LT}^{(h)}$, meV	$\hbar\omega_{LT}^{(l)}$, meV	$\hbar\Gamma^{(h)}$, meV	$\hbar\Gamma^{(l)}$, meV
2.8086	2.8242	0.70	0.57	1.8	1.5	1.1	1.7

which belong to the levels of dimensional quantization (15) of heavy ($H1$, $H2$, …) and light ($L1$, $L2$, …) excitons. The obtained values of fitting parameters of excitons for sample I are listed in the table. The parameters for sample II differ insignificantly, whereas the structure of spectra for sample III was insufficiently clear for reliable fitting.

Let us discuss the results listed in the table and certain relevant estimates. The translation mass obtained for the heavy exciton $M^{(h)} = 0.7m_0$ is within the range of magnitudes $M^{(h)}$ found from various optical experiments for the [100] direction in bulk ZnSe [14]. The translation mass of the light exciton $M^{(l)} = 0.57m_0$ is somewhat larger than for bulk samples [14]. However, this mass is close to $M^{(l)} = 0.6m_0$ obtained by Lankes *et al.* for a single wide QW [9]. As was already noted, the energy-band structure with $\omega_0^{(h)} < \omega_0^{(l)}$ corresponds to the lateral compression of ZnSe QWs in the heterostructures under consideration. Using the model of deformation potential [10], the strain $e_{xx} = e_{yy} = -2.9 \times 10^{-3}$ is found for sample I. This magnitude corresponds to splitting of valence subbands $E_v^{(l)} - E_v^{(h)} \approx -\Delta_e$ equal to –15.6 eV and to the shift of the valence band δE_g^v = 13.6 meV. For these experimental parameters for the exciton Rydberg energy $Ry^* = E_g + \delta E_g^v \mp \Delta_e/2 - \hbar\omega_0^{(h,l)}$, we obtain a value of 17.2 meV, which practically coincides with the value of 17.4 meV known for bulk excitons [21]. From a linear interpolation between the band parameters of ZnSe and ZnS [22] for the ZnS_xSe_{1-x} solid solution, the value $x \approx 0.10$ is found for the samples under investigation. This corresponds to a lattice constant of 5.65 Å, and the band gap of the barrier layer $E_g(ZnSe_{0.9}S_{0.1}) = 2.93$ eV. The separate variation in background permittivities of QWs ε_0 and barrier layers ε_b showed that the difference between these permittivities is insignificant.

In conclusion, let us discuss the damping parameters of excitons $\hbar\Gamma^{(j)}$ from the table, which considerably exceed the values 0.2 meV [23] or 0.4 meV [15] known for bulk excitons in ZnSe. According to the table, the condition $\omega_{LT}^{(l)} < \Gamma^{(l)}$ is satisfied for the light exciton. This could cast doubt on the existence of a polariton, if we interpret the value of $\Gamma^{(l)}$ as a true parameter of exciton damping. For the heavy exciton, the parameters listed in the table yield $\Gamma_c^{(h)} \lesssim \Gamma^{(h)}$, where

$$\Gamma_c^{(h)} = 2\omega_0^{(h)}\sqrt{2\varepsilon_0\hbar\omega_{LT}^{(h)}/(M^{(h)}c^2)}$$

is the critical value of the parameter of dissipative damping for a bulk exciton; if this value is exceeded, the effects of spatial dispersion in the propagation of polaritons vanish [24]. However, our experimental spectra show that this is not the case: the multipeaked structure observed is caused precisely by the spatial dispersion and associated quantization (13). These two contradictions mean that the effective damping parameters $\Gamma^{(j)}$ given in the table are overestimated compared to the true values. The probable causes of the observed additional contribution to the width of exciton absorption lines are the radiation damping of excitons in QWs whose width is smaller than the wavelength of light, inhomogeneous broadening of exciton levels due to exciton potential fluctuations, and so on. A similar situation was noted for the case when the exciton parameters were determined from the spectrum of surface excitonic polaritons [15].

4. CONCLUSION

For $ZnSe/ZnS_xSe_{1-x}$ periodic structures, which consist of a small number of identical wide QWs, optical spectra of reflection and transmission are measured at 2 K. Due to elimination of the modulation caused by Fabry–Perot interference, optical density spectra with a multipeaked structure are obtained. To interpret the spectra of bounded superlattices, the matrix-transfer method is developed taking into account two exciton resonances that have almost the same frequencies; each of these resonances possesses its own spatial dispersion. For heterostructures based on II–VI cubic semiconductors, such resonance states are the heavy and the light excitons, which are related to hole subbands. The latter have a slight strain-induced splitting due to the lattice mismatch between the semiconductors. Based on this theory, the series of peaks observed in the absorption spectra are attributed to the levels of dimensional quantization of motion for both heavy- and light-hole excitons in wide quantum wells. In the context of the formalism developed, the effective translation masses of heavy and light excitons, as well as the parameters of their longitudinal–transverse splitting and damping in quantum wells, are determined.

ACKNOWLEDGMENTS

This study was supported by the Russian Foundation for Basic Research, project no. 02-02-17601 and 02-02-17635.

We thank S.V. Ivanov and S.V. Sorokin for preparing the samples for this research.

REFERENCES

1. E. L. Ivchenko and G. E. Pikus, *Superlattices and Other Heterostructures. Symmetry and Optical Phenomena*, 2nd ed. (Springer, Berlin, 1997).
2. E. L. Ivchenko and V. A. Kosobukin, Fiz. Tekh. Poluprovodn. (Leningrad) **22**, 24 (1988) [Sov. Phys. Semicond. **22**, 15 (1988)].
3. S. I. Pekar, *Crystal Optics and Additional Light Waves* (Naukova Dumka, Kiev, 1982).

4. V. A. Kiselev, B. S. Razbirin, and I. N. Ural'tsev, Pis'ma Zh. Éksp. Teor. Fiz. **18**, 504 (1973) [JETP Lett. **18**, 296 (1973)].
5. V. A. Kiselev, B. S. Razbirin, and I. N. Uraltsev, Phys. Status Solidi B **72**, 161 (1975).
6. Y. Chen, F. Bassani, J. Massies, *et al.*, Europhys. Lett. **14**, 483 (1991); A. Tredicucci, Y. Chen, F. Bassani, *et al.*, Phys. Rev. B **47**, 10348 (1993).
7. G. N. Aliev, N. V. Luk'yanova, R. P. Seisyan, *et al.*, Phys. Status Solidi A **164**, 193 (1997).
8. Y. Merle D'Aubigné, H. Mariette, N. Magnea, *et al.*, J. Cryst. Growth **101**, 650 (1990).
9. S. Lankes, M. Meier, T. Reisinger, and W. Gebhardt, J. Appl. Phys. **80**, 4049 (1996).
10. G. L. Bir and G. E. Pikus, *Symmetry and Strain-Induced Effects in Semiconductors* (Nauka, Moscow, 1972; Wiley, New York, 1975).
11. E. O. Kane, Phys. Rev. B **11**, 3850 (1975).
12. G. Fishman, Solid State Commun. **27**, 1097 (1978).
13. G. Palamidas and D. R. Tilley, J. Phys. C: Solid State Phys. **14**, 2951 (1981).
14. B. Sermage and G. Fishman, Phys. Rev. Lett. **43**, 1043 (1979); Phys. Rev. B **23**, 5107 (1981).
15. J. Lagois, Phys. Rev. B **23**, 5511 (1981).
16. R. P. Seĭsyan, *Spectroscopy of Diamagnetic Excitons* (Nauka, Moscow, 1984).
17. V. A. Kosobukin, Fiz. Tverd. Tela (St. Petersburg) **34**, 3107 (1992) [Sov. Phys. Solid State **34**, 1662 (1992)].
18. H. Mathieu, Y. Chen, J. Camassel, *et al.*, Phys. Rev. B **32**, 4042 (1985).
19. V. A. Kosobukin, Phys. Status Solidi B **208**, 271 (1998).
20. D. S. Gerber and G. N. Maracas, J. Quantum Electron. **29**, 2589 (1993).
21. *Landolt-Börnstein, Numerical Data and Functional Relationships in Science and Technology*, Ed. by K.-H. Hellwege (Springer, Berlin, 1982), Group III, Vol. 17b.
22. T.-Y. Chung, J. H. Oh, S.-G. Lee, *et al.*, Semicond. Sci. Technol. **12**, 701 (1997).
23. A. D'Andrea and R. Del Sole, Phys. Rev. B **25**, 3714 (1982).
24. N. N. Akhmediev, Zh. Éksp. Teor. Fiz. **79**, 1534 (1980) [Sov. Phys. JETP **52**, 773 (1980)].

Translated by N. Korovin

Semiconductors, Vol. 38, No. 2, 2004, pp. 232–236. Translated from Fizika i Tekhnika Poluprovodnikov, Vol. 38, No. 2, 2004, pp. 237–241.

PHYSICS OF SEMICONDUCTOR DEVICES

Ultrafast Electron Drift in Field-Effect Semiconductor Structures with a Sectioned Channel

V. A. Gergel', Yu. V. Gulyaev, A. P. Zelenyĭ, and M. N. Yakupov*

Institute of Radio Engineering and Electronics, Russian Academy of Sciences, ul. Mokhovaya 18, Moscow, 101999 Russia

**e-mail: yamt@mail.ru*

Submitted May 27, 2003; accepted for publication May 27, 2003

Abstract—Characteristic features of high-field electron drift in specific semiconductor structures were studied. In these structures, the drift region with a relatively high resistivity is separated into several nanometer regions by a corresponding number of low-resistivity inclusions of nanometer length. It is shown that the electron temperature significantly decreases in the low-resistivity regions through which electrons drift, which ensures conservation of high electron mobility in the high-resistivity regions. As a result, the well-known effect of reduction of the electron mobility is suppressed, and it becomes possible to attain relatively high (significantly exceeding the saturation velocity) effective drift velocities of electrons. *© 2004 MAIK "Nauka/Interperiodica".*

1. PRINCIPLE OF LOCAL COOLING

As is well known, the increase in the transconductance and operating speed of field transistors is one of the main areas of development of microelectronic technologies. This goal can be attained by minimizing the transistor-channel length using all the possibilities of modern lithography and materials with high carrier mobility; i.e., by using High Electron Mobility Transistor (HEMT) technology. Modern technology provides minimum channel length $L_g \approx 0.1$–0.2 μm and maximum electron mobility $\mu \approx 10^5$ cm^2/(V s) at $T = 77$ K and $\mu \approx 10^4$ cm^2/(V s) at $T = 300$ K in a 2D electron gas at the GaAs/AlGaAs interface. With characteristic operating voltages $V \simeq 1$V, the limiting frequency $f_T = \frac{\mu V}{2\pi L^2}$ corresponding to these parameters should amount to thousands of gigahertz, which would more than satisfy the requirements for existing and future transfer- and processing-data systems. However, the Joule heating of electrons in strong electric fields (~10^5 V/cm) in the channel reduces the effective electron mobility to $\mu \approx 10^2$ cm^2/(V s) and, hence, the limiting frequency to 150–180 GHz. At first glance, the fundamental nature of the mobility reduction in strong fields and the difficulties involved in significantly reducing the channel length by increasing the lithography resolution limit the operating speed of field transistors to values of a few hundred gigahertz.

The above considerations refer to conventional transistor technology, i.e., to devices with uniform distribution of the gate parameters along the channel length. Let us now assume that we can form a number of local independent regions in the transistor channel with a higher conductivity (and, accordingly, a higher electron density n) compared to the average conductivity. In this case, the channel will have the form of a succession of alternating high- and low-resistivity regions of approximately equal length l (about 20–70 nm). Obviously, as follows from the current-conservation condition, the electric field E in the channel of this transistor will oscillate according to the ratio of electron densities; i.e., the strong electric field E_1 in the high-resistivity regions alternates with the weak field E_2 in the low-resistivity regions ($E_1/E_2 = n_2/n_1$), as is shown qualitatively in Fig. 1. We now consider the specific feature of the Joule heating of electrons in semiconductors that is of interest in this context. Specifically, electrons are heated to the quasi-steady-state temperature $T = T_0 + \mu E^2 \tau_0$ (T_0 is the equilibrium electron temperature) during the so-called energy relaxation time τ_0 rather than instantaneously. The energy relaxation time is defined

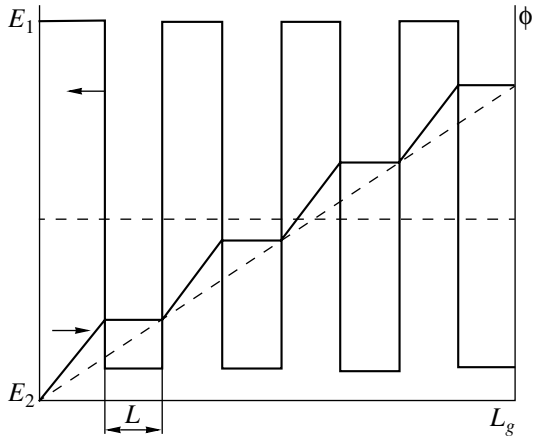

Fig. 1. Distributions of the potential ϕ and the electric field E in the channel of a profiled transistor; dashed lines show the corresponding distributions in a uniform channel.

as the time during which drifting electrons pass the distance $L_T = \mu E \tau_0$. It turns out that, if the electron density n_2 in low-resistivity inclusions is sufficiently high ($n_2 > 10n_1$), the following system of inequalities is satisfied: $L_{T_1} > l > L_{T_2}$. In this case, when electrons pass through a high-resistivity region, they do not have enough time to be heated to the high quasi-steady-state temperature $\mu E_1^2 \tau_0$ corresponding to the strong field $E_1 \approx 2V/L$. Thus, the drifting electrons acquire only a fairly low portion of thermal energy equal to $2V/5\nu$, where ν is the number of low-resistivity regions in the profiled channel under consideration. At the same time, when passing through a low-resistivity region, electrons have enough time to be cooled to low quasi-steady-state temperature $T_0 + \mu E_2^2 \tau_0$, which only slightly exceeds the equilibrium temperature T_0. Thus, the motion of electrons in a profiled channel with a strongly oscillating electric field will be characterized by the relatively low average electron temperature

$$T = T_0 + \mu E_2^2 \tau_0 + \frac{V}{5\nu}$$

with small ($\sim V/5\nu$) oscillations (Fig. 2). This circumstance ensures conservation of high electron mobility throughout the channel length, and, hence, a high average velocity of the peculiar electron drift with intermediate cooling of carriers along their path. The average velocity of this drift may significantly exceed the so-called saturation velocity $V_s \approx 10^7$ cm/s. It is precisely this phenomenon that is referred to in the title of this paper.

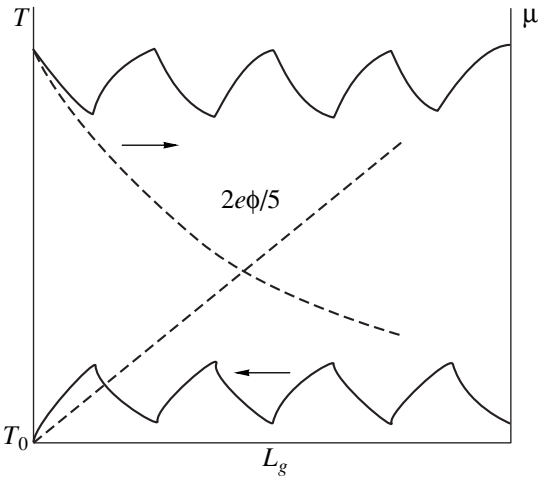

Fig. 2. Distributions of the electron temperature T and the mobility μ in a profiled transistor.

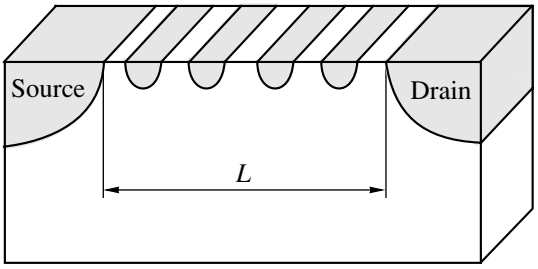

Fig. 3. Schematic representation of the gate region of a sectioned-channel MOS transistor.

2. SIMULATION OF THE CHARACTERISTICS OF A MOS TRANSISTOR WITH A SECTIONED CHANNEL

In the previous section, we formulated the basic concept of the possibility of significantly increasing the transconductance and operating speed of a field transistor by sectioning its channel with low-resistivity local inclusions, providing an efficient cooling of electrons and the corresponding increase in their mobility and drift velocity. The quantitative estimates of the advantages of the proposed structural modification of the transistor channel reported in [1] were based on the quasi-hydrodynamic (thermal) model of electron drift [2] disregarding the thermal relaxation and the thermal electron current. Nevertheless, these estimates reveal the main feature of the so-called overshoot effect [3]. The above consideration was restricted to the case of a constant average electric field, and only the ratio of the maximum and minimum electric fields sufficient for efficient cooling of carriers in low-resistivity regions was analyzed. However, it is well known [4] that, in the operating modes close to saturation, an electric field in the channel of a MOS transistor is strongly inhomogeneous (increases from the source to the drain). Basically, the average electric field in the structure sectioned by low-resistivity inclusions should have the same degree of inhomogeneity. In this section, we present a mathematical model for adequate calculation of the current–voltage (I–V) characteristics of a sectioned transistor, which takes into account the noted spatial inhomogeneity of the average field and provides corresponding test calculations of the I–V characteristics. These calculations demonstrate the advantages of the proposed sectioned structure, which include a high average carrier velocity in the transistor channel and a high transconductance.

We will consider a hypothetical transistor structure (Fig. 3) whose channel is separated into N parts by specific low-resistivity regions formed by corresponding local doping. The local-doping level and, accordingly, the conductivity of the doped regions are assumed to be quite high. In this case, we can disregard the voltage drop across these regions and assume that the electrons emerging from these regions are completely cooled (i.e., cooled to the equilibrium temperature). We then use the classical concepts of the electron drift in the channel of a MOS transistor [4] in the form

$$IL = C_0 \int_0^{V_D} \mu(V_G - \phi) d\phi, \qquad (1)$$

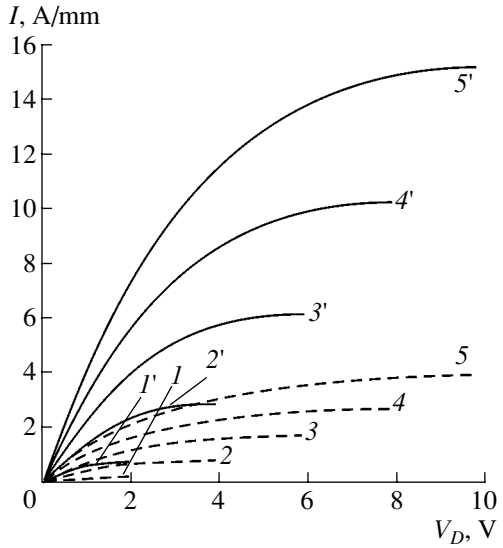

Fig. 4. Current–voltage characteristics of a sectioned (solid lines) and conventional (dashed lines) transistors. The gate voltage V_G = (*1*, *1*') 2, (*2*, *2*') 4, (*3*, *3*') 6, (*4*, *4*') 8, and (*5*, *5*') 10 V.

where V_D is the drain potential, and the ultraquasihydrodynamic dependence of the mobility on the potential (proposed by us in [2])

$$\mu \equiv \mu(\phi) = \frac{\mu_0}{\sqrt{1 + \dfrac{\phi}{\phi_0}}}, \tag{2}$$

where $\phi_0 = 5T_0/2 \approx 0.065$ V in the simplest case. On the basis of (1) and (2), the following equation for each high-resistivity region of the channel can be derived:

$$\frac{Il_i}{\mu_0 C_0} = \sqrt{\phi_0} \int_{V_{i-1}}^{V_i} \frac{V_G - \phi}{\sqrt{\phi_0 + \phi - V_{i-1}}} d\phi. \tag{3}$$

Here, as usual, I is the current density per unit channel width; C_0 and μ_0 are the specific capacitance of the oxide and the initial (weak-field) mobility, respectively; V_G is the gate voltage counted from the threshold value; l_i is the length of the ith high-resistivity section; V_{i-1} and V_i are the potentials at the boundaries of the ith section; and $i = \{1\ldots n\}$. The boundary conditions for this system of n equations are as follows: the potential at the beginning of the first section is equal to the source potential, i.e., to zero ($V_0 = 0$), and the potential at the end of the last section is equal to the drain potential ($V_n = V_D$).

We developed a very simple algorithm to successively solve system of equations (3), which consists in the following. For a certain value of the current I, the numerical integration of the first equation ($i = 1$) yields the value of V_1 that enters the second equation as a parameter. The solution to the second equation yields V_2, and so on up to $V_n = V_D$. Carrying out similar calculations for the corresponding sequence of currents, we can plot the sought current–voltage characteristic $I = I(V_G, V_D)$.

The corresponding test calculation was performed for a typical transistor structure with a channel of length $L = 0.95$ μm divided into ten high-resistivity sections of length $l_i = 50$ nm by nine low-resistivity inclusions of the same size. The specific capacitance was assumed to be equal to 3.5×10^{-7} F/cm, which corresponds to an oxide thickness of 10 nm. The initial mobility μ_0 was assumed to be equal to 700 cm^2/(V s), which is a typical value for an n-type inversion layer in Si ($\phi_0 = 0.2$ V corresponds to this value of μ_0). In this case, Eq. (3) acquires the form

$$I \approx 5 \int_{V_{i-1}}^{V_i} \frac{(V_G - \phi)}{\sqrt{1 + \dfrac{\phi - V_{i-1}}{0.2}}} d\phi, \tag{4}$$

where $i = \{1\ldots n\}$, the dimension of I is A/mm, and the voltage and potential are measured, as usual, in volts. The results of the numerical solution of system (4) for the characteristic values of the gate voltage V_G = 2–10 V are shown in Fig. 4. For comparison, the calculated I–V characteristics of a conventional MOS transistor with a uniform channel of the same length (0.95 μm), which correspond to the equation

$$I \approx \frac{5}{19} \int_0^{V_D} \frac{(V_G - \phi)}{\sqrt{1 + \dfrac{\phi}{0.2}}} d\phi \tag{5}$$

are shown by the dashed lines in Fig. 4. It can be seen that the current in a transistor with a sectioned channel significantly exceeds the current in a conventional structure. Figure 5 shows the dependences of the transconductance on the gate voltage,

$$S = \frac{\partial}{\partial V_G} I(V_D = V_G),$$

which demonstrates the extremely high transconductance of a structure with a sectioned channel compared to a conventional transistor with a uniform channel.

3. ANALYSIS OF THE RESULTS AND THE LIMITING POSSIBILITIES OF SECTIONING

We now return to the initial system of equations (3) in order to solve it analytically with corresponding simplifications and derive the corresponding formula, which will make it easier to understand and qualitatively analyze the features of high-field electron drift in a spatially inhomogeneous structure with low-resistivity sections.

For this purpose, we will use the current-conservation equation corresponding to expression (1)

$$I = C_0\mu_0\frac{(V_G-\phi)}{\sqrt{1+\dfrac{\phi-V_{i-1}}{\phi_0}}}\frac{d\phi}{dx} \quad (6)$$

as the initial equation. Let us replace the variable $(\phi - V_{i-1})$ under the root sign in (6) with its quantitative estimate $\alpha(V_i - V_{i-1})$, where α is a fitting coefficient of about 1/2. The quantity $\alpha(V_i - V_{i-1})$ corresponds to the average electron temperature in the ith high-resistivity region and, therefore, to the averaged local mobility

$$\mu = \frac{\mu_0}{\sqrt{1+\dfrac{\alpha(V_i-V_{i-1})}{\phi_0}}}. \quad (7)$$

Then, assuming that the electric field $d\phi/dx$ only weakly changes within one high-resistivity region, we will replace $V_i - V_{i-1}$ in expressions (6) and (7) with $\frac{d\phi}{dx}l_i$:

$$\frac{I}{C_0\mu_0} = \frac{(V_G-\phi)\dfrac{d\phi}{dx}}{\sqrt{1+\dfrac{\alpha l_i}{\phi_0}\dfrac{d\phi}{dx}}}. \quad (8)$$

After this procedure, expressions (6) and (8) are transformed into

$$\frac{d\phi}{dx}\frac{1}{2E_i}\left(\sqrt{1+4\frac{C_0^2\mu_0^2(V-\phi)^2}{I^2}E_i^2}-1\right) = 1, \quad (9)$$

where $E_i = \dfrac{\phi_0}{\alpha l_i}$.

If we assume that the active high-resistivity regions have the same length $l_i = l_0 \approx 50$ nm, the only thing to do is to integrate (9) over ϕ from 0 to V_D and over x from 0 to Nl_0. One can easily see that expression (9) can be integrated in quadratures, but, in this case, the general expression containing hyperbolic functions is too awkward to be used in subsequent qualitative analysis. Hence, instead of integrating, we will first write out the asymptotic solutions to (9) corresponding to two limiting cases.

(1) For low currents,

$$I = \frac{C_0\mu_0}{Nl_0}V_GV_D, \quad (10)$$

which coincides with the well-known expression from the theory of the ideal MOS transistor.

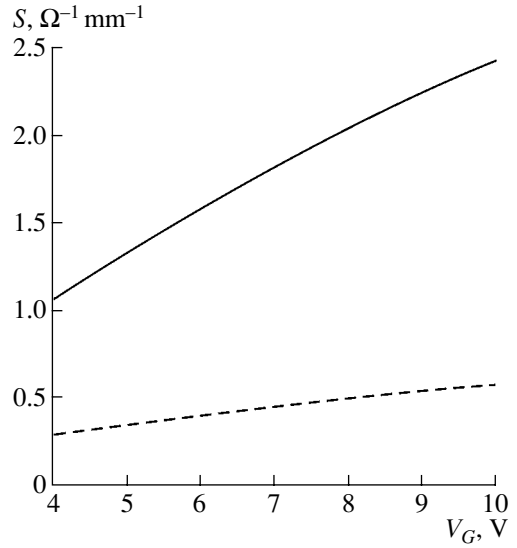

Fig. 5. Dependences of the maximum transconductance $S = \dfrac{\partial I}{\partial V_G}$ on the gate voltage V_G for sectioned (solid line) and conventional (dashed line) transistors.

(2) For high currents,

$$I = \frac{C_0\mu_0}{Nl_0}V_GV_D\sqrt{\frac{\phi_0 N}{\alpha V_D}\left(1-\frac{V_D}{V_G}+\frac{1}{3}\frac{V_D^2}{V_G^2}\right)}. \quad (11)$$

Matching solutions (10) and (11) according to the less-than-least rule, we obtain the resulting approximate expression for the current–voltage characteristic

$$I = \frac{2C_0\mu_0}{L}V_GV_D\sqrt{\frac{1-\dfrac{V_D}{V_G}+\dfrac{1}{3}\dfrac{V_D^2}{V_G^2}}{\dfrac{V_D\alpha}{\phi_0 N}+\left(1-\dfrac{V_D}{V_G}+\dfrac{1}{3}\dfrac{V_D^2}{V_G^2}\right)}}, \quad (12)$$

where the evident relation $2Nl_0 = L$ is used; L is the lithographic channel length (from source to drain).

The shape of the current–voltage curves corresponding to Eq. (12) is similar to that of the relevant dependences obtained by numerical integration (see Fig. 6); in this case, the quantitative correspondence is obtained at a quite realistic value of the fitting parameter $\alpha \approx 0.63$.

The value of the approximate formula (12) derived here for the current–voltage characteristic of a sectioned transistor lies in the fact that this formula makes it significantly easier to interpret the physical interpretation of the effect under consideration, specifically, the ultrafast electron drift. Formula (12) clearly demonstrates that cooling in low-resistivity regions significantly (by a factor of N) reduces the "heating" potential: $V_D \longrightarrow V_D/N$, which, respectively, expands the ini-

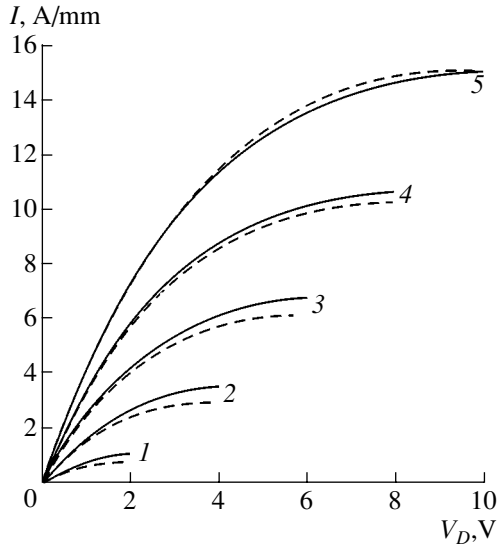

Fig. 6. Comparison of the current–voltage characteristics obtained by numerical analysis (dashed lines) and by using approximation (12) (solid lines). Designations 1–5 are the same as in Fig. 4.

tial portion of the characteristics responsible for the initial weak-field mobility μ_0 and reduces the decrease in μ_0 due to the heating at higher voltages by a factor of $\sqrt{N}$. For the case under consideration, this effect leads to values of the effective drift velocity of about 5×10^7 cm/s, which are almost five times greater than the saturation velocity in *n*-type inversion layers of conventional MOS transistors. Formula (12) also shows that the effective reduction (by a factor of 2 in our case) of the "electric" channel length (which, accordingly, doubles the value of the drawing electric field) plays a no less important role in the acceleration of electrons. In addition, formula (12) makes it possible to estimate easily the characteristic number of sections $N \approx \alpha V_D/\phi_0$ at which the decrease in the mobility due to heating of the electric field is suppressed almost completely. In this case, the *I–V* characteristic of the sectioned transistor under study transforms into the *I–V* characteristic of an ideal transistor with a halved channel length. It is clear that a further increase in *N* will not significantly improve the obtained ideal curve with extremely high transconductance. Obviously, high values of transconductance suggest high operating speeds.

4. CONCLUSION

In our opinion, the results of this study clearly and convincingly demonstrate the advantages of the highly promising concept that we have proposed. These results should stimulate the search for specific technical solutions for the practical implementation of the proposed concept.

ACKNOWLEDGMENTS

This study was supported by the Russian Foundation for Basic Research, project no. 01-02-16360.

REFERENCES

1. V. A. Gergel' and V. G. Mokerov, Dokl. Akad. Nauk **375**, 609 (2000) [Dokl. Phys. **45**, 647 (2000)].
2. V. A. Gergel', V. G. Mokerov, M. V. Timofeev, and Yu. V. Fedorov, Fiz. Tekh. Poluprovodn. (St. Petersburg) **34**, 239 (2000) [Semiconductors **34**, 233 (2000)].
3. T. Enoki, S. Sugitani, and Y. Yamane, IEEE Trans. Electron Devices **37**, 935 (1990).
4. S. M. Sze, *Physics of Semiconductor Devices*, 2nd ed. (Wiley, New York, 1981; Mir, Moscow, 1984).

Translated by Yu. Sin'kov

Semiconductors, Vol. 38, No. 2, 2004, pp. 237–238. Translated from Fizika i Tekhnika Poluprovodnikov, Vol. 38, No. 2, 2004, pp. 242–243.

PHYSICS OF SEMICONDUCTOR DEVICES

Experimental Study of SiC *p–i–n* Diodes in the 3-cm Range

K. V. Vasilevskiĭ*, P. B. Gamuletskaya, A. V. Kirillov**, A. A. Lebedev*, L. P. Romanov**, and V. A. Smirnov****

**Ioffe Physicotechnical Institute, Russian Academy of Sciences, St. Petersburg, 194021 Russia*

***Svetlana-Elektronpribor Closed Corporation, St. Petersburg, 194156 Russia*

Submitted May 28, 2003; accepted for publication June 2, 2003

Abstract—Results of an experimental study of SiC *p–i–n* diodes in a switch for the 3-cm range were studied in a slot line. The isolation ensured by the switch was found to be 18.5–23 dB at a control current of 100 mA. Comparative estimates of the series resistance of Si and SiC *p–i–n* diodes at 10 GHz and of their low-frequency differential resistance were made. © *2004 MAIK "Nauka/Interperiodica".*

It is known that, owing to its unique electrical parameters, silicon carbide is a promising material for power electronics [1]. However, the still high density of defects in epitaxial SiC structures is delaying the beginning of industrial manufacture of high-current devices from this material. At the same time, microwave devices, which have small geometrical dimensions, exhibit characteristics close to those predicted theoretically, and this circumstance has led to the swift development of SiC-based microwave devices.

In this study, the operation of a switch based on a SiC *p–i–n* diode was for the first time analyzed at frequencies of ~10 GHz. 4*H*-SiC *p–i–n* diode chips with mesa structures 60, 80, and 100 μm in diameter were soldered onto a $0.6 \times 0.8 \times 2$ mm^3 gold-plated copper holder. The technology of chip fabrication was described in detail in [2].

The study was carried out in a specially designed measuring chamber based on a slot line at microwave frequencies f = 9–10 GHz (3-cm range). The characteristic impedance of the line at the place of diode insertion into the microwave transmission line was 95 Ω. An additional capacitor was connected in series with the diode. Its capacitance was chosen in such a way that it ensured a series resonance in the frequency range f = 9–10 GHz. Since the reactances cancel out at the resonance frequency, the slot line is actually shunted by the low resistance of the forward-biased diode. In this case, the shunting loss resistance of the diode can be found from the known relation [3, 4]

$$L_f = \left(1 + \frac{W}{2R_g}\right)^2,$$

where L_f is the isolation; W, the characteristic impedance of the transmission line; and R_g, the loss resistance of the forward-biased diode at microwave frequencies.

Figure 1 shows how the loss resistance of the diode at microwave frequencies R_g depends on the control current for four SiC avalanche transit-time diode chips (sample nos. 8, 16, 18, and 21) and a commercial silicon *p–i–n* diode for the 3-cm range. It can be seen that the loss resistance of forward-biased SiC diodes (I_f = 100 mA) is approximately two times that for the silicon *p–i–n* diode. It is worth noting the weak dependence of the loss resistance on the control current. For example, with a control current varying from 1 to 100 mA (by two orders of magnitude), the loss resistance R_g changes by approximately a factor of 3 (from 5.4 to 1.7 Ω for the silicon *p–i–n* diode and from 8.6 to 3.6 Ω for the SiC avalanche transit-time diodes).

It follows from the data presented that the loss resistance of SiC *p–i–n* diodes at microwave frequencies is within 3.6–6.4 Ω at a current of 100 mA and 5–8.6 Ω at 1 mA.

Figure 2 shows for the same diodes the dependences of the differential resistance R_d at low frequency on forward current. It can be seen that the low-frequency differential resistance is approximately half the loss resistance of the diodes at microwave frequencies of 9–

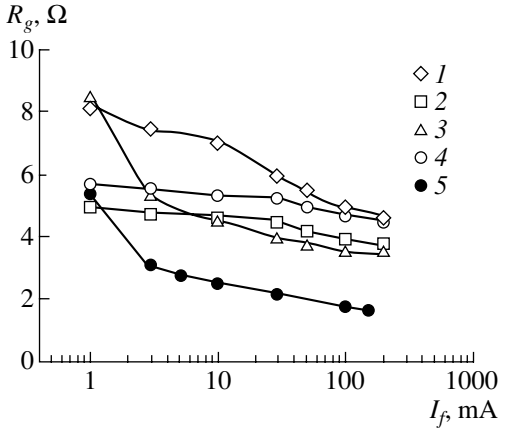

Fig. 1. Loss resistance of diodes at microwave frequencies vs. forward current. SiC diode nos.: (*1*) 8, (*2*) 16, (*3*) 18, and (*4*) 21; (*5*) Si *p–i–n* diode; the same for Fig. 2.

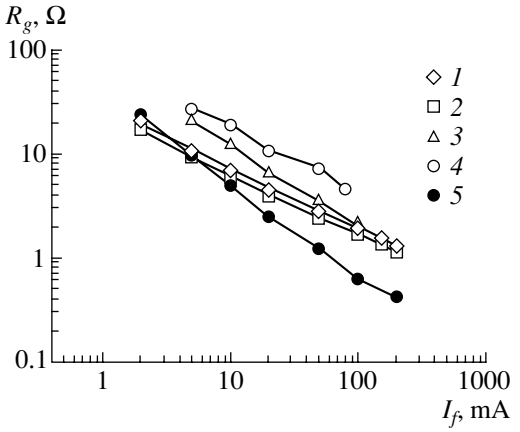

Fig. 2. Low-frequency differential resistance of diodes vs. forward current. Sample numbers of SiC diodes: (*1*) 8, (*2*) 16, (*3*) 18, and (*4*) 21; (*5*) corresponds to a Si *p–i–n* diode.

10 GHz, which agrees with the known data [5]. It is noteworthy that, with a current varying from 1 to 100 mA (by two orders of magnitude), the differential resistance at low frequency changes by a factor of 30, and the loss resistance at microwave frequencies, by only a factor of 3.

The table lists the results of measurements of the isolation ensured by the switch at a resonance frequency of 9.6 GHz, with SiC *p–i–n* diodes and a commercial silicon *p–i–n* diode used as switching elements.

It follows from the data presented that a switch based on a commercial silicon *p–i–n* diode ensures much higher isolation (28.6 dB), which is due to its lower series loss resistance.

The problem of the insertion loss of the switch (loss in the unactuated state) was disregarded, since the structure capacitance of the SiC diodes under study was absolutely unacceptable for the 3-cm range (several picofarads), which led to high insertion loss (3 to 10 dB).

Measured isolation losses

Samples	SiC *p–i–n* diodes						Si *p–i–n* diodes
	8	16	17	18	20	21	
L_f, dB	20.4	22.3	18.5	23.0	19.7	20.6	28.6

Note: I_f = 100 mA, f = 9.5 GHz.

It should be noted for comparison that a switch based on a commercial silicon *p–i–n* diode with a structure capacitance of 0.2 pF is characterized by a loss of 0.5 dB, i.e., is an order of magnitude lower.

The results obtained in the study of SiC *p–i–n* diodes at microwave frequencies led to the following conclusions.

(1) The loss resistance of the SiC diodes studied at frequencies of 9–10 GHz is 2–3.5 times that for a commercial Si *p–i–n* diode intended for operation in the same frequency range.

(2) The values obtained for the series loss resistance of SiC diodes make it possible to develop on the basis of a slot line a switch for the 9- to 10-GHz range, with an isolation of 18.5–23 dB, whereas a switch based on the silicon *p–i–n* diode considered above ensures much higher isolation (28.6 dB) in the same frequency range.

(3) On the whole, the possibility of using SiC *p–i–n* diodes as microwave switches was demonstrated for the first time. These devices have advantages over Si-based devices because of their higher working temperatures and better radiation hardness. However, to create a switch based on SiC *p–i–n* diodes, which would ensure the same isolation as that in Si diodes, it is necessary to make the differential resistance of the SiC diodes a factor of 2–3 lower.

This study was supported by INTAS (project 01-603) and NATO (project SfP-978011).

REFERENCES

1. A. A. Lebedev and V. E. Chelnokov, Fiz. Tekh. Poluprovodn. (St. Petersburg) **33**, 1096 (1999) [Semiconductors **33**, 999 (1999)].
2. K. Vasilevski, K. Zekentes, G. Constantinidis, and A. Strel'chuk, Solid-State Electron. **44**, 1173 (2000).
3. G. B. Dzekhtser and O. S. Orlov, *P-I-N Diodes in Broadband Devices* (Sovetskoe Radio, Moscow, 1970).
4. *Microwave Devices on the Basis of Semiconductor Diodes: Design and Calculation*, Ed. by N. V. Mol'skiĭ and B. V. Sestroretskiĭ (Sovetskoe Radio, Moscow, 1969).
5. V. A. Vaĭsblat, *Microwave Commutation Devices on the Basis of Semiconductor Diodes* (Radio i Svyaz', Moscow, 1987).

Translated by M. Tagirdzhanov

Semiconductors, Vol. 38, No. 2, 2004, pp. 239–242. Translated from Fizika i Tekhnika Poluprovodnikov, Vol. 38, No. 2, 2004, pp. 244–248.

PHYSICS OF SEMICONDUCTOR DEVICES

Nonlinear Generation of Far Infrared Mode in Double-Frequency Heterojunction Lasers

A. A. Afonenko*, V. Ya. Aleshkin^, and A. A. Dubinov**^^**

**Belarusian State University, pr. Fr. Scorini 4, Minsk, 220050 Belarus*

e-mail: afonenko@bsu.by

***Institute for Physics of Microstructures, Russian Academy of Sciences, Nizhni Novgorod, 603950 Russia*

^e-mail: aleshkin@ipm.sci-nnov.ru

^^e-mail: sanya@ ipm.sci-nnov.ru

Submitted May 27, 2003; accepted for publication June 18, 2003

Abstract—Nonlinear generation of the difference mode in an injection semiconductor laser is studied. A design of laser based on an InGaAs–GaAs–InGaP heterostructure is suggested; this design provides for the presence of two modes in 1 μm region and the initiation of the difference plasma mode in the ranges 15–35 and 45–80 μm. It is shown that the power of the difference mode generated by 10-W short-wavelength modes in a 100-μm-wide waveguide at room temperature can be ~1 μW. *© 2004 MAIK "Nauka/Interperiodica".*

INTRODUCTION

Semiconductor lasers operating in the medium and far-infrared (IR) regions attract considerable interest in view of their high potential in the field of communications, gas analysis, and spectroscopy applications. Cascade medium-IR lasers capable of room-temperature operation have been successfully implemented [1], while the generation of far-IR lasers based on cascade structures has been achieved only at cryogenic temperatures [2]. The operation range of far-IR lasers based on a *p*-Ge structure [3, 4] is also restricted to cryogenic temperatures. An alternative approach to obtaining medium- and far-IR radiation, which may provide room-temperature lasing, is to make use of nonlinear effects. For example, the difference mode can be generated in a two-mode short-wavelength laser by using the electronic nonlinearity in a three-level quantum well (QW) [5] or the nonlinear properties of a semiconductor material of the active region [6].

In order to attain effective nonlinear generation, the phase-matching condition should be satisfied, which presents a difficulty in a medium with normal dispersion of the refractive index, since the phase velocity of the nonlinear polarization wave is lower than that of the difference mode. According to [6], the phase-matching condition can be met by using the fundamental short-wavelength mode ω_1 and a side mode with $\omega_2 > \omega_1$. In this case, the interaction between 10-W high-frequency (of ~1 μm) modes induces the difference mode at ~10 μm with a power of 100 μW for the absorption coefficient ~10 cm^{-1}. However, for longer wavelengths, the difference mode is less compactly localized in the vicinity of the active region and the conversion efficiency is lower.

One minor shortcoming of the method suggested in [6] is the small factor of overlap between the nonlinear polarization wave at the difference frequency and the waveguide mode being excited. This smallness is due to two reasons. First, the nonlinear polarization at the difference frequency is proportional to the product of the near orthogonal modes, and this fact changes the polarization sign in the direction across the layers at the scale of the high-frequency width of the waveguide layer. Second, the spatial period of changes in the difference mode in this direction considerably exceeds that in the polarization wave. Furthermore, the parameters of the dielectric waveguide suggested in [6] are very sensitive to the configuration of the structure, so that even a small variation in the thickness of layers may decrease the output power by several orders of magnitude. The latter circumstance stems from the fact that, in such a waveguide, the phase-matching condition is met for a single separate mode only.

In this study, we suggest meeting the phase-matching condition using an alternative method based on the properties of the long-wavelength plasmon waves in doped semiconductor crystals. An advantage of this method is that the phase velocity of the difference frequency wave can be readily controlled by varying the permittivity, which is attained by doping. The second advantage is that the low-frequency difference mode is generated by two fundamental high-frequency modes, ω_1 and ω_2, and the overlap factor for the difference mode is not small (the high-frequency modes are not orthogonal). The third benefit of the method suggested is the possibility of realizing a situation where the phase-matching condition is met for a number of adjacent modes. In this case, the power is a slowly varying function of frequency and the output power is not very

1063-7826/04/3802-0239$26.00 © 2004 MAIK "Nauka/Interperiodica"

sensitive to variations in the structure parameters. The results of our calculations indicate that, under the phase-matching condition and at the high-frequency modes generated with a power of 10 W in a 1-μm region, the difference mode can be generated with a power of ~1 μW in the ranges 15–35 and 45–80 μm in lasers with a 100-μm-wide waveguide.

2. RETARDATION OF MODES IN A PLASMA WAVEGUIDE

Plasmon modes exist at the interface between media with permittivities ε_a and ε_b of opposite signs. In the simplest case of the material contact, the propagation constant of the difference mode $\omega = \omega_2 - \omega_1$ is defined by [7]

$$k^2 = \frac{\omega^2}{c^2}\frac{|\varepsilon_b|\varepsilon_a}{|\varepsilon_b| - \varepsilon_a}. \quad (1)$$

To retard the mode, i.e., to make k appreciably higher than the propagation constant in material a, $k_a = \sqrt{\varepsilon_a}\,\omega/c$, requires the permittivity ε_b to be comparable in absolute value to ε_a. Therefore, no metal can be used as a medium with negative permittivity, since $|\varepsilon_b| \gg 1$ and $k \approx k_a$ in this case.

By appropriate doping of semiconductors, one can obtain a material with negative permittivity of a given magnitude in the IR spectral region. A simple estimate of the contribution of the plasma of free carriers and optical phonons to the permittivity is provided by the Drude formula, which is applicable both to *n*- and *p*-type semiconductor materials [8–10]:

$$\varepsilon(\omega) = \varepsilon_\infty + \frac{\omega_{TO}^2(\varepsilon_0 - \varepsilon_\infty)}{\omega_{TO}^2 - \omega^2 - i\Gamma\omega} - \frac{\omega_p^2\varepsilon_\infty}{\omega^2 + i\gamma\omega}, \quad (2)$$

where ε_0 and ε_∞ are the low- and the high-frequency permittivities of undoped semiconductor material, ω_{TO} is the transverse optical-phonon frequency, Γ is the factor of the phonon-induced attenuation of the wave, $\gamma = q/m^*\mu$ is the factor of wave attenuation due to the free-carrier absorption, $\omega_p^2 = 4\pi nq^2/m^*\varepsilon_\infty$ is the squared plasma frequency, n and m^* are the density and the effective mass of the charge carriers, and q is the elementary charge. The values of Γ and ω_{TO} were taken from review [8], and the value of γ was determined from the data on the mobility as a function of the dopant concentration [11]. The absorption spectrum calculated on the basis of formula (2) is in good agreement with the experimental dependences [8] with the exception of multiphoton effects, which have only a slight influence on the absorption.

3. CALCULATION OF THE DIFFERENCE MODE POWER

In the case when the laser structure is grown on a (001)-plane substrate and the high-frequency modes have TE polarization, the nonlinear polarization in GaAs is normal to the plane of layers and the TM mode is generated at the difference frequency [6]. The coordinate dependence of the magnetic field strength in the thus generated wave H_y can be determined from the equation

$$\varepsilon(z,\omega)\frac{d}{dz}\frac{1}{\varepsilon(z,\omega)}\frac{dH_y}{dz} + \left(\varepsilon(z,\omega)\frac{\omega^2}{c^2} - k_x^2\right)H_y = -2\varepsilon^{(2)}\frac{k_x\omega}{c}A_1^*(z)A_2(z). \quad (3)$$

Here, the z axis is directed along the crystallographic direction [001] and $\varepsilon^{(2)}$ is the nonlinear susceptibility. The coordinate dependences of the electric field amplitudes in high-frequency modes A_1 and A_2, as well as the difference between their propagation constants $k_x = k_2 - k_1$, are determined by solving the wave equation with a particular refractive-index profile. The electric field component of the difference mode E_z and its power P are defined by expressions

$$E_z = -\frac{1}{\varepsilon(z,\omega)}\left(\frac{ck_x}{\omega}H_y + 2\varepsilon^{(2)}A_1^*(z)A_2(z)\right) \quad (4)$$

and

$$P = -\frac{cL_y}{2\pi}\int_{-\infty}^{\infty}\mathrm{Re}(H_yE_z^*)dz, \quad (5)$$

where L_y is the width of the laser-diode stripe contact.

The table lists the parameters of the InGaAs–GaAs–InGaP heterostructure. In order to generate short-wavelength modes by two spectrally spaced wavelengths, the active region should include InGaAs–GaAs QWs of two types. The waveguide for short-wavelength radiation is formed by sandwiching the narrow-gap GaAs between the wide-gap InGAP emitter layers with a lower refractive index. The following expressions for the refractive indices of GaAs [11] and InGaP were used:

$$n_{GaAs}(\hbar\omega) = \sqrt{7.1 + \frac{3.78}{1 - 0.18(\hbar\omega)^2}}, \quad (6)$$
$$n_{InGaP}(\hbar\omega) = n_{GaAs}(\hbar\omega) - 0.3.$$

The heavily doped GaAs layer, which forms the plasma waveguide for the difference mode, also serves as a contact *n*-type layer to the structure grown on semi-insulating gallium arsenide.

The effective refractive index of the difference polarization wave $n_{eff} = (k_{2x} - k_{1x})/(\omega_2 - \omega_1)$ is defined by the "high-frequency" structure of the laser and is almost independent of the plasma waveguide design. According to Fig. 1, the effective refractive index

Characteristics of heterostructure layers

No. of layer	Material	Thickness of the layer, μm	Doping		Mobility, $cm^2/(V\ s)$
			type	concentration, cm^{-3}	
1	Au	1	–	–	–
2	GaAs	0.1	*p*	1×10^{18}	156
3	InGaP	0.6	*p*	5×10^{16}	64
4	GaAs, 2 QWs	0.8	*n*	3×10^{16}	6556
5	InGaP	0.6	*n*	5×10^{16}	755
6	GaAs	2	*n*	5×10^{18}	2917
7	GaAs	–	*n*	5×10^{16}	6111

shows a weak linear dependence on the photon energy of the plasma wave and is approximately equal to the group refractive index of the high-frequency modes.

We calculate the medium- and far-IR permittivity of InGaP under the assumption that half the TO phonons in the solid solution are taken such as they are in InP and the other half, as in GaP; i.e., we disregarded the variations in interatomic distances compared to those in the binary InP and GaP compounds. The total permittivity was calculated as the average of those for InP and GaP. In reality, the material of solid solution is inhomogeneous: it consists of ordered and unordered phases in which even the band-gap widths are considerably different. We failed to find any references to studies on refractive index in this context.

It should be noted that, in order to reduce the losses, the concentration of dopant was lower than usual. The resulting large valence-band offset in the InGaP–GaAs system gives rise to a potential barrier to holes and, thus, inhibits the injection of carriers into the active region. This circumstance causes the formation of a 3-nm-thick layer enriched with holes with a typical concentration of 4×10^{13} cm^{-2} at the heterojunction. However, estimates show that this layer makes no significant contribution to the absorption and the effective refractive index for the plasma modes and, hence, can be disregarded in the following calculation.

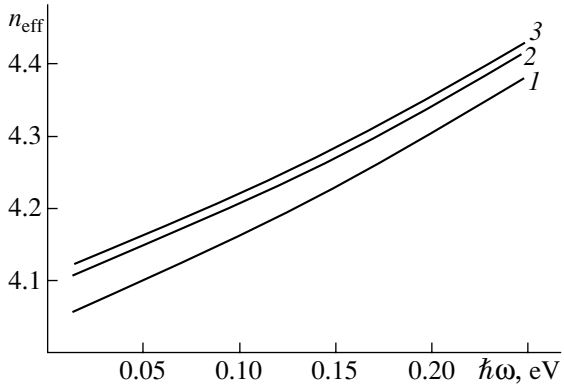

Fig. 1. The effective refractive index for the difference polarization wave vs. the photon energy for the GaAs central-layer thickness of (*1*) 0.2, (*2*) 0.5, and (*3*) 1 μm. The high-frequency mode with longest wavelength $\lambda_1 = 1$ μm is fixed.

The calculated difference-mode power is shown in Fig. 2. The spectral dependence of power features a number of resonance peaks. With the exception of the peak with the shortest wavelength, all peaks are related to the anomalous-dispersion regions that are present in InP and GaAs. As the doping level of the plasma waveguide increases, the resonances shift to shorter wavelengths. Despite the fact that only two fundamental short-wavelength modes are required to obtain nonlinear polarization, the resulting powers turn out to be an order of magnitude lower than those attained in the 10-μm region in [6]. This fact is attributed to an appreciable increase in the free-carrier absorption as one proceeds to the far IR spectral region: for example, even in a lightly doped semiconductor, losses at a wavelength of 50 μm are more than 20 times higher than those at 10 μm.

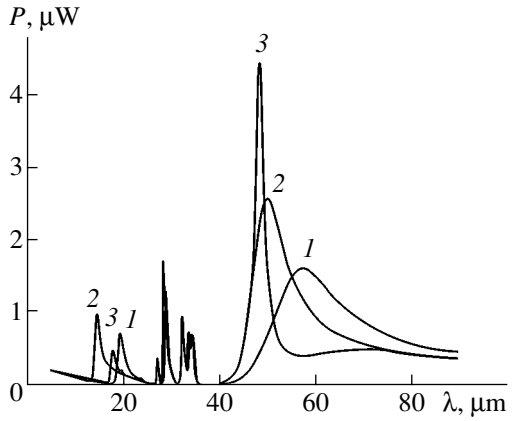

Fig. 2. The difference mode power vs. the wavelength in heterostructures with different parameters: (*1*) in accordance with the table, (*2*) the electron concentration in layer 6 is $n = 2 \times 10^{19}$ cm^{-3}, (*3*) the electron concentration in layer 7 is $n = 1 \times 10^{14}$ cm^{-3} and layer 6 is 0.8-μm-thick. $\varepsilon^{(2)}_{GaAs} = 1.7 \times 10^{-8}$ cm/V, $L_y = 100$ μm, and $\lambda_1 = 1$ μm.

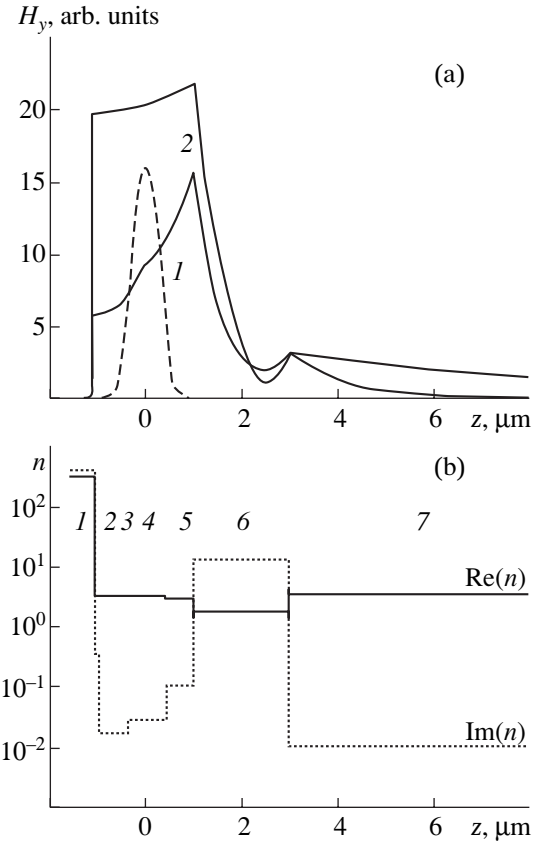

Fig. 3. (a) Spatial profiles of the absolute value of the magnetic field strength in the difference mode generated at (*1*) 20 and (*2*) 58 μm (the amplitude of high-frequency modes is shown in arbitrary units by dashed line); (b) the real and imaginary parts of the refractive index *n* at the wavelength 58 μm (the layers are numbered in accordance with the table data).

Because of the high absorption coefficients, the resonance peak in the surface-wave power spectrum is fairly broad. Specifically, in a structure with the parameters listed in the table, the surface-wave power decreases only by half within the wavelength range 50–70 μm. This means that the output power only slightly depends on the parameters of the system in a wide range of values.

On the one hand, the phonon absorption exerts a detrimental effect in the range ~40 μm inducing a dip in the generation power. On the other hand, due to the anomalous dispersion in the long-wavelength region adjacent to the peak of the photon absorption, the refractive index is considerably increased as compared to its high-frequency value. As a result, the velocity required for phase matching is attained even at a smaller fraction of the wave located in the heavily doped material (Fig. 3), which leads to a certain reduction of the effective mode loss factor and increases the lasing power.

Furthermore, by using a semi-insulating substrate instead of the doped one and increasing, by appropriate choice of the parameters, the fraction of IR radiation propagating in the substrate, one can reduce the effective mode loss and raise the peak power of generation to 4.5 μW (Fig. 2). At the same time, the resonance shifts to the shorter wavelengths (~48 μm) and the generation peak narrows substantially.

CONCLUSION

The suggested design of semiconductor injection laser provides for the output power of ~1 μW in the far-IR region at room temperature. Only the fundamental short-wavelength modes in a 1-μm range are used to obtain nonlinear polarization. The phase-matching condition is met due to the slowing down of the long-wavelength IR radiation in a plasma waveguide. The generation power is only slightly dependent on the system parameters in a wide range of their values.

ACKNOWLEDGMENTS

This study was supported by the Russian Foundation for Basic Research–Belarusian Republican Foundation for Fundamental Research, program F02R-095, project no. 02-02-81036; the Ministry of Industry and Science of the Russian Federation; the Program "Low-Dimensional Quantum Structures" of the Presidium of the Russian Academy of Sciences (RAS); the RAS Physical Sciences Division "Semiconductor Lasers" Program; and International Science and Technology Center (ISTC), project no. 2293.

REFERENCES

1. F. Capasso, A. Tredicucci, C. Gmachl, *et al.*, IEEE J. Sel. Top. Quantum Electron. **5**, 792 (1999).
2. M. Rochat, L. Ajili, H. Willenberg, and J. Faist, Appl. Phys. Lett. **81**, 1381 (2002).
3. A. Andronov and E. Gornik, Opt. Quantum Electron. **23** (2) (1991).
4. I. V. Altukhov, M. S. Kagan, K. A. Korolev, *et al.*, Zh. Éksp. Teor. Fiz. **101**, 756 (1992) [Sov. Phys. JETP **74**, 404 (1992)].
5. A. A. Belyanin, F. Capasso, V. V. Kocharovsky, *et al.*, Phys. Rev. A **63**, 053803 (2001).
6. V. Ya. Aleshkin, A. A. Afonenko, and N. B. Zvonkov, Fiz. Tekh. Poluprovodn. (St. Petersburg) **35**, 1256 (2001) [Semiconductors **35**, 1203 (2001)].
7. L. D. Landau and E. M. Lifshitz, *Course of Theoretical Physics*, Vol. 8: *Electrodynamics of Continuous Media*, 2nd ed. (Nauka, Moscow, 1982; Pergamon Press, Oxford, 1984), Chap. 10.
8. J. S. Blackmore, J. Appl. Phys. **53**, R123 (1982).
9. H. R. Chandrasekhar and A. K. Ramdas, Phys. Rev. B **21**, 1511 (1980).
10. W. Songprakob, R. Zallen, W. K. Liu, and K. L. Bacher, Phys. Rev. B **62**, 4501 (2000).
11. A. Dargys and J. Kundrotas, *Handbook on Physical Properties of Ge, Si, GaAs, and InP* (Science and Encyclopedia, Vilnius, 1994).

Translated by A. Sidorova

Semiconductors, Vol. 38, No. 2, 2004, pp. 243–244. Translated from Fizika i Tekhnika Poluprovodnikov, Vol. 38, No. 2, 2004, p. 249.

PERSONALIA

Vitaliĭ Ivanovich Stafeev (on his 75th birthday)

Vitaliĭ Ivanovich Stafeev was 75 on his last birthday (January 1, 2004); in addition, 50 years have passed since the beginning of his scientific, teaching, and organizational activity. Stafeev is a prominent scientist, professor, doctor of science (physics and mathematics), honored scientist of the Russian Federation, and recipient of State Prizes of the USSR and a State Prize of the Russian Federation. He has made an outstanding contribution to the development of semiconductor physics, semiconductor electronics, microelectronics, and photoelectronics.

Stafeev was born January 1, 1929. After graduating in 1952 from the physicomathematical faculty of Kazakh State University in Alma-Ata, he was assigned to the Ioffe Physicotechnical Institute of the USSR Academy of Sciences and worked there until 1964. In 1964, he was appointed the director of the Research Institute of Physical Problems. In 1969, he transferred to the Research Institute of Applied Physics (now, the State Scientific Center NPO Orion) and still works there at present.

Stafeev is a founder of a scientific school. His pupils include more than 20 doctors of science and several dozen candidates of science. He is an author of more than ten monographs and of several hundred scientific papers and inventions. His most important achievements include the following:

(i) Theoretical and experimental studies of long-base diodes. These studies led to the discovery of mechanisms of internal amplification of signals and to the development of internationally recognized new devices, e.g., magnetodiodes, injection-based photodetectors, and diodes with *S*-type characteristics.

(ii) Studies of properties of hot charge carriers in semiconductors. These studies led to the development of lasers operating in the far-infrared region of the spectrum and fast-acting modulators of infrared radiation.

(iii) Development and investigation of photodetectors, including injection-based photodiodes for the ultraviolet region of the spectrum on the basis of III–V compounds.

(iv) Development and investigation of semiconductor analogues of neurons and the circuit and system engineering based on these analogues. These studies were performed before similar publications dealing with neuron networks appeared in foreign journals.

(v) Studies of molecular films (the Langmuir–Blodgett films) and of the feasibility of using these films in microelectronic devices.

(vi) Research in the field of phase transitions and nucleation of condensed phases (including biological media).

(vii) Prediction and discovery of a new physical phenomenon (i.e., injection-related heat transport in structures with *p*–*n* junctions) and the use of this phenomenon in a novel class of semiconductor-based cooling devices.

(viii) Initiation and management of research and development in the field of narrow-gap semiconductors in the Soviet Union: organization of research and advanced development; organization of All-Union special symposia, workshops, and schools; and foundation of an affiliated branch of the Research Institute of Applied Physics in Baku (now, the Institute of Photoelectronics, Academy of Sciences of Azerbaijan).

The following scientific achievements of Stafeev were awarded State Prizes:

(I) Development of technology and organization of production of both the new microphotoelectronic semiconductor CdHgTe and photodetectors (including photodetector arrays) based on this compound and designed for operation in the 3–5 and 8–12 μm spectral regions for modern thermal-imaging systems (2000).

(II) Development of the scientific basis and technology and also organization of commercial production of magnetoresistve sensors (1982).

(III) Discovery and investigation of a new class of materials, specifically, zero-gap semiconductors (1976).

Stafeev was awarded a medal “for devoted work” for his scientific activity that was related to the first nuclear submarine (1958–1959) and initiated the development of high-power semiconductor electronics in the Soviet Union.

He was awarded a Lebedev medal for outstanding achievements in the field of applied physical optics.

Stafeev made an outstanding contribution to the foundation of the Research Center for Microelectronics at Zelenograd. He was a founder and the first director of the Research Institute for Physical Problems; the chairman of Interdepartmental Coordination Council

1063-7826/04/3802-0243$26.00

on Microelectronics; an initiator of the publication of *Mikroélektronika*, a collection of scientific and technical papers; an organizer and the editor-in-chief of the 22nd series of the journal *Voprosy Oboronnoĭ Tekhniki, Mikroélektronika* (Issues in Military Technology, Microelectronics); a founder and the first head of the basic microelectronics department at the Moscow Physicotechnical Institute; and the chairman of the Microelectronics Section in the Council for Semiconductor Physics at the Presidium of the Academy of Sciences of the Soviet Union.

Stafeev was a member of the council of experts on the Committee for the Lenin and State Prizes of the Soviet Union, a member of the council of experts on the Supreme Attestation Commission, and a member of the editorial boards of the journals *Fizika i Tekhnika Poluprovodnikov* and *Radiotekhnika i Élektronika.*

Academician Zh.I. Alferov

Professor L.E. Vorob'ev

Editorial board of the journal
Fizika i Tekhnika Poluprovodnikov

Translated by A. Spitsyn